Measuring and modelling deformation during the Dabbahu (Afar) rifting episode

Ian James Hamling

Submitted in accordance with the requirements for the degree of
Doctor of Philosophy

The University of Leeds

School of Earth and Environment

April 2010

Declaration

The candidate confirms that the work submitted is his own, except where work which has formed part of jointly-authored publications has been included. The contribution of the candidate and the other authors to this work has been explicitly indicated overleaf. The candidate confirms that appropriate credit has been given within the thesis where reference has been made to the work of others.

Chapter 3 contains material from the publication:

- **Hamling. I. J., Ayele. A., Bennati. L., Calais. E., Ebinger. C. J., Keir., Lewi. E., Wright. T. J., Yirgu. G.**. 2009 Geodetic observations of the ongoing Dabbahu rifting episode: new dyke intrusions in 2006 and 2007. Geophysical Journal International. **178**, 989-1003.

In this work Laura Bennati and Eric Calais collected and processed all of the GPS data; Atalay Ayele, Cynthia Ebinger, Derek Keir, Elias Lewi and Gezaheyn Yirgu provided comments on the text; Tim Wright provided the code which was used by Ian Hamling to produce the models for each of the dyke intrusions who also wrote the article.

The first part of Chapter 4 contains material from the publication:

- **Hamling. I. J., Wright. T. J., Calais. E., Bennati. L., Lewi. E.,**. 2010 Testing whether stress controls the location of magmatic intrusions. Submitted to Nature Geoscience

In this work Ian Hamling and Tim Wright processed the InSAR data. Laura Bennati and Eric Calais and Elias Lewi collected and processed all of the GPS data; Ian Hamling carried out the elastic modelling and wrote the article.

Acknowledgements

Firstly I'd like to thank my supervisors Dr Tim Wright and Professor Greg Houseman, without their support and patience this work would not have been possible. I am eternally grateful for the opportunities and knowledge you have shared with me and for your guidance and advice over the past three years. I hope that I will be able to continue our work together and, perhaps, one day return to Leeds.

I am also grateful to Eric Calais and Laura Bennati for providing GPS data used in this thesis and to the rest of the Afar Consortium for providing stimulating conversion, not to mention some rather off key singing! I have had numerous useful discussions about all aspects of dyke intrusion and East Africa with Roger Buck, Joe Cann, Cindy Ebinger, Eleonora Rivalta, Derek Keir, Dave Cornwell, Carolina Pagli and Locko Neuberg for which I am extremely grateful. My thanks also go to Jon Mound for agreeing to be my internal examiner and to Andy Hooper who stepped in at the last minute to be my external.

I would like to acknowledge NERC and COMET for the studentship that has provided financial support over the past three years and for additional funding for field work and conferences. I also thank the RAS for providing additional funding to attend the AGU meeting in 2009.

There are too many people to thank individually for all the support and entertainment over the last three years, however, since this is the most read part of the thesis I will give it a go! Thanks to all the guys in the office both past and present (in no particular order): Chris, Kirsty, Carl (Q man), Tom (Q boy), Matt (InSAR boy), Paddy (Montserrat man), Ben (mwaaahh man), Sheona, Barbara (the Hoff), Hannah, Julia, Dulce and all the others who have helped make the last three years some of the best I've ever had. Thanks also to the bar staff across Leeds who have helped maintain a certain level of sanity amongst all of those named above. To Claire, for all your love, support and gentle pushing to keep me focussed over the last few months. I don't think I could have done it without you. Finally, I thank my parents and brother. Without your love and support, none of this would have been possible.

Abstract

In September 2005, a 60-km-long dyke intruded the Dabbahu segment of the Nubia-Arabia plate boundary (Afar, Ethiopia), marking the beginning of an ongoing rifting episode. Continued activity has been monitored using Satellite Radar Interferometry, GPS instruments and seismometers deployed around the rift in response to the initial intrusion. These data show that a sequence of 12 new dyke intrusions have reintruded the central and southern section of the Dabbahu segment. Modelling of InSAR data indicates the dykes were between 0.5 and 3 m wide, up to ∼10 km long and confined to the upper 10 km of crust. Seismicity data imply that the dykes were probably fed from a source near the centre of the segment. The new dykes are concentrated in areas where the 2005 dyke did not produce significant opening, implying that residual tensile tectonic stresses are higher in this location and are focusing the later intrusions. Geodetic data, which quantify the location and extension occurring in each of the events, allows the identification of regions where tensile stress has been increased. Here I demonstrate for the first time the high probability of a link involving stress transfer and dyke intrusions.

Since the September 2005 intrusion, background displacement rates are significantly larger than the average secular divergence between Nubia and Arabia. Some of this deformation can be explained using viscoelastic models, which suggest an elastic crustal thickness of 13 km and upper mantle viscosity of $10^{18.5}$ Pas. The presence of multiple magmatic sources around the rift zone, however, cause large residuals between the data and model suggesting that viscoelastic relaxation alone cannot account for the observed deformation. It is likely that, with a continued magma supply, dykes will continue to be intruded until the tectonic stress is fully relieved with more eruptions as the rifting episode is concluded.

Contents

List of Figures

List of Tables

Chapter 1

Introduction

1.1 Overview

Oceanic lithosphere, which covers over two-thirds of the Earth's surface (Fig. 1.1), is formed beneath mid-ocean ridges through the upwelling of hot mantle rocks which ascend to fill the gap between separating tectonic plates. A decrease in pressure, generated as the rock ascends, causes the rock to intersect the solidus temperature and melt (Turcotte & Schubert, 2002). The newly formed magma, predominately of basaltic composition, rises up into vertical cracks in the form of dykes which, together with faulting, accommodate the increasing separation between the plates.

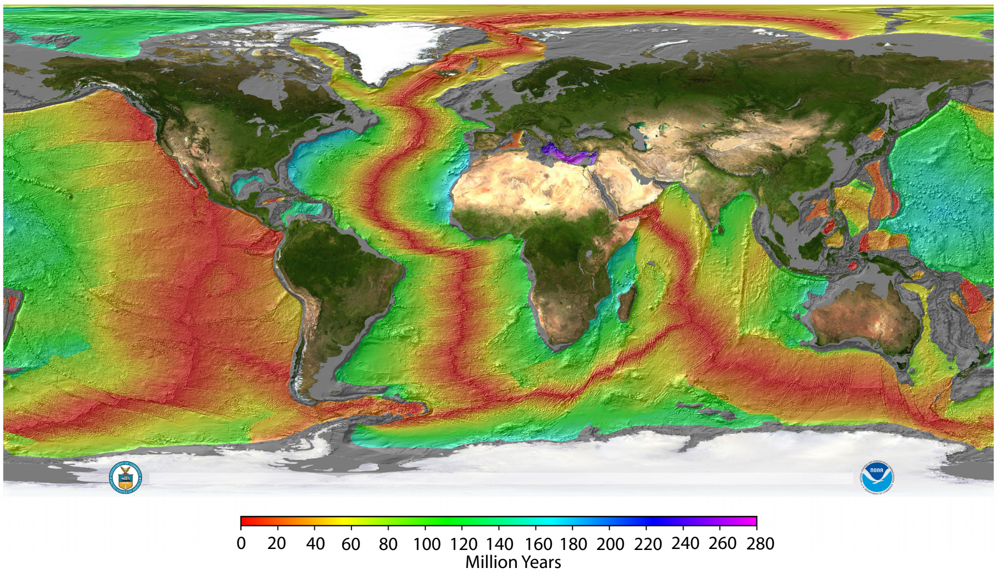

Figure 1.1: Age-area distribution of Oceanic Lithosphere. Image created by Elliot Lim, Cooperative Institute for Research in Environmental Sciences, NOAA National Geophysical Data Center (NGDC) Marine geology and geophysics division. Data source (Muller et al., 2008)

The 80,000 km-long mid-ocean ridge systems is not continuous but split into 30-80 km-long, 2nd-3rd order magmatic segments separated by large transform zones (Schouten et al., 1985). The gross morphology of the along axis spreading centre is thought to be controlled primarily by the spreading rates which, in turn, are governed by the generation, storage and eruption of magma along the plate boundary (Macdonald, 1982). Despite the large proportion of the Earth covered by oceanic lithosphere our understanding of the processes involved in oceanic rifting is constrained by a few, albeit well documented, episodes along segments of the Juan de Fuca ridge (e.g. Dziak et al., 1995, 2007), East Pacific Rise (e.g. Dziak et al., 2009; Tolstoy et al., 2006) and Mid-Atlantic Ridge (e.g. Dziak et al., 2004; Tolstoy et al., 2001). However, sub-aerial rifting episodes provide the rare opportunity to examine the tectonic and magmatic processes at mid-ocean ridges without the use of submersible instruments. The most recent known examples occurred at Krafla, Northern Iceland, where a series of 20 dykes were intruded over a 9 year period from 1975 (Buck et al., 2006; Einarsson & Brandsdóttir, 1980; Tryggvason, 1984) and in the Asal rift, Ethiopia, in 1978, where 2 m of extension was achieved with the intrusion of a dyke along a new eruptive centre (Abdallah et al., 1979; Cattin et al., 2005a; Vigny et al., 2007).

In this chapter I will discuss some of the mechanisms thought to be responsible for seafloor spreading and continental rifting, examine the rifting cycle at divergent plate boundaries and present an overview of the structure and geology of the Red Sea and East African Rift system. In the final part of the chapter I will discuss the September 2005 rifting event which occurred along the Dabbahu rift segment in Afar and summarise the work which will be presented in later Chapters.

1.2 Seafloor Spreading and Continental Rifting

1.2.1 Seafloor Spreading

Early observations, which led to the theory of Plate Tectonics (Wegener, 1929), noted that the coasts of Europe and West Africa matched the shape of the coasts of North and South America. This revelation implied that the continents could be split apart allowing the formation of oceanic crust. It is estimated that ∼20 km^3 of new basaltic material is emplaced along the Earth's mid-ocean ridge systems every year (Crisp, 1984). Models describing the petrological processes at ocean ridges suggest that hot asthenosheric material rapidly ascends through a narrow zone beneath the spreading centre. As it ascends, it passes through the basalt melting curve generating a molten fraction with basaltic composition. As the asthenospheric material continues to rise the proportion of melt increases causing its volume to increases (Cann, 1970). Eventually the basaltic component departs its parental material to form a magma chamber within the lower part of oceanic crust (Cann, 1970, 1974). The presence of magma chambers beneath ocean ridges is now widely accepted and have been imaged beneath slow (Singh et al., 2006), intermediate (Canales et al., 2005; Collier & Sinha, 1990) and fast (Detrick et al., 1987; Kent et al., 2000) spreading centres. It is from these chambers where magma is episodically intruded into the overlying crust toward the seafloor to form dykes (Cann, 1970, 1974; Delaney et al., 1998). Although these rifting events are widespread, only a few episodes have ever been detected (e.g Dziak et al., 1995, 2004, 2007; Nooner & Chadwick, 2010; Tolstoy et al., 2001) making it difficult to understand the dynamics of seafloor spreading. Pressure sensors deployed around the Juan de Fuca ridge in the Pacific ocean have been used to monitor volcanic uplift along Axial Seamount (e.g. Nooner & Chadwick, 2010) with some success but lack the resolution required to fully constrain the processes at work.

1.2.2 Continental Rifting

In the case where rifting has progressed to seafloor spreading a rift may be described as a zone where the entire lithosphere has ruptured in extension (Burke, 1977). Alternatively, a more generic definition may be an elongated depression where the entire lithosphere has been modified by extension (Olsen & Morgan, 1995). Many models have been proposed to explain the mechanical processes of continental extension. The simplest models assume the rapid stretching of the lithosphere and upwelling of asthenospheric material (e.g. McKenzie, 1978). Although these models have been able to explain many features observed along continental rifts and passive margins recent observations show that most margins and rift zones involve large volumes of magmatism which, in some cases, predate the onset of faulting and subsidence (e.g. Segnör & Burke, 1978). For example, data collected both on and offshore the North American East Coast, once thought to be a non-volcanic margin, indicate large volumes of magma as is observed at other continental margins (Holbrook & Kelemen, 1993). Furthermore, early rifting along the Red Sea is associated with large volumes of flood basalts and dyke intrusions (Menzies et al., 1992; Pallister, 1987) and yet models of rifting along the Red Sea chose initially to ignore the effects of magma (e.g. Buck et al., 1988; Chery et al., 1992; Steckler, 1985; Wernicke, 1985).

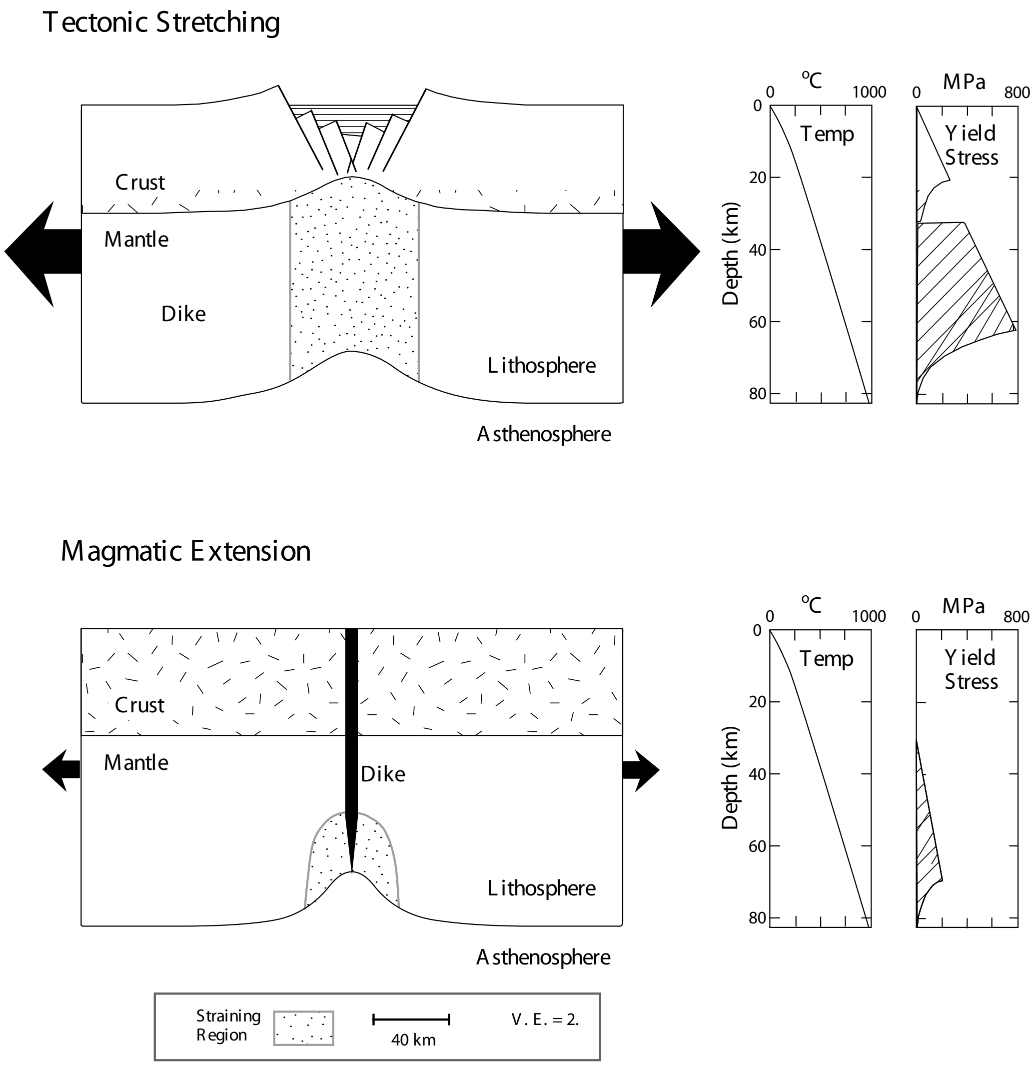

Figure 1.2: Schematic of the difference between extension of thick lithosphere with and without magmatic intrusion. Note the large difference in the yield stress, the stress difference needed to get extensional separation of two lithospheric blocks after Buck (2004).

Tectonic forces available to initiate continental rifting, thought to be generated at plate boundaries, are of the order 3-5 TN/m (Forsyth & Uyeda, 1975; Solomon et al., 1980). If the lithosphere is thin or there is a high heat flow it may be possible for rifting to initiate at these forces; however, for thick lithosphere with normal heat flow the potential driving force available may be substantially lower than that needed for amagmatic extension to occur (Hooper & Buck, 1993; Kusznir & Park, 1987). By introducing melt into the system the deformation of the lithosphere will occur not only by fault slip and ductile flow (e.g. Kusznir & Ziegler, 1992) but also by magmatic intrusions (e.g. Buck, 2004). The magma assisted rifting model proposed by Buck (2004) (Fig. 1.2) shows a significant reduction in the yield stress for the lithosphere (the deviatoric extensional stresses at a given depth required for the separation of two lithospheric blocks). In this model magma initially intrudes the lower lithosphere where it feeds dykes which intrude to higher levels. As the lithosphere continues to stretch, through distributed pure shear, the strength of the plate is reduced through heat transfer and lithospheric thinning, enabling the magma to be intruded to shallower levels. The buoyancy forces generated by the melt, at least to mid-crustal levels, reinforce the plate driving forces compared with friction on fault surfaces which oppose the plate separation. Thus, magmatic injection permits greater strain at lower driving forces than faulting (Buck, 2004; Ebinger, 2005).

1.3 The Rifting Cycle

Over the last few decades it has become apparent that rifting episodes, like those observed in Iceland, are cyclic and may only occur every 10^{2-3}yrs (Sigmundsson, 2006). These episodes are key to understanding the processes involved in generating new oceanic crust and provides important constraints on the rheology in an area of incipient seafloor spreading. The deformation associated with the rifting cycle can be described in terms of the inter-rifting, pre-rifting, co-rifting and post-rifting deformation. During the inter-rifting period steady state extension is observed across the plate boundary equivalent to the average long term spreading rate; the pre-rifting period may only occur in the months or weeks preceding the co-rifting episode and is frequently characterised by localised deformation beneath the rift zone resulting from the shallow accumulation of magma. The co-rifting period can occur over a few weeks or over a number of years and is often associated with multiple dyke injections (Buck et al., 2006; Einarsson & Brandsdóttir, 1980; Hamling et al., 2009; Tryggvason, 1984) but may also consist of a single dyke intrusion (Abdallah et al., 1979; Biggs et al., 2009; Cattin et al., 2005a; Vigny et al., 2007). Following the rifting episode the post-rifting period is characterised by increased spreading rates across the plate boundary and may continue for decades until all of the stresses are relieved.

1.3.1 Inter-rifting deformation

The volcanic systems of Iceland have been extensively studied over the past few decades and show all stages of the rifting cycle. The eastern volcanic zone (EVZ) in southern

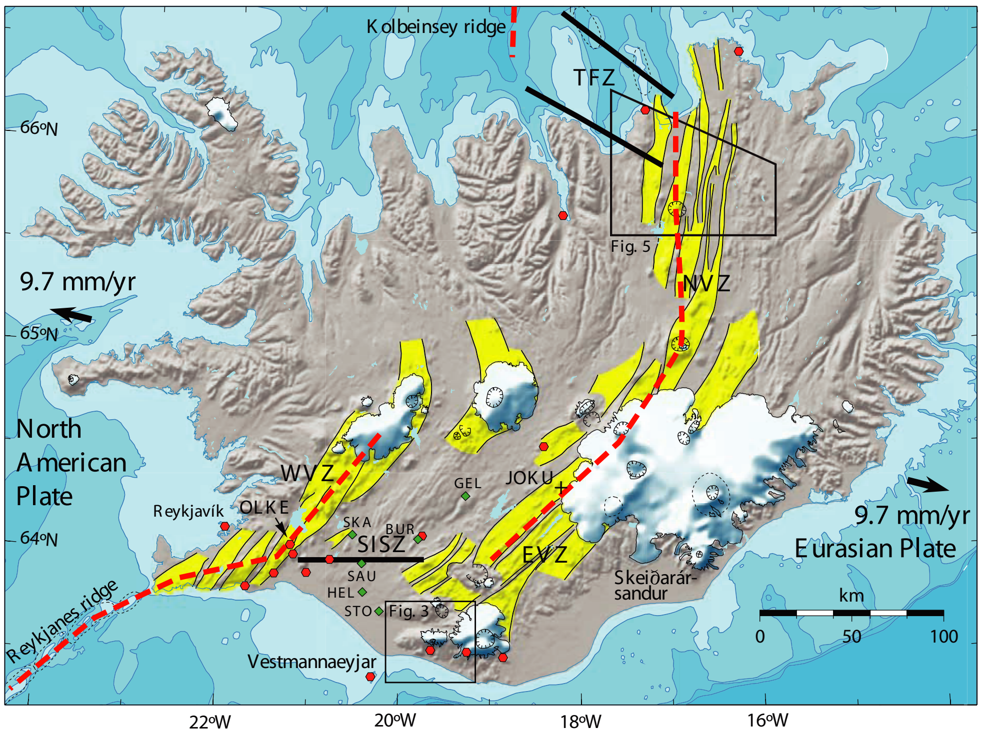

Figure 1.3: Map of Iceland with the general outline of the volcanic systems (in yellow, along the plate boundary (dashed red line), which is offset by two transform fault systems (black lines). The neovolcanic zone across Iceland is divided into the northern volcanic zone (NVZ), the western volcanic zone (WVZ) and the eastern volcanic zone (EVZ). The EVZ and the WVZ are parallel and connected by the south Iceland Seismic zone (SISZ), a transform fault zone, after Sturkell et al. (2006)

Iceland is the most representative of the inter-rifting period with the last rifting episode occurring 150 yrs ago. GPS measurements across the EVZ reveal spreading rates of ∼20 mm/yr. Using a model with an elastic crust overlying a viscoelastic substrate LaFemina et al. (2005) were able to reproduce the horizontal deformation field. However, this simple model is unable to explain the subsidence, associated with plate separation, observed along many of the volcanic systems (e.g. Hreinsdóttir et al., 2001; Pagli et al., 2006; Vadon & Sigmundsson, 1997).

A large number of early models used to describe deformation across rift zones neglect the vertical deformation due to the errors associated with GPS measurements. However, over the last few years the use of InSAR combined with improvements in the accuracy of the vertical component of GPS has provided the opportunity to model both the horizontal and vertical components of the deformation field. A recent study of the northern volcanic zone (NVZ), Iceland, used a combination of InSAR and GPS to improve the estimates of

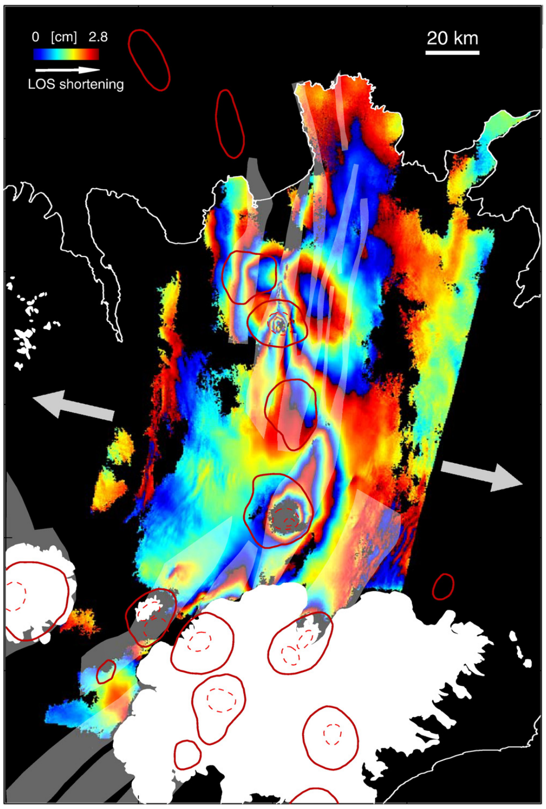

Figure 1.4: Conventional interferogram from the NVZ. The image is showing 5 years of surface deformation in the plate boundary area from 26/06/1993 - 18/08/1998, after Pedersen et al. (2009)

vertical deformation across the plate boundary. Using this improved data set Pedersen et al. (2009) have incorporated laterally varying rheologies into 3D viscoelastic models to explain the focused subsidence observed along the Krafla fissure swarms (Fig. 1.4). However, such focussed subsidence could also be explained by the movement of magma beneath the segment as has been suggested under the Askja fissure swarm (Pagli et al., 2006).

1.3.2 Rifting episodes

There have been a number of well documented sub-aerial rifting episodes along divergent plate boundaries over the last few hundred years. One of the earliest on record occurred within the EVZ, Iceland, along the Laki fissure system during the 18th century. The 8-month-long Laki eruption, occurred between June 1783 and February 1784, had an eruptive volume of ~14.7±1 km^3 (Thordarson & Self, 2003) and caused the deaths of thousands of people across Europe including ~20% of the Icelandic population (Hálfdánarson, 1984). During the 1970s and 80s a major rifting episode occurred along the Krafla volcanic system in northern Iceland (e.g. Björnsson et al., 1979; Einarsson, 1978, 1991; Tryggvason, 1980) and in 1978 a portion of the Asal rift in Afar, east Africa, ruptured leading to 2 m of extension associated with the intrusion of a dyke at a new eruptive centre (Abdallah et al., 1979; Cattin et al., 2005a; Vigny et al., 2007). More recently a dyke was intruded along an immature section of the East African Rift (EAR) system within the Natron Basin, Tanzania (Baer et al., 2008; Biggs et al., 2009; Calais et al., 2008).

Unlike the episodes in Laki and East Africa, which lasted a few months with only one major dyking event, the Krafla episode occurred over a period of 9 years and resulted in the injection of 20 discrete dykes. The Krafla system lies within the Northern Volcanic Zone (NVZ, Fig. 1.3) and, as with most of the volcanic systems across Iceland, is characterised by fissure swarms that run along the plate boundary, and a central volcano (Björnsson et al., 1977). During the Krafla magmatic-tectonic event a shallow magma chamber beneath the volcano's caldera, thought to reside at ∼3 km depth (Brandsdóttir et al., 1997; Einarsson, 1978), steadily inflated between sudden deflation events when the magma was laterally intruded along the fissure swarms to the north and south. The episode began on 20 December 1975 with a small eruption within the Krafla caldera coincident with rapid deflation and the lateral injection of magma along the fissure swarms (Björnsson et al., 1977). Over the next 5 years a further 11 intrusions were detected (Fig. 1.5), each affecting only a portion of the volcanic system (Björnsson et al., 1979; Einarsson, 1991; Tryggvason, 1980). After 1980 the style of rifting became more eruptive with a series of fissure eruptions which concluded the episode. Over the 9 year episode a total of 20 dyke intrusions resulted in the widening of the fissure swarm by up to 9 m (Tryggvason, 1994) and the emplacement of an estimated 1.1 km^3 of new material along the fissure swarm with a further 0.25 km^3 of basaltic lavas erupted on the surface (Tryggvason, 1984).

1.3.3 Post-rifting deformation

In the years following the Krafla rifting episode a number of GPS surveys were conducted and revealed increased spreading rates across the plate boundary. A network of 40 GPS sites, concentrated within the Krafla volcanic system but extending 130 km onto the neighbouring plates, was measured in 1987 and remeasured in 1990. Over this period

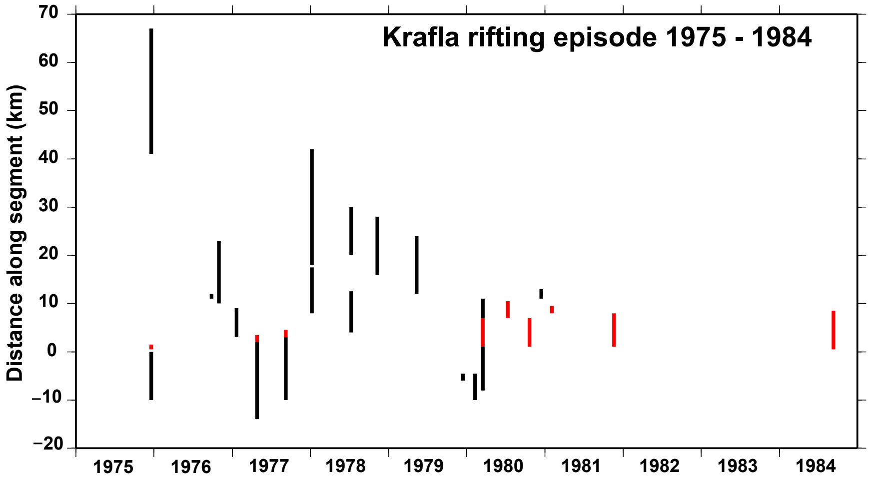

Figure 1.5: Along-strike movement of dyking activity with time during the 1974 - 1989 Krafla episode, (after Einarsson (1991)). Black lines show the length of each dyke without extrusion of lava, red lines show length of dyke with extrusion.

the extension rates were up to three times the average spreading rate (1.9 cm/yr) an observation that has been explained by the transient post-rifting stress relaxation (Foulger et al., 1992). There have been a number of attempts to model the stress relaxation signal following the Krafla rifting event using the GPS derived deformation field (Foulger et al., 1992; Hofton & Foulger, 1996a,b; Pollitz & Sacks, 1996) and more recently using the deformation observed by InSAR (de Zeeuw-van Dalfsen et al., 2004). Early modelling by Foulger et al. (1992) used a simple 2 layer model consisting of an elastic layer over a Newtonian viscous layer which rests on a rigid substratum. The stress relaxation is then initiated by dyke opening in the elastic layer. More recent modelling efforts have considered the viscoelasticty of the underlying mantle. Hofton & Foulger (1996a,b) used a 10 km thick uniform elastic layer and estimated the underlying material to have a viscosity of 1.1 $\times 10^{18}$ Pas while Pollitz & Sacks (1996) have used a three layer model and produce a viscosity of 3 $\times 10^{19}$ Pas and 3 $\times 10^{18}$ Pas for the lower crust and mantle respectively. Other models use elastic dislocation models to simulate the gradual opening of a dyke at depth. de Zeeuw-van Dalfsen et al. (2004) explained the post-rifting deformation across the Krafla volcanic system with a dyke opening at rates of 3.4 cm/yr between 1993-1999 decreasing to 2.7 cm/yr between 1996-1999. A similar model was considered for the post-rifting deformation following the Asal rifting event (Cattin et al., 2005a) and for the Dabbahu rifting episode in Afar by Nooner et al. (2009). In the Dabbahu case, the model required opening at depths between 20-25 km and was thought implausible as it would require opening below the Moho, therefore it was discounted for a more realistic viscoelastic relaxation model.

1.4 The Red Sea and East African Rift (EAR)

The East African Rift system (EARS) offers the opportunity to study all stages of continental breakup from young fault systems all the way through to sea-floor spreading in the Red Sea and Gulf of Aden. The surface expression of the EAR can be traced by a series of adjoining tectonic basins or rift valleys that stretch from the Afar triple junction in the north to the Zambezi fault in Southern Africa (Chorowitz, 2005) (Fig. 1.6). The EAR is composed of two main sections: the ~2200 km-long Eastern branch and the ~2100 km-long Western branch. The eastern branch runs from the Afar triangle through the Main Ethiopian Rift (MER), the Omo-Turkana lows, the Kenyan and Gregory rifts and ends in the basins of the North-Tanzanian divergence zone, while the Western branch runs from Lake Albert to Lake Malawi in the south (Chorowitz, 2005)(Fig. 1.6).

1.4.1 The Red Sea

The Red Sea forms a 250-450 km elongate north-west trending basin between the Arabian and African shields (Ghebread, 1998)(Fig. 1.6). From as early as 1929 the Red Sea has been regarded as an example of where two continents have split apart (Wegener, 1929) and was one of the first places to be described in terms of plate tectonics (McKenzie et al., 1970).

There are few constraints on the timing of the breakup between Nubia and Arabia. Estimates from volcanic sequences from the southern Red Sea suggest that breakup began at 26-18 Ma (Utstins et al., 2002) while Hughes et al. (1991) suggest 27.5-23 Ma based on detailed biostratigraphy of exploration wells. The Red Sea can be divided into distinct zones, each with a characteristic morphology and structure (Cochran, 1983; Cochran et al., 1986; Ghebread, 1998). 1) *Late stage continental rifting*: The northern Red Sea is characterised by a simple trough structure, whilst there is no evidence for a spreading centre a number of deeps have been identified from bathymetric data (Girdler & Southren, 1987). 2) *Transition Zone*: A transition zone has been identified in the central Red Sea between 20°N and 20°30'N where the axial trough become discontinuous in a complex transform zone. 3) *Active sea floor spreading*: Rifting in the southern Red Sea

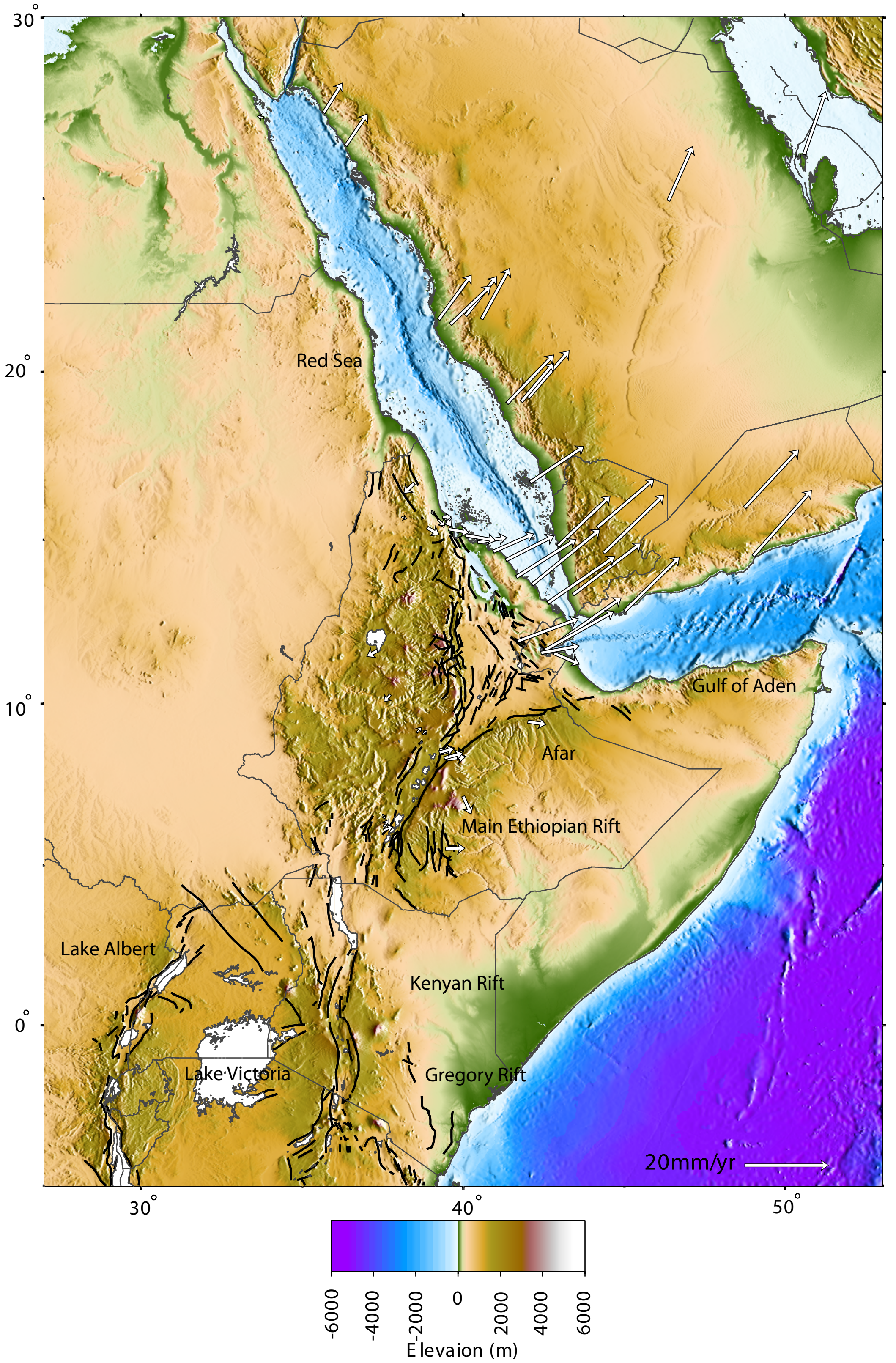

Figure 1.6: Topographic map of the East African Rift System (EAR). Elevations generated from SRTM30 PLUS (see http://topex.ucsd.edu/WWW_html/srtm30_plus.html) with main faults shown as black lines. White arrows show the GPS derived velocities with respect to Eurasia after (McClusky et al., 2010)

has progressed to seafloor spreading between ∼21° and ∼15°N, characterised by a well developed axial trough, spreading is thought to have initiated from around 12-9 Ma (Makris & Rhim, 1991) to 5 Ma (Girdler & Styles, 1974; LaBreque & Zitellini, 1985). South of ∼15°N spreading is offset into northern Afar where it eventually meets the Gulf of Aden and Main Ethiopian Rift to form the Afar triple junction. Geodetic and geological data from across the Red Sea suggest an average spreading rate of <20 mm/yr (Chu & Gordon, 1998; Stamps et al., 2008; Vigny et al., 2006).

1.4.2 The Afar Depression

The Afar depression, comprising the Afar triple junction, covers an area of ∼200,000 km^2 and formed as a result of rifting between Africa and Arabia over the past ∼30 My. It is bounded by the Ethiopian plateau in the west, by the Somalian plateau to the south east and the NW-SE trending Danakil block on its eastern edge, thought to be a rotating rigid block (e.g. Eagles et al., 2002; McClusky et al., 2010; Souriot & Brun, 1992; Vigny et al., 2006) (Fig. 1.7). The three arms of the triple junction, the Red Sea, Gulf of Aden and East African rifts (Fig. 1.7), formed within a Paleogene flood basalt province associated with the Afar mantle plume (Ebinger & Sleep, 1998; Hofmann et al., 1997; Schilling et al., 1992), roughly coincident with the onset of rifting in the Red Sea and Gulf of Aden (Wolfenden et al., 2004). Low P- and S-wave velocities in the upper mantle beneath the uplifted plateau of Arabia and NE Africa indicate that the thermal anomaly associated with the plume still exists today (Bastow et al., 2008; Benoit et al., 2003, 2006).

A number of authors have sought to investigate the nature of the lithosphere beneath the Afar Depression. By matching the coastlines on either side of the Red Sea McKenzie et al. (1970), suggested that the Afar depression was largely derived from mantle materials during the opening of the Red Sea and Gulf of Aden. The crustal thickness, estimated from seismic refraction and reflection studies of the highly intruded and extended Afar crust, varies from 14 km thick in the north to 26 km in the south (Berckhemer et al., 1975; Makris & Ginzburg, 1987; Stuart et al., 2006; Tiberi et al., 2005). Deep seismic investigations by Berckhemer et al. (1975) showed that the majority of the Afar lithosphere has a seismic velocity of between 6.6 and 6.8 km/s overlying an anomalous mantle with a V_p of 7.3-7.6 km/s and interpreted a lithosphere that is transitional between continental

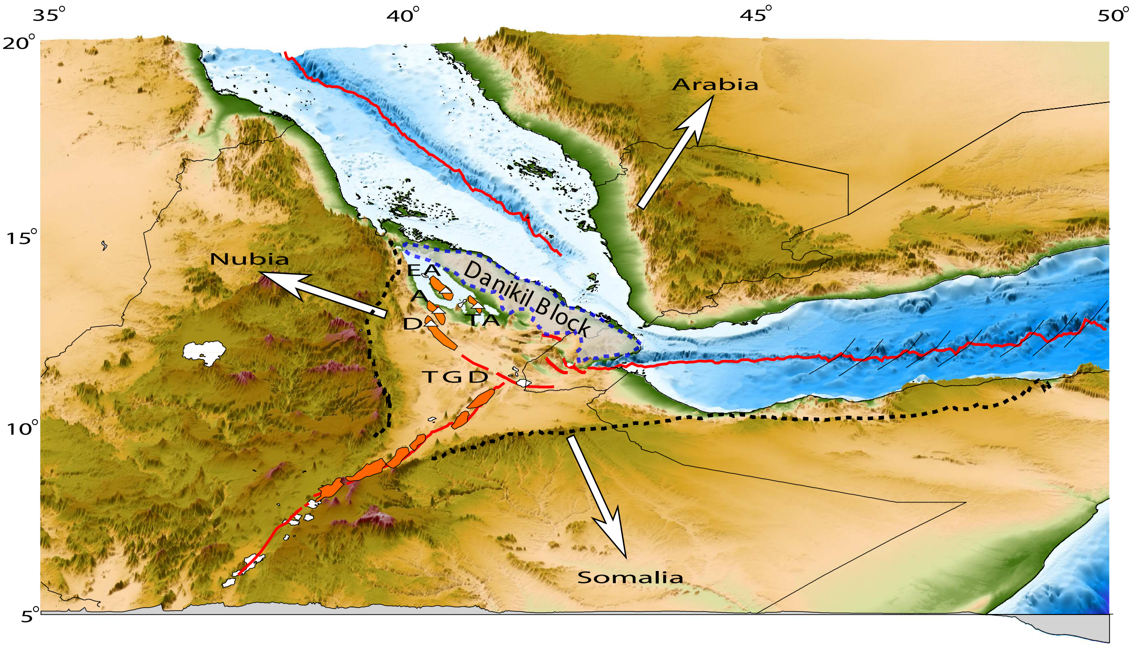

Figure 1.7: The Main Ethiopian Rift (MER) and Afar Depression. Red lines show the location of the Red Sea (RS), Gulf of Aden (GA) and East African Rift (EAR) systems. Orange areas show the location of magmatic segments through the MER and into Afar and their corresponding volcanoes (white triangles - Dabbahu (D), Alayta (A), Tat'Ale (TA) and Erta'Ale (EA)) (Hayward & Ebinger, 1996). TGD is the Tendaho-Gobaad discontinuity. The area highlighted in blue shows the location of the Danakil block and the large white arrows denote the approximate plate motions of Nubia, Somalia and Arabia.

and oceanic (Fig. 1.8). Reanalysis of the seismic (Berckhemer et al., 1975; Ruegg, 1975) and gravity data (Makris, 1975) by Makris & Ginzburg (1987) led to a conclusion that the Afar lithosphere is abnormally thinned lithosphere intermediate between continental and oceanic.

The geological units of the Afar depression can be divided into four main groups: 1) Neoproterozoic basement, Mesozoic sedimentary rocks and Eocene-Miocene basalts; 2) Miocene igneous rocks; 3) Pliocene volcanic rocks and 4) Quaternary volcanic and sedimentary rocks (Fig. 1.9, Beyene & Abdelsalam (2005); Varet (1978)). Although not found within the Afar depression the Neoproterozoic basement and sedimentary rocks, part of the Arabian-Nubian Shield, cover large areas around its edge (Stern, 1985; Vail, 1985). Many authors have concluded however, that the development of the Main Ethiopian, Red Sea, and Gulf of Aden rifts have been significantly influenced by pre-existing Neoproterozoic structures as in the Red Sea (Almond, 1986; Bosworth & McClay, 2001; Crane & Bonatti, 1987; Montenat et al., 1998; Sultan et al., 1992). The flood basalts of the Trap series were the first major volcanic series since Neoproterozoic times (Beyene & Abdelsalam, 2005). Berhe et al. (1987) suggest that the series was emplaced in three distinct stages at

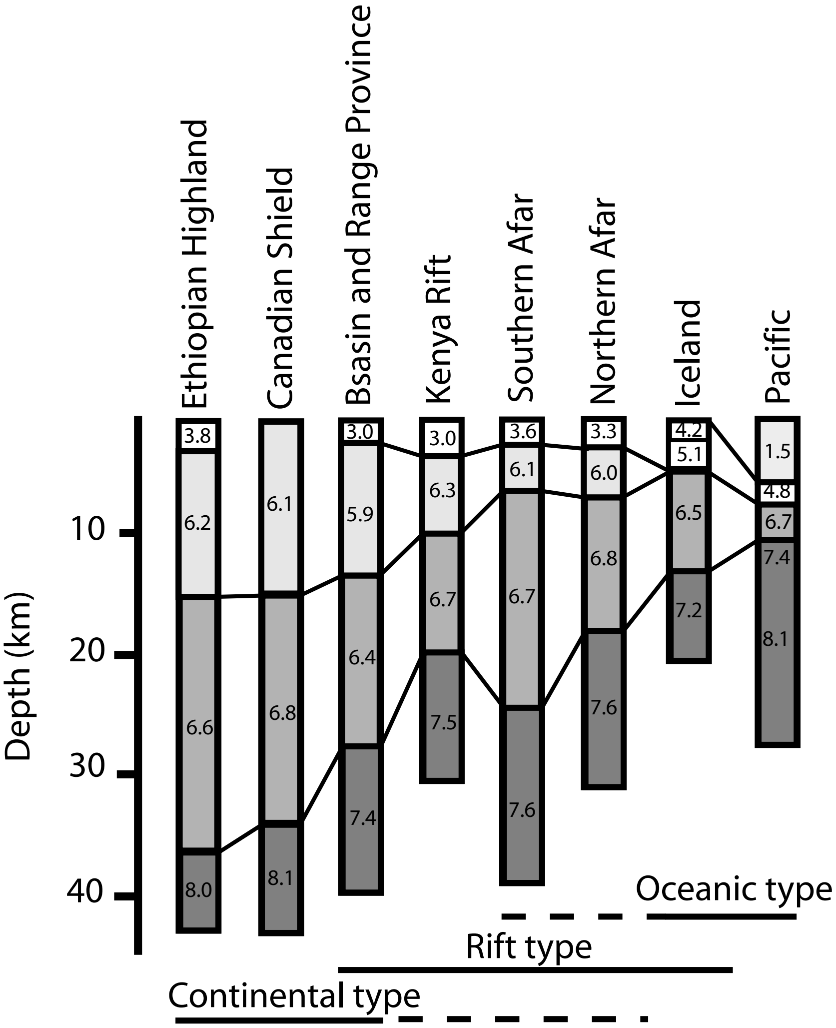

Figure 1.8: Comparison of seismic velocity profiles through the lithospheres of Continental rifts, the Afar Depression and other spreading centres (after Berckhemer et al. (1975)). The northern Afar profile runs from Afdera to Dallol while the southern profile runs from Asayta to Afdera

~50-40, 40-30, and 30 Ma, some authors suggest that the main phase of volcanism took place between 45 and 30 Ma (Ebinger et al., 1993) while others propose that the sequence was erupted over a short period of time at ~30 Ma (Hofmann et al., 1997). Hofmann et al. (1997) and Kazmin & Byakov (2000) estimated the thickness of the sequence to be ~2 km.

During the Miocene a series of alkaline to per-alkaline rocks was intruded along the western and eastern margins and in parts of northern Afar (Beyene & Abdelsalam, 2005) and are reported to be derived from a mantle source associated with early continental breakup (Barberi et al., 1972, 1974). Two additional sequences were erupted within the Afar Depression: the Mabla series consisting of rhyolites, ignimbrites and some minor basaltic flows (Varet, 1978; Vellutini, 1990) and the Dahla series consisting of basaltic flows up to

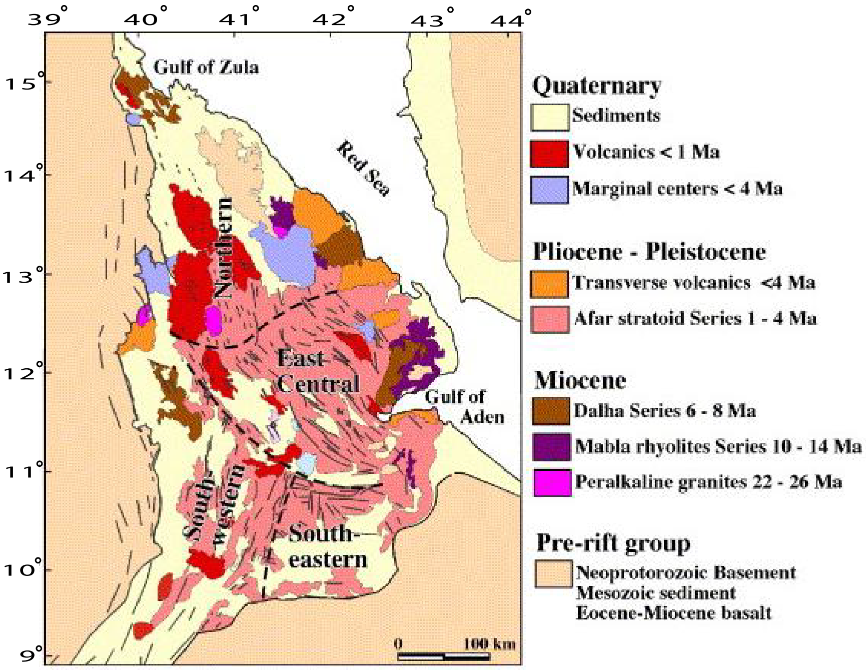

Figure 1.9: Geological map of the Afar Depression after (Acton & Stein, 1991; Varet, 1978)

∼ 800 m thick interbedded with rare sedimentary rocks and ignimbrites (Varet, 1978).

The next significant period of volcanism in Afar occurred during the Pliocene and Pleistocene. The Afar Stratoid series, which covers more than 2/3 of the Afar Depression, is separated by a non-conformity suggesting a prolonged period of erosion and reduced magmatism (Varet, 1978). Approximately 2/5 of the series is composed of basalts and the thickness of the series is up to 1500 m with the thickness of individual flows ranging from 1 to 6 m (Barberi et al., 1974; Tefera et al., 1996; Varet, 1978).

Quaternary volcanism in Afar is characterised by basaltic flows, scoria cones and silicic rocks (Tefera et al., 1996). Since ∼3 My, faulting and volcanism in Afar, have localised to ∼60-km-long, 20-km-wide axial volcanic ranges of aligned magmatic centres, similar in size, morphology, and spacing to the second-order, non-transform offset segmentation of slow-spreading mid-oceanic ridges (Hayward & Ebinger, 1996; Manighetti et al., 1998). The subaerial section of the Red Sea rift is comprised of numerous, previously-mapped magmatic segments (Hayward & Ebinger, 1996). The axial ranges of Northern Afar show symmetrical magnetic anomalies and share many characteristics with Mid-ocean ridges. This led Barberi & Varet (1977) to suggest that these axial ranges are the equivalent of oceanic spreading centres. The northern Afar region, also known as the Danakil depression, is a low lying region with mean elevations of ∼200 m dropping to 120 m below sea level in some areas. It is characterised by a series of shield volcanoes including Erta Ale, Tat'Ale and Alayta (Fig. 1.7). Erta Ale, after which the range is named, comprises six distinct volcanic centres (Barberi & Varet, 1970) and is home to a lava lake which has been active over the last 100 yrs (Barberi et al., 1973; Oppenheimer & Francis, 1998). In November 2008 a 3-day eruption occurred at the Alu-Dalafilla volcanic centre ∼30 km north of the crater lake. The eruption started on 3 November on two en-echelon fissures to the southeast of Alu with fissural lavas flowing to the east and north of Dalafilla (Pagli et al., 2009).

South of Erta'Ale are the shield volcanoes of Tat'Ale and Alayta, Tat'Ale is located to the East of Lake Afdera. Located to the southwest of Lake Afdera is Alayta which was last active at the turn of the 20th century. South of Alayta is the Manda-Harraro segment, including the currently active Dabbahu segment, which unlike the more northern magmatic segments is characterised by a 35 km-wide depression (Rowland et al., 2007). Both the Manda Harraro and Asal-Manda Inakir segments are dominated by young (∼1 Ma) basaltic rocks (Beyene & Abdelsalam, 2005). Barberi & Varet (1975) state that the Manda-Harraro segment is the only place in Afar where typical mid-oceanic basalts occur. More recent geochemical analysis of Manda-Harraro basalts, dated at ∼30 ka (Lahitte et al., 2003), show both enriched, and depleted light rare earth element (LREE) suggesting the involvement of two different mantle components (Barrat et al., 2003). The Tendaho-Gobaad discontinuity, south of Manda-Harraro, marks the boundary between the NE-SW opening of the Red Sea rift and the ∼E-W opening of the East African Rift (Beyene & Abdelsalam, 2005)(Fig. 1.7).

The volcanism of the Afar depression has been summarised by Vellutini (1990) into four major episodes: 1) basalts older than ∼25 Ma formed by fissural flows over Mesozoic sedimentary rocks; 2) between ∼25-19 Ma and ∼14-9.5 Ma two phases of rhyolitic volcanism occurred; 3) between ∼9 Ma and ∼1 Ma there was a sequence of basaltic flows; 4) recent (<1 Ma) fissural flows, predominantly basaltic, have occurred along elongated narrow bodies along rift zones. Using geochemical analysis from the Main Ethiopian Rift and Afar Hart et al. (1989) suggest a model for the volcanic evolution and propose that the Afar basalts are the result of melting hybrid MORB-PREMA mantle or mixing between MORB and PREMA melts.

1.4.3 The Main Ethiopian and Kenyan (Gregory) Rifts

The Main Ethiopian Rift (MER) forms the northern most section of the East African Rift before entering the Afar depression. It was formed within the Precambrian metamorphic basement of the Pan-African shield and was subsequently covered by a sequence of 1 km thick Mesozoic to early Tertiary marine sequences associated with an ancient passive margin (Kazmin et al., 1978). This is followed by a series of Oligocene to early Miocene basalt-ignimbrite sequences between 1 and 2 km thick (Abebe et al., 2005). Striking predominantly NE-SW the rift floor forms a ~330 km long, ~50 km wide incision through the Ethiopian Plateau (Fig. 1.7). The rift shoulders on either side of the MER rise to 1800-3500 m in the west and 2500-3000 m in the east. At its northern end the rift floor sits at ~750 m a.s.l, to the southwest the floor rises to 1700 m before dropping back to ~1000 m in the south. The rift is segmented into a number of asymmetric graben basins, filled with lava flows and evaporites and bounded on their eastern side by steep Miocene border faults (WoldeGabriel et al., 1990). Sometime between 6.6 and 3 Ma the extension direction changed from N130°E to N105°E and the extensional strain migrated away from the large offset border faults to smaller offset faults and aligned magmatic centres (Wolfenden et al., 2004). As in the Afar Depression these Quaternary volcanic centres form a series of 20 km wide, ~60 km long magmatic segments (Figs. 1.7). Elongate high velocity zones ($V_p > 6.5$ km/s) have been observed beneath the magmatic centres and are thought to represent cooled mafic intrusions (Keranen et al., 2004; MacKenzie et al., 2005).

The crustal thickness beneath the MER, estimated from receiver function and wide angle seismic data, is thought to be ~38 km in the south reducing to ~24 km beneath Fentale on the edge of the Afar Depression (Dugda et al., 2005) (Fig. 1.10). This trend is consistent with observations of increased crustal extension and magmatism toward the north (Maguire et al., 2006; Stuart et al., 2006; Tiberi et al., 2005). Mantle velocities beneath the MER of 7.7 km/s have been interpreted to represent the presence of 3-5% partial melt (Maguire et al., 2006). Similar velocities observed beneath the Kenya rift (Mechie et al., 1994a) coincide with tomographic images of a narrow zone of low velocity material extending from 70 km to at least 250 km below the rift axis (Bastow et al., 2005, 2008). Furthermore, SKS splitting results show a systematic variation in orientation of

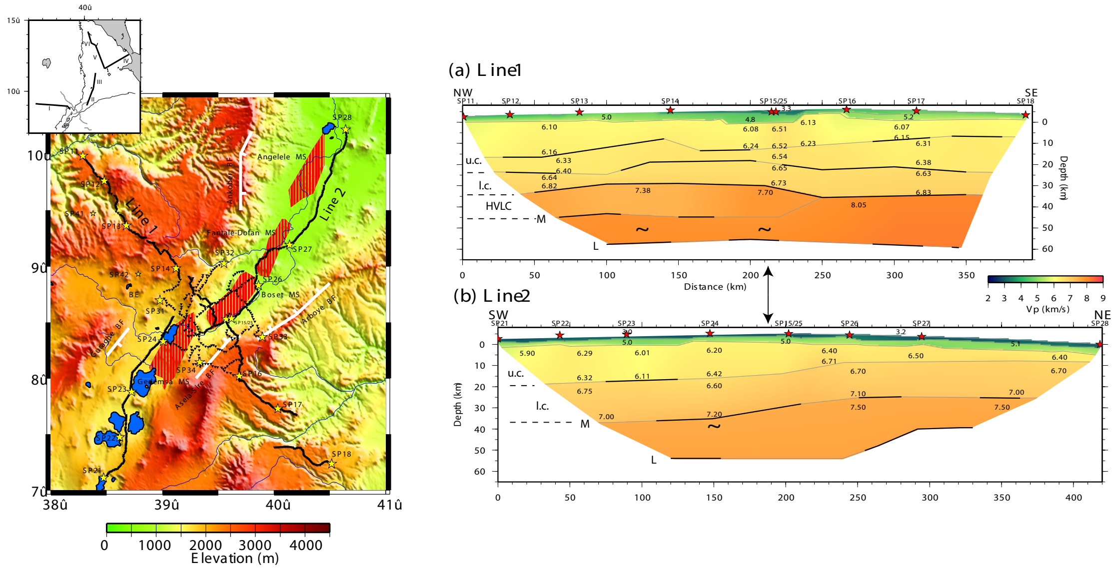

Figure 1.10: Final ray-trace P-wave velocity models for (a) across-axis profile (after (MacKenzie et al., 2005; Maguire et al., 2006)) and (b) along-axis profile of the EAGLE controlled source experiment (after (Maguire et al., 2006)). The crust beneath the southeastern plateau is ∼ 40 km-thick, whereas the western side of the rift is underlain by 45-50 km-thick crust with a ∼10-15 km high-velocity lower crust believed to be underplate (labelled HVLC). Crustal thickness beneath the MER decreases from 38 km in the south beneath the caldera lakes to 24 km beneath Fentale volcano in the southern Afar depression.

the fast shear wave polarisation direction from NE away from the magmatic segments to NNE in the rift axis. This alignment of seismic anisotropy has been interpreted as being caused by partial melt in the form of dykes which penetrate through thinned lithosphere (Gashawbeza et al., 2004; Kendall et al., 2005) (Fig. 1.11).

At the southern end of the MER are the Omo-Turkana lowlands which separate the elevated Ethiopian and Kenyan domes (Fig. 1.12). Although this region shows no pronounced rift, there are a number of N to NE striking half-graben basins filled with up to 7 km of Cenozoic sediments (Chorowitz, 2005). The crustal thickness beneath the Omo is ∼30 km, significantly lower than that found in the plateaus of the MER (∼51 km), and drops to ∼20 km in the Turkana area (Mahatsente et al., 1999) before thickening towards the Kenyan rift.

The Kenyan rift, located at the southern end of the MER, cuts through the northern section of the Kenyan dome. At its northern end the Kenyan rift consists of two parallel rift valleys at elevations of ∼1100 m separated by the Kamasia horst (Chorowitz, 2005). A large number of studies have been conducted along the Kenyan rift including seismic refraction, wide angle reflection (Keller et al., 1994; Mechie et al., 1997) and gravity (e.g. Maguire et al., 1994; Nyblade & Pollack, 1992; Swain et al., 1981). Crustal thickness beneath the graben valley is estimated at ∼30 km thickening to 35 and 40 km on the eastern

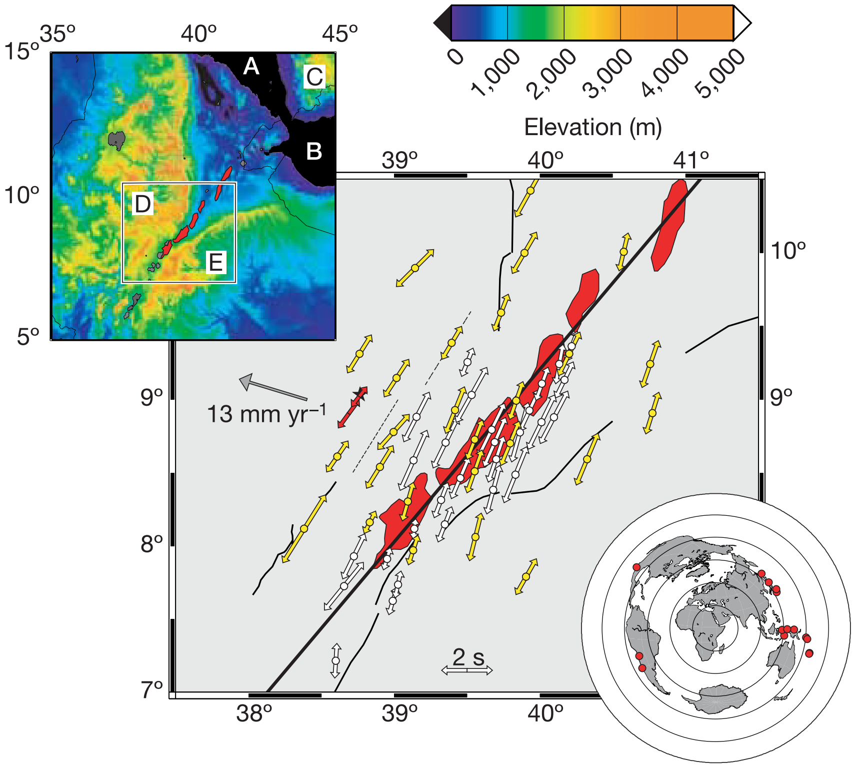

Figure 1.11: SKS splitting results from the MER. The orientation and size of the arrows shows the direction of the fast shear wave and magnitude of the splitting respectively. Yellow arrows mark results at seismic stations deployed for 16 months, white arrows are for stations deployed for three months, and red arrows are for the IRIS permanent stations FURI and AAE. Heavy black lines show major border faults, dashed lines shows monclines and magmatic segments are marked red. Top left inset shows topography (A, Red Sea; B, Gulf of Aden; C, Arabian plate; D, Nubian plate; E, Somalian plate). The lower right inset shows the locations of events used for analysis. From (Kendall et al., 2005)

and western flanks respectively (Achauer et al., 1992)(Fig. 1.13). Low mantle velocities to over 150 km and well defined lithospheric thinning have been reported by Keller et al. (1994) in addition to a positive Bougeur anomaly in the middle of the graben interpreted as dyke injections related to magma reservoirs.

Using a combination of GPS and earthquake slip data the present day extension rate along the Main Ethiopian and Kenyan rifts have been estimated at ∼6 and ∼4 mm/yr respectively (Stamps et al., 2008)(Fig. 1.14) and are thought to have been constant over the last 3.2 Myrs. These rates are consistent with a number of earlier studies which used marine magnetic anomalies (Chu & Gordon, 1999; Jestin et al., 1994) to determine the long term average.

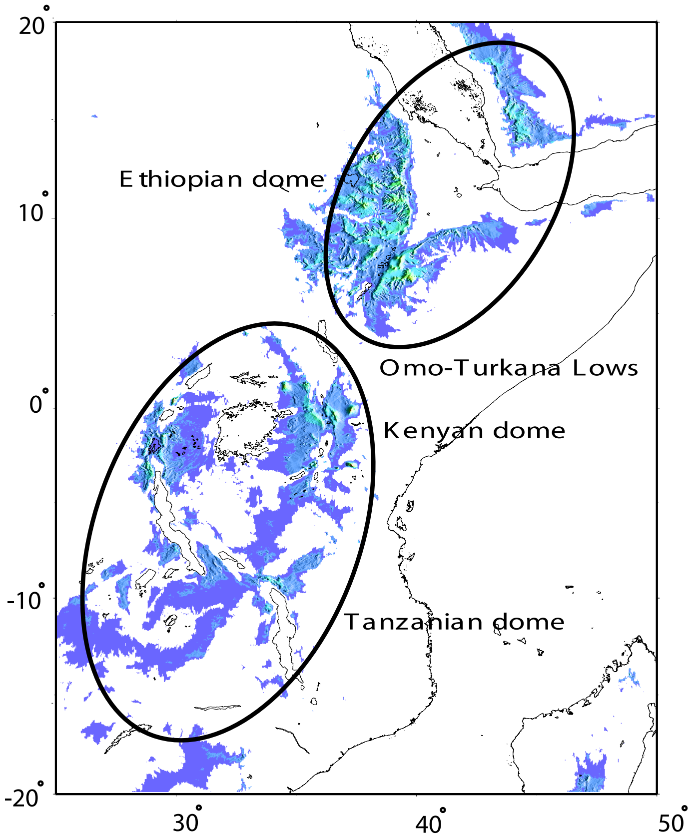

Figure 1.12: Map of East Africa highlighting regions of high elevation (>1200 m) which define the Ethiopian and Kenyan domes

1.4.4 Deformation along the Dabbahu rift segment

Unlike the volcanic systems in Iceland, where activity has been documented over the past few thousand years, there have been no recorded rifting episodes along the Dabbahu segment prior to September 2005. Interferograms covering the years preceding the rifting event in 2005 show deformation concentrated along the rift axis. In the 9 yr period from 1993 the central axis subsided by ~3 cm (Fig. 1.15a) similar to observations of the inter-rifting period along many of the fissure swarms in Iceland (Sigmundsson, 2006). Of the two volcanoes at the northern end of the Dabbahu segment, Gabho and Dabbahu, only Gabho shows significant deformation over this period. The deformation between 1996 and 1997 suggest the intrusion of a shallow dyke beneath Gabho after which inflation began. Inflation at Gabho was observed between October 1999 and December 2002 and between April 2004 and May 2005 (Figs. 1.15b,c).

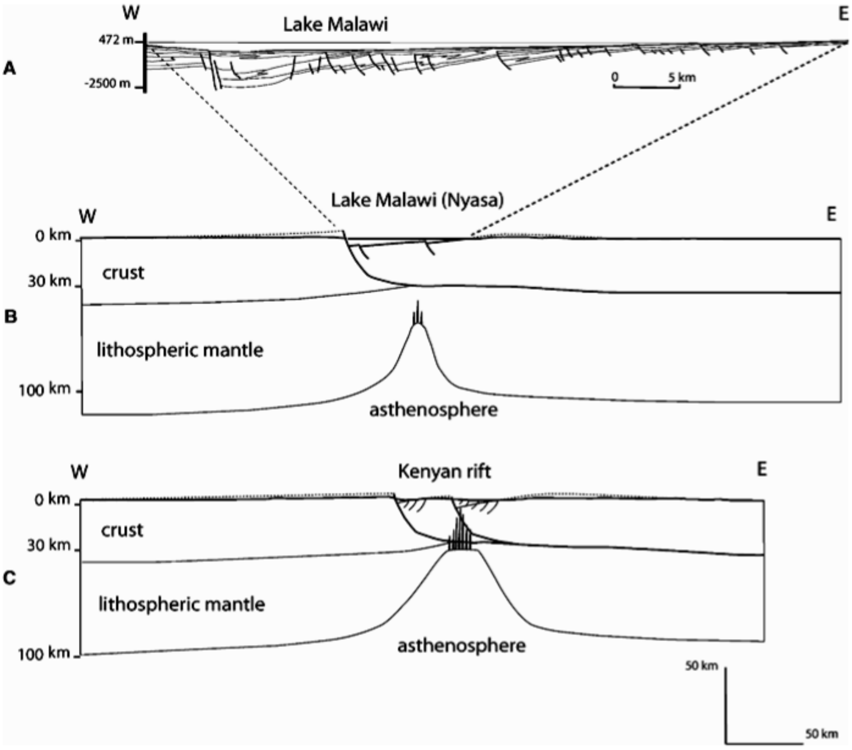

Figure 1.13: Representative lithospheric profiles across the EARS after Chorowitz (2005). Vertical lines are inferred dyke intrusions and dotted lines show the envelope surface before erosion. A) Seismic reflection profile across Lake Malawi (Rosendahl et al., 1992; Specht & Rosendahl, 1989). B) Inferred lithospheric cross-section of Lake Malawi. C) Inferred lithospheric cross-section of the northern Kenya rift.

September 2005 Rifting event

The first signs of activity along the Dabbahu segment came from the detection of seismicity beneath Dabbahu and Gabho volcanoes in April 2005. After a ~4 month period of quiescence a magnitude 4.3 M_w earthquake was detected on 4 September (Ayele et al., 2009). On 14 September 2005 a swarm of earthquakes was detected with a maximum magnitude of (M_w) ~5.0. In total 162 earthquakes (magnitude 4.1 - 5.2) were recorded by the National Earthquake Information Center (NEIC) between 20 September and 4 October, coinciding with the opening of a new 400-m-long, 80-m-wide volcanic vent on the eastern flank of Dabbahu volcano (Fig. 1.16A) (Ayele et al., 2007, 2009; Rowland et al., 2007; Wright et al., 2006; Yirgu et al., 2006). The Geophysical Observatory at Addis Ababa University recorded nearly continuous activity between 24 and 26 September with the number of earthquakes declining on 27 September (Yirgu et al., 2006). An earthquake of magnitude 5.2 on 26 September occurred approximately half an hour before the onset of the volcanic eruption, according to local pastoralists. The eruption was composed of pumice, fine ash and silicic lava. Initial analysis of the erupted rhyolitic pumice indicated

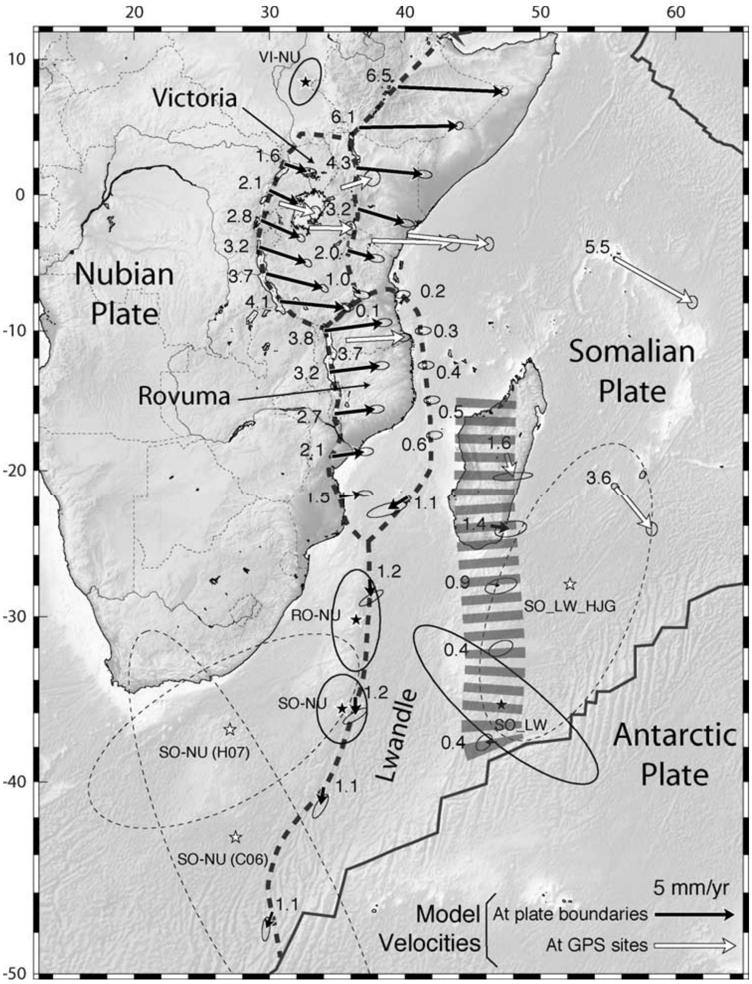

Figure 1.14: Best fitting modelled velocities along the EAR. Relative motions along plate or block boundaries are shown with black arrows, and numbers are model velocities in mm.yr^{-1}. The hatched area over Madagascar is the diffuse plate boundary between Somalia and Lwandle, after Stamps et al. (2008)

a felsic source at a depth of <6 km (Wright et al., 2006). Surface deformation estimated from radar interferometry indicated a maximum horizontal opening of 8 m perpendicular to the rift (Ayele et al., 2007; Barisin et al., 2009; Grandin et al., 2009; Wright et al., 2006). A maximum uplift of ∼1.5 m occurred on both rift flanks relative to the far field, and extended along most of the segment. A 2-3-km-wide central zone subsided by up to 2 m with a further 2-3 m of subsidence occurring around Dabbahu and Gabho volcanoes at the northern end of the segment. The observed surface deformation was in accordance with the injection of a 60-km-long dyke, between 2 and 9 km depth along the length of the segment (Ayele et al., 2007; Rowland et al., 2007; Wright et al., 2006; Yirgu et al., 2006) (Fig. 1.17). The majority of the recorded earthquakes were associated with normal faulting and concentrated within the deforming area, other earthquakes were detected up

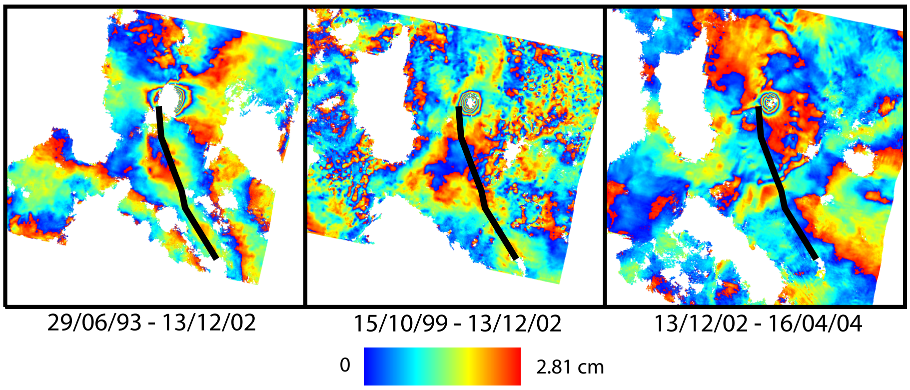

Figure 1.15: Deformation around the Dabbahu rift segment prior to the onset of rifting in September 2005. *Left*, interferogram covering a 9 yr period from 1993 including a shallow dyke intrusion at the northern end of the segment. *Middle*, Interferogram from 1999 to 2002 showing uplift concentrated at Gabho. *Right*, Interferogram from 2002 to 2004 showing continued uplift at Gabho prior to the 2005 dyke intrusion. Black line shows the surface trace of the September 2005 dyke.

to 60 km further south and are inferred to be the result of changes in the Coulomb stress field (Fig. 1.16B) (Ayele et al., 2009). Subsidence observed at Dabbahu and Gabho suggested that the dyke was, at least partly, fed by shallow magma chambers beneath the volcanoes, leading to the hypothesis that the dyke propagated to the south (Wright et al., 2006). Re-analysis of seismicity associated with the intrusions by Ayele et al. (2009) has shown three distinct feeding zones. Seismicity began beneath Dabbahu and Gabho before jumping to the Ado'Ale complex from which the dyke propagated both north and south. Evidence of an an additional source in the centre of the rift segment lead Grandin et al. (2009) to include an additional magma source beneath the Ado'Ale complex. The effect of this source was to increase the opening along the dyke plane in this portion of the rift segment.

1.5 Thesis aims and outline

Although the mid-ocean ridge system is continuously active and can be traced across the entire globe, rifting episodes, where new crust is added through the intrusion of multiple dykes are difficult to observe and, as such, the dynamics of sea-floor spreading is poorly understood. Unfortunately sub-aerial rifting episodes are extremely rare and may only occur once a century. The ongoing rifting episode in Afar offers a unique opportunity to examine the dynamics of rifting events with high resolution satellite data for the first time. The aim of this thesis is to measure and model the deformation resulting from this ongoing rifting episode which started in September 2005 (Ayele et al., 2007; Ebinger et al.,

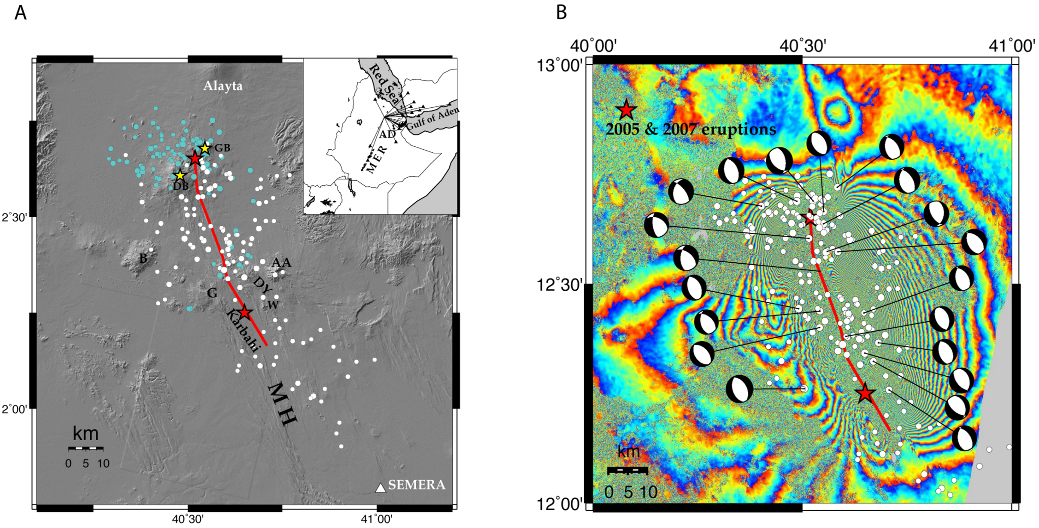

Figure 1.16: **a**: Earthquake distribution during the Sept. 4 to Oct. 4, 2005 episode in the Manda-Harraro rift. The red line near the rift axis shows the surface projection of the dike. Light blue circles represent earthquakes during Sept. 4-24 and white circles are epicentres during Sept. 25 to October 4. Circle size is scaled to magnitude. **b**: Seismicity (white circles) as in **a** and fault plane solutions of major earthquakes displayed on a descending interferogram formed using radar images acquired on 6 May and 28 October 2005, after (Ayele et al., 2009)

2008; Rowland et al., 2007; Wright et al., 2006; Yirgu et al., 2006). Specifically, this thesis aims to answer two main questions.

- What are the controls on the distribution of magma along an active rift system?
- Can measurements of the Earth's response to large scale magmatic intrusions be used to determine the rheology of an area of incipient sea floor spreading?

This thesis is composed of 6 Chapters including this introduction:

- Chapter 2 is split into three main sections. In the first section I briefly describe the theory and method of Satellite Radar Interferometry (InSAR). In section 2 I discuss the algorithm used to compute displacement rates around the Dabbahu segment and finally describe the theory behind the modelling methods used to describe the observed deformation.
- Chapter 3 details a sequence of 12 dyke intrusions emplaced along the Dabbahu rift segment between June 2006 and June 2009 and presents elastic dislocation models for each intrusion.

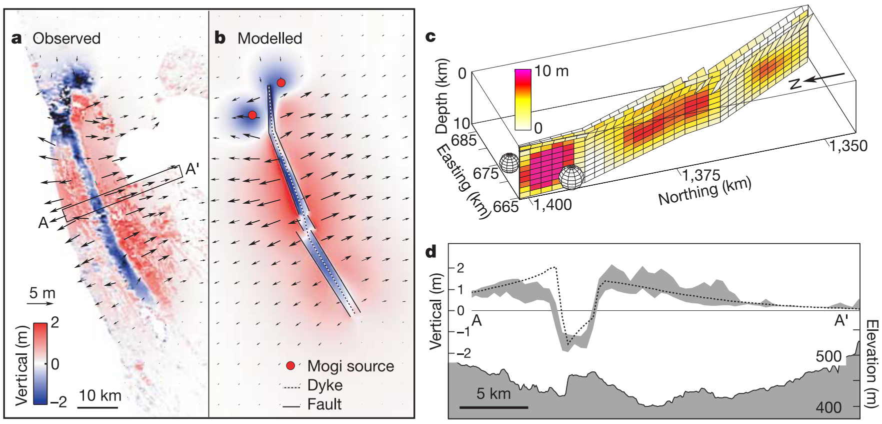

Figure 1.17: **a**, Three-dimensional deformation field created from interferograms and range and azimuth offsets. Arrows represent the horizontal component and colours represent the vertical component. **b**, Modelled three-dimensional displacement field. **c**, Elastic dislocation model consisting of a dyke and two deflating Mogi sources beneath Gabho and Dabbahu volcanoes. **d**, Profile across the dyke (A-A' in **a**), showing observed (top) and modelled (bottom) vertical deformation and topography after (Wright et al., 2006)

- Chapter 4 is split into 2 sections. In the first section I use the elastic dislocation models described in Chapter 3 to calculate the stress change induced by each event and assess its implications for the distribution of magma along the rift segment. In the second section I use the same dyke models to test the affects of magmatic intrusions on faults along the rift.

- Chapter 5 examines the long-term post-rifting displacements following the September 2005 dyking event and tests viscoelastic relaxation models against InSAR observations.

- Chapter 6 summarises the main findings of the thesis, discusses the implications of the results and details plans for future work.

Chapter 2

Methods

2.1 SAR and its application for InSAR

Satellite Radar Interferometry (InSAR) is a widely used technique for monitoring deformation of the Earth's surface. By differencing the phase from two radar images acquired at different times, maps of range change between the radar and ground can be obtained with centimetre precision (Massonnet & Feigl, 1998). A number of review papers have been published on InSAR (e.g. Bamler & Hartl, 1998; Bürgmann et al., 2000; Massonnet & Feigl, 1998; Rosen et al., 2000). In this chapter I will summarise some of the basic principles in forming interferograms and describe the processing chain using by ROI_PAC. In the second part of this chapter I will describe the methods which have been used for modelling the deformation in Afar.

2.1.1 Synthetic Aperture Radar (SAR) imaging

Radar (Radio Detection and Ranging), developed in the mid 1930's, was originally designed as a tool for detecting aircraft and providing an estimate of their distance away from the antenna. However, advancements in radar technology have provided modern radar systems with a much wider range of applications, such as remote sensing. Radar imaging is an active remote sensing technique which uses electromagnetic waves, usually of microwave frequency (1-10 GHz), to image or illuminate a target. By selecting a radar frequency which minimises atmospheric attenuation it is possible to achieve almost 100% transmissivity. Thus, a system operating in this frequency range is always able to image the Earth's surface, regardless of the weather (Curlander & McDonough, 1991). Radar uses the round trip travel time from the antenna to a target to determine distances. The characteristics of the returning wave (power, phase, polarisation) depend on the properties of the Earth's surface, predominantly the electrical properties and surface roughness (Curlander & McDonough, 1991).

Side-Looking Aperture Radar

Most airborne remote sensing applications of radar use a side looking aperture radar configuration (Fig. 2.1). It operates in the same way as a conventional radar system, pulses of electromagnetic energy are emitted from the antenna, usually carried on either an aeroplane or satellite at a constant altitude and velocity.

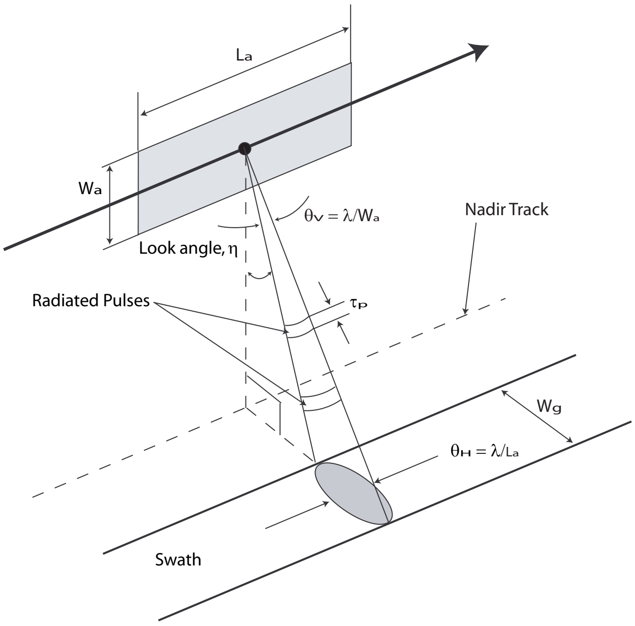

Figure 2.1: Geometry for a side-looking real-aperture radar, redrawn from Curlander & McDonough (1991).

The resolution of a traditional radar image,in the range and along track directions, is largely contolled by the the duration of the radar pulse and the size of the antenna. In order to achieve the desired resolution of ∼20 m, in the range direction, the duration of the radar pulse needs to be no longer than ∼50 ns. Unfortunately, power restrictions prevent sufficiently short pulses to be generated with enough power to produce a reasonable signal to noise ratio. To get around this problem a frequency modulated (chirped) pulse is used. With suitable processing the pulse is given a shorter effective pulse length equal to $\frac{1}{B}$, where B is the bandwidth (16 MHz for Envisat). This technique is known as range compression and, for Envisat, produces a ground range resolution of between 36 m and

13 m for IS1 to IS7 respectively.

For an antenna mounted on an aircraft, an along-track resolution of ~20 m is easily achived with an antenna length of ~10 m. However, for the case of space-borne radar system, orbiting at ~800 km, the length of the antenna would need to be $\sim 4.8\ km$ long, clearly not practical for being launched into space, in order to achieve the same resolution. The solution to this problem is known as Synthetic Aperture Radar (SAR).

In essence, the principle of SAR is to simulate a much larger antenna by combining the radar returns from consecutive radar pulses. A target on the ground, such as B in Figure 2.2, will be illuminated throughout the time interval $t_1 \leq t_2 \leq t_3$ (Wright, 2000). During which time, the satellite moves over a distance equal to the azimuth beam width. By combining all of the returns over this time, a synthetic aperture antenna is created which will have an effective length equivalent to the beam width of the real aperture, which for Envisat is $\sim$ 4.8 km.

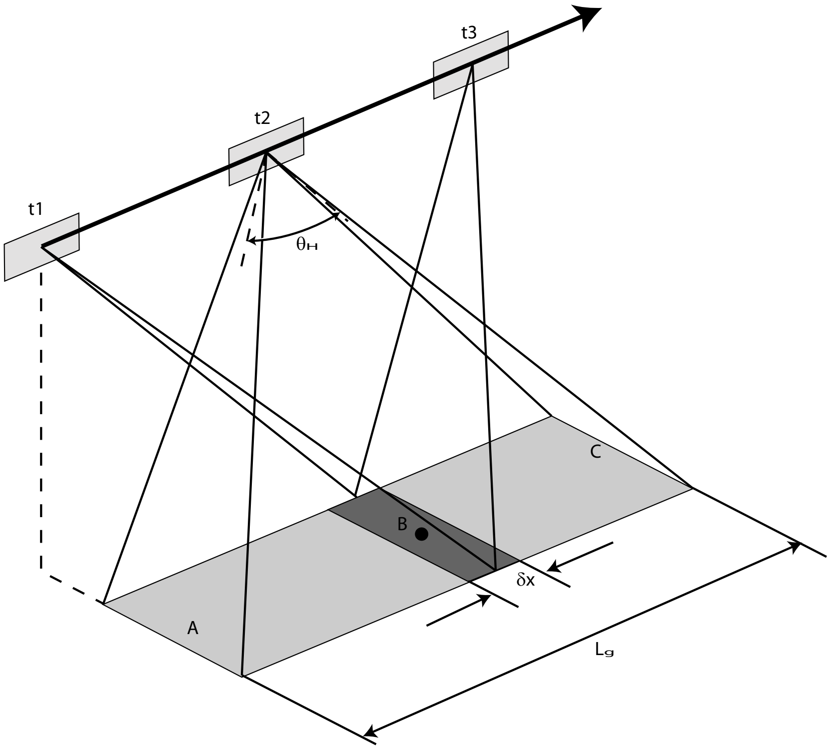

Figure 2.2: Illustration of Synthetic Aperture Radar, using a moving SLAR antenna, redrawn from Wright (2000). The length of the illuminated area along track, ΔA_g, is such that the target, B, is illuminated for the period between t_1 and t_3. By combining all the echoes during this time, the resolution is improved from ΔA_g to δx.

The first observation which led to the development of SAR was made by Wiley (1965). Wiley observed that any two targets on the ground will have different speeds in relation to a moving radar. Thus, the reflected radar pulse from the two targets will have distinct Doppler shifts with respect to the transmitted frequency (Fig. 2.3). By combining the two-way travel time of the radar pulse, which gives the range between the satellite and target, and the information from the doppler shift, and describes a circle on the ground, with its centre directly below the satellite the location of targets within the radar swath can be identified with a resolution of ∼5 m in azimuth. This is a process known as azimuth compression. Range and azimuth compression are applied to the raw data to form a single look complex (SLC), which contains the amplitude and phase information for each pixel.

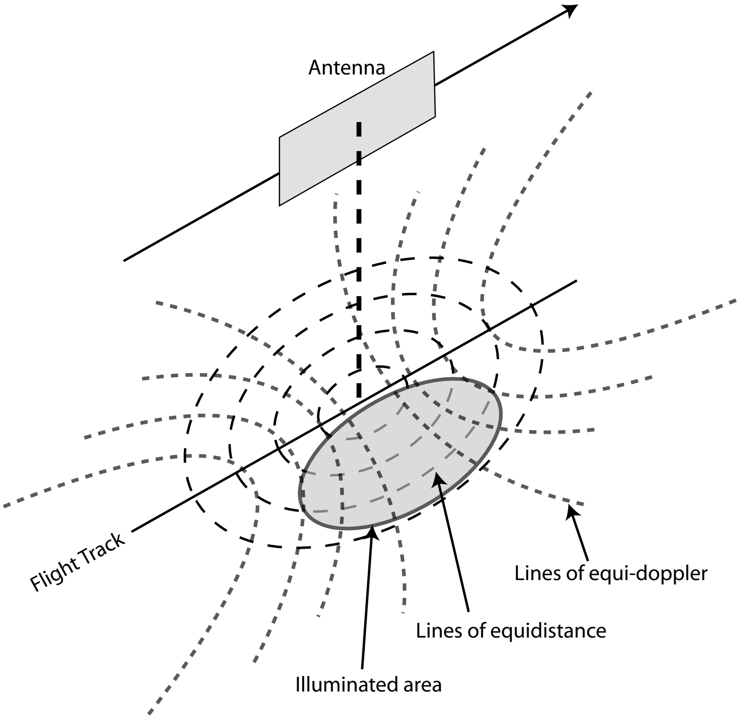

Figure 2.3: Coordinate system for synthetic aperture imaging, redrawn from Ford et al. (1989)). Reflections from targets located on a sphere centred at the nadir point will be received by the sensor at the same time. This results in a series of concentric spheres intersecting with the plane being imaged, these represent points of equi-distance from the sensor (Elachi (1987)). Any point lying on a given hyperbola will have equi-Doppler returns. Hence the imaged surface can be referenced to a coordinate system of concentric circles and coaxial hyperbolas, enabling any point to be uniquely identified from its two-way travel time and Doppler shift (Elachi (1987)).

2.1.2 Properties of the Single Look Complex

The SLC image contains information on both the amplitude and phase of the returned radar energy. The amplitude records the reflectivity of the surface being imaged. Depending on the terrain the amplitude image varies from being dark, where little energy is returned to the satellite, or bright where more of the energy is returned. For example, a calm lake will appear dark in the radar image as most of the energy is reflected away from the satellite (Fig. 2.4).

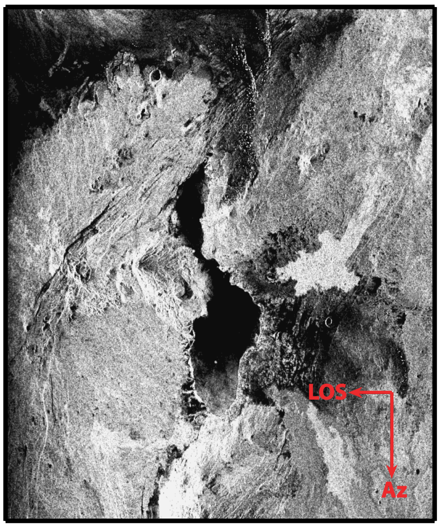

Figure 2.4: Amplitude component of an SLC image of Lake Afdera in Northern Afar, notice the dark region in the centre of the image where the lake is situated.

The basic principle behind radar interferometry is a comparison of the phase component from two SLC's acquired at different times. The phase value for any given pixel within an SLC is random as it is composed of contributions from multiple scatterers within the pixel. The key to interferometry is the removal of this random contribution. By subtracting the phase component from two radar images separated in time, providing the backscattering characteristics of the ground remain unchanged and that the same area is being imaged, the random phase component can be removed. Any residual phase is then a result of the difference in the path length between the acquisitions and differences in the atmospheric path delay ϕ_{atmos}. Additional changes in the path length result from the viewing geometry, ϕ_{geom}, topography, ϕ_{topo}, deformation, ϕ_{defo} and noise ϕ_{noise}

There are a number of sources of noise in the measured phase change including thermal noise and decorrelation. Decorrelation occurs when the phase reflection from a pixel has changed between the two acquisitions. In this case, when the phase values are subtracted the random component of the phase is not removed causing neighbouring pixels to lack coherence. The main cause of decorrelation is temporal decorrelation and it can occur on a variety of time scales depending on the characteristics of the surface being imaged. Heavily vegetated areas, such as forests, are generally incoherent while operating in C-band because of multiple reflections which occur in the forest canopy.

Phase contribution due to geometry (ϕ_{geom})

In order for interferometry to work the characteristics of the pixel must not too much change between acquisitions, this is dependent on the individual reflectors within a pixel remaining unchanged. If the path length difference between echoes from the near and far side of the pixel is greater than the radar wavelength, λ, then the internal phase contributions in a pixel will sum differently in each image and will not cancel after subtraction (Massonnet & Feigl, 1998). For ENVISAT, this limits the separation between the satellite's to less than ~1 km while operating in IS2 (23°).

Although ENVISAT is steered in order to maintain its nominal orbit, the position of the satellite for any two acquisitions is rarely the same. Therefore, for most interferograms there will be path difference, δ, related to the position of the antenna at each acquisition. This corresponds to a round-trip phase shift of $\phi = \frac{4\pi\delta}{\lambda}$. The change in phase across the interferogram can be approxamated by

$$\frac{\partial\phi}{\partial\gamma} \approx \frac{4\pi B_{\perp}}{\lambda} \tag{2.1}$$

where γ is the incidence angle, $B_{\perp}$ is the perpendicular baseline and λ is the wavelength. Thus, as the incidence angle, γ, changes across the radar swath, there is a phase change due to the perpendicular baseline between the two antennae assuming a flat earth and constant $B_{\perp}$. Due to the parallel component of the baseline, $B_{||}$, there is a phase shift in the interferogram, which varies slightly across the swath as the incidence angle changes. Differences in the orbital trajectories for each satellite pass cause $B_{\perp}$ and $B_{||}$ to vary in the azimuth direction. Variations in $B_{||}$ lead to an additional phase ramp in the azimuth direction while variations in $B_{\perp}$ cause a twist in the phase ramp. However, with knowledge of the satellites orbits these effects can be can be largely removed from the final interferogram (Fig. 2.5).

Phase contribution due to topography (ϕ_{topo})

The phase contribution from topography is due to the stereoscopic effect when observing the ground from a different position. From Figure 2.6,

$$z = h - r\cos\gamma \tag{2.2}$$

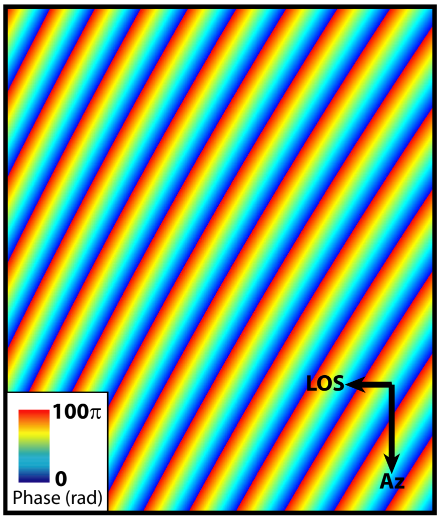

Figure 2.5: Orbital ramp correction for a pair of ENVISAT images acquired on 24/01/2009 and 28/02/2009 of the Dabbahu segment, Afar, Ethiopia. Each fringe represents 100π of phase change.

and

$$\frac{\partial z}{\partial \gamma} = r \sin \gamma. \tag{2.3}$$

Using equation 2.1,

$$\frac{\partial \phi}{\partial z} = \frac{\partial \gamma}{\partial z} \times \frac{\partial \phi}{\partial \gamma} \approx \frac{4\pi B_{\perp}}{r\lambda \sin \gamma}. \tag{2.4}$$

If the topography is not corrected for then the result is a series of fringes, where 1 fringe is equal to a change in phase of 2π, which follow the topography like contour lines. The altitude of ambiguity, h$_a$, is defined as the change in altitude needed to produce a single 2π fringe (Massonnet & Feigl (1998)). Using equation 2.4

$$h_a = \frac{R_s \lambda \sin \gamma}{2B_{\perp}}, \tag{2.5}$$

where R$_s$ is the range from the slave trajectory to the target. Interferograms with B$_\perp$ of 100m will contain 1 fringe for every $\sim 100\ m$ of topography. With knowledge of B$_\perp$ and a digital elevation model (DEM), fringes generated due to the topography can be removed (Fig. 2.7).

Phase contribution from the Atmosphere (ϕ_{atmos})

For repeat pass interferometry the atmosphere will never be identical in both of the radar acquisitions; therefore adding an additional phase contribution to the final interferogram. The pressure, temperature and water vapour content control the size of refractive index which, in turn, determines the amount of atmospheric phase delay. The biggest atmo-

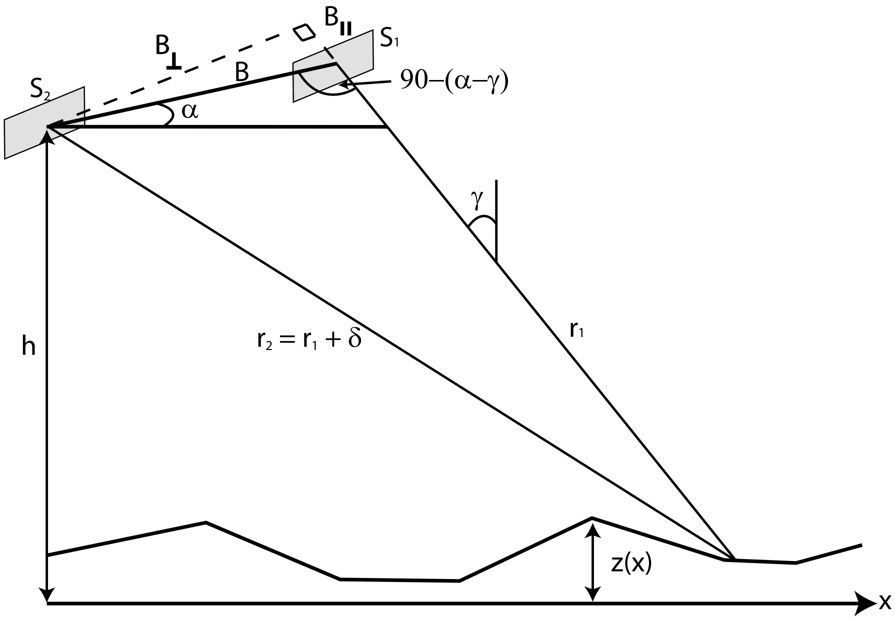

Figure 2.6: Imaging geometry for radar interferometry. Where S_1 and S_2 are the different satellite positions separated by a distance B, $B_{\parallel}$ and $B_{\perp}$ are the components of B, parallel and perpendicular to the look direction respectively and γ is the incidence angle of the first radar image, modified from Bürgmann et al. (2000)

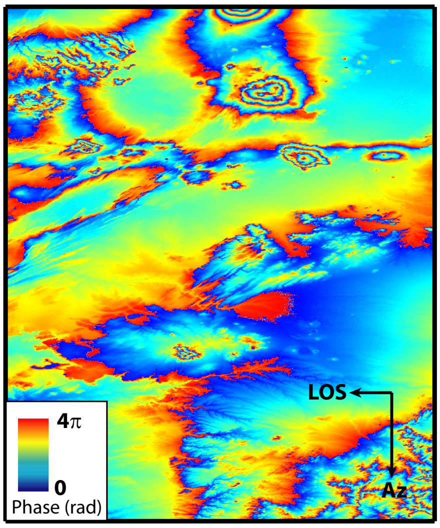

Figure 2.7: Topographic phase correction for a pair of ENVISAT images acquired on 24/01/2009 and 28/02/2009 of the Dabbahu segment, Afar, Ethiopia. The correction is calculated using the 90 m SRTM DEM (Farr & Kobrick, 2000). With a $B_{\perp}$ of -235 m and an altitude of ambiguity of ~65 m each fringe in this figure, which is wrapped to 4π, represents ~130 m.

spheric source for interferometry is the amount of water vapour in the troposphere. Although attempts have been made to remove the atmospheric delay using GPS (Li et al., 2005) and satellite instruments (Li et al., 2005, 2006) the availability and resolution of the data is usually too poor for most deformation studies.

Phase contribution from deformation (ϕ_{defo})

If the phase change contributions from the surface topography and viewing geometry have been removed, the remaining phase components are a result of atmospheric path delays and surface deformation.

If the atmospheric path delay is small, then it can be assumed that any phase change is a result of a change in the range, Δr, between the ground and radar antenna. Changes in the range are recorded in the satellite's line-of-sight (LOS), therefore a change in the interferometric phase as a result of surface displacement is

$$\Delta\phi = \frac{4\pi\Delta r}{\lambda} = -(\frac{4\pi}{\lambda})\hat{\mathbf{l}} \cdot \mathbf{u}. \tag{2.6}$$

where $\hat{l}$ is a unit vector pointing from the target on the ground to the satellite. For Envisat, with $\lambda \approx 5.6$ cm, a surface displacement of half a wavelength in the satellites LOS will generate a single fringe in the interferogram.

Measurements of deformation using InSAR are limited by both its magnitude and its spatial scale. InSAR is bounded by four physical limits (Massonnet & Feigl, 1998): **a) Pixel size** - if the deformation is on a spatial scale which is smaller than the pixel size (20 m at maximum resolution using Envisat) then it cannot be detected. **b) Swath width** - if the deformation signal is larger than the swath width then it can be impossible to measure. However, this can be overcome with Envisat by forming long interferograms in the along track direction (~1400 km) and by using Envisat's ScanSAR mode which has a swath width of ~ 400 km in the cross-track direction. **c) Phase gradient** - because only the relative phase between pixels is measured and the phase can only have an amplitude of $\pm\pi$, if the phase change is greater than π radians between adjacent pixels then the phase gradient becomes ambiguous. At the other end of the scale, if the amount of deformation across a swath is less than ~ 1 fringe then it is difficult to distinguish from errors in the measurement. **d) Cycle slicing** - identifying phase values separated by less than a tenth of a fringe is difficult, for C-band radar this places a lower limit of a few millimetres on the magnitude of deformation.

2.1.3 Processing with ROI_PAC

All of the interferograms in this thesis have been processed using ROI_PAC (Rosen et al. (2004)). Below is a brief description of the processing chain used in ROI_PAC, full details of the algorithms used in the software are described in Buckley (1998); Rosen et al. (2000) .

Creating an SLC

Before forming an interferogram the master (first acquisition) and slave (second acquisition) SLC images must be formed from the raw data. Firstly the raw data is pre-processed to extract information needed for processing, such as radar wavelength and pulse duration, and to compute the Doppler centroid. Computation of the Doppler centroid is required because of non-zero Doppler shifts in the direction perpendicular to the track caused by changes in the yaw and pitch of the satellite. The next step is to focus the image in the range and azimuth directions and perform a range migration. Focussing in the range direction takes advantage of the frequency modulated pulse which causes targets with different ranges to have different frequencies. Similarly in azimuth, frequency shifts caused by the motion of the satellite are used to focus the image. Range migration removes the effect of the satellites motion which causes echoes, with constant range, to be spread over a parabolic arc much the same as normal moveout in seismic processing.

Coregistration and interferogram formation

Once the SLCs have been processed to the same Doppler centroid the two images must be coregistered. This is the process of resampling the slave image (second acquisition) into the master (first acquisition) image geometry. This is done using the amplitude component of each image: the image matching is done in the Fourier domain by cross-correlating the master image with the slave. Once coregistered, the complex phasor of the master image is multiplied by the complex conjugate phasor of the slave image to form an interferogram. If M is the master image and S is the slave then

$$M = r_1 e^{i\phi_1} \tag{2.7}$$

and

$$S = r_2 e^{i\phi_2} \tag{2.8}$$

thus

$$MS^* = r_1 r_2 e^{i(\phi_1 - \phi_2)} \tag{2.9}$$

At this stage, to improve the signal to noise ratio, the interferogram is averaged (taking looks) in the azimuth direction. The pixel size for Envisat is ∼5 m in azimuth and ∼20 m in range. To make the pixels in the interferogram square, five looks are taken in azimuth.

Orbital and Topographic corrections

Using the satellite's orbital information, the phase ramp due to the different viewing geometries is removed in a step known as orbital flattening. Next, the effect of the topography is removed using a Digital Elevation Model (DEM). In this stage an interferogram containing the expected phase information due to the topography, generated using the DEM, is coregistered with the master image and subtracted from the interferogram.

Filtering, unwrapping and geocoding

To further improve the signal to noise ratio a non-linear power spectrum filter is typically applied (Goldstein & Werner, 1998). The advantage of this filter is that it adapts to the local phase slope, enhancing the frequency component that has the highest power. The filter is calculated by dividing the interferogram up into overlapping rectangular patches and the power spectrum, $Z(u, v)$, is computed by smoothing the intensity of the 2D FFT. The response of the filter is then given by

$$H(u, v) = |Z(u, v)|^{\alpha}. \tag{2.10}$$

When α is zero, no filtering occurs, while for $\alpha = 1$ the filtering is strong.

The next stage is the process of converting the modulo 2π interferometric phase into a continuous signal, in a process know as phase unwrapping. ROI_PAC uses a branch cut algorithm based on Goldstein et al. (1988) to unwrap the interferogram. For error-free data this is a simple process. A number of algorithms, such as the branch cut used by ROI_PAC, have been developed for cases where conditions are less favourable.

Finally the interferogram is mapped into geographic coordinates using the information gathered while matching the simulated amplitude image from the DEM to the master geometry.

2.2 InSAR Time Series Analysis

2.2.1 Stacking and Chain Stacking

Many of the signals detected by InSAR which are of interest to Earth scientists, such as magmatic intrusions and earthquakes, have large magnitudes and occur within the time scale of a single interferogram. The study of smaller scale deformations however, like those associated with strain accumulation around faults, requires interferograms to cover a sufficiently large period of time such that the signal of interest is discernible from unwanted noise (Biggs, 2007). Unfortunately interferograms are often limited by temporal decorrelation preventing interferograms with large temporal separations to be formed. In certain circumstances this problem can be overcome by combining interferograms in a process known as stacking. Assuming that the signal being measured is steady over long periods then combining a set of N interferograms will create a deformation signal that is N times larger than in a single interferogram whilst increasing the noise by a factor of $\sqrt{N}$. A number of studies have successfully used the stacking method for measuring inter-seismic strain along major fault zones in California (Fialko, 2006; Peltzer et al., 2001), Turkey (Wright et al., 2001) and Tibet (Wright et al., 2004b). In other areas, where temporal decorrelation is a problem, the method can break down as there are not enough stable pixels over the time period being measured (Biggs, 2007). Attempts have been made to overcome this problem by ranking each of the interferograms according to the percentage of coherent pixels. However, a study around the Denali Fault in Alaska by Biggs (2007) found that stacks with large numbers of interferograms, covering a sufficiently long period of time, lack in common coherent pixels whilst smaller stacks, with sufficient spatial coherence, do not have a long enough temporal duration for the signal to exceed the atmospheric noise.

An alternative method to stacking is chain stacking whereby the slave of one interferogram becomes the master of the next. In this situation the orbital and atmospheric errors from the middle acquisition are cancelled leaving the contributions from only the first master and last slave. The advantage of the chain method is that it can be constructed from a set of short time-period interferograms which do not suffer from the effects of temporal decorrelation like in the traditional stacking method. However, only pixels which are coherent in every interferogram remain.

2.2.2 Simple Time Series for analysis of post-rifting deformation

Unlike many inter-seismic signals, which are considered to be steady over geological time, post-seismic or post-rifting signals represent the transient response of the lithosphere as the stresses are relaxed. Some of the processes thought to be responsible for post rifting transients are discussed in Chapter 1 and may include the viscoelastic response in the lower crust or upper mantle (Hofton & Foulger, 1996a,b; Nooner et al., 2009; Pollitz & Sacks, 1996) or continued dyke opening at depth (de Zeeuw-van Dalfsen et al., 2004). Previous studies of post-rifting deformation have primarily used levelling and GPS datasets to constrain the deformation around the plate boundary. With regular acquisitions and good spatial resolution InSAR provides an excellent opportunity to monitor the post-rifting response along divergent boundaries.

If, for a given set of SAR acquisitions, it is possible to construct an interferogram between each of the images, $A\phi_i$ and $A\phi_{i+1}$, then a time series can be constructed. Unfortunately for many applications this condition cannot be met due to large baselines or poor coherence preventing interferogram formation. However, a time series can still be formed providing that the interferometric chain remains unbroken and that there are at least as many independent interferograms as there are acquisitions. If this is the case then a standard least-squares inversion can be performed (i.e. $\mathbf{G}^T\mathbf{G}\mathbf{m} = \mathbf{G}^T\mathbf{d}$) to find the time series of displacements such that $\mathbf{G}\mathbf{m} = \mathbf{d}$, where $\mathbf{G}$ is the design matrix, $\mathbf{m}$ is the displacement vector to be solved for and $\mathbf{d}$ is a vector containing the observed displacement from each interferogram. Using an example given by Biggs (2007) for a set of images acquired on the dates A, B, C, and D, collected with a time interval of 1 year in each case, the interferograms AB, BC, BD, AC have observed displacements of 1, 1, 2, and 2 mm respectively. In matrix form:

$$\begin{pmatrix} -1 & +1 & 0 & 0 \\ 0 & -1 & +1 & 0 \\ 0 & -1 & 0 & +1 \\ -1 & 0 & +1 & 0 \end{pmatrix} \begin{pmatrix} \phi_A \\ \phi_B \\ \phi_C \\ \phi_D \end{pmatrix} = \begin{pmatrix} 1 \\ 1 \\ 2 \\ 2 \end{pmatrix} \tag{2.11}$$

Although there are four equations and four unknowns in the above example, the rank of the matrix is one less than the number of unknowns as the fourth equation is the sum of the first two equations. Therefore, in order to solve for the displacements, $\phi_A - D$, a reference acquisition must be chosen where there is assumed to be zero displacement. This can be done in two ways, either explicitly (Eq. 2.12) whereby an additional constraint is added or implicitly (Eq. 2.13) where an unknown is removed.

$$\begin{pmatrix} -1 & +1 & 0 & 0 \\ 0 & -1 & +1 & 0 \\ 0 & -1 & 0 & +1 \\ -1 & 0 & +1 & 0 \\ 1 & 0 & 0 & 0 \end{pmatrix} \begin{pmatrix} \phi_A \\ \phi_B \\ \phi_C \\ \phi_D \end{pmatrix} = \begin{pmatrix} 1 \\ 1 \\ 2 \\ 2 \\ 0 \end{pmatrix} \tag{2.12}$$

$$\begin{pmatrix} +1 & 0 & 0 \\ -1 & +1 & 0 \\ -1 & 0 & +1 \\ 0 & +1 & 0 \end{pmatrix} \begin{pmatrix} \phi_B \\ \phi_C \\ \phi_D \end{pmatrix} = \begin{pmatrix} 1 \\ 1 \\ 2 \\ 2 \end{pmatrix} \tag{2.13}$$

2.2.3 Rate map formation using $\pi rate$

The $\pi rate$ software was developed by Hua Wang at the University of Leeds with contributions for Tim Wright, Juliet Biggs (University of Oxford) and John Elliot (University of Oxford). Here I will give an overview of the processing steps used by $\pi rate$ which will be used to examine the post-rifting deformation in Afar in Chapter 5.

Algorithm Overview

In order to use $\pi rate$ all of the data must first be geocoded and unwrapped. The algorithm consists of four main steps: an orbital error correction, an atmospheric correction, construction of a rate map and estimation of the associated errors (Fig. 2.8). For a given interferogram network a minimum spanning tree (MST) algorithm (Kruskal, 1956) is applied based on the fraction of unwrapped pixels. The value of each pixel within every interferogram is checked to ensure that it is non-zero, if it is zero in more than X interferograms, where X is a user-selected threshold, then it is discarded from the network. Once all of the pixels have been selected from the network a method similar to coregistration is used to find a reference point that is common to all interferograms. A number of tie points are selected and, using a window around the tie point, the fraction of coherent pixels and their standard deviation are calculated. The tie point with the maximum number of coherent pixels and minimum standard deviation is then selected as the reference point.

Orbital Correction

With the network of interferograms selected the next step is to estimate and remove the orbital error using the method of Biggs et al. (2007). Although processing software, such as *ROI_PAC*, removes the effect of the baseline from the interferogram it is based on the assumption that the Earth is a smooth ellipsoid and that the satellite orbits are accurately known. However, in reality our knowledge of the satellite orbits is based on models with reported accuracies of 5-7 cm radially and 10-15 cm cross-track (Scharoo & Visser, 1998). As such, an orbital error still remains even after the effects of the baseline are removed (Zebker et al., 1994). Most earlier studies calculate the orbital contributions on individual interferograms. However, Biggs et al. (2007) showed that a network approach can be used such that orbital contributions can be estimated from many interferograms. For a given interferogram the orbital contribution can be thought of as the difference between the orbital contributions at each acquisition (Biggs et al., 2007). For correcting the orbital error it is assumed that the interferogram is dominated by the orbital contribution and that all other contributions to the phase are a source of noise. Assuming a planar orbital error, a pixel, p at the location x_p, y_p has an interferometric phase, ϕ_{12p}, which is composed of the linear combination of two parameters, u and v for each acquisition, *1* and *2*, and a reference frame shift for the interferogram, w_{12}, such that:

$$\phi_{12} = u_1 x_p - u_2 x_p + v_1 y_p - v_2 y_p + w_{12}. \tag{2.14}$$

Since there is always at least one fewer interferograms than acquisitions the problem is underdetermined. Therefore, a truncated single value decomposition is used, with a threshold of 1×10^{-6} for truncating the values, to find the minimum norm solution. Because only the long wavelength signal is of interest, the interferogram can be multilooked to reduce the number of points from $\sim 10^7$ to a more reasonable $\sim 10^3$. To further improve the computation time this part of the inversion is performed without a variance-covariance matrix. The final part of this step is to use a forward model which is representative of the orbital error. This is then upsampled to construct a full resolution version of the orbital contribution for each interferogram (Fig. 2.9).

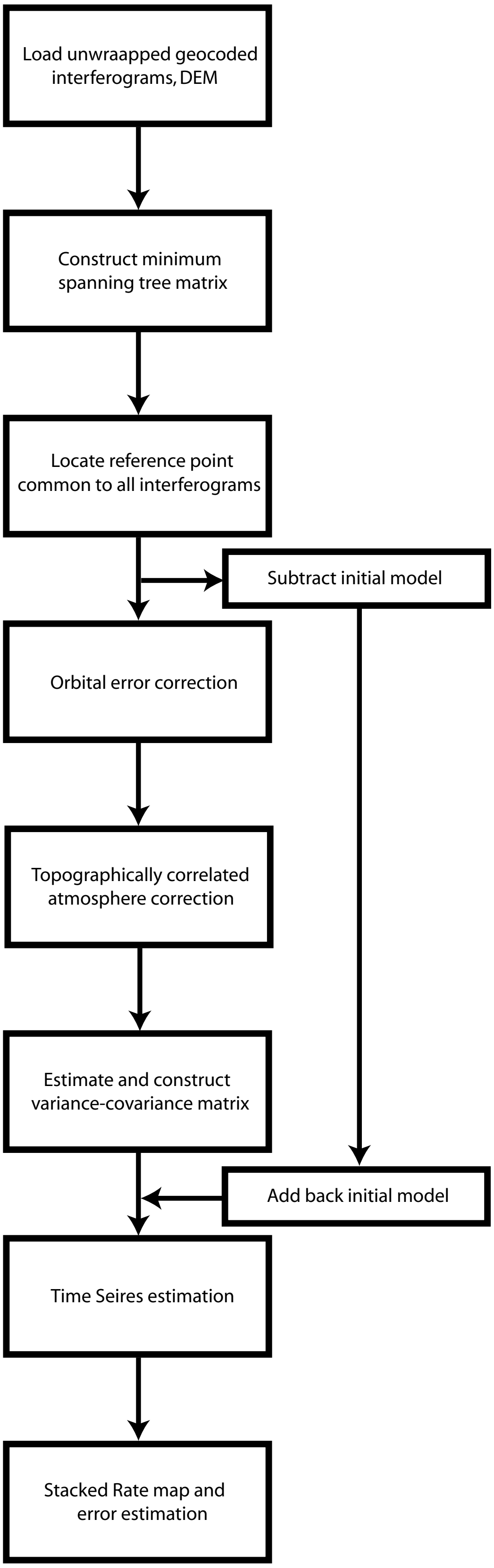

Figure 2.8: Flowchart showing the main processing steps for calculating a rate map using πrate

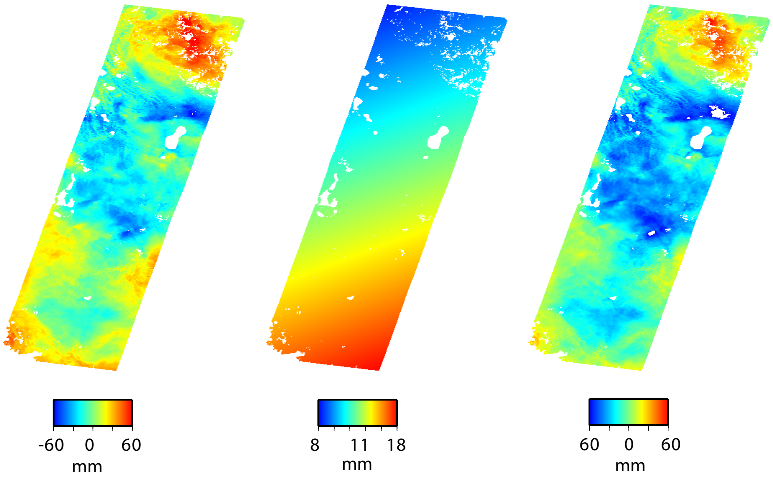

Figure 2.9: An example of an interferogram corrected using the network orbital correction. (*Left*) Original unwrapped interferogram. (*Centre*) Estimated orbital error calculated by solving Equation 2.14. (*right*) Corrected interferogram.

Atmospheric Correction

A number of studies have shown that the atmospheric contribution to the phase change detected using InSAR is strongly correlated with topography. Cavalié et al. (2007) demonstrated that range changes detected in the Lake Mead region, Nevada, where linearly related to the elevation. Similarly, Cavalié et al. (2008) showed that a linear trend could be used to approximate the range change detected across the Haiyaun Fault, Tibet.

To correct for the atmosphere $\pi rate$ adopts the same approach used to estimate the orbital errors described above. As with the orbital correction, each of the interferograms is downsampled by taking a further 10 looks. The phase value at each pixel in all of the interferograms, ϕ_{ijk}, is then used to invert for the correlation of phase change with topography using a downsampled DEM such that:

$$\phi_{ijk} = (w_j - w_i)h_k + c_{ij}, \tag{2.15}$$

where $w_{i,j}$ are the phase gradients for the ith and jth pixels, h is the elevation and c is a static offset in the interferogram. Once solved for the gradients are forward modelled to generate a synthetic interferogram of atmospheric noise which is subsequently removed

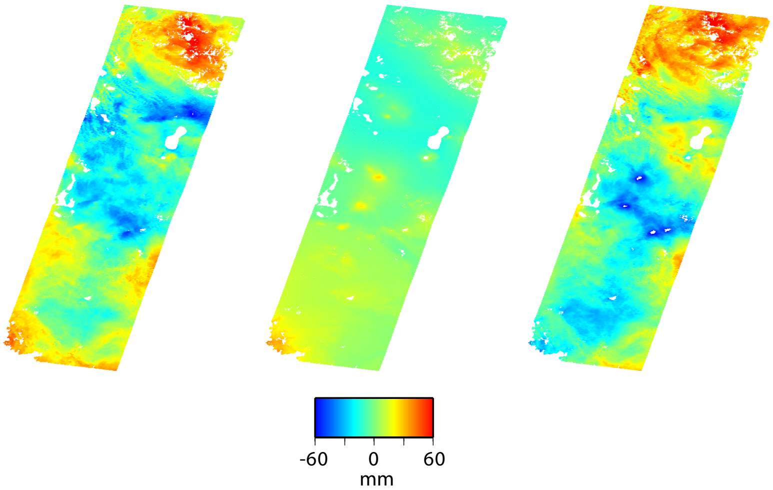

Figure 2.10: An example of an interferogram corrected using the network atmosphere correction. (*Left*) Original unwrapped interferogram. (*Centre*) Estimated atmospheric error calculated by solving Equation 2.15. (*right*) Corrected interferogram.

from each of the interferograms in the network (Fig. 2.10). Using this method utilises all of the data available in each interferogram and, because it is applied after the orbital correction, reduces the error in the estimate of atmospheric noise.

Variance-covariance estimation

The variance-covariance matrix (VCM) is calculated using a 1-D covariance function specific to each interferogram. It is assumed that the principle source of noise in the interferogram is due to different levels of water vapour in the troposphere between acquisitions. Water vapour bodies can be spatially continuous over tens to hundreds of kilometres, and therefore any noise associated with these bodies are assumed to be spatially correlated over similar wavelengths (Hanssen, 2001; Parsons et al., 2006; Wright et al., 2003). Using an interferogram which has had the deformation signal removed leaving only the far field signal, a 1D covariance function is estimated for the data, the problem is 1D as it is assumed that the covariance is only a function of distance. The 1D covariance function is the radial average of the interferogram's auto-covariance calculated in either the spatial or spectral domains. Once the covariance function has been calculated, it is used to construct the variance-covariance matrix (VCM) by fitting a functional form to the data such as

$$c(r_{ij}) = \sigma^2 e^{(\frac{-r_{ij}}{\alpha})} \tag{2.16}$$

where $c(r_{ij})$ is the covariance between pixels i and j, σ^2 is the variance; r is the distance between the pixels, and α is a constants governing the length scale of decay.

Time Series Estimation

For most applications it can be assumed that the surface displacements are smooth with time. To minimise the effects of any residual atmospheric noise, orbital and unwrapping errors a smoothing constraint can be included to reduce these errors. There are a number of methods to calculate the smoothing constraint including finite difference approximations (Schmidt & Burgmann, 2003) and singular value decomposition (Berardino et al., 2002).

The Laplacian smoothing method utilises the finite difference approximation of the second order differential of the time series as a smoothing constraint such that

$$\begin{pmatrix} \mathbf{G} & 0 \\ \gamma^2 & \frac{d^2}{dt^2} \end{pmatrix} \mathbf{m} = \begin{pmatrix} \mathbf{d} \\ 0 \end{pmatrix} \tag{2.17}$$

where γ^2 is the weighting for the smoothing parameter. For $\gamma = \mathit{0}$ no smoothing is applied and the time series will be rough and prone to sharp fluctuations from one time step to another, for large values of γ the time series will be dampened. For the case where acquisitions are not evenly spaced in time additional information on the temporal separation must be included in the finite difference expression. Assuming that the velocity, v, during two time periods, AB and BC, are equal then

$$\frac{\phi_B - \phi_A}{t_B - t_A} = \frac{\phi_C - \phi_B}{t_C - t_B} \tag{2.18}$$

which can be converted into a smoothing constraint and weighted for use in the inversion

$$\begin{pmatrix} \gamma^2(t_B - t_A) & \gamma^2(t_C - t_A) & \gamma^2(t_C - t_B) \end{pmatrix} \begin{pmatrix} \phi_A \\ \phi_B \\ \phi_C \end{pmatrix} = 0. \tag{2.19}$$

Thus, the smoothing constraint assumes that the deformation in short duration interferograms is less than that in interferograms with a longer temporal baseline.

If $\mathbf{G}$ is rank deficient, as is the case for a network of interferograms which cannot be connected, and therefore G^TG is singular, it is not possible to find the inverse of $\mathbf{G}$ directly. To overcome this problem $\mathbf{G}$ can be decomposed using the SVD method whereby the pseudo-inverse of $\mathbf{G}$, which gives the minimum-norm least squares solution, is obtained.

$$\mathbf{G} = \mathbf{USV^T} \tag{2.20}$$

where $\mathbf{U}$ is an $M \times M$ matrix whose first N columns are the eigenvectors of $\mathbf{GG^T}$, $\mathbf{V}$ is an $N \times M$ matrix whose columns are the eigenvectors of $\mathbf{G^TG}$ and $\mathbf{S}$ is a square diagonal matrix containing the singular values of $\mathbf{G}$, σ_n, equal to the square root of the corresponding eigenvalues from $\mathbf{GG^T}$. The inverse of $\mathbf{G}$ is then given by

$$\mathbf{G^{-1}} = \mathbf{VS^{-1}U^T}. \tag{2.21}$$

Since $\mathbf{S}$ is diagonal its inverse, $\mathbf{S^{-1}}$, is given by

$$\mathbf{S^{-1}} = diag(\frac{1}{\sigma_1}, \frac{1}{\sigma_2}, ...\frac{1}{\sigma_n}) \tag{2.22}$$

where the largest singular values represent the most important part of the signal. When $\mathbf{G}$ is rank deficient, a number of the singular values will be equal to, or very close to, zero. Taking the inverse of these values would result in a matrix with values tending towards infinity, thus they are typically replaced with zero values to form a pseudo-inverse matrix. Removing these values removes any small scale fluctuations in the time series and as a result can be used as a smoothing constraint by adjusting the threshold where singular values are replaced.

Stacking and rate map formation

The final processing step is the formation of the rate map. In forming the rate map it is necessary to combine all of the measurements from pixels which are coherent in some but not all of the interferograms. This is done using the MST matrix created earlier, each interferogram is checked to ensure that the minimum number of observations is available for each pixel and a least squares inversion is adopted on a pixel-by-pixel basis to find the best fitting rate, r_{los}.

$$\frac{2\pi}{\lambda}\mathbf{T}r_{los} = \mathbf{P} \tag{2.23}$$

where T is a vector containing the time-spans, $[t_{12}, t_{23}, t_{34}, t_{nn+1}]^T$, and P is a vector of phase values, $[\phi_{12}, \phi_{23}\phi_{34}, \phi_{nn+1}]^T$ at each pixel in each interferogram.

To account for the correlation between interferograms and any residual atmospheric and orbital noise the inversion is weighted using a variance-covariance matrix, Σ_p. Each element, σ_{lm-nq}, within the variance-covariance matrix depends on the atmospheric error for each interferogram, σ_{lm} and σ_{nq}, the orbital error for each pixel, σ_p and the correlation between interferograms, c_{lm-nq}.

$$\sigma_{lm-nq} = (\sigma_{lm}\sigma_{nq} + \sigma_p^2)c_{lm-nq} \tag{2.24}$$

In the case where the variance is equal in both interferograms, $\sigma_{lm} = \sigma_{nq}$, then for interferograms with a common master or a common slave image ($l = n$ or $m = q$) c_{lm-nq} = 0.5, if the master of one interferogram is the slave of another ($l = q$ or $m = n$) then c_{lm-nq} = -0.5, if the interferograms are completely independent then $c_{lm-nq} = 1$ (Biggs et al., 2007). To simplify matters the atmospheric error in each interferogram is assumed to be constant and is equal to the median value generated from analysis of atmospheric noise described above. The rate and associated error are then

$$\frac{\lambda}{2\pi}[\mathbf{T}^T\Sigma_{\mathbf{P}}^{-1}\mathbf{T}]^{-1}\mathbf{T}^T\Sigma_{\mathbf{P}}^{-1}\mathbf{P} \tag{2.25}$$

$$\Sigma_{\mathbf{r}} = [\mathbf{T}^T\Sigma_{\mathbf{P}}^{-1}\mathbf{T}]^{-1} \tag{2.26}$$

To ensure that unreliable pixels aren't included in the final rate map the variance for each pixel is compared with an a priori value, typically 2 mm. If the variance is greater then this value then the pixel is removed from the rate map. Once the rate map is formed the standard deviation at each pixel is examined and compared with a user defined allowable maximum error. Any pixels with standard deviations that exceed this value are then removed from the final rate map.

2.3 Modelling Methods

A number of different modelling methods have been used in this thesis to describe the ongoing deformation in Afar, these include elastic dislocation models, point source models, stress change calculations and finite element models. This section will summarise the theory behind the methods that have been used in the subsequent chapters.

2.3.1 Dislocation modelling of dykes and faults

Elastic dislocation theory is widely employed for the modelling of earthquakes and magmatic intrusions (e.g. Hamling et al., 2009; Massonnet et al., 1993; Pedersen & Sigmundsson, 2004; Wright et al., 2006). It was first introduced into the field of seismology by Steketee (1958) who showed that the displacement field, $u_i(x_1, x_2, x_3)$, due to a dislocation, $\Delta u_j(\xi_1, \xi_2, \xi_3)$, over a surface, $\sum$, in an isotropic medium is given by

$$u_i = \frac{1}{F}\int\int_{\sum} \Delta u_j \left[\lambda\delta_{jk}\frac{\partial u_i{}^n}{\partial \xi_n} + \mu\left(\frac{\partial u_i{}^j}{\partial \xi_k} + \frac{\partial u_i{}^k}{\partial \xi_j}\right)\right]\nu_k d\sum \tag{2.27}$$

where δ_{jk} is the Kronecker delta, λ and μ are Lamé's constants and ν_k is the direction cosine of the normal to the surface element $d\sum$. u_i^j is the ith component of the displacement at (x_1, x_2, x_3) due to the jth direction point force of magnitude $\mathbf{F}$ at (ξ_1, ξ_2, ξ_3).

Explicit analytic solutions to this integral are given by Okada (1985) enabling the calculation of surface displacements due to buried shear and tensile faults in an elastic half-space, the geometry and co-ordinate space is shown in Figure 2.11a. A single dislocation can be described by nine parameters: the top and bottom depths, length, strike, dip, rake, latitude and longitude and the magnitude of slip or opening. For more complex fault models or to model a fault or dyke with non-uniform slip/opening, the surface displacements from multiple dyke or fault patches can be summed together.

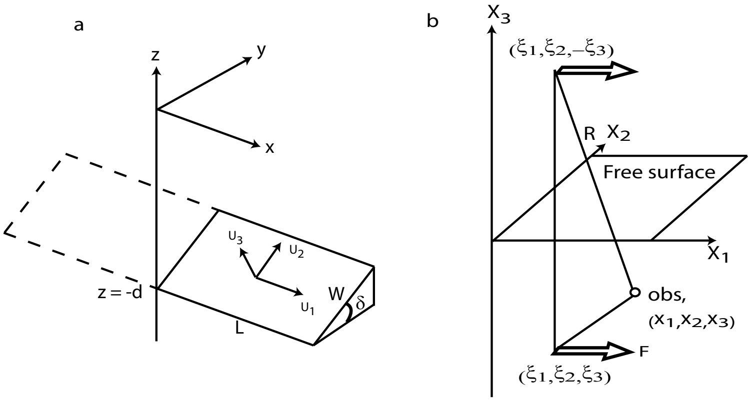

Figure 2.11: **a**) Geometry for the elastic dislocation source model after Okada (1985), **b**) Co-ordinate system adopted for internal displacement and strain fields, after Okada (1992).

This work was extended by Okada (1992) to calculate the internal deformation fields due to shear and tensile faults in a half space. Based on equation 2.27 and body force equivalent relations, Okada showed that the internal displacement field, u°, can be expressed as the combination of the displacement fields due to strain nuclei, $\partial u^j/\partial \xi_k$. Figure 2.11b shows the coordinate system adopted for this study. The closed analytic solutions given by Okada (1992) enable the calculation of the internal stress fields which will be discussed more fully in Section 2.4 and in Chapter 4.

2.3.2 Point source models of inflating and deflating magma chambers

A large number of studies of volcanic processes use the 'Mogi model' (Mogi, 1958) to describe the deformation caused by the inflation or deflation of a magma chamber at depth. The Mogi model represents the accumulation of magma within the crust as a point pressure source in an elastic half-space with a Poisson's ratio of 0.25. For a pressure change, ΔP, the resulting horizontal and vertical surface displacements are given by

$$U_h = C\frac{r}{(d^2+r^2)^{\frac{3}{2}}} \tag{2.28}$$

$$U_z = C\frac{d}{(d^2+r^2)^{\frac{3}{2}}} \tag{2.29}$$

where $C = \frac{3a^3\Delta P}{4\mu}$, a is the radius, μ is the shear modulus, d is the source depth and r is the horizontal distance away from the source (Fig. 2.12b). An alternate expression for C, which relates the injection volume to the volume of the uplifted surface, is given by $C = \frac{3\Delta V}{4\pi}$ (McTigue, 1987). In the example in Figure 2.12a a point source is inflating by 0.01 km^3 at a depth of 3 km. By integrating the vertical displacements over the free surface, Delaney & McTigue (1994) have shown that the volume of uplift is given by

$$\Delta V_{up} = 2\pi U_z^{max} d^2 \tag{2.30}$$

and that the ratio of uplift volume to injection volume is

$$\frac{\Delta V_{up}}{\Delta V_{in}} = 2(1-\nu) \tag{2.31}$$

For the example given in Figure 2.12a the maximum uplift, U_z^{max}, is 0.265 m giving an uplift volume of 0.015 km^3 and a ratio of uplift to injection volumes of $\frac{3}{2}$. Equation 2.31 indicates that for incompressible materials ($\nu = 0.5$) the uplift and injection volumes are equal. However, for compressible materials ($\nu < 0.5$) the uplift volume increases relative to the injection volume.

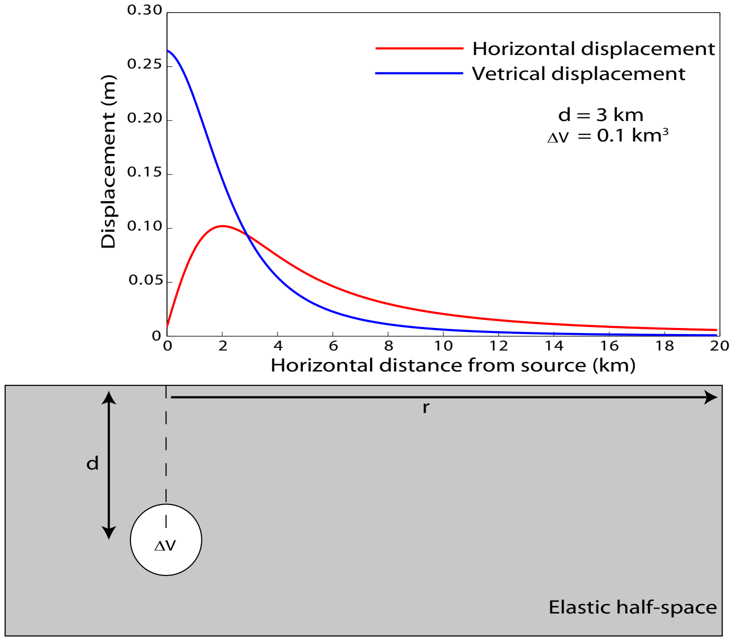

Figure 2.12: The Mogi Model. **a**) Vertical and horizontal displacements.**b**) Schematic view.

An alternate expression for a point source in an elastic half space was given by Okada (1992), the advantage of this formulation is that it allows for the calculation of the displacement and strain fields anywhere in the half-space (Section 2.3.1). For an Okada point source the displacement field is given by

$$u^{\circ} = \frac{M_0}{F} \frac{\partial u^n}{\partial \xi_n} \tag{2.32}$$

where M_0 is the volume change of the source.

2.4 Elastic stress change modelling

In the last few decades there have been a large number of published articles on the role of static stress changes, generated by earthquakes, influencing the location and timing of subsequent events. These studies have been conducted in a range of tectonic settings, for example in the Asal Rift in northeast Africa (e.g. Jacques et al., 1996), in Japan (e.g. Okada & Kasahara, 1990; Pollitz & Sacks, 1995, 1997) and in California (e.g. Harris & Simpson, 1996; King et al., 1994; Reasenberg & Simpson, 1992; Stein, 1999). In addition to the study of earthquakes, stress change calculations have been used to analyse the spatial pattern of magmatic intrusions and the interaction between volcanic and tectonic processes (e.g. Amelung et al., 2007; Cayol et al., 2000; Jónsson, 2008; Toda et al., 2002).

To calculate the stress change, many of the studies use the internal deformation fields calculated using the elastic dislocation models of Okada (1992). The stress field at any given point is then easily evaluated using the following expressions

$$\epsilon_{ij} = \frac{1}{2}(\frac{\partial u_i}{\partial x_j} + \frac{\partial u_j}{\partial x_i}), \tag{2.33}$$

$$\sigma_{ij} = \lambda \epsilon_{kk} \delta_{ij} + 2\mu\epsilon_{ij}, \tag{2.34}$$

where ϵ and σ are the strain and stress, $\frac{\partial u}{\partial x}$ is the rate of change of displacement, λ and μ are Lame's constants and δ is the Kronecker delta. For assessing the effect of stress transfer on the location of future earthquakes many authors calculate the Coulomb failure stress, ΔCFS (Equation 2.35).

$$\begin{aligned} \Delta CFS &= \Delta\sigma_s + \mu(\Delta\sigma_n + \Delta P) \\ &= \Delta\sigma_s + \mu'\Delta\sigma_n \end{aligned} \tag{2.35}$$

where $\Delta\sigma_s$ is the change in shear stress, μ is the coefficient of friction, $\Delta\sigma_n$ is the change in normal stress and ΔP is the pore pressure change in the fault zone. The parameter μ' is known as the apparent coefficient of friction and includes the effects of pore fluids and material properties in the fault zone. The Coulomb failure stress is used to evaluate whether faults in a given region are brought closer to, or farther from, failure after an earthquake or volcanic event. For $\Delta CFS > 0$, the fault is brought closer to failure, if $\Delta CFS < 0$ the likelihood of failure is reduced.

Chapter 3

New dyking in the Dabbahu rift segment between 2006 and 2009

Following the September 2005 rifting episode regular ASAR acquisitions were acquired over the Dabbahu magmatic segment (Fig. 3.1). Continued activity has been monitored using Satellite Radar Interferometry (InSAR), data from Global Positioning System (GPS) instruments and seismometers deployed around the rift in response to the initial intrusion. These data show that a sequence of new dyke intrusions has reintruded the central and southern section of the Dabbahu segment. Dyking events were detected in June, July, September and December of 2006, in January, August and November of 2007. The rifting episode continued in 2008 and 2009 with the intrusion of three dykes in 2008 and two dykes in 2009. Modelling of InSAR data indicates the dykes were between 0.5 and 3 m wide, up to ∼10 km long and confined to the upper 10 km of crust. Intrusions in August 2007 and June 2009 were associated with ∼5-km-long basaltic fissural eruptions. During the new dyke injections, InSAR and GPS data show no subsidence at either of the volcanoes at the northern end of the segment, which partly fed the September 2005 dyke. Seismicity data imply that the dykes were probably fed from a source near the Ado'Ale Silicic Complex at the centre of the segment. The new dykes are concentrated in areas where the 2005 dyke did not produce significant opening, implying that residual tensile tectonic stresses are higher in this location and are focusing the later intrusions. The sequence of dyke intrusions observed so far is similar to those seen in Iceland during the Krafla rifting episode, which lasted 9 years from 1975-1984. It is likely that, with a continued magma supply, dykes will continue to be intruded until the tectonic stress is fully relieved. This chapter presents a number of ascending and descending interferograms from June 2006 to July 2009 covering each of the new dyke intrusions. I use elastic modelling of InSAR and, where available, GPS data to determine the geometry and amount of opening for each event and compare the results with the 1975 - 1984 Krafla rifting episode.

3.1 Deformation following the September 2005 dyke intrusion

Deformation, at rates of a few cm per month, was observed around the rift segment in the months following the initial intrusion (Ebinger et al., 2008) (Fig. 3.2 and 3.4). Between 19 December 2005 and 23 January 2006 (Fig. 3.2a) $\sim$ 9 cm of inflation was observed at Gabho, there was little deformation observed at Dabbahu but $\sim$ 6 cm of subsidence was observed on its southern flank. In the centre of the segment, $\sim$ 6 cm of inflation and westward motion was observed, consistent with GPS measurements. Similar deformation patterns were observed in the interferogram spanning 23 January to 27 February (Fig. 3.2b), between 27 February and 3 April (Fig. 3.2c) over $\sim$ 9 cm of inflation was observed at both the volcanoes and a further 12 cm of uplift and westward motion in the centre of the rift segment. Between 3 March and 12 June inflation at the volcanoes slowed with Gabho showing $\sim$ 6 cm of uplift. Seismicity suggests that the deformation, along the rift segment, observed in this time may have been the result of continued magma injection into the September 2005 dyke. The deformation style changed dramatically during June 2006 when a new dyke was intruded in the vicinity and to the south of the Ado'Ale volcanic complex — a dissected, central silicic centre, 30 km south of Dabbahu volcano (Keir et al., 2009). Between June 2006 and July 2009 a further 12 dykes were intruded into the Dabbahu segment emplacing an additional 1 km^3 of material.

3.1.1 InSAR data

Each of the interferograms covering a new dyke intrusion have been processed using the JPL/Caltech ROI_PAC software (Rosen et al., 2004) described in Chapter 2. Topographic corrections were made using a 3 arc-second (90 m) digital elevation model (DEM) generated by the NASA Shuttle Radar Topography Mission (Farr & Kobrick, 2000). Interferograms were filtered using a power spectrum filter (Goldstein & Werner, 1998) and unwrapped using the branch cut algorithm (Goldstein et al., 1988). The unwrapped interferograms are checked for any unwrapping errors and corrected where necessary. In cases where ambiguities could not be reliably determined, I removed the ambiguous phase

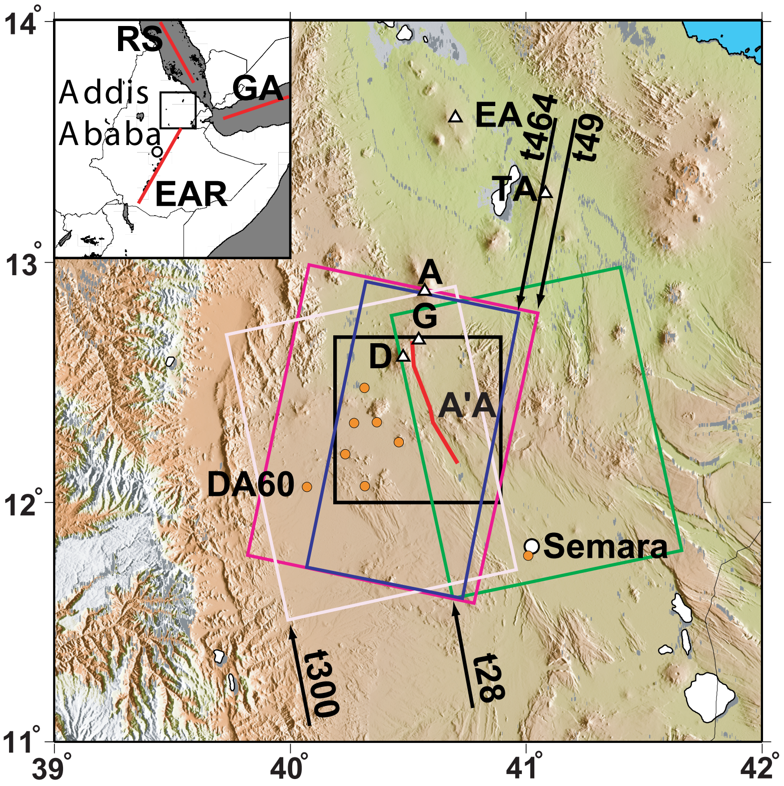

Figure 3.1: Colour shaded relief map of northern Afar. Inset shows the location of the study area (black square); red lines show the location of the Red Sea (RS), Gulf of Aden (GA) and East African Rift (EAR) systems. Main figure shows the location of the dyke (red line) intruded in 2005, Gabho (G), Dabbahu (D), Alayta (A), Ado'Ale (A'A), Tat'Ale (TA) and Erta'Ale (EA) volcanoes (white triangles) and Semara, the regional capital (white circle). The coloured boxes indicate the available InSAR coverage - tracks 28 (green box), 49 (pink box), 300 (white box) and 464 (blue box). Orange circles indicate the continuous GPS stations used in the joint inversion of InSAR and GPS data. The black box indicates the region covered by the interferograms in Figs. 3.11-3.17. The Manda-Hararo segment runs from Dabbahu to Semara.

from the unwrapped interferograms. Where data exist, and perpendicular baselines allow, interferograms were formed with the shortest possible time span (Fig. 3.3).

3.1.2 GPS Data

In addition to the InSAR data, continuously-recording GPS data from up to 11 sites, installed in and around the rift segment in response to the 2005 dyke injection, were available covering the 2006 - 2009 dyke sequence (Fig. 3.1, 3.4, 3.9). These data were analysed and processed by Eric Calais at Purdue University.

In a first step, the phase and pseudorange GPS data were processed in single-day solutions using the GAMIT software (King & Bock, 2005). Station coordinates and phase ambigu-

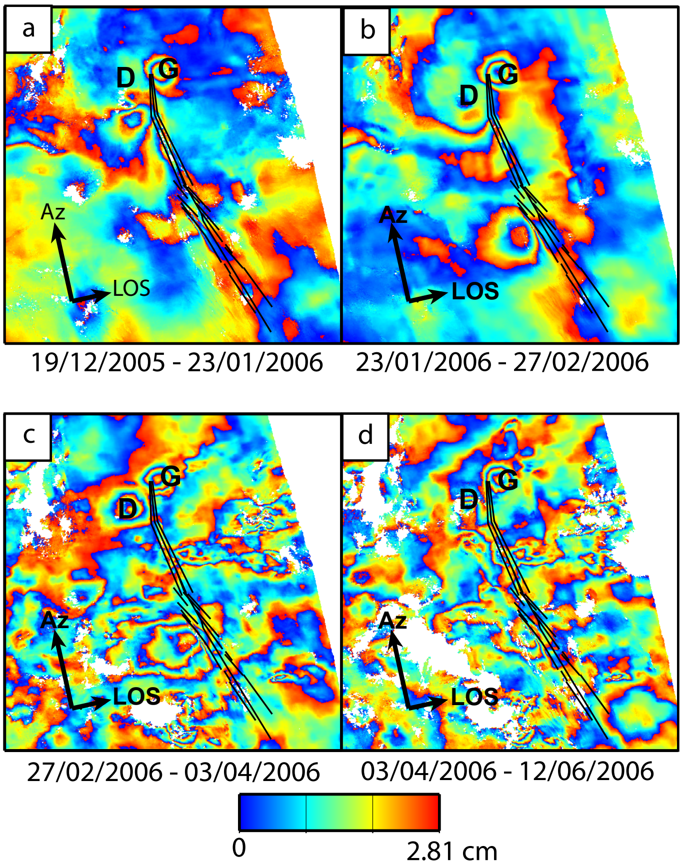

Figure 3.2: InSAR time series showing the deformation between 19 December 2005 and 12 June 2006. **a**, Interferogram from 19 December 2005 - 23 January 2006. **b**, Interferogram from 23 January 2006 - 27 February 2006. **c**, Interferogram from 27 February 2006 - 03 April 2006. **d**, Interferogram from 03 April 2006 - 12 June 2006. **D** and **G** mark the locations of Dabbahu and Gabho respectively

ities were solved for using doubly-differenced GPS phase measurements. Next, azimuth and elevation dependent absolute antenna phase centre models were applied following the table recommended by the IGS. Finally, the reference frame was implemented by tightly constraining the GPS orbits and IERS earth orientation parameters to the final IGS values and map site positions with respect to site DA60 (Fig. 3.1, 3.4).

With the exception of the sites located at the volcanoes, DABB and GABH, most of the sites show steady long-term westward velocities, likely to be the result of long term relaxation following the September 2005 intrusion (Fig. 3.4). Sites nearest the rift also show sudden displacements on the dates of dyke injections. To calculate the size of these jumps, site positions were modelled as the sum of (1) a linear term representing a long-term (constant) velocity, (2) an annual and semi-annual periodic term representing seasonal effects not modelled in the GPS data analysis, and (3) DC offsets at the time of dyke

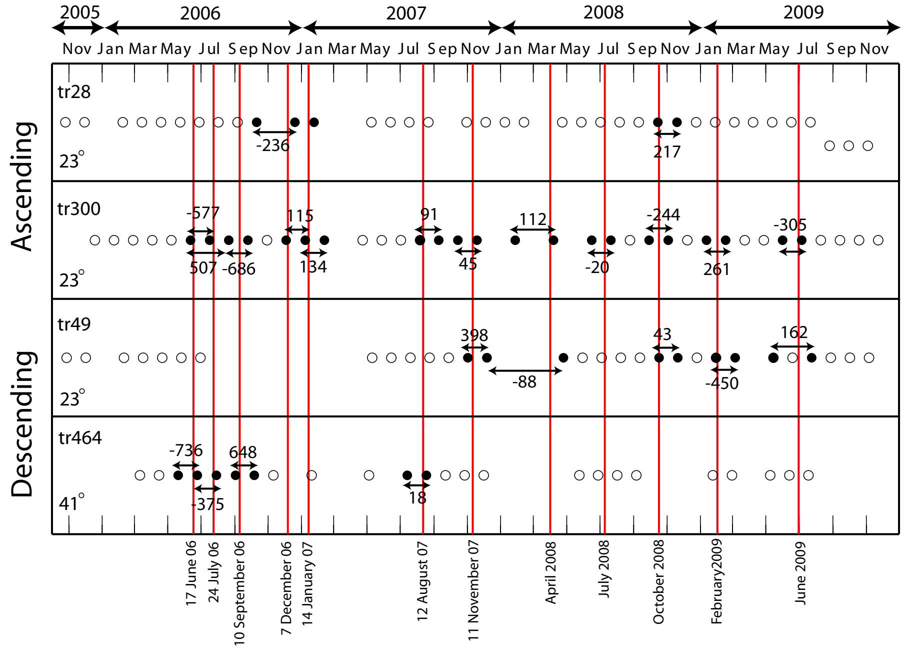

Figure 3.3: Time line from 1 October 2005 to 31 December 2009 showing available ASAR acquisitions. Red lines indicate the intrusion of a dyke into the segment. Circles indicate the available ASAR images for each of the 4 tracks, the filled circles are the images used for this study. The black arrows indicate the ASAR pairs used to construct each interferogram with the perpendicular baseline (m) labelled.

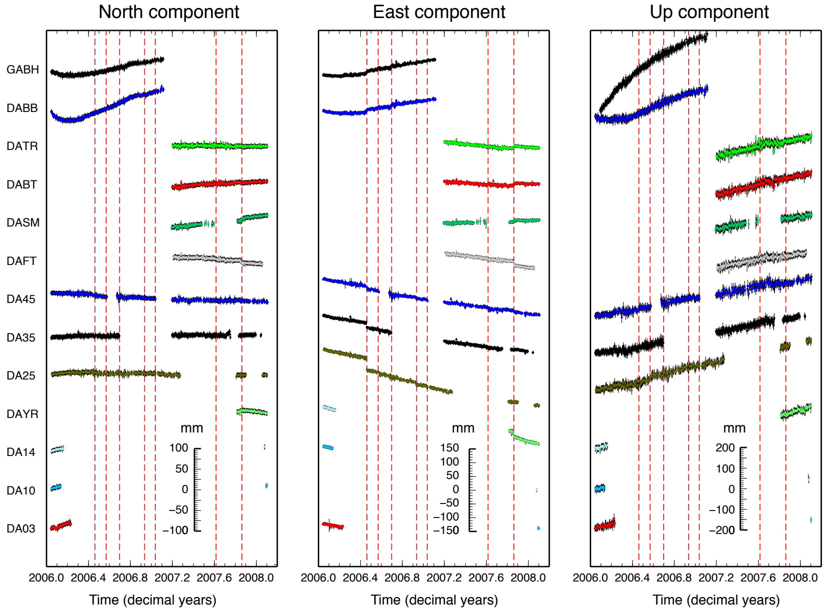

Figure 3.4: Position time series at continuous GPS sites. Site names are listed on the left side of the figure. Y-axis scale is indicated within each panel and is different for each of the north, east, and up components. Red dashed line indicate the time of diking events. Location of each of the GPS stations is shown in Figure 3.9**h**.

intrusions. The model equation is:

$$y = at + b + \sum_{i=1}^{n} c_i H(t_i) + d\sin(2\pi t) + e\cos(2\pi t) + f\sin(4\pi t) + g\cos(4\pi t) \tag{3.1}$$

where a, b, c$_i$, d, e, f, and g are estimated by inverting the site position data y using a singular value decomposition scheme. H(t$_i$) is the Heaviside step function that shifts from null to unity at the time t$_i$ of the ith dyke intrusion, where t measures time in years from the beginning of GPS observations in 2006 (Press et al., 1986). The modelled site positions, corrected for the annual and semi-annual terms, were used to compute site displacement between the time of the two SAR scenes that compose each interferogram.

3.1.3 Elastic Dislocation Modelling

Uniform opening model

Initially each dyke was modelled as a rectangular dislocation in an elastic half space, after the formulations of Okada (1985) (Chapter 2). The 3D displacements calculated by the model are projected into the satellite line-of-sight (LOS) and solutions are found that minimise the square misfit between the observed and calculated LOS displacements (Wright et al., 1999). To make the inversion possible, the InSAR data are first subsampled using a Quadtree algorithm (e.g. Jónsson et al., 2002), which reduces the number of data points from $\sim 10^7$ to $\sim 10^3$. In this method, the unwrapped interferogram is divided into four quadrants. If the variance within a quadrant is above a given threshold (4 radians^2 in this case) the quadrant is subdivided into four. This process is repeated until the variance is less than the given threshold, (Wright et al., 2004c) (Fig. 3.5). The value of the variance threshold should be set such that the number of data points, after subsampling, is sufficient to describe all of the observed deformation. A hybrid Monte-Carlo, downhill simplex inversion is used to determine a set of parameters with minimum square misfit, D$_{rms}$, between the observed displacements, d$_{obs}$, and the displacements calculated using the Okada formulae, d$_{calc}$, where

$$D_{rms} = \sqrt{\frac{1}{N}\sum(d_{obs} - d_{calc})^2} \tag{3.2}$$

where N is the number of data points. Local minima are avoided in the inversion by using a Monte-Carlo approach; the inversion is started 100 times using random starting parameters, with the lowest minimum being retained as the final solution (Wright et al. (1999)).

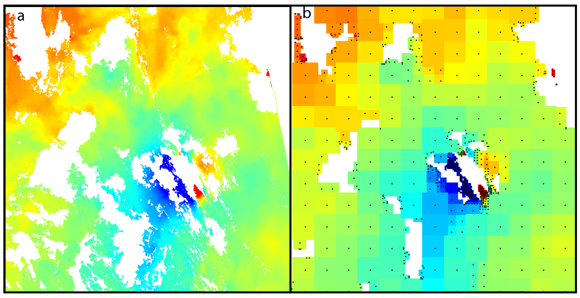

Figure 3.5: **a**, Unwrapped interferogram covering the July 2006 dyke intrusion. **b**, Example of the interferogram in a) after it has been subsampled using the quadtree algorithm (Section 3.1.3). Black dots represent sample points, notice the increased sampling in the deforming region.

Using the InSAR data I solve for the position, dip and strike of the rectangular dislocation, its length and depth extent, and the opening displacement which is constant and normal to the dyke (Table 3.1). Parameter uncertainties are calculated using a Monte-Carlo simulation in which correlated noise is added to the data (Parsons et al., 2006; Wright et al., 2003) generated using the variance-covariance matrix of each interferogram. Using the VCM for each interferogram a set of 100 simulations of spatially correlated noise is created and then added to the original observations. Each new perturbed data set is inverted, using the method described above, providing a range of model parameters (Fig. 3.6). Assuming that this is representative of the atmospheric noise in the deforming area, then the distribution of model parameters provides an estimate of their uncertainty.

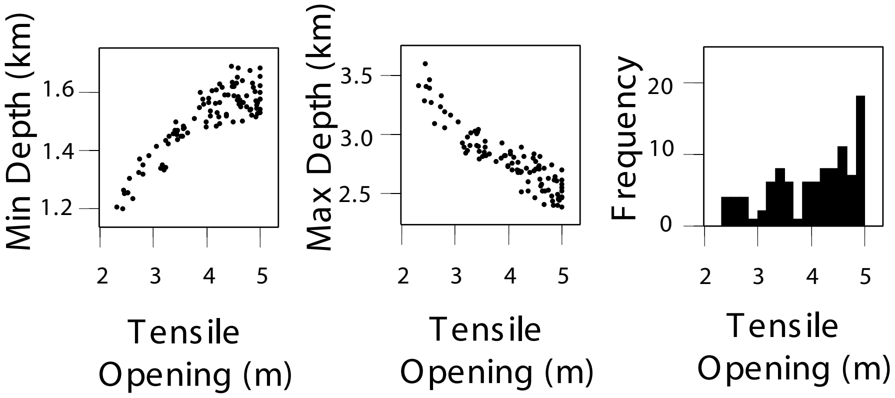

Figure 3.6: Monte Carlo estimates for parameter errors associated with the July 2006 dyke intrusion. Notice the strong tradeoff between depth and dyke opening.

The models provide useful constraints on the geometry of each of the dykes (Table 3.1). Despite the relatively poor misfit between predicted and observed displacements (~20 mm < rms < ~50 mm), I was able to use the data to determine the location of the surface trace for each of the dykes. Figure 3.7 is a density plot showing the location of the 100 best fitting dyke models, for all 12 of the post September 2005 dyke intrusions. The grid is divided into 1 × 1 km squares; each time a dyke passes through a patch, a counter is incremented by 1. The patches with the highest density of intersections are plotted with darker colours. The preferred locations for the dykes form a narrow NW-SE, ∼25-km-long cluster, offset by ∼2 km close to the Ado'Ale volcanic complex and all lie within the subsiding zone associated with the September 2005 intrusion. The inverted dyke locations are consistent with the reintrusion of the September 2005 dyke plane, within uncertainties.

Date	Length (km)	Strike (°)	Max Opening (m)	Dip (°)	rms (mm)
June 2006	8.2 ±0.4	335.4 ±2.5	1.9 ±0.1	89.9 ±0.1	27
July 2006	9.9 ±0.3	332.5 ±0.6	4.0 ±0.7	87.7 ±1.1	38
September 2006	8.3 ±1.6	330 ±2	1.5 ±0.4	89 ±1.6	36
December 2006	8.2 ±0.4	335.3 ±2.5	1.9 ±0.1	89.9 ±0.1	50
January 2007	8.2 ±0.4	331.8 ±0.6	1.6 ±0.1	89.9 ±0.1	20
August 2007	9.1 ±0.1	334.9 ±1.3	1.6 ±0.1	89.9 ±1.2	45
November 2007	11.6 ±0.3	331.2 ±1.5	1.6 ±0.1	87.9 ±0.9	30
April 2008	8.9 ±2.1	327.9 ±1.2	1.7 ±0.6	89.9 ±0.2	18
July 2008	9.7 ±0.7	331.7 ±1.5	1.0 ±0.1	89.12 ±1.0	30
October 2008	10.3 ±0.2	334.0 ±1.5	2.4 ±0.1	89.9 ±0.1	32
February 2009	9.2 ±0.2	343.1 ±0.4	2.7 ±0.2	89.9 ±0.2	18
June 2009	9.1 ±0.3	330.6 ±1.3	1.3 ±0.03	88.1 ±0.8	30

Table 3.1: Uniform opening model outputs for each of the new dykes.

Distributed opening model

To improve the fit to the data (Table 3.2) and make the model more realistic, I next solved for a distributed opening model. The extent and shape of the dyke is determined from the uniform opening models described, and the surface trace of the dyke is shown by the red dashed line in Fig. 3.7. Field observations indicate that existing faults are reactivated after new dyke intrusions (Rowland et al., 2007). In the model, a generalised fault geometry has been traced from a DEM. Faults extend to a depth of 2 km dipping at 65 ° (black lines in Fig. 3.7), and were discretised into 1 km by 2 km patches along strike and down dip respectively. The dyke is assumed to be vertical as uniform opening models indicate that the dykes all dip within 3° of the vertical. It is ∼75 km-long, is fixed to a depth range of 0-10 km and has been divided into 750, 1 × 1 km patches. The northern 25 km of the model uses the fault and dyke geometry of Wright et al. (2006). Displacement along the dyke is normal to the dislocation plane and fault slip is pure normal dip-slip. The dyke opening model, **m**, for the specified geometry is determined by solving the following

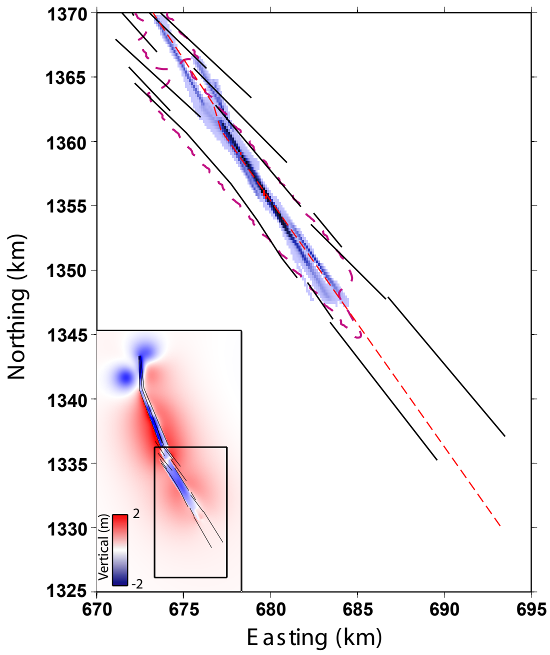

Figure 3.7: Density plot of the set of best fitting dykes for the 7 post 2005 intrusions, black lines show the location of normal faults traced from DEM. Dashed purple line is the outline of the area of subsidence associated with the September 05 intrusion (Rowland et al., 2007; Wright et al., 2006). The dashed red line is the chosen simplified geometry for the distributed opening model described in section 3.1.3. The sub-plot shows the modelled vertical displacements from the September 2005 intrusion. Coordinates are in UTM Zone 37.

equation:

$$\begin{pmatrix} \mathbf{A_{asc}} & \mathbf{x} & \mathbf{y} & 1 & 0 & 0 & 0 & 0 & 0 & 0 \\ \mathbf{A_{dsc}} & 0 & 0 & 0 & \mathbf{x} & \mathbf{y} & 1 & 0 & 0 & 0 \\ \mathbf{A_{gpsx}} & 0 & 0 & 0 & 0 & 0 & 0 & 1 & 0 & 0 \\ \mathbf{A_{gpsy}} & 0 & 0 & 0 & 0 & 0 & 0 & 0 & 1 & 0 \\ \mathbf{A_{gpsz}} & 0 & 0 & 0 & 0 & 0 & 0 & 0 & 0 & 1 \\ \kappa\boldsymbol{\nabla^2} & 0 & 0 & 0 & 0 & 0 & 0 & 0 & 0 & 0 \end{pmatrix} \begin{pmatrix} \mathbf{m} \\ a_{asc} \\ b_{asc} \\ c_{asc} \\ a_{dsc} \\ b_{dsc} \\ c_{dsc} \\ c_{gpsx} \\ c_{gpsy} \\ c_{gpsz} \end{pmatrix} = \begin{pmatrix} \mathbf{d_{asc}} \\ \mathbf{d_{dsc}} \\ \mathbf{d_{gpsx}} \\ \mathbf{d_{gpsy}} \\ \mathbf{d_{gpsz}} \\ 0 \end{pmatrix}, \qquad (3.3)$$

where $\mathbf{A}_{asc}$, $\mathbf{A}_{dsc}$, $\mathbf{A}_{gpsx}$, $\mathbf{A}_{gpsy}$ and $\mathbf{A}_{gpsz}$ are a set of matrices representing Green's functions for the ascending and descending interferograms, GPS displacements in the x, y and z directions which, multiplied by $\mathbf{m}$ produce the model displacements at the observation points, $\mathbf{x}$ and $\mathbf{y}$, using the elastic dislocation formulation of Okada (1985); ∇^2 is the finite difference approximation of the Laplacian operator, which acts to smooth the distribution of slip and opening, the relative importance of which is governed by the size of the scalar smoothing factor κ; a and b are phase gradients in the x- and y-direction respectively; c are offsets to account for the unknown zero phase level (InSAR) or displacements at the reference GPS station (subscripts indicate data source); and **d** is a vector containing the observed displacements (Wright et al., 2004c). For the cases where GPS data where not inverted, equation 3.3 reduces to:

$$\begin{pmatrix} \mathbf{A_{asc}} & \mathbf{x} & \mathbf{y} & 1 & 0 & 0 & 0 \\ \mathbf{A_{dsc}} & 0 & 0 & 0 & \mathbf{x} & \mathbf{y} & 1 \\ \kappa\nabla^{\mathbf{2}} & 0 & 0 & 0 & 0 & 0 & 0 \end{pmatrix} \begin{pmatrix} \mathbf{m} \\ a_{asc} \\ b_{asc} \\ c_{asc} \\ a_{dsc} \\ b_{dsc} \\ c_{dsc} \end{pmatrix} = \begin{pmatrix} \mathbf{d_{asc}} \\ \mathbf{d_{dsc}} \\ 0 \end{pmatrix} \tag{3.4}$$

Using a shear modulus of 32 GPa and a Poisson's ratio of 0.25, I solved for the best fitting opening distribution using a non-negative least-squares inversion (Bro & Jong, 1997). The best fit solution depends on the size of the smoothing factor κ. High values generate an over-smooth solution with a larger misfit while low values cause small misfits, but oscillating opening distributions. By plotting solution roughness (the mean absolute Laplacian of the slip model) against misfit, solutions that have both low misfit and roughness are selected.

Date	Moment (10^{18} Nm)	Volume (km^3)	Max Opening (m)	Depth (km)	rms (mm)
June 2006	5.44	0.12 ±0.01	2.2 ±0.2	0-10	22
July 2006	3.25	0.042 ±0.017	1.1 ±0.1	0-6	19
September 2006	3.24	0.088 ±0.014	1.2 ±0.1	3-10	23
December 2006	3.05	0.058 ±0.011	1.78 ±0.1	1-6	27
January 2007	2.07	0.037 ±0.013	0.7 ±0.1	2-7	10
August 2007	2.41	0.048 ±0.001	2.4 ±0.1	0-3	26
November 2007	6.01	0.15 ±0.01	1.7 ±0.1	0-8	21
April 2008	3.72	0.088 ± 0.02	0.9 ±0.1	4-10	22
July 2008	3.21	0.066 ±0.02	1.3 ±0.2	0-5	21
October 2008	7.88	0.17 ±0.001	3.1 ±0.16	1-9	30
February 2009	3.02	0.077 ±0.005	1.5 ±0.1	0-9	14
June 2009	1.81	0.046 ±0.007	1.6 ±0.1	0-5	14

Table 3.2: Distributed opening model parameters for each of the dykes (see Section 3.1.3 for details). The depth range is delimited by condition that dyke opening is $\frac{1}{e}$ of the maximum.

For the dyke intrusions between June 2006 and November 2007, where I perform a joint inversion with both InSAR and GPS data, I account for the different quantities and uncertainties of the GPS and InSAR data by varying the relative weighting of each dataset and assessing the affect on the rms misfit (Pedersen et al., 2003). Increasing the weight of the GPS data relative to the InSAR shows little improvement to the fit for the GPS data but causes a significant increase in the misfit with the InSAR data. For example, setting the GPS weight to zero for the inversion of the June 2006 data set results in a rms misfit of 22.5 mm and 19.4 mm for the ascending and descending interferograms respectively and 2.7 mm, 2.4 mm and 4.2 mm for the GPS in the x, y and z directions. When the InSAR data is given zero weight, the misfit to the GPS reduces to 1.1 mm, 1.6 mm and 2.8 mm, respectively, but the fit to the InSAR data deteriorates significantly (300 mm, 232 mm). A good compromise can be made by giving equal weights to both data sets whereby a good fit to both GPS and InSAR data is achieved (24 mm, 21 mm, 1.5 mm, 2.0 mm and 4.1 mm). It is worth noting that the fit to the GPS data is good even when it has zero weight, so it is not adding a lot of additional information to the inversion.

3.2 2006 - 2009 Dyke sequence

Based on the observed migration patterns I have separated the sequence of new intrusions into four subsequences. Subsequence 1 consists of dyking events in June, July and September 2006; subsequence 2 includes the intrusions in December 2006 and in January and August 2007; subsequence 3 includes the events in November 2007, April and July 2008 and finally dyking in October 2008, February and June 2009 form subsequence 4.

3.2.1 Subsequence 1

June 2006

The first event of subsequence 1 occurred on June 17 2006, when five earthquakes of M_b 3.9 - 4.6 were reported by NEIC within the Dabbahu rift. The local seismic station network, deployed following the 2005 event, recorded a swarm of earthquakes (M_L 2.4 - 4.7) concentrated in the vicinity of the Ado'Ale volcanic complex (Keir et al., 2009)(Fig. 3.8).

Ascending and descending interferograms formed covering the June earthquake swarm (Figs. 3.3 and 3.11) indicated new activity in the centre of the Dabbahu segment. Images acquired on May 20 and June 24 were used to construct a 35-day descending interferogram (Fig. 3.11d). A large baseline, ~1200 m, prevents the formation of the ascending interferogram using images acquired on June 12 and July 17 on track 300. Instead I used the interferogram from June 12 to August 21, which includes deformation from intrusions in both June and July. To isolate the signal for the June intrusion, the deformation associated with the July event was removed by subtracting the 35-day ascending interferogram from

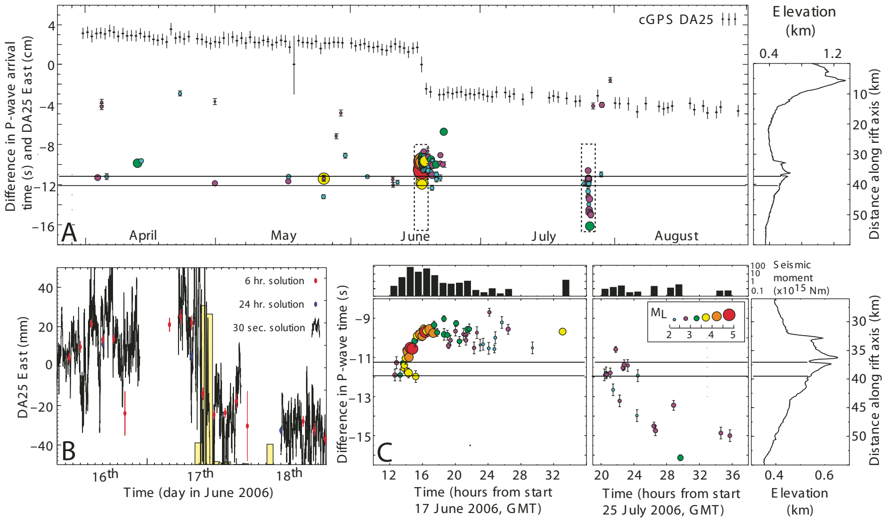

Figure 3.8: **A**: East-west motion at continuous global positioning system station (cGPS) DA25 and along-axis position of earthquakes in the Dabbahu segment against time. Earthquakes are coloured and scaled by magnitude, and error bars are measured errors in arrival times. Two horizontal lines correspond to inferred dyke source. Data within dashed rectangles are enlarged for detail. Along-axis topographic profile is in right panel. **B**: Three days east-west motion at cGPS DA25. Shaded histograms are seismic moment release in 2 hour intervals and show that rift opening is coincident with peak in seismicity. **C**: Along-axis position in seismicity, as in A, but over 1 day, showing migration of seismic swarms away from Ado'Ale Volcanic Complex. Histograms show seismic moment release binned at hour intervals and plotted on log scale. GMT - Greenwich Mean Time, after Keir et al. (2009).

July 17 to August 21 acquired on the same track giving an effective baseline of ∼272 m (Massonnet & Feigl, 1998). Three of the GPS sites show relative displacements with respect to the most distant site, DA60 (Fig. 3.9a). The closest of these was 25 km west of the rift axis (DA25), and recorded a westward displacement of 47 mm (Fig. 3.9a). An epoch-by-epoch analysis of GPS data shows that the intrusion occurred in approximately 4 hours (Keir et al., 2009)(Fig. 3.8). Analysis of the cumulative seismic release and the E-W displacements recorded at DA25 show a drop in seismic moment and a corresponding break in the observed displacements over a ∼2 hr period an hour after dyke initiation (Fig. 3.10). This suggests that either the dyke stalled as it was propagating or that two separate dyking events were observed (D.Keir and E. Calais personal communication, 2009).

Deformation was concentrated in the centre of the rift segment and the location of seismicity correlates well with the InSAR data (Keir et al., 2009). Surface deformation patterns are in agreement with the displacement field from the intrusion of a ∼10 km long dyke oriented NNW-SSE. In the ascending interferogram (Fig. 3.11a) 19 fringes were observed on the western flank indicating a maximum line-of-site displacement of ∼54 cm towards the satellite (range decrease). On the eastern flank, a maximum range increase of ∼12 cm was observed. The asymmetric deformation pattern is a result of the viewing geometry.

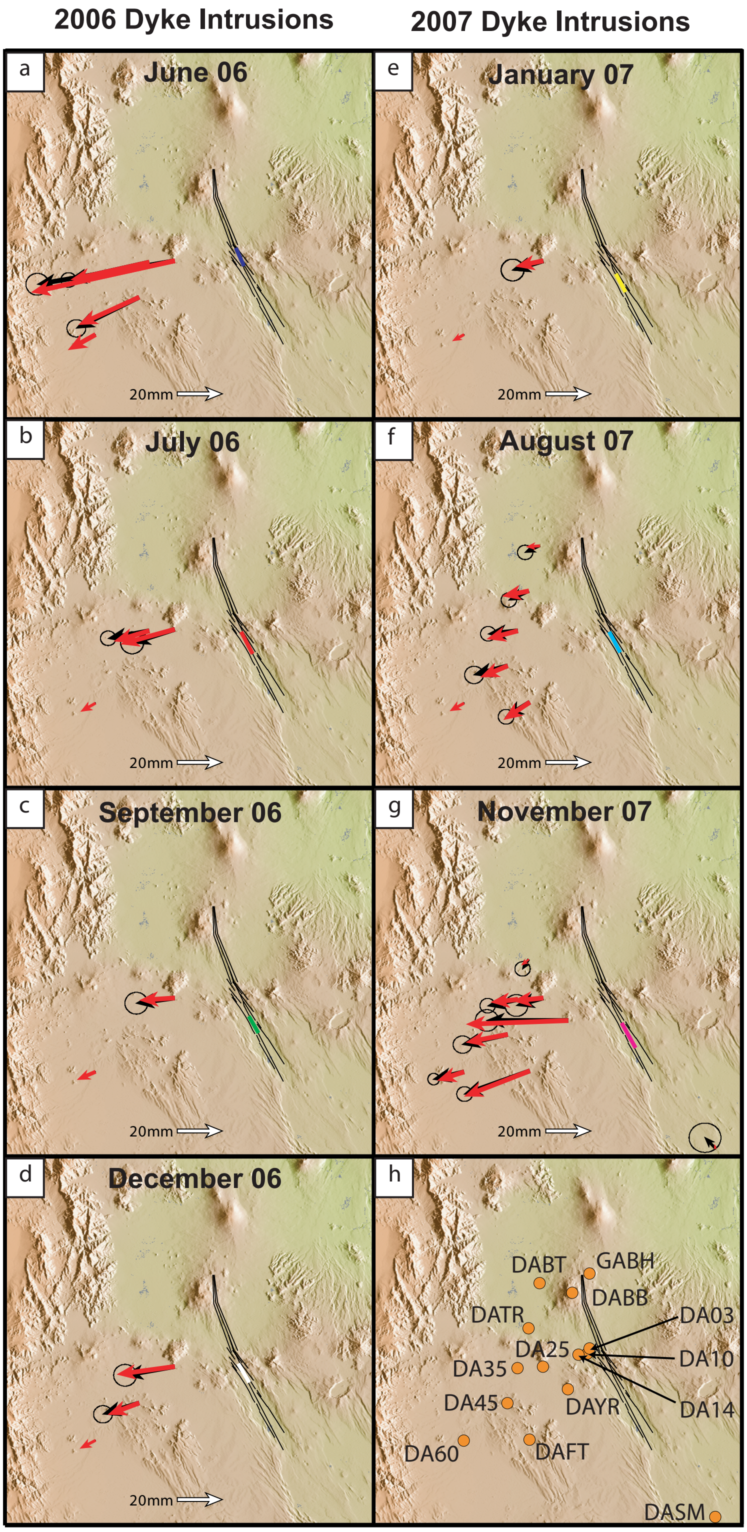

Figure 3.9: Observed and modelled GPS data covering each of the new dyke intrusions (**a** - **g**). Black arrows show the observed GPS displacements, with 95% confidence ellipse for each of the dyke intrusions, with the offset determined during the inversion added, (see Section 3.1.2 for details). Red arrows show the corresponding modelled displacements from the joint inversion of InSAR and GPS data. Black lines show the location of the dyke model, coloured lines show the location of the individual dykes. **h**, location of all continuous GPS sites around the Dabbahu rift segment. The number of GPS stations present varies with time as a function of deployment schedule and technical interruptions at the sites (see also Figure 3.4)

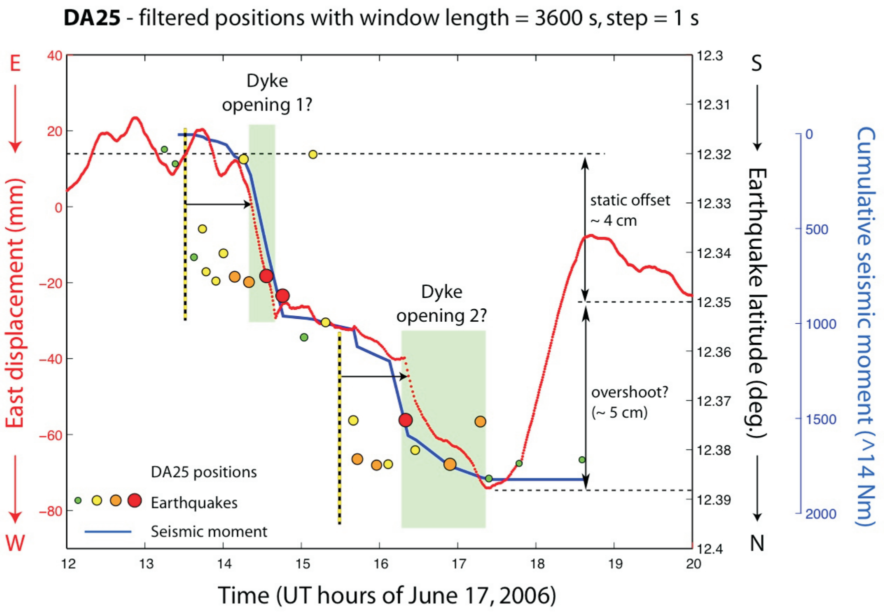

Figure 3.10: Comparison between the migration of seismicity and E-W displacement measured at DA25 for the June 2006 dyke intrusion. Red line shows the time averaged position of DA25; blue line shows the cumulative seismic moment and circles show the position of individual earthquakes against time.

In the east-looking ascending interferogram (Fig. 3.11a), horizontal and vertical displacements to the west of the dyke are towards the satellite and sum constructively, whereas, on the east side of the dyke displacement is towards the satellite in the vertical direction but away from the satellite in the horizontal. The asymmetry is reversed for the west-looking descending track (Fig. 3.11d), where -23 (∼65 cm) and +9 (∼19 cm) fringes were observed on the eastern flank and western flanks respectively. The larger signal is mainly due to a higher incidence angle used for this acquisition (45°), making the satellite more sensitive to horizontal motion. Displacements recorded by GPS were used in a joint inversion of InSAR and GPS data. The modelled GPS displacements provide a good fit to the data and lie within the 95% confidence ellipses for the GPS estimates of displacement (Fig. 3.9), if three additional free parameters are included to account for the motion of reference point DA60. Additional deformation was also observed at Dabbahu volcano, which was inflating over this period. This pattern of defromation is observed in many of the interferograms used in this study. Both InSAR and GPS show that this activity is unrelated to the new intrusions occurring in the centre of the rift segment. Therefore, as this Chapter is chiefly concerned with new dyke activity in the center of the segment I chose not to include a magmatic source, at this location, in the inversion. Due to the large ditance between the current activity and Dabbahu (∼30 km) there is no effect on the inversion other than to generate small amounts of opening at the northern section of the model domain which is not incorporated into the estimate of dyke opening or volume.

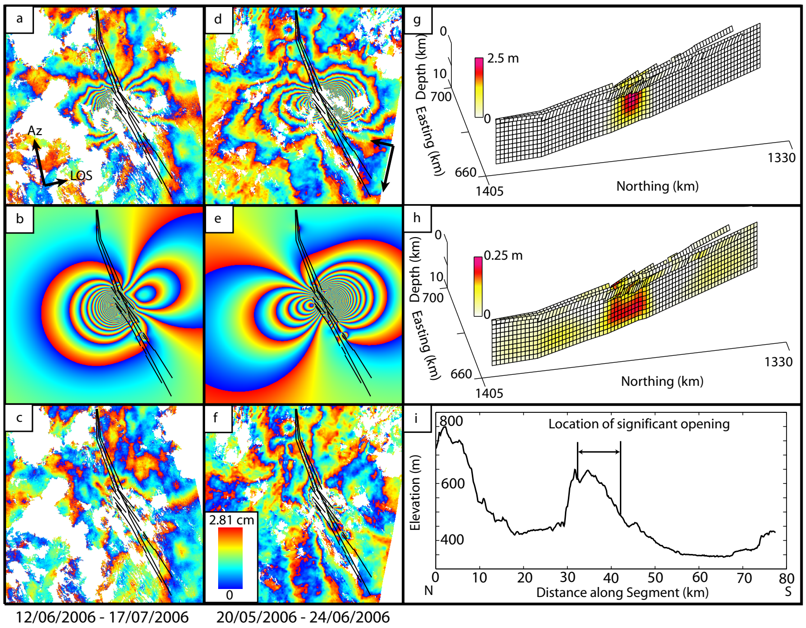

Figure 3.11: **a** and **d**, Observed ascending and descending interferograms covering June 17 dyke intrusion. Arrows indicate the satellites flight (Az) and look (LOS) directions. **b** and **e**, Simulated ascending and descending interferograms, constructed using the distributed opening model **g**, described in the text. **c** and **f**, Residual ascending and descending interferograms for each of the distributed opening models, generated by subtracting the model interferograms from the data. **h**, 1-σ error projected onto best fitting model. **i**, along axis topography - black lines indicate region above significant dyke opening.

The best fitting model (Figs. 3.11b,e,g) suggests the dyke was ~10 km long, agreeing with observed seismicity, with a maximum opening of 2.2 m, and that normal faults slip by no more than 1.3 m. Most opening occurred between 2 and 8 km depth, with little opening below 9 km or above 1 km. A total of 0.12 km^3 of magma was intruded, only ~5% of the September 2005 intrusion, giving a geodetic moment of 3.7×10^{18} Nm. Errors in opening, calculated using the Monte Carlo simulations described in Section 3.1.3, are plotted on the dyke model (Fig. 3.11h), revealing areas where the opening is less well constrained. The 1-σ errors in the inversion are less than 22 cm throughout the model, with maximum errors occurring in regions of incoherence in the InSAR data. The model explains most of the deformation with rms misfit to the LOS data of 21 mm (Figs. 3.11c,f), comparable to the level of noise in the far field (~20 mm). Larger misfits occur close to the dyke where data coherence is poor and where the simplified geometry does not fully reflect the complexity of real faults. Misfits at the northern end of the dyke occur where inflation of Dabbahu and Gabho volcanoes is not modelled. Table 3.2 gives values for the seismic moment, amount of opening, volume and depth for each of the dykes intruded between June 2006 and July 2009.

July 2006

Seismicity in the Dabbahu rift was low after the June intrusion until July 25-26, when a swarm of M_L2-3 earthquakes were recorded by the local network to the south of Ado'Ale (Keir et al., 2009). Two 35-day interferograms, one ascending and one descending (Figs. 3.12a,d), formed covering the month of July revealed the intrusion of a new dyke. The ascending interferogram, using images acquired on July 17 and August 21, has a 564 m baseline causing some coherence loss compared with the descending interferogram, (June 24 - July 29), which has a smaller baseline of 365 m.

The intrusion was smaller in size and located to the south of the June intrusion. The displacements are consistent with the intrusion of another dyke oriented NNW-SSE and correlates with the spatial distribution of seismicity (Keir et al., 2009). In the ascending interferogram (Fig. 3.12a), there is $\sim$37 cm of range decrease on the western flank and $\sim$8.5 cm of range increase on the eastern flank. On the descending track (Fig. 3.12d) $\sim$56 cm of displacement has occurred on the eastern flank and $\sim$11 cm in the west. In addition, $\sim$6 cm of uplift was observed at Dabbahu at the northern end of the segment. Displacement vectors at 2 sites, DA25 and DA35 (Fig. 3.9), also recorded the dyke intrusion with a westward displacement of 18 and 17 mm, respectively.

Modelling (Figs. 3.12b,e,g) suggests a 9-km-long dyke, intruded between depths of 0 and 5 km. Maximum opening of 1.1 m occurred in the centre of the dyke and the normal faults above slipped by up to 1 m. A total volume of 0.042 km^3 was intruded (2.7% of September 05). The 1-σ error in model opening is less than 13 cm with a maximum occurring in regions close to the dyke, (Fig. 3.12h). Most of the observed deformation is explained by the model with a rms misfit of 19 mm. The largest misfits occur close to the dyke where the effect of the near-surface faults is felt. A broad residual to the north of the intrusion, most notably on the descending track (Fig. 3.12f), is probably a result of atmospheric noise and continued relaxation of the crust being modelled as opening. Modelled GPS displacements fit the data well and lie close to or within the error ellipse for each site (Fig. 3.9b).

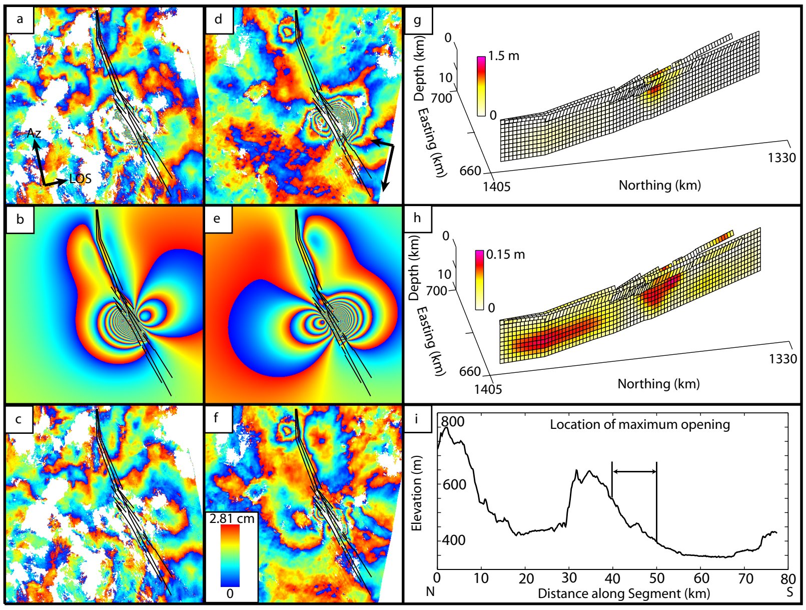

17/07/2006 - 21/08/2006 24/06/2006 - 29/07/2006

Figure 3.12: **a** and **d**, Observed ascending and descending interferograms covering the July 24 2006 dyke intrusion. Arrows indicate the satellites flight (Az) and look (LOS) directions. **b** and **e**, Simulated ascending and descending interferograms, constructed using the distributed opening model, **g**, described in the text. **c** and **f**, Residual ascending and descending interferograms for each of the distributed opening models, generated by subtracting the model interferograms from the data. **h**, 1-σ error projected onto best fitting model. **i**, along axis topography - black lines indicate region above significant dyke opening.

September 2006

During August 2006, little seismicity was observed in the Dabbahu segment. However, on September 10 2006 a swarm of 14 M_L2.6-3.4 earthquakes were detected near Ado'Ale (D.Keir personal communication, 2008). Ascending and descending interferograms (Figs. 3.13a,d) formed between August 21 - September 25 and September 2 - October 7 respectively, indicate the intrusion of a third dyke, oriented NNW-SSE and located to the south of the July intrusion. The deformation was less than that caused by previous intrusions, with a maximum ~14 cm of range decrease in the ascending interferogram and ~19 cm in the descending. This was mirrored in the GPS data (Fig. 3.9c), only the station at DA25 records the intrusion showing a maximum westward displacement of ~11 mm.

The model for the September 2006 event is able to explain most of the deformation (Figs. 3.13b,e,g) yielding an rms misfit to LOS data of 20 mm. Maximum opening of 1.2 m occurred between 3 and 8 km depth with normal faults slipping up to a maximum of 0.5 m. The total intruded volume was 0.088 km^3, again small (3.6%) relative to the event of September 2005. The moment release from the recorded earthquakes was only ~0.1% of the total geodetic moment (2.1 × 10^{18} Nm). The model has a 1-σ error of less than

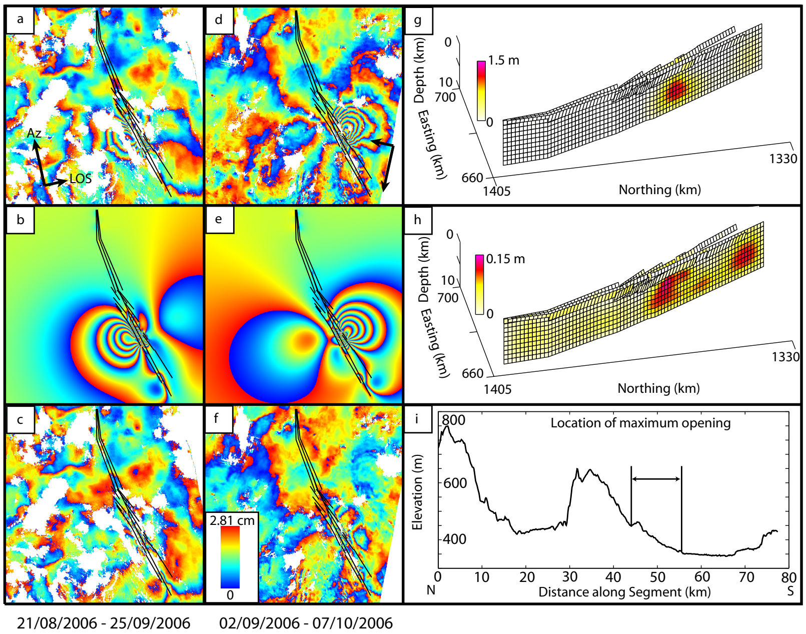

Figure 3.13: **a** and **d**, Observed ascending and descending interferograms covering the September 10 2006 dyke intrusion. Arrows indicate the satellites flight (Az) and look (LOS) directions. **b** and **e**, Simulated ascending and descending interferograms, constructed using the distributed opening model, **g**, described in the text. **c** and **f**, Residual ascending and descending interferograms for each of the distributed opening models, generated by subtracting the model interferograms from the data. **h**, 1-σ error projected onto best fitting model. **i**, along axis topography - black lines indicate region above significant dyke opening.

15 cm everywhere, with the largest errors occurring where displacement is greatest and further south where the model may be influenced by an atmospheric signal.

3.2.2 Subsequence 2

December 2006

The first dyke of the second subsequence occurred during December 2006. The event was captured by GPS (Fig. 3.9d) indicating that the intrusion occurred on December 7. Two ascending interferograms (Figs. 3.14a,d), on tracks 300 and 28, show deformation concentrated to the north of the September 2006 event and between the intrusions of June and July 2006. Interferograms on the descending track cover both of the intrusions in December and January, therefore only ascending interferograms isolate the event and are modelled. The pattern of deformation was similar to that observed for the intrusions in June and July; ~50 cm of motion was detected towards the satellite with the ground moving away by ~8.5 cm on the eastern flank.

The model for the December 2006 event suggests a 7-8 km long dyke intruded between

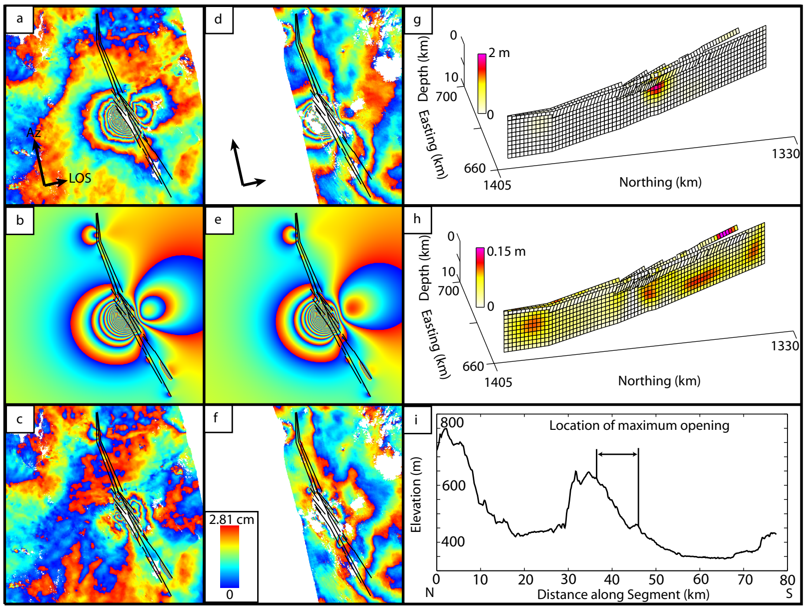

04/12/2006 - 08/01/2007 20/12/2006 - 24/01/2007

Figure 3.14: **a** and **d**, Two ascending interferograms covering December dyke intrusion. Arrows indicate the satellites flight (Az) and look (LOS) directions. **b** and **e**, Simulated ascending and descending interferograms, constructed using the distributed opening model, **g**, described in the text. **c** and **f**, Residual ascending and descending interferograms for each of the distributed opening models, generated by subtracting the model interferograms from the data. **h**, 1-σ error projected onto best fitting model. **i**, along axis topography - black lines indicate region above significant dyke opening.

1 and 6 km depth. Maximum opening of 1.8 m occurred between 2 and 5 km depth and normal faults slipped by no more than 0.9 m. Approximately 0.06 km^3 of magma was intruded. The 1-σ error of the opening is less than 15 cm for the entire model, with most parts having an error of $< \sim$10 cm. The model is able to explain most of the deformation observed in the interferograms, (Figs. 3.14b,e) with an rms misfit to the LOS data of 19 mm. Greatest residuals occur close to the dyke and in the north, residuals in the north are due to the inflation of Dabbahu volcano being modelled as opening on the dyke.

January 2007

Further dyking occurred during January 2007, located in the south of the segment. The dyke was intruded along the same section as the September 2006 event. The surface deformation was very similar in the ascending interferogram, with ~19 cm of motion detected toward the satellite and ~3 cm away (Fig. 3.15a). GPS displacements reveal that the intrusion occurred on January 14 (Fig. 3.9e). As for the December event, no descending interferograms can be formed which capture this event without including the deformation from the previous intrusion.

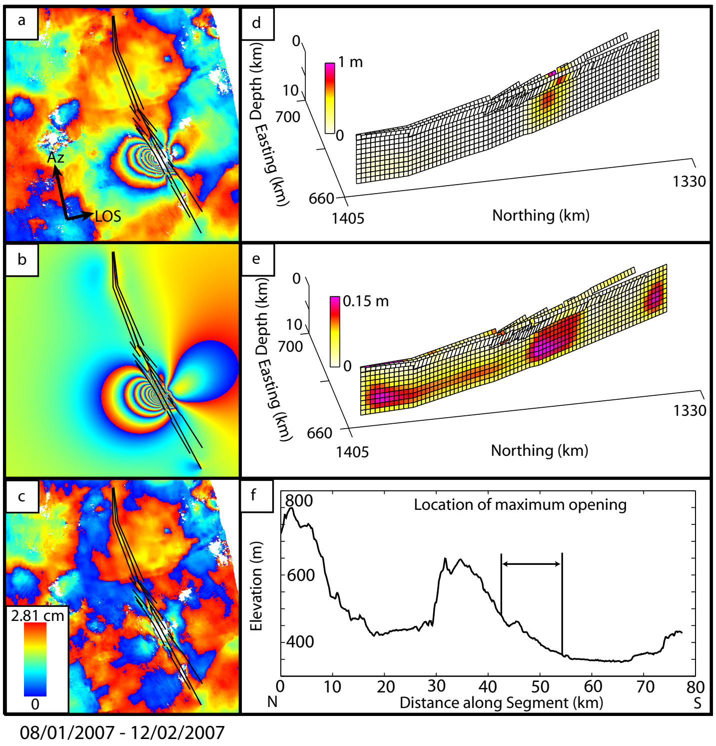

Figure 3.15: **a**, Observed ascending interferogram covering the January 2007 dyke intrusion. Arrows indicate the satellites flight (Az) and look (LOS) directions. **b**, Simulated ascending interferogram, constructed using the distributed opening model, **d**, described in the text. **c**, Residual ascending interferogram for the distributed opening model, generated by subtracting the model interferogram from the data. **e**, 1-σ error projected onto best fitting model. **f**, along axis topography - black lines indicate region above significant dyke opening.

The best fitting model, (Figs. 3.15b,d) suggests a dyke with a maximum opening of 0.7 m between 4 and 8 km depth. The opening was 9-10 km long at depth but narrowed toward the surface where normal faults slipped by no more than 1.1 m. Only 0.045 km^3 of magma was intruded, 1.6% of the volume intruded during the September 2005 event, resulting in a total geodetic moment of 1.4 × 10^{18} Nm. The 1-σ error is less than 11 cm everywhere with the largest errors occurring close to the areas of maximum opening (Fig. 3.15e). High coherence and low atmospheric noise across the scene means that residuals are relatively small with an rms misfit of 10 mm to the LOS data (Fig. 3.15c).

August 2007

Deformation in the Dabbahu segment between January and the end of July 2007, following the January intrusion, was small and isolated around Dabbahu volcano and the centre of the rift segment. However, information given to the Geophysical Observatory in Addis Ababa reported activity in the Karbahi region, close to the Ado'Ale volcanic complex in early August. On 13 August local pastoralists reported seeing "fire" and smoke in the vicinity, which continued until 16 August. Hot-spots associated with the eruption were detected by NASA's MODerate-resolution Imaging Spectrometer (Wright et al., 2004a) over this period. Ground investigations carried out by a team from Addis Ababa University revealed that fresh basaltic lavas were erupted from long fissures over a total distance of ~5 km. The observed flows travelled a few hundreds of metres from their associated fissure vents (Yirgu et al., 2007).

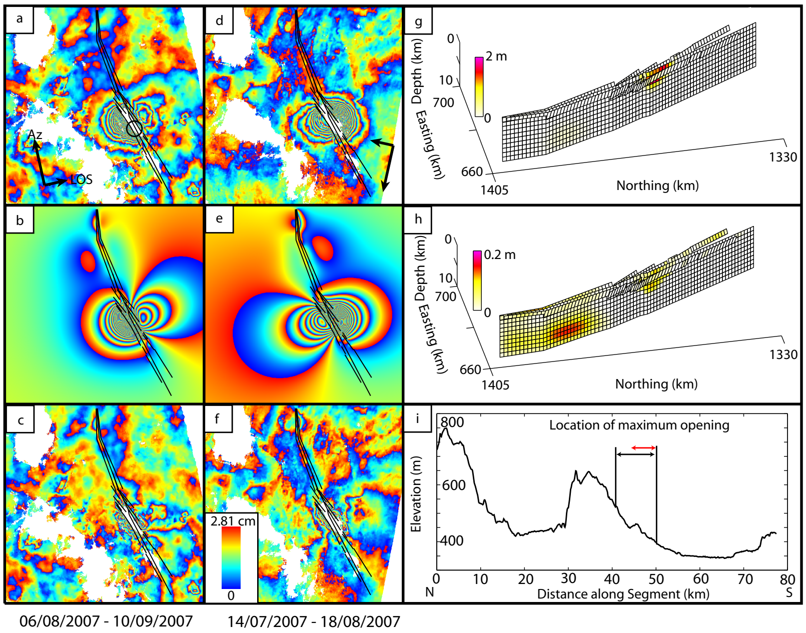

Figure 3.16: **a** and **d**, Observed ascending and descending interferograms covering the August 2007 dyke intrusion. Arrows indicate the satellites flight (Az) and look (LOS) directions. The black circle shows the approximate location of the surface eruption. **b** and **e**, Simulated ascending and descending interferograms, constructed using the distributed opening model, **g**, described in the text. **c** and **f**, Residual ascending and descending interferograms for each of the distributed opening models, generated by subtracting the model interferograms from the data. **h**, 1-σ error projected onto best fitting model. **i**, along axis topography - black lines indicate region above significant dyke opening and red indicates the extent of the surface flows.

Interferograms covering the period were available on both ascending and descending tracks (Figs. 3.16a,d) and reveal the intrusion of a dyke in the centre of the rift segment, in approximately the same location as the July 2006 dyke intrusion (Fig 3.12a,d). In the ascending interferogram the ground was displaced by ~54 cm towards the satellite on the western flank and moved away by ~12 cm on the east side with similar displacements observed in the descending interferogram. Hot-spots and field observations of lava flows associated with the dyke, were located along the southern ~4 km of the deformation field implying that the whole dyke did not rupture the surface.

The model provides a good fit to the LOS displacements, with an rms misfit of 22 mm. The best fitting model (Fig. 3.16b,e,g) suggests a dyke with a maximum opening of 2.4 m intruded between 0 and 3 km depth and with normal faults that slip by no more than 0.7 m. The dyke was 9-10 km long with more opening at the southern end in accordance with field observations that surface flows were observed in this location. A total volume of 0.048 km^3 of magma was intruded resulting in a total geodetic moment of 1.6×10^{18} Nm. The eruption was ~4 km long and covered an area of ~2.2 km^2, field observations indicate that the total erupted volume was <0.004 km^3, only 6% of the total intruded volume (Ferguson et al., 2010). The location of the dyke is very similar to the July dyke but maximum opening has occurred at a shallower depth. The intrusion is captured by multiple GPS sites around the rift and the modelled displacements provide a good fit with the data (Fig. 3.9f). The 1-σ error is less than 15 cm everywhere with maximum errors occurring close to the areas of greatest opening (Fig. 3.16h) and further north where there is a secondary signal in the data which may be unrelated to the dyke event.

3.2.3 Subsequence 3

November 2007

The dyke intrusions forming the 3rd subsequence are all located in the southern section of the Dabbahu segment. Little deformation was observed during September and October 2007 before the event in November. The event was captured in multiple interferograms (Figs. 3.17a,d) and the available GPS data indicates that the intrusion occurred on 12 November. In both the ascending and descending interferograms up to ~40 cm of displacement occurs towards the satellite and ~15 cm away. To the northern end of the dyke there was a zone of up to ~8.5 cm of subsidence, implying that at least some of the magma may have been sourced from a shallower chamber, something that has not been observed during the previous intrusions.

Modelling (Figs. 3.17b,e,g), suggests a dyke intruded between 0 and 8 km depth with a maximum opening of 1.8 m. Normal faults slip by up to 1.9 m on the western flank. The total intruded volume was 0.15 km^3, making it the most voluminous of the dykes since September 2005, with a geodetic moment release of 6.0×10^{18} Nm. The model explains most of the observed deformation with a rms misfit to the LOS displacement of 22 mm

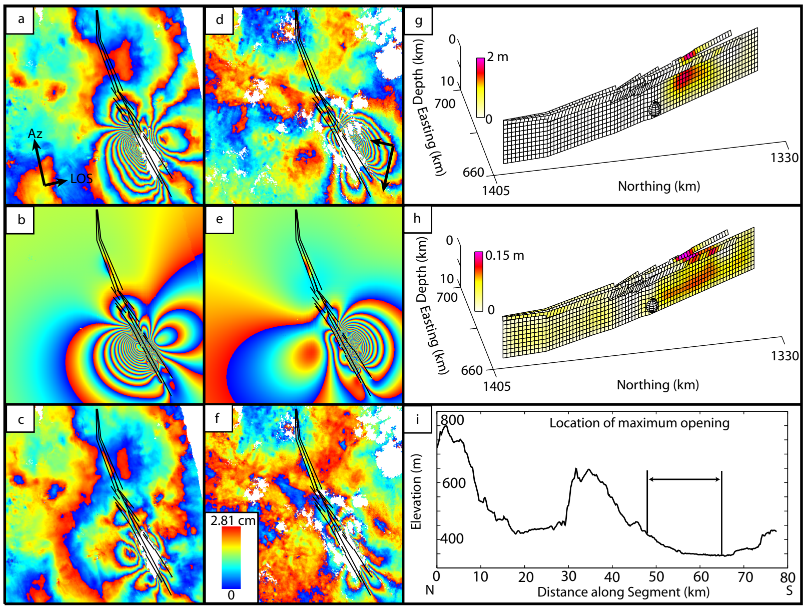

15/10/2007 - 19/11/2007 02/11/2007 - 07/12/2007

Figure 3.17: **a** and **d**, Observed ascending and descending interferograms covering the November 07 intrusion, arrows indicate the satellites flight (Az) and look (LOS) directions. **b** and **e**, Simulated ascending and descending interferograms, constructed using the distributed opening model, **g**, described in the text. **c** and **f**, Residual ascending and descending interferograms for each of the distributed opening models, generated by subtracting the model interferograms. **h**, 1-σ error projected onto best fitting model. **i**, along axis topography - black lines indicate region above significant dyke opening.

(Figs. 3.17c and 3.17f). The 1-σ error is less than 20 cm with maximum errors occurring close to the dyke where coherence is low. The zone of subsidence to the north of the dyke can be explained with a point pressure source (Mogi, 1958) (Equations 2.28, 2.29), deflating by between 0.019 and 0.032 km^3 (12%-14% of total), at 7-10 km depth (Fig. 3.17g). Modelled GPS displacements fit the data well (Fig. 3.9g) with the exception of the station at DAYR, where the displacement is overestimated by ~9 mm.

April 2008

Deformation in the interferograms following the November 2007 intrusion show an isolated zone of uplift in the centre of the rift segment. Approximately 3 cm/month of inflation was observed centred above the region which deflated during the previous event. The intrusion was captured in both ascending and descending interferograms (Fig. 3.18a,d) in the ascending, ~15 cm of displacement occurred toward the satellite and ~3 cm away with similar displacements observed in the descending interferogram. In addition, a zone above the dyke subsided by ~6 cm.

The modelling (Figs. 3.18b,e,g) suggests a dyke was emplaced between 4 and 10 km at the base of the November intrusion with a maximum opening of ~1 m. Normal faults

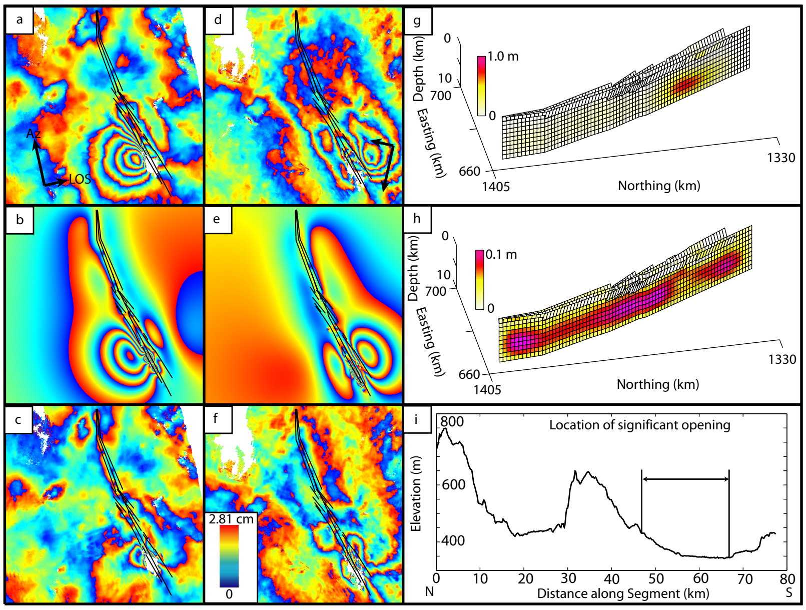

28/01/08 - 07/04/2008

07/12/2007 - 25/04/2008

Figure 3.18: **a** and **d**, Observed ascending and descending interferograms covering the April 08 intrusion, arrows indicate the satellites flight (Az) and look (LOS) directions. **b** and **e**, Simulated ascending and descending interferograms, constructed using the distributed opening model, **g**, described in the text. **c** and **f**, Residual ascending and descending interferograms for each of the distributed opening models, generated by subtracting the model interferograms. **h**, 1-σ error projected onto best fitting model. **i**, along axis topography - black lines indicate region above significant dyke opening.

slipped by no more than 0.5 m and the total intruded volume was 0.09 km^3. Most of the deformation is explained by the model with a rms misfit of 21 mm to the LOS displacements (Figs 3.18c,f). The 1-σ error is less than 10 cm with maximum errors occurring to the north of the dyke where atmospheric noise is modelled as opening (Fig. 3.18h).

July 2008

Between 7 April and 16 June the centre of the segment shows a similar inflation signal as observed between previous intrusions. Interferograms spanning 16 June to 21 July indicate the intrusion of a 9th dyke. Both ascending and descending interferograms image the intrusion (Fig. 3.19a,d), with ~35 cm of displacement toward the satellite. Compared with many of the previous dykes the region of deformation is relatively narrow (13 km) in both the ascending and descending interferograms suggesting that the intrusion was emplaced at a shallow depth although there is no evidence to suggest that the dyke breached the surface.

The model suggests (Figs. 3.19b,e,g) that the majority of opening was in the upper 4 km with a maximum opening of ~1.3 m. Interestingly, the opening distribution extends, at depth, northward towards the inferred source location beneath Ado'Ale. The model

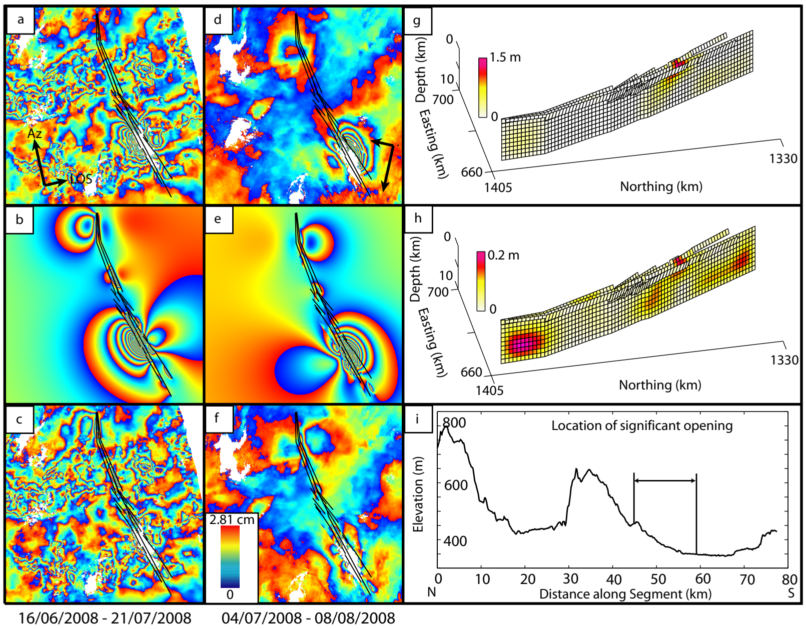

Figure 3.19: **a** and **d**, Observed ascending and descending interferograms covering the July 08 intrusion, arrows indicate the satellites flight (Az) and look (LOS) directions. **b** and **e**, Simulated ascending and descending interferograms, constructed using the distributed opening model, **g**, described in the text. **c** and **f**, Residual ascending and descending interferograms for each of the distributed opening models, generated by subtracting the model interferograms. **h**, 1-σ error projected onto best fitting model. **i**, along axis topography - black lines indicate region above significant dyke opening.

explains most of the deformation, rms = 20 mm (Fig. 3.19c,f); errors in the opening are most pronounced at the northern end of the model where inflation near Dabbahu is modelled as opening along the dyke and along some of the faults where noise, mostly in the ascending track, is modelled as slip (Fig. 3.19g).

3.2.4 Subsequence 4

October 2008

The first dyke of the final subsequence occurred during October 2008, the intrusion was captured on both ascending and descending interferograms (Fig. 3.20a,d). The deformation is concentrated in the vicinity and to the north of Ado'Ale, an area previously unaffected by new dyking. The observed deformation signal was much larger than any of the previous dykes with ~72 cm of motion toward the satellite in the ascending interferogram (Fig. 3.20a). As with the November 2007 intrusion, there is a deflation signal near Ado'Ale suggesting the removal of material from a shallow magma chamber.

The best-fitting model suggests that the dyke was ~11 km long with a maximum opening of ~3 m, making it the largest intrusion since September 2005. The total volume was

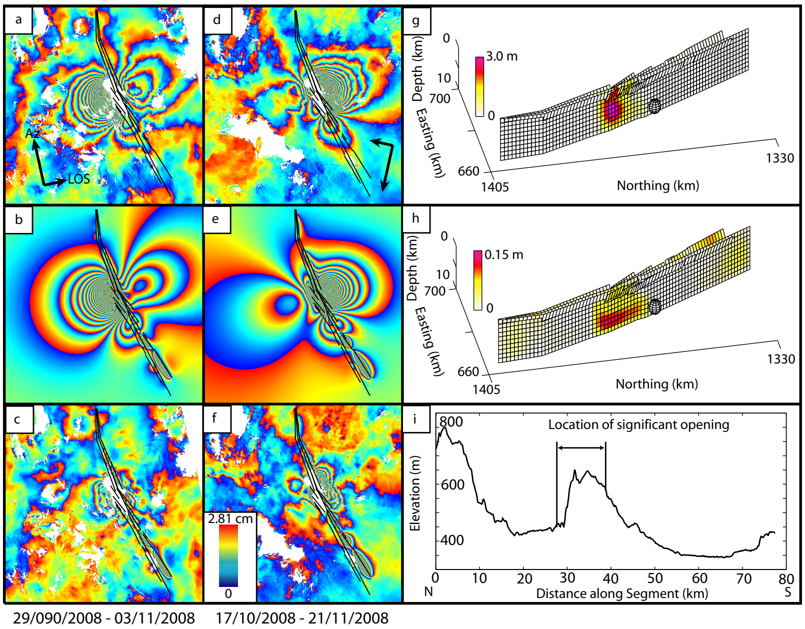

Figure 3.20: **a** and **d**, Observed ascending and descending interferograms covering the October 08 intrusion, arrows indicate the satellites flight (Az) and look (LOS) directions. **b** and **e**, Simulated ascending and descending interferograms, constructed using the distributed opening model, **g**, described in the text. **c** and **f**, Residual ascending and descending interferograms for each of the distributed opening models, generated by subtracting the model interferograms. **h**, 1-σ error projected onto best fitting model. **i**, along axis topography - black lines indicate region above significant dyke opening.

0.17 km^3 with only 0.03 km^3 coming from the point source at its southern end, assuming a depth of 8 km. Compared with the earlier models, the misfit to the data is poor (rms = 30 mm). The model underestimates the deformation with residual fringes remaining in both the ascending and descending interferograms (Figs. 3.20c, f). Furthermore, at the southern end of the segment modelled slip on faults causes a number of residual fringes where parts of the signal associated with the deflation source is modelled as slip.

February 2009

In the months following the October intrusion there was ~9 cm of inflation in the centre of the segment. Interferograms formed covering the month of February reveal the intrusion of another dyke at the southern end of the October intrusion. Located in a similar position to the June 2006 dyke, ~50 cm of displacement is observed towards the satellite in both the ascending and descending interferograms.

Modelling indicates that the dyke was ~9 km long and had a maximum opening of 1.6 m and a volume of 0.08km^3 (Fig. 3.21b,e,f). The model explains most of the deformation (rms = 14 mm) and the 1-σ error is less than 7.5 cm everywhere (Fig. 3.21h). There is a

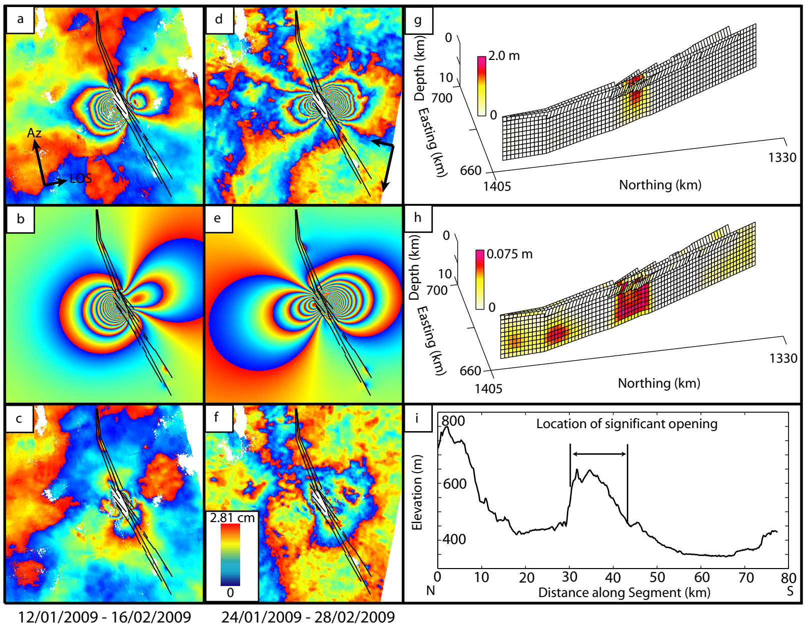

Figure 3.21: **a** and **d**, Observed ascending and descending interferograms covering the February 09 intrusion, arrows indicate the satellites flight (Az) and look (LOS) directions. **b** and **e**, Simulated ascending and descending interferograms, constructed using the distributed opening model, **g**, described in the text. **c** and **f**, Residual ascending and descending interferograms for each of the distributed opening models, generated by subtracting the model interferograms. **h**, 1-σ error projected onto best fitting model. **i**, along axis topography - black lines indicate region above significant dyke opening.

broad residual fringe in the descending track generated by the model overestimating the displacements and close to the dyke in the ascending. Unlike the previous intrusion there is no evidence of a deflating source at Ado'Ale nor at either of the two northern volcanoes.

June 2009

As with the earlier dyking events, inflation around the Ado'Ale complex was observed during the inter-dyking period following the February intrusion. On 28 June 2009 thermal anomalies were recorded by MODIS (Fig. 3.23a) south of Ado'Ale in a similar location to those observed during the August 2007 eruption. Field observations on 4th July revealed the formation of new scoria cones (Fig 3.23b), which were still emitting moderate levels of gas (D. Ferguson perrs. comm), and lava flows. The erupted lavas were similar in style to the earlier August flows and were still producing significant thermal anomalies (Fig. 3.23c)(Ferguson et al., 2010). Ascending and descending interferograms covering the intrusion indicate that the dyke was emplaced in approximately the same along axis location as the August intrusion.

The best fit model explains most of the observed deformation with an rms misfit of ~14 mm and a 1-σ of < 10 cm. Residual fringes occur close to the dyke where the model has un-

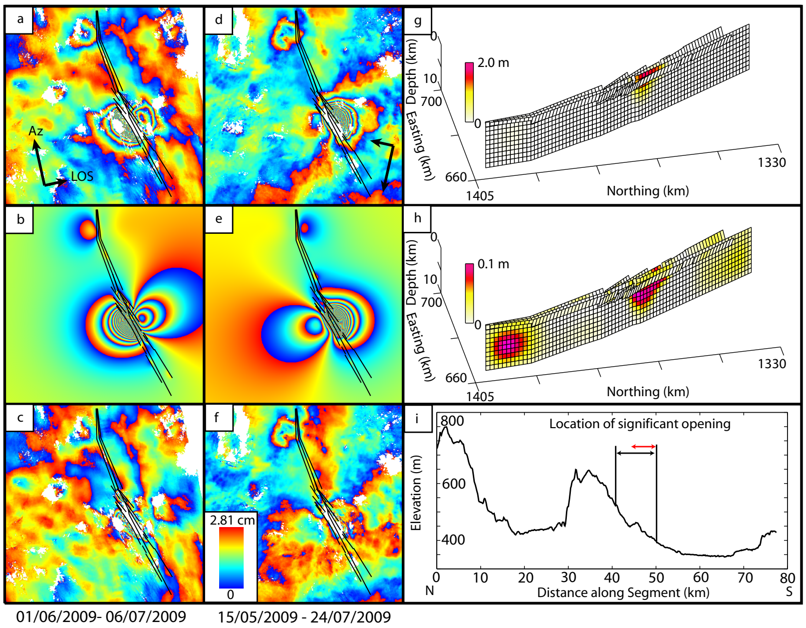

01/06/2009- 06/07/2009   15/05/2009 - 24/07/2009

Figure 3.22: **a** and **d**, Observed ascending and descending interferograms covering the June 09 intrusion, arrows indicate the satellites flight (Az) and look (LOS) directions. **b** and **e**, Simulated ascending and descending interferograms, constructed using the distributed opening model, **g**, described in the text. **c** and **f**, Residual ascending and descending interferograms for each of the distributed opening models, generated by subtracting the model interferograms. **h**, 1-σ error projected onto best fitting model. **i**, along axis topography - black lines indicate region above significant dyke opening and red indicates the extent of the surface flows.

derestimated the displacements and in the north where inflation at Dabbahu is modelled as dyke opening. The dyke was smaller than the August event with a maximum opening of 1.6 m and a total intruded volume of ~0.045 km^3. The estimated volume of erupted material from field observations is ~0.009 km^3 (Ferguson et al., 2010), only 19% of the modelled volume, implying that the majority of new material was intruded rather than extruded.

3.3 Discussion

Most of the deformation associated with the June 2006 to June 2009 dyke intrusions can be explained by the simple models described above. The ability to combine seismicity, GPS and InSAR data provide a data set with high temporal and spatial resolutions.

The pattern of dyke intrusion observed within the Dabbahu rift segment shows many temporal and spatial similarities with the 1975 - 84 Krafla rifting episode in Northern Iceland, where 9 m of rift opening occurred through 20 discrete dyke intrusions (Fig. 3.24). To date, the intrusion of 13 dykes has been observed in the Dabbahu rift segment

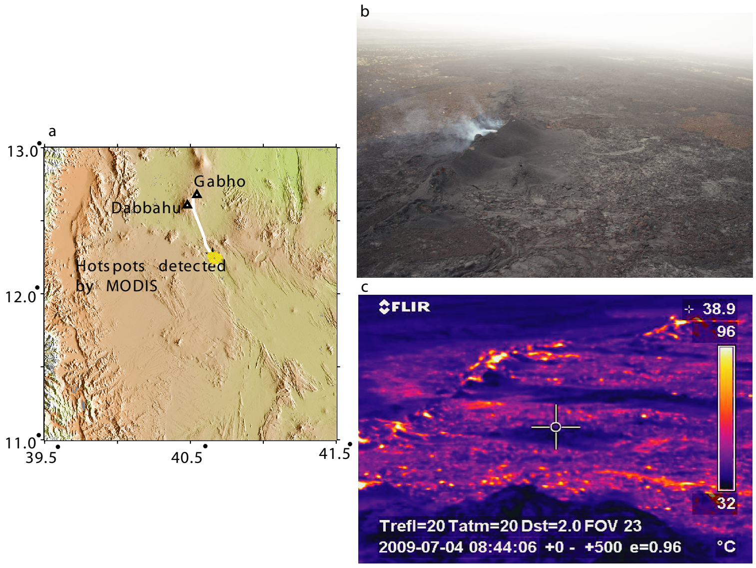

Figure 3.23: **a:** Map showing the location of Hotspots detected by MODIS on 29/06/2009. **b:** Photograph of eruptive fissure near Ado'Ale taken by field team on 04/07/2009 **c:** Thermal image of **b** taken on 04/07/2009, red colours indicate heat.

in Afar. Seismicity associated with both the June and July 2006 dyke intrusions indicate that the intrusions occurred over several hours on 17 June and 25 July, and that the dykes propagated at velocities of ∼1-2 m/s (Keir et al., 2009), similar to those observed during the Krafla episode (Einarsson & Brandsdóttir, 1980). The total volume estimated to have been intruded during the Krafla rifting episode was ∼1.1 km^3 (Tryggvason, 1984). The volume of magma intruded during September 2005 was ∼2-2.5 km^3 (Grandin et al., 2009; Wright et al., 2006) and a further ∼1 km^3 was intruded between June 2006 and June 2009.

With the exception of the November 2007 and October 2008 intrusions, we do not observe any subsidence in the InSAR data at the volcanic centres in the Dabbahu rift segment following any of the intrusions. However, the withdrawal of magma from crustal magma chambers and the subsequent deflation of volcanic centres is frequently observed during dyke intrusions (Björnsson et al., 1977, 1979; Cervelli et al., 2002; Tryggvason, 1980, 1984, 1994). During the Krafla rifting episode, intrusions were accompanied by rapid deflation of the Krafla caldera, after which inflation resumed. The primary magma chamber beneath Krafla is at about 3 km depth. Assuming that 0.12 km^3 of magma was intruded in the June 2006 dyke then the surface deformation caused by a Mogi source deflating by the same amount, at 3 km depth, would cause ∼3 m of surface displacement. A source located at 15 km depth would cause a maximum of ∼15 cm of subsidence over a broad area and we would expect to see some subsidence at the GPS sites 25 and 35 km away.

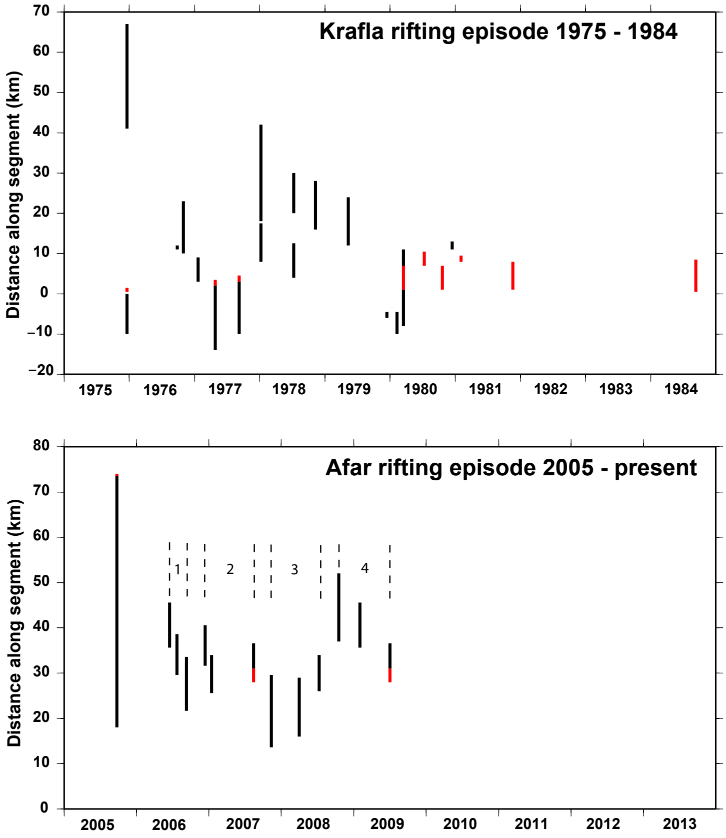

Figure 3.24: Along-strike movement of dyking activity with time during the 1974 - 1989 Krafla episode, (after Einarsson (1991)) and for the ongoing Afar episode. Black lines show the length of each dyke without extrusion of lava, red lines show length of dyke with extrusion.

However, this is not observed following any of the intrusions except in November 2007 and October 2008 where minor localised subsidence was observed at Ado'Ale silicic complex. Simple Mogi modelling for this magma chamber indicates a source located at ∼7-10 km depth, releasing a maximum of ∼0.023 km^3 and 0.03 km^3 of magma respectively, only a fraction of the total intruded volume. This discrepancy could be explained by magma compressibility (Delaney & McTigue, 1994), incorrect Poisson's ratio (Johnson et al., 2000), or the difference in compliance between the magma chamber and the dyke (Rivalta & Segall, 2008). In order to generate this discrepancy with the Poisson's ratio alone is unlikely as it would require a value approaching ∼0.9. Rivalta & Segall (2008), on the other hand, have shown for a number of examples, including the September 2005 intrusion, that the difference in compliance is sufficient to cause volume discrepencies of this magnitude. Another possibility could be that the magma supply rate is equal to the drainage rate during the intrusions, therefore no deflation of the chamber would be be observed (Mériaux & Jaupart, 1995) or that the magma source could be at depth such that we do not observe any measurable signal at the surface. The presence of a deep source situated at the crust-mantle boundary beneath the Krafla volcanic system has been suggested by de Zeeuw-van Dalfsen et al. (2004) and cannot be ruled out in the Dabbahu segment. The modelled vertical displacement at DA25, associated with the June 2006 dyke, is 24 mm, while the observed displacement at the same site was ∼15 mm (±5.8 mm). If we assume that the difference in vertical signal is the result of a deflating body and take into account the vertical offset at DA60, then a point source deflating by 0.12 km^3 would have to be between ∼33 and ∼160 km deep.

Simulations of dyke intrusions indicate that dyke propagation is largely controlled by the difference between tectonic stress and magma pressure (Buck et al., 2006). Maximum opening during the September 2005 event occurred north of Ado'Ale, locally relieving the tectonic stress in the upper crust. Figure 3.25 shows the depth averaged, cumulative dyke opening versus distance along the segment. The new dyke intrusions have largely been intruded into regions where the opening associated with the September 2005 event (orange line) was lowest and therefore where the tectonic stresses probably remained high. In addition, to the north and south of Ado'Ale the orientation of the segment changes relative to the regional extension direction. South of Ado'Ale the segment is near orthogonal to the regional extension direction (NW-SE). However, to the north, the segment swings by ∼20° to a more northerly orientation where it becomes more oblique, approximately 60°, to the regional extension direction (Rowland et al., 2007), causing a difference in stress to the north and south of Ado'Ale.

Dyking in Afar has largely been at depth, with only two dykes resulting in a surface eruption. In comparison, 9 of the 20 dykes intruded during the Krafla rifting episode resulted in surface basaltic flows, with 3 of those occurring in the first 2 years. Models of dyke propagation following the Krafla rifting episode (Buck et al., 2006) indicate that extrusive eruptions will only occur when the magma pressure at the surface of an open dyke is positive. In these models, this will occur when the principal horizontal stress is equal to or greater than the vertical stress, defined as $-\rho(g)z$ where ρ is the density, g is gravity and z is the depth. As a result eruptions will only occur when most of the tectonic stress has been relieved. In Afar, only the southern ∼5 km of the August 2007 and June 2009 dyke intrusions results in the extrusion of basaltic material implying that the tectonic stress was locally relieved during the intrusion. In addition, the topography at the southern end of the dyke is likely to have had an influence on where the extrusion occurred. The

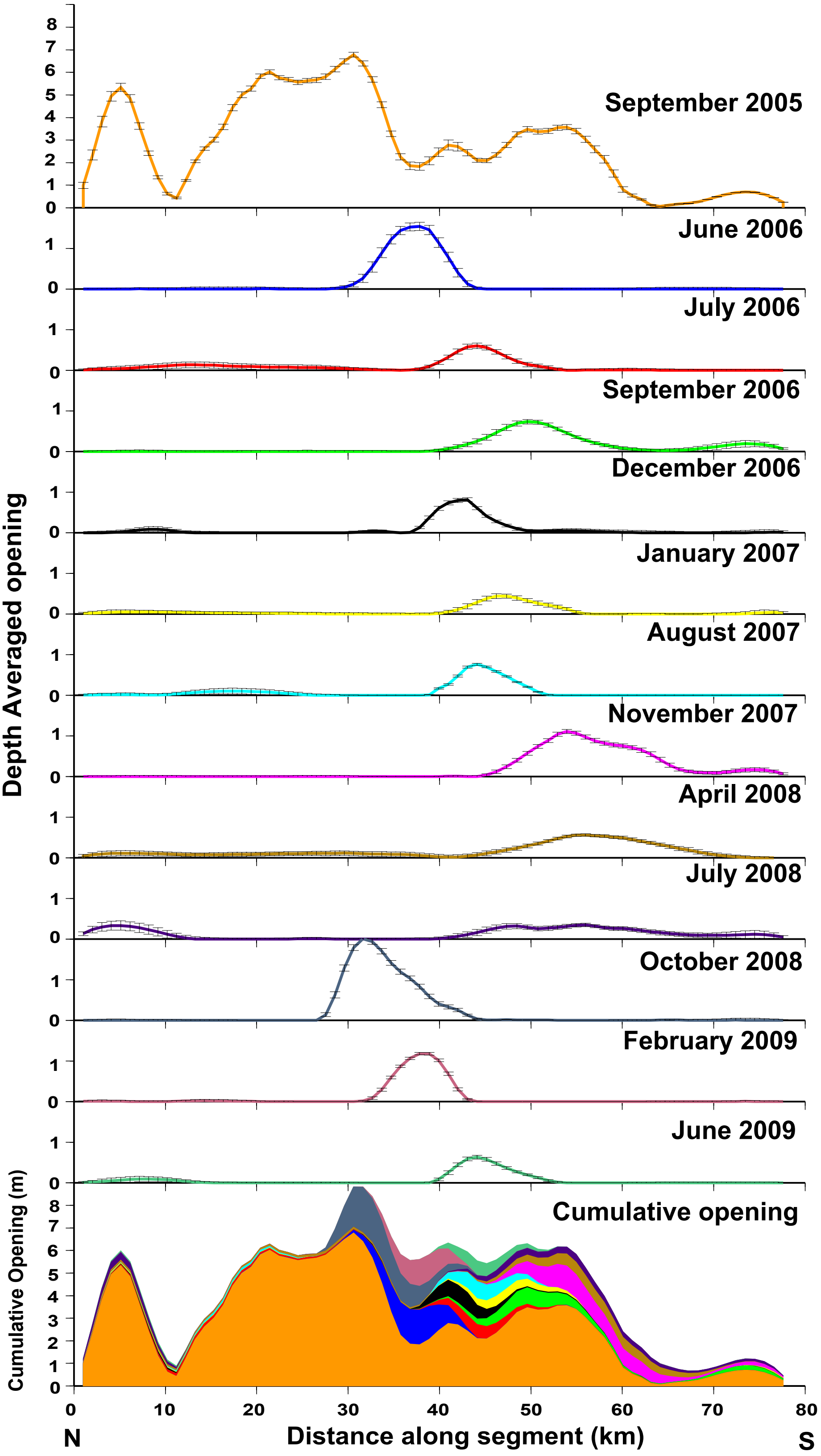

Figure 3.25: Depth averaged dyke opening for the top 10 km versus distance along the segment from north to south. Lines represent the average opening for each of the dyke intrusions (labelled). Solid graph shows the cumulative opening for all of the dykes, September 05 (orange), September 05 - June 06 (blue line), September 05 - July 06 (red), September 05 - September 06 (green), September 05 - December 06 (black), September 05 - January 07 (yellow), September 05 - August 07 (cyan) and September 05 - November 07 (pink). The dashed line shows the 5-6 m opening envelope, area beneath the line are the regions which have not achieved 5-6 m of opening.

southern end of the dyke corresponds to a topographic low (Fig. 3.16i). Assuming the dyke is intruded at a shallow depth, as with the June 2009 intrusion, then the ∼200 m lower topography may have enabled the dyke to intercept the surface in this region.

It is clear, from the available data, that magma intruded during the June 2006 to June 2009 dykes was not sourced from either of the volcanoes at the northern end of the segment, Dabbahu and Gabho, which provided some of the magma for the 2005 intrusion. Lateral migration of seismicity away from Ado'Ale during the June and July 2006 intrusions (Keir et al., 2009), the broad zone of uplift observed in both InSAR and GPS data prior to the June intrusion, and the subsidence observed in November 2007 and October 2008 point toward a magma source located beneath the Ado'Ale volcanic complex.

Observations from the Krafla rifting episode (Fig. 3.24) suggest that dyking in the Dabbahu segment will continue while a magma source persists and until the tectonic stress has been relieved. It is evident that new dyking occurs in regions where less opening has occurred in previous intrusions (Fig. 3.25). Assuming that the tectonic stress along the segment is smooth spatially then we expect 9-10 m of opening everywhere along the segment. Thus, if the pattern of intrusion continues then we expect that any new dykes will be intruded into regions along the segment which have yet to experience ∼10 m of opening. It is therefore likely that any new dyking will be focused in the area of current activity south of Ado'Ale and in the region in the north of the segment, ∼5-20 km south of Dabbahu volcano, or possibly on the neighbouring segments, Hararo in the south and Alayta in the north. To further examine the spatial pattern of magmatism along the Dabbahu rift segment the next chapter will focus on the stress change induced by each of the new intrusions.

Chapter 4

Dyke induced stress change

It is now well established that stress transfer from a major earthquake may trigger subsequent earthquakes in nearby regions (Harris & Simpson, 1996; King et al., 1994; Reasenberg & Simpson, 1992). Such a mechanism has not been demonstrated for magmatic intrusions and eruptions, though it has been suggested for a few isolated cases (Amelung et al., 2007; Calais et al., 2008; Walter & Amelung, 2006). Confirmation of the triggering of one earthquake by another is possible since numerous earthquakes occur in aftershock sequences after major events (Fig. 4.1). Magmatic events are often more isolated, and systematic relations are hard to establish. In this chapter I demonstrate for the first time the high probability of a link involving stress transfer between a chain of thirteen dyke intrusion events. Furthermore, I evaluate the change in Coulomb stress on fault planes located along the Dabbahu rift segment and show that fault slip must occur during dyke propagation rather than after emplacement.

4.1 Stress change along dyke plane

In Chapter 3, distributed opening models were used to explain the deformation associated with a sequence of dyke intrusions between June 2006 and July 2009. In this chapter I will calculate the static stress change induced by each of the new intrusions, assess its affect on the position of future events and examine the Coulomb stress change on faults above the dyke. I use the same inversion method described in Chapter 3 but allow opening to occur down to a depth of 20 km. The majority of the intrusions are located in the upper 10-12 km; opening below 10 km is small relative to the main intrusion and is, in general, a result of the inversion fitting long wavelength signals unrelated to dyke opening.

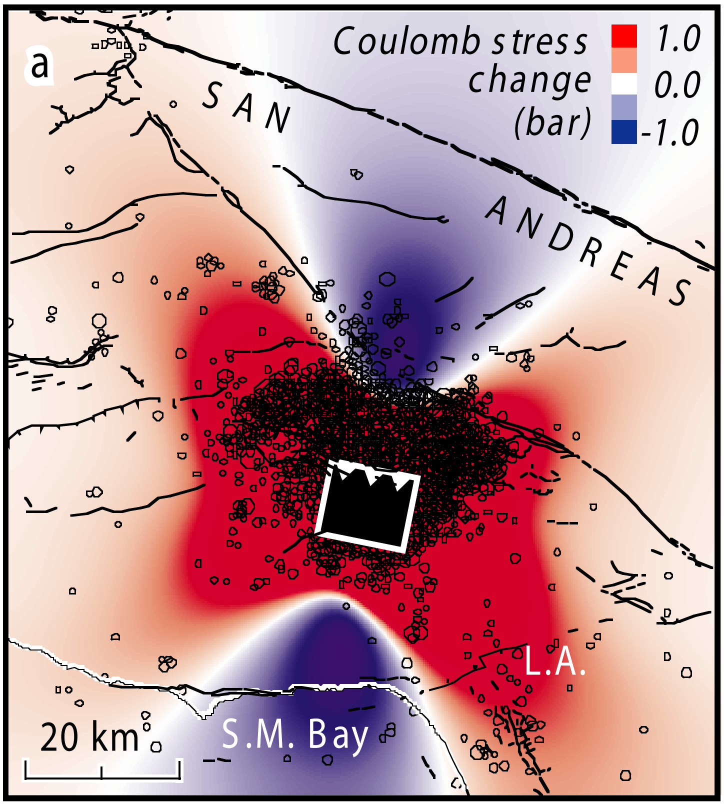

Figure 4.1: Coulomb stress change for the 1994 $M_w = 6.7$ Northridge earthquake. The Coulomb stress change is calculated on optimally orientated thrust or strike-slip faults at 3-10 km depth. The locations of active surface faults and aftershocks $\geq M_w$ 1.5 are shown in black, after Stein (1999).

Therefore, before I calculate the change in stress the opening models are filtered to remove areas of opening which are smaller than the maximum 2-σ uncertainties (typically ~0.3-0.4 m). The resultant opening models are then used to compute the internal strain and stress fields (Equations 2.33 and 2.34) in an elastic halfspace (Okada, 1992). I assume a value of 32 GPa for λ and μ giving a Young's modulus and Poisson's ratio of 8 GPa and 0.25 respectively. The dyke model, shown in Figure 4.2, is discretised into 1500 ~1 km by ~1 km patches and the change in stress is calculated at the centre of each patch (Fig. 4.3).

In order to determine the tensile stress perpendicular to the the plane of the dyke, the stress tensor must first be rotated. Cauchy (1823) showed that the traction vector, **t**, at a point on any surface can be defined, using indicial notation, by

$$\mathbf{t_i}(n) = \sigma_{\mathbf{ji}}\mathbf{\hat{n}_j}, \tag{4.1}$$

where $\mathbf{\hat{n}}$ is the outward normal vector, calculated by taking the cross product of **a** and **b**

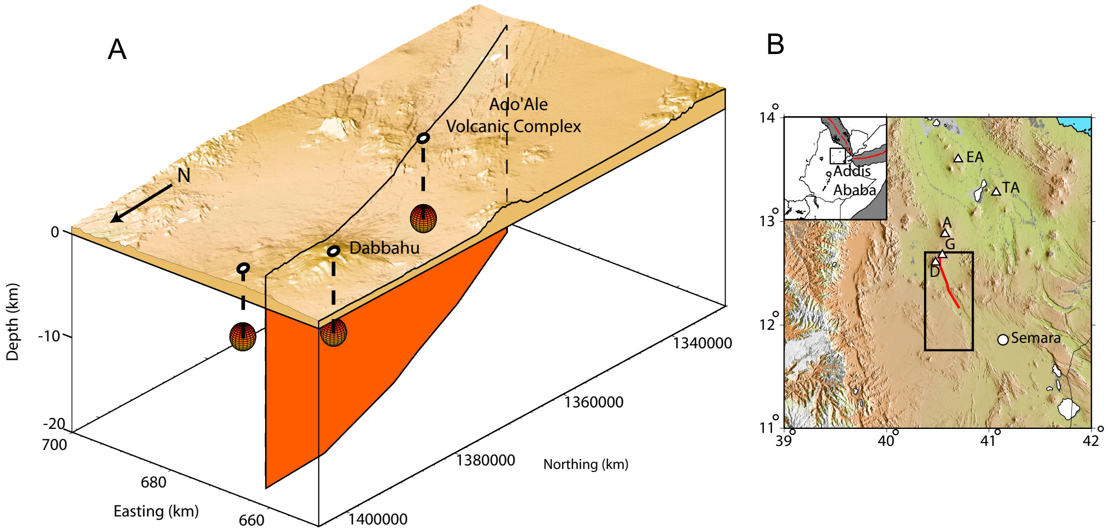

Figure 4.2: Colour shaded relief map of northern Afar and the model geometry used for stress change calculations. Subfigure shows the location of the dyke (red line) intruded in 2005, Gabho (G), Dabbahu (D), Alayta (A), Ado'Ale (A'A), Tat'Ale (TA) and Erta'Ale (EA) volcanoes (white triangles) and Semara, the regional capital (white circle). The black box indicates the region shown in the main figure. The Manda-Hararo segment runs from Dabbahu to Semara. Main figure shows the model geometry used for this study. The rectangular region shows the location of the dyke along the rift segment, the orange spheres represent point source magma chambers at 5 km depth beneath Gabho and Dabbahu and at 8 km beneath Ado'Ale.

(Fig. 4.3). Expressed in matrix notation, in Cartesian co-ordinates, equation 4.1 is given by

$$\begin{bmatrix} t_x(n) \\ t_y(n) \\ t_z(n) \end{bmatrix} = \begin{bmatrix} \sigma_{xx} & \sigma_{yx} & \sigma_{zx} \\ \sigma_{xy} & \sigma_{yy} & \sigma_{zy} \\ \sigma_{xz} & \sigma_{yz} & \sigma_{zz} \end{bmatrix} \begin{bmatrix} n_x \\ n_y \\ n_z \end{bmatrix}. \tag{4.2}$$

The magnitude of the traction vector normal to the dyke ($\sigma_{\perp\perp}$) is then given by ($\mathbf{t} \cdot \hat{\mathbf{n}}$) (Fig. 4.3). For all of the stress change calculations I define compressive stress change as negative and tensile as positive.

Although the initial state of stress along the rift segment is unknown prior to the onset of rifting in 2005 I have tested whether the spatial pattern of magmatic intrusion during the recent activity can be explained by the transfer of stress after each event. If this is the case I would expect new dyking to occur in areas of positive stress change (unclamping) but no intrusion in regions of compressive stress change (clamping) (Amelung et al., 2007).

The September 2005 dyking event ruptured the length of the Dabbahu rift segment. The intrusion resulted in a stress drop along much of the rift segment with the largest stress change occurring north of the Ado'Ale volcanic complex (Fig. 4.4). This would imply

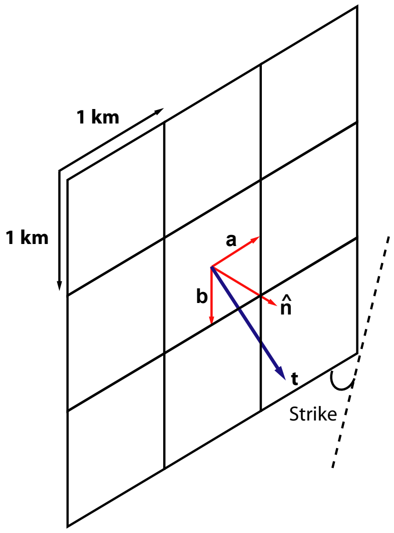

Figure 4.3: Schematic diagram showing the vector components used to calculate the stress change.

that most of the rift segment became clamped preventing further intrusions. Assuming, however, that the tectonic stress, built up after the previous rifting episode (~500 yrs), was spatially smooth along the length of the segment before the September 2005 intrusion then only parts of the northern section of the rift segment may have become clamped while much of the central and southern sections have remained unclamped. This is supported by earthquake observations after the 2005 dyke which continue to be a result of normal faulting (Ebinger et al., 2008).

All of the dykes intruded since 2006 have been emplaced in a section of the rift segment where the amount of opening associated with the September 2005 dyke was lower, approximately one fifth of the maximum (Chapter 3). To assess whether stress transfer is important in controlling the location of the next event I examine the percentage of dyke opening occurring in regions of positive stress change greater than 0.1 MPa (1 bar). I set a generous lower threshold of 0.1 MPa (1 bar) to ensure that small stress changes do not bias the result. For the first intrusion, emplaced in June 2006 I find that 45% of the opening is in sections unclamped by the September 2005 event. The next intrusion, located to the south of the dyke 1, had 91% of its opening in regions unclamped by the previous intrusion (Fig. 4.4) and ~89% of the third dyke occurred in areas unclamped by the second intrusion (Table 4.1, Fig. 4.4).

The fourth intrusion was located to the north of the previous event in a similar position to dyke 2 (Fig. 4.4); in this case, ~95% of the opening occurred in an area of positive stress change. Dyke 5 was located at the southern end of the previous intrusion, 58% of the

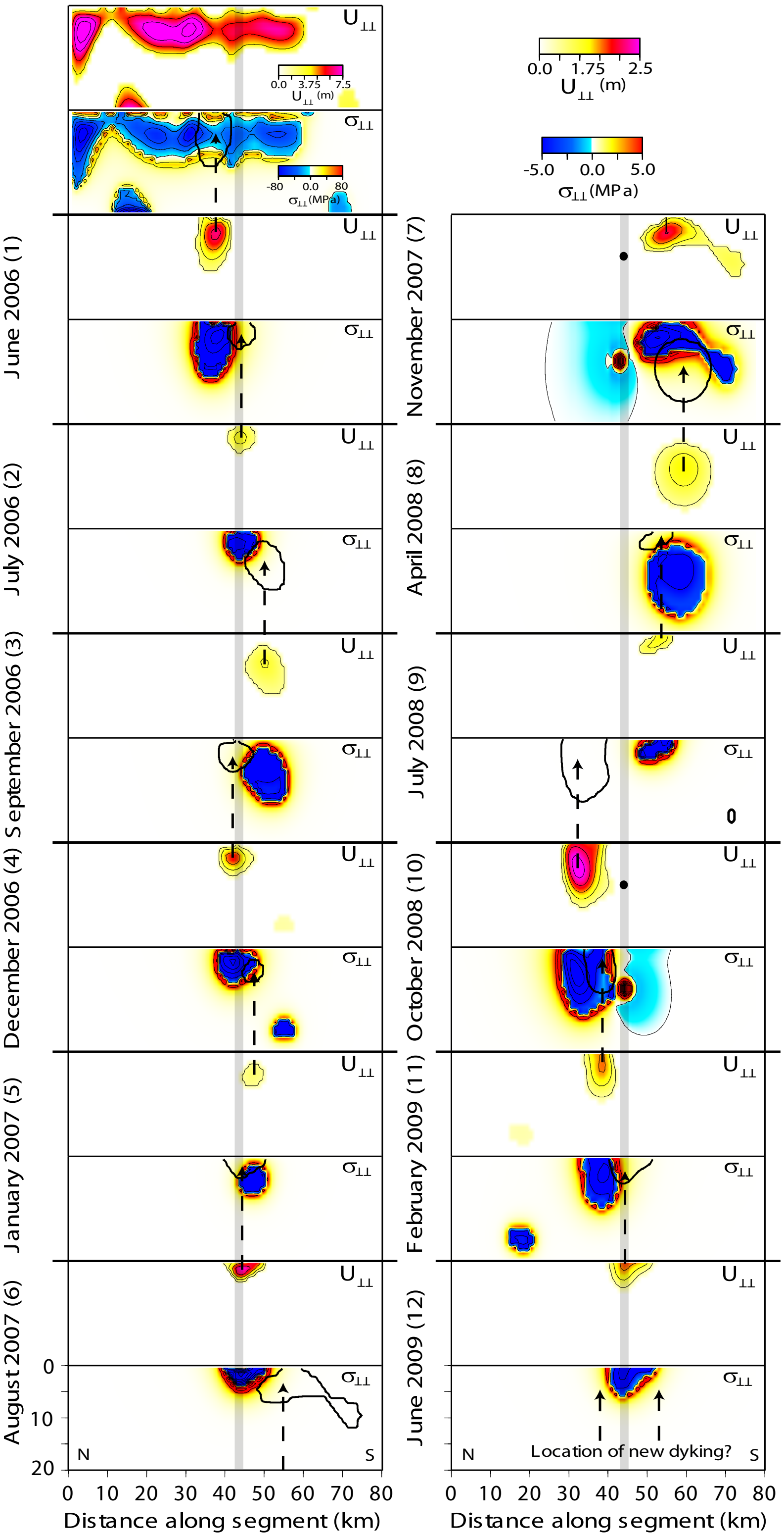

Figure 4.4: Distributed opening models and stress change calculated for each of the dyke intrusions between September 2005 and June 2009. The top and bottom panels for each intrusion show the opening model and stress change respectively. The arrows and black outlines link the maximum opening of dyke *N* to the stress change induced by dyke *N-1*, and black circles represent deflating point sources for the intrusions in November 2007 and October 2008. The grey solid line shows the location of Ado'Ale.

Dyke number	Date	Max Opening (m)	% opening in unclamped section	Likelihood
1	June 2006	2.2 ±0.2	45	0.62
2	July 2006	1.1 ±0.1	91	0.37
3	September 2006	1.2 ±0.1	81	0.23
4	December 2006	1.8 ±0.1	95	0.11
5	January 2007	0.7 ±0.1	58	0.62
6	August 2007	2.4 ±0.1	89	0.06
7	November 2007	1.7 ±0.1	55	0.47
8	April 2008	1.0 ±0.1	78	0.18
9	July 2008	1.3 ±0.2	100	0.24
10	October 2008	3.1 ±0.16	4	0.78
11	February 2009	1.5 ±0.1	35	0.56
12	June 2009	1.6 ±0.1	85	0.3

Table 4.1: Values of maximum opening, the % of opening in an unclamped section of the rift segment and the likelihood of a dyke having the same amount of opening in regions of tensile stress as observed (see text for details). For dyke 1 this shows that there is a 62% chance that an intrusion would have 45% of its opening in unclamped sections of the rift.

opening occurred in a region of unclamping with a tensile stress change of ~9.5 MPa at the point of maximum opening. The sixth dyke, intruded in August 2007, was emplaced north of dyke 5 with ~80% of the opening occurring in regions of tensile stress change. Dyke 7 was emplaced at the southern end of the rift segment with 56% of the opening in a region of unclamping caused by the previous intrusion. The eighth intrusion initially appeared to reintrude the same area as the previous dyke; however, the inversion revealed that it was intruded directly beneath dyke 7 with 82% of the opening in a region of unclamping with a tensile stress change of 1.8 MPa at the point of maximum opening. The next event was located above dyke 8 at its northern end, the dyke was relatively small (Table 4.1) but all of the opening occurred in an area of unclamping induced by the previous intrusion. Dyke 10 was located to the north of Ado'Ale, ~5 km from of the previous dyke and with only 4% of the opening occurring in regions of significant tensile stress generated by the previous intrusion. The two following events begin to migrate southwards as with the first 3 dykes: dyke 11 was intruded to the south of the previous intrusion in a similar position to dyke 1. Approximately one third of the opening occurred in regions of unclamping (Table 4.1, Fig. 4.4). The twelfth intrusion, emplaced in June 2009, was located at the southern end of dyke 11 with ~86% of the opening in areas of unclamping generated from the previous event.

To test whether the stress change induced by a dyking event is a controlling factor on the location of subsequent intrusions I calculate the probability of a dyke being intruded with the equivalent percentage of opening in unclamped regions as observed (Fig. 4.4). To determine the probability, I first calculate a probability function (Fig. 4.5) based on the location of dyke opening between 2006 and 2009. For each along axis and depth position I sum the number of dyke intrusions which have had opening at that location (Fig. 4.5)

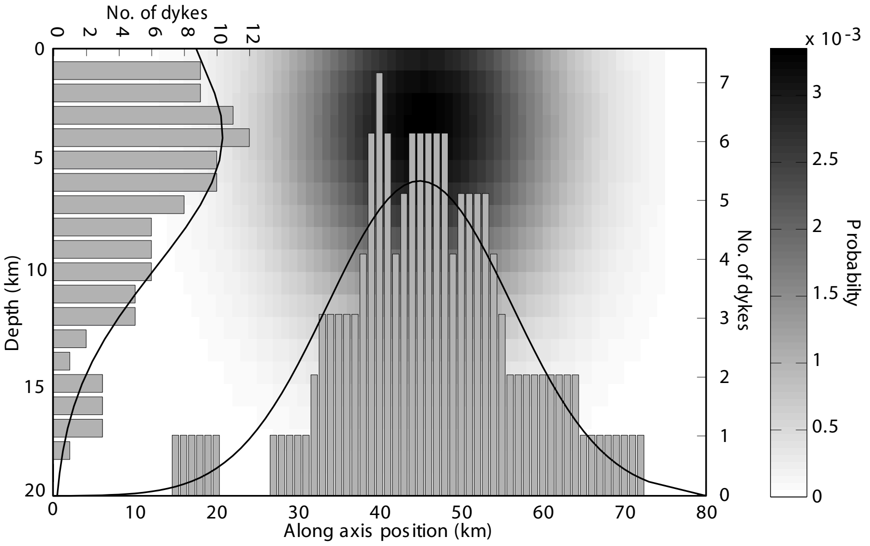

Figure 4.5: Histograms showing the number of dykes opening at each along axis and depth position for the period between June 2006 and July 2009. The background image shows the probability function used to calculate the likelihoods discussed in the text and listed in Table 1. The function is calculated using the two superimposed distributions shown by the solid black lines.

and fit a probability function of the form:

$$y = \frac{1}{\sigma\sqrt{2\pi}} \exp^{-\frac{(x-\bar{x})^2}{2\sigma^2}} \tag{4.3}$$

where σ is the standard deviation and $\bar{x}$ is the mean. The probability grid is then calculated by multiplying together the two functions for depth and along axis position. Taking the opening models shown in Figure 4.4, I reposition each model at every possible location across the modelled dyke plane while keeping the stress change from the previous intrusion fixed (Fig. 4.6). For each of the repositioned dykes I assess the percentage of opening in areas of unclamping and assign a likelihood, corresponding to the probability value generated from the probability function, at the centre of the dyke which is dependent on its position within the model domain. The probability of a dyke having x% of its opening in regions of unclamping then becomes the sum of the likelihoods for all of the repositioned dykes with the same amount of opening in unclamped sections of the rift.

$$P_{tot}(D_{x\%}) = \sum P_{ind}(D_{x\%}) \tag{4.4}$$

The Cumulative Probability Function (CDF), plotted in Figure 4.7, for each intrusion is then

$$\left\{ P(D_{<x\%}) = \textstyle\sum_0^x P(D_{x\%}) \quad \lim_{x\to+\infty} P(D_{<x\%}) = 1. \right. \tag{4.5}$$

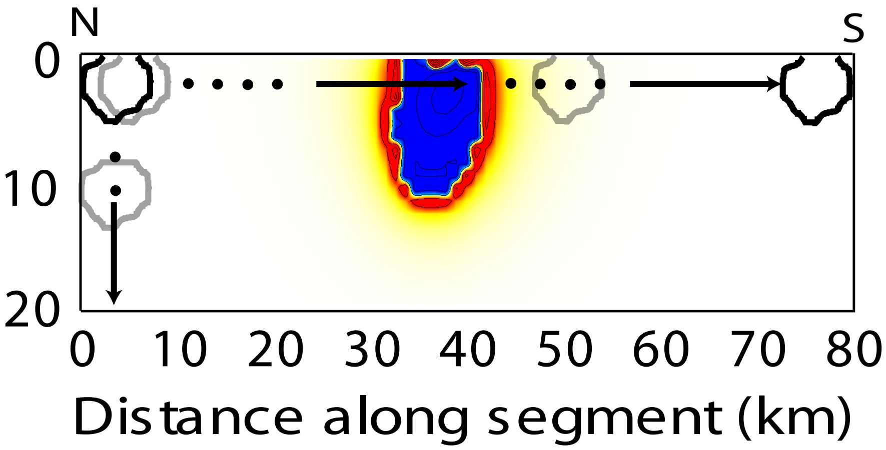

Figure 4.6: Diagram showing the location of repositioned dykes around the model domain for the June 2006 intrusion.

The probabilities plotted in each of the histograms in Figure 4.7 represent the likelihood, $P(D_{x\%})$, of each dyke having less than x% of it's opening in sections of unclamping. For example, the probability of a dyke have less than 100% of it's opening in unclamped sections is always 1. This is because, regardless of it'sposition in the moodel domain, it will always have less than 100% of it's opening in unclamped sections.

During the Dabbahu rifting episode the mean amount of opening in unclamped sections of the rift has been 70% with eight of twelve dykes having over 75% of their opening in regions of unclamping. On average, there is a 0.3 chance of the simulated dykes having this degree of opening in regions of unclamping, with probabilities for individual dykes occurring in areas with the same amount of unclamping ranging from 0.06 to 0.78 (Fig. 4.7, Table 4.1). Therefore, the cumulative probability, calculated by multiplying all of the individual likelihoods in Table 4.1 together, for the entire sequence of dykes occurring in areas with the observed amount of opening in unclamped regions, if the stress change were not a controlling factor, is vanishingly small (1 in 2 million).

The amount of opening in unclamped sections of the rift for four events (5, 7, 10 and 11) was lower than the average and ranged from 3 to 58%. Event 5, intruded in January 2007, was the smallest of the 2006-2009 dykes with a maximum opening of ~0.7 m (Hamling et al., 2009), 58% of its opening was located in areas unclamped by the December 2006 event. Although there is considerable overlap between the intrusions, the region of maximum opening was located in an unclamped section. Furthermore, the small size of the intrusion and the short time period since the previous event (38 days) may allow the dyke to re-intrude the southern end of the earlier dyke where opening was less (∼0.5 m). For dyke 7, intruded in November 2007, only 55% of the opening was in sections of the rift significantly unclamped by the previous dyke. The portion of the dyke with greater than 1 m of opening all lies within a section of the segment unclamped by more than 0.1 MPa; however, the region of deep opening located to the south, which opened by ∼0.8 m or less, was still located in regions of unclamping induced by the previous dyke. The tenth intrusion in October 2008 had over twice the average volume and a maximum opening of ∼3 m but only 3% of its opening was in an area significantly unclamped by the July 2008 event. The dyke was the most northerly of all the intrusions and was largely emplaced in a region which had not yet been reintruded by the post 2005 dykes. As such, I consider the cumulative stress change caused by the dyking events since June 2006. In this case, ∼55% of the opening is in areas of tensile stress change and the stress change at the point of maximum opening is ∼8.7 MPa. Dyke 11 was intruded at the southern end of the tenth dyke in approximately the same along axis position as the June 2006 intrusion (dyke 1). Only ∼35% of the modelled opening was located in regions of tensile stress change induced by the previous intrusion with a large portion of the dyke re-intruding the southern section of the previous event. The magma source for all of the new dyke injections is located at Ado'Ale indicating that this event must have propagated northward toward a region of high tensile stress induced by the previous dyke. This is not surprising; numerical simulations of the Krafla rifting episode in Iceland between 1975-84 suggest that dykes will preferentially propagate into regions of higher tensile stress (Buck et al., 2006) which would explain this northward migration. The modelled opening for the October intrusion extends to a depth of ∼14 km into a zone of high conductivity imaged using MT (Desissa et al., 2009) which may prevent the dyke from cooling between the two intrusions thus allowing it to be re-intruded.

4.2 Influence of dyking on overlying faults

Observations of actively deforming rift zones have shown the reactivation and formation of faults during episodes of dyke intrusions (Einarsson & Brandsdóttir, 1980; Keir et al., 2009; Toda et al., 2002). In many cases lateral migration of seismicity has been used as a method to track the position of a laterally propagating dyke (e.g. Dziak et al., 1995; Einarsson & Brandsdóttir, 1980; Keir et al., 2009). Similar patterns of seismicity and

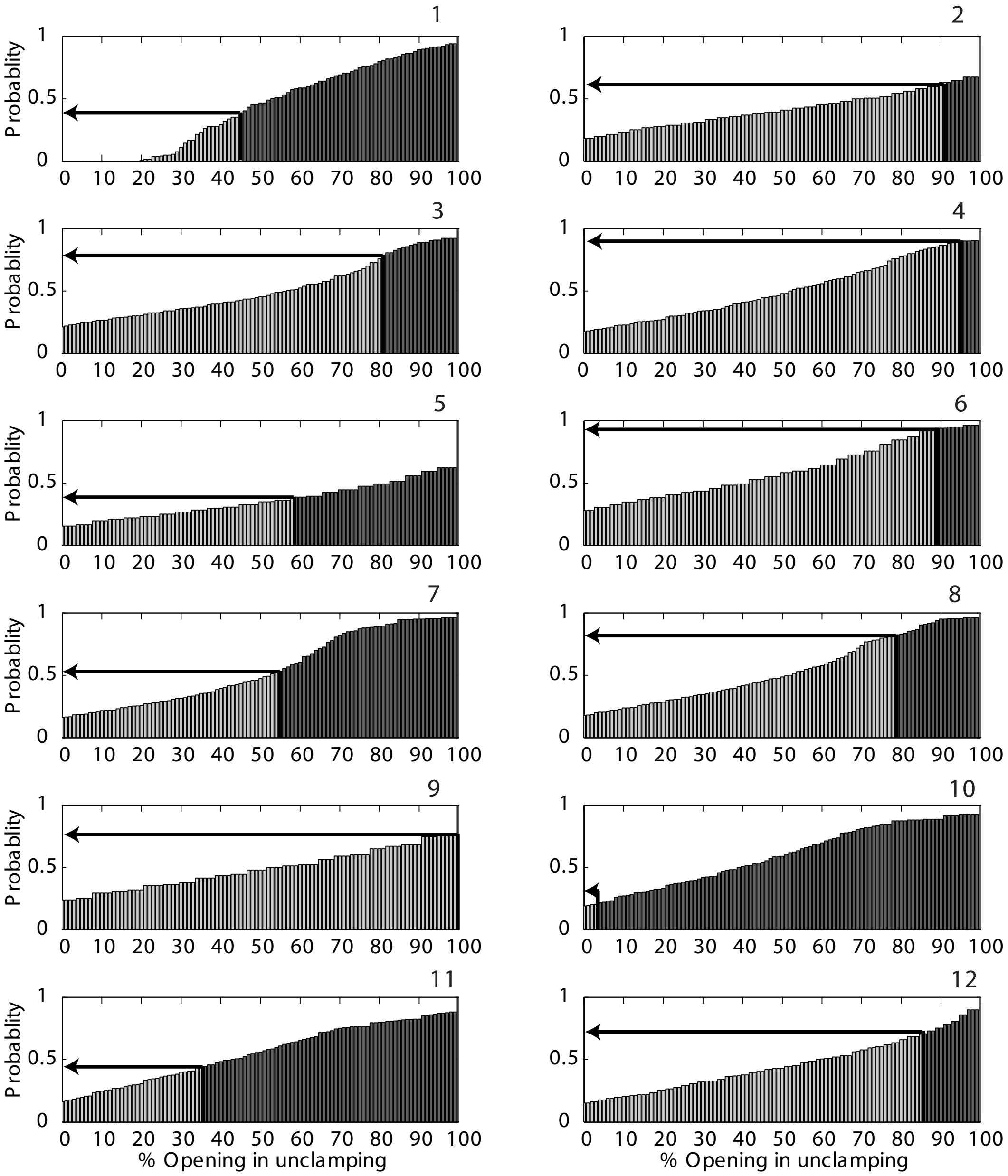

Figure 4.7: Histograms showing the percentage of opening in an unclamped section of the rift segment generated using 100 randomly positioned opening models for each intrusion. The black line shows the value associated with the actual intrusion.

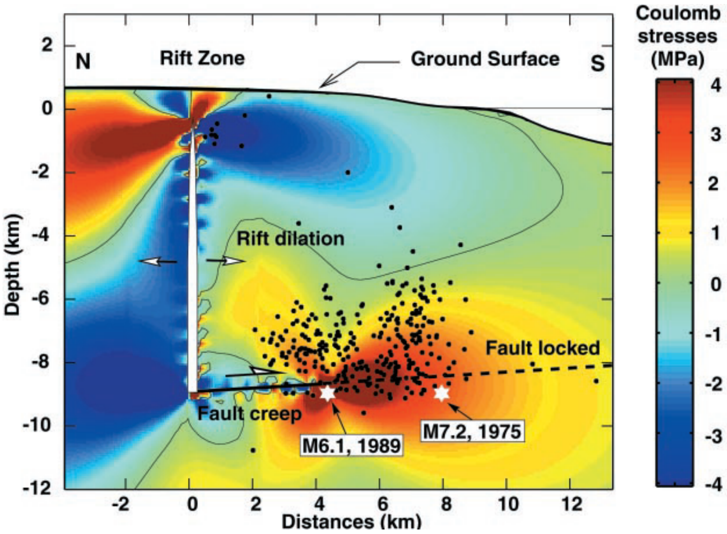

Figure 4.8: Coulomb stress change and $M \geq 1.5$ earthquakes (black circles) between 1976 and 1982. The section goes through the east rift zone. The creeping portion of the fault is represented by a solid line and the locked portion is represented by a dashed line. Potential failure planes considered are subhorizontal, with a seaward slip direction such that positive Coulomb stress variations indicate promotion of seaward slip, after Cayol et al. (2000)

faulting have been observed along the Dabbahu segment during the September 2005 event and new dyke intrusions. To assess the the affect of dyke inflation on overlying faults I calculate the normal, shear and coulomb stress changes for each of the modelled fault patches described in Chapter 3 and compare the magnitude of the stress change induced by each dyke intrusion with the amount of modelled slip to see if there is a correlation between fault slip and Coulomb stress change.

There have been a number of studies over the past few decades which have linked the location of aftershock sequences with areas of increased Coulomb stress induced by large earthquakes (Harris, 1998; Stein, 1999, e.g.)(Fig. 4.1). Coulomb stress change calculations are based on the idea that a fault surface can be brought closer to failure by increasing the normal stress, such that the fault surface is pulled apart, and by increasing the shear stress where by the fault surfaces are forced to slip against each other

$$\Delta CFS = \Delta\sigma_s + \mu'\Delta\sigma_n, \tag{4.6}$$

where $\Delta\sigma_s$ is the change in shear stress, μ' is the apparent coefficient of friction and $\Delta\sigma_n$ is the change in normal stress. The results of these studies suggest that static stress changes as low as 0.01 MPa (1 bar) can affect the location of aftershocks, in other words, locations where the faults have been brought closer to failure. Similar studies have been conducted examining the effects of magmatic processes on faulting (e.g. Cayol et al., 2000; Jónsson, 2008). Cayol et al. (2000) suggested that earthquakes along a fault beneath the southern flank of Kilauea can be explained by the Coulomb stress change related to rift dilatation prior to the 1983 Pu'u O'o eruption (Fig. 4.8) while Jónsson (2008) showed that faulting at Sierra Negra volcano was promoted by an inflating sill beneath the caldera. An earlier study by (Rubin & Pollard, 1988) examined the effects of a dyke intrusion on faults in rift zones and found that faults located in a narrow region above a dyke intrusion have an increased tendency to fail (Fig 4.9). Similarly, the expected Coulomb failure stress, which is a combination of the shear and normal stresses, associated with the intrusion of a dyke also predicts that faults above a dyke are more likely to fail. Figure 4.9 shows the expected Coulomb stress change associated with two dykes; one intruded between 0-7 km and the other from 2-9 km.

For the example in Figure 4.9, where the dyke is buried, the region around the dyke where failure is expected to occur forms an elongate ∼12 km wide, ∼2 km deep and 35 km long zone directly above the dyke and extending for ∼10 km at either end. In contrast, if the dyke reaches to the surface then the zone of likely failure is confined to a much smaller area in the vicinity of the intrusion. For a dyke opening at depth the horizontal tensile stresses are increased as the region above the intrusion subsides causing fault surfaces parallel to the dyke to become unclamped. In addition, the subsiding block increases the amount of down-dip shear stress on those surfaces bringing them closer to failure. In the case where the dyke approaches the surface, however, the affect of the dyke opening forces fault surfaces on either side of the dyke closer together and increases the up-dip component of the shear stress which, with a high enough magnitude, may result in reverse faulting (Gudmundsson et al., 2008).

Modelled Stress change along the Dabbahu segment

Using the method described earlier, I now calculate the stress change on each of the modelled fault patches but rotate the stress tensor to find both the normal ($\Delta\sigma_n$) and shear ($\Delta\sigma_s$) stress components, from which the Coulomb failure stress (ΔCFS) can then be calculated using Equation 4.6.

Using the same dyke opening models described in Section 4.1 I calculate the expected

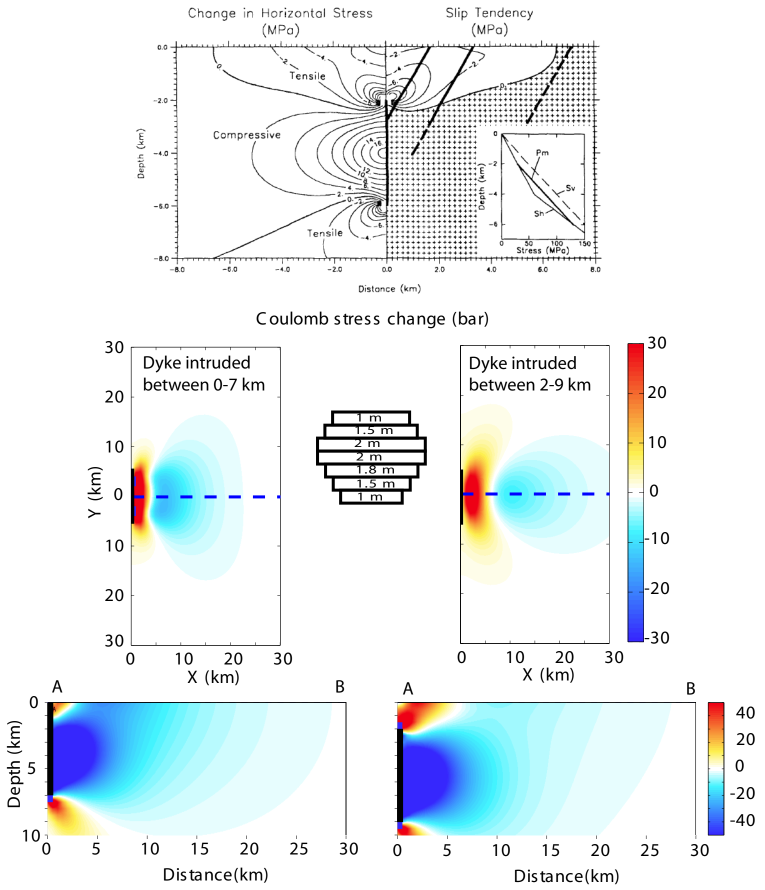

Figure 4.9: *top*, Change in horizontal stress and slip tendency on faults dipping at 60° after a dyke intrusion. Negative slip tendencies represent normal faulting whilst shaded region indicates no faulting, after Rubin & Pollard (1988). *middle left*, Coulomb stress change for normal faults oriented parallel to a dyke intruded between 0 and 7 km, the opening distribution is shown in the centre. Bottom panel shows a cross section across the black line.*middle right*, Coulomb stress change for normal faults parallel to a dyke intruded between 2 and 9 km. Bottom panel shows a cross section across the blue dashed line. Figures produced using the free USGS Coulomb 3.1.09 developed by Toda et al. (2008).

stress change at the centre of each fault patch, centred at 1 km depth, as a result of each dyke intrusion. To assess the effect of the dyke intrusion on the overlying faults I compare the amount of modelled slip on each of the fault patches with the predicted normal and shear stress change on the same patch. For faults to have slipped Coulomb stress criterion suggests that the Coulomb stress change should be positive. Figure 4.11 shows the change in shear and normal stresses, for each patch, scaled by the amount of modelled slip. Counter to the Coulomb stress criterion Figure 4.11 suggests that there is no correlation between the amount of slip and the magnitude of the stress change. Only 23% of modelled faults, with more than 0.5 m of slip, have an increased Coulomb stress and in many cases the largest slip is occuring on faults with a negative Coulomb stress change. The dyke intrusions in September 2006, January 2007 and April 2008, however, do show some correlation with much of the largest slip occurring on faults with the largest

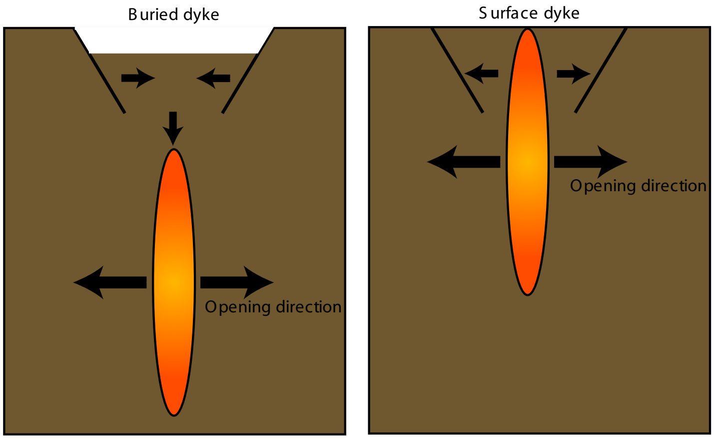

Figure 4.10: Schematic diagram showing the effect of a dyke intrusion on overlying faults. *Left* For a dyke emplaced at depth. *Right* For a dyke reaching the surface

stress change (Fig 4.12).

Although there is no correlation between the magnitude of the stress change and the amount of slip, comparing the number of slipping faults with those with an increased Coulomb stress shows that a large portion of the faults (42-93%), which are modelled as slipping, do have a Coulomb stress change of more than 0.01 MPa (Table 4.2). If, however, the slip threshold is increased such that only faults with more than 0.1 m and 0.2 m are counted then this portion of slipping faults, with the exception of the September 2006, January 2007 and April 2008 intrusions, is significantly reduced. For the three aforementioned intrusions the portion of faults slipping increases as the slip threshold is increased (Table 4.2). The reason for this difference is that these three intrusion are all emplaced at depth and therefore the faults above the dyke, as in Figures 4.9 and 4.10, always have an increased chance of failure. For the other intrusions, which have opening near the surface, the faults on either side of the intrusion are clamped (negative stress drop) and should prevent slip occurring. Despite this, a large portion of the modelled faults do slip, comparing the slip distribution with the expected Coulomb stress (Fig. 4.13) shows that failure is expected on faults located at the tips of the dyke, where the models predict small amounts of slip, leading to the apparent correlation on these fault patches.

All of the stress calculations described above are centred on the middle of the fault planes at 1 km depth which, for dykes approaching the surface, may explain the discrepancies between the modelled fault slip and stress change. To test the effects of depth on the stress

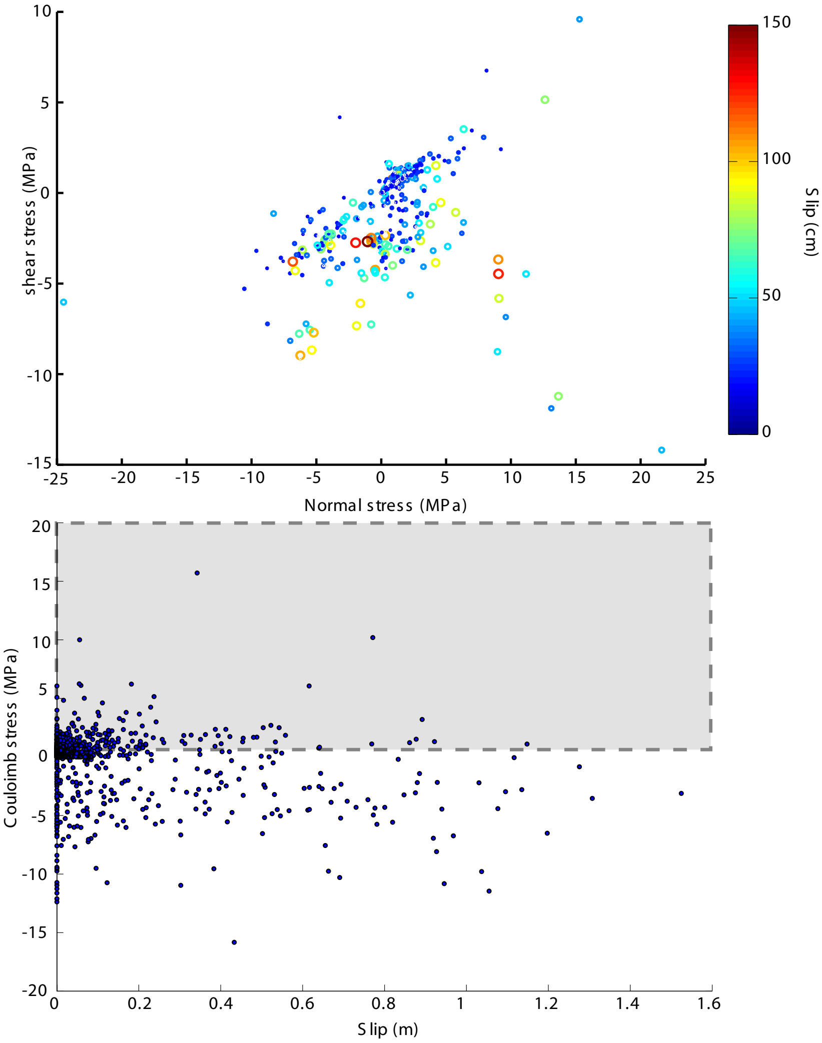

Figure 4.11: Correlation between stress change and fault slip for the June 2006 - June 2009 dyke intrusions. *Top*: Change in normal stress plotted against the change in shear stress. The size and colour of the circles represent the amount of slip while the shaded. *Bottom*: Coulomb stress change plotted against modelled slip. Grey region highlights the area where ΔCFS is always greater than 0.

distribution I re-invert each of the dyke models but discretise each of the fault planes in depth into four 0.5 km patches and re-calculate the stress at the centre of each new patch. For each intrusion, at each depth increment, I compare fault patches which have slipped and have a Coulomb stress change of more than 0.01 MPa (Table 4.3, 4.4, Figs. 4.14).

In contrast to the calculation at 1 km 55 and 46% of the faults, with more than 0.5 m of slip, have a Coulomb stress change of more than 0.01 MPa at 0.25 and 0.75 km respectively compared with only 22% at 1 km (Fig. 4.14). As with the 1 km depth interval, however, a large number of fault patches are still modelled to have slipped despite being located in regions where a stress drop has occurred. This is most notable at 1.25 and 1.75 km where many of the slipping faults occur when there is either no change in the stress or a stress

Dyke number	Date	Max slip (m)	% of faults slipping with $\Delta CFS \geq 0.01$ MPa		
			Slip >0 m	Slip >0.1 m	Slip >0.2 m
1	June 2006	1.3	62	42	25
2	July 2006	1.0	42	8	5
3	September 2006	0.5	93	100	100
4	December 2006	0.9	80	55	52
5	January 2007	1.1	71	100	100
6	August 2007	0.6	58	47	42
7	November 2007	1.9	79	59	54
8	April 2008	0.5	72	100	100
9	July 2008	1.2	69	30	25
10	October 2008	1.1	63	25	0
11	February 2009	0.7	67	35	20
12	June 2009	0.2	64	16	0

Table 4.2: Percentage of slipping fault patches with ΔCFS of more than 0.01 MPa at 1 km depth

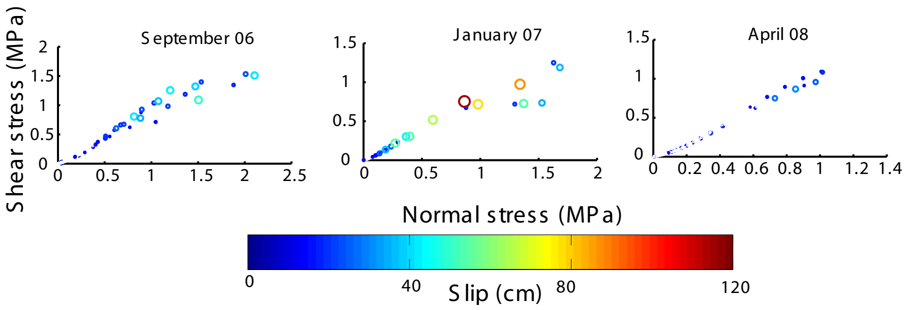

Figure 4.12: Correlation between stress change and fault slip for the September 2006, January 2007 and April 2008. The size and colour of the circles represent the amount of slip

drop. This is highlighted in Figure 4.15 where fault slip is plotted against the Coulomb stress change for each fault patch, for each intrusion, and at each depth interval. For each depth interval ~75 % of the fault patches have a Coulomb stress increase of more than 0.01 MPa, of these however, only ~5-10 % have more than 0.1 m of slip.

Although the calculation of the stress change at shallower levels still suggests that there is no correlation between the amount of slip and the magnitude of the stress change it does show a much larger portion of faults, modelled as slipping, also have an increased Coulomb stress (Tables 4.3, 4.4). For the June 2006 dyke the percentage of faults slipping by more than 0.1 m at 1 km depth was 42% whilst at 0.25 and 0.75 km this increases to 78 and 74% respectively.

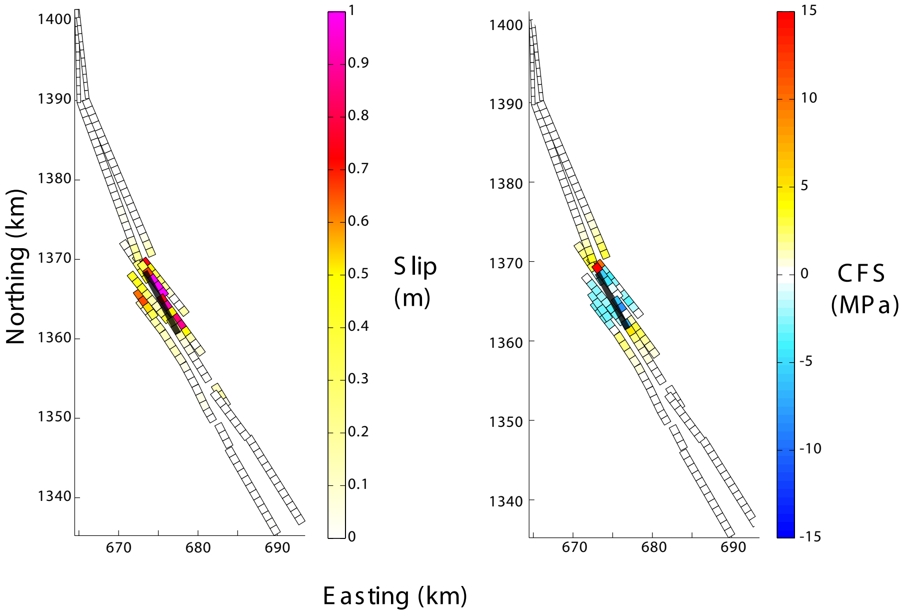

Figure 4.13: Comparison between fault slip and Coulomb stress change for the June 2006 dyke intrusion. The bold black line in both images shows the location of the dyke intrusion.

4.3 Discussion

4.3.1 Influence of stress transfer on dyking in Afar

In this Chapter I have examined the effects of stress transfer on dyking events along the Dabbahu segment and tested whether the stress change on subsurface faults can be correlated with predicted slip. The Dabbahu rifting episode has presented a unique opportunity to study the effects of stress transfer on the accumulation of magma in an active rift. Although well established in earthquake sequences there are few studies which have examined the role of stress transfer in magma emplacement (Amelung et al., 2007; Walter & Amelung, 2006). Amelung et al. (2007) showed that magma intruded between 2002 and 2005 at Mauna Loa was focused into regions of the rift segment unclamped by earlier events (Fig. 4.16). Similarly, the dominant control on the location of the new dyking along the Dabbahu segment appears to be related to the stress change caused by the 2005 intrusion with the majority of new magmatism occurring in regions of low opening during the 2005 event. Furthermore, this result suggests that the dominant control in the location of the intrusions emplaced between June 2006 and July 2009 is the stress change caused by the previous intrusion rather than the cumulative stress of all the preceding intrusions. If I consider only the previous intrusion then the average amount of opening in regions of unclamping is ∼70%, considering the cumulative stress from the preceding two intrusions

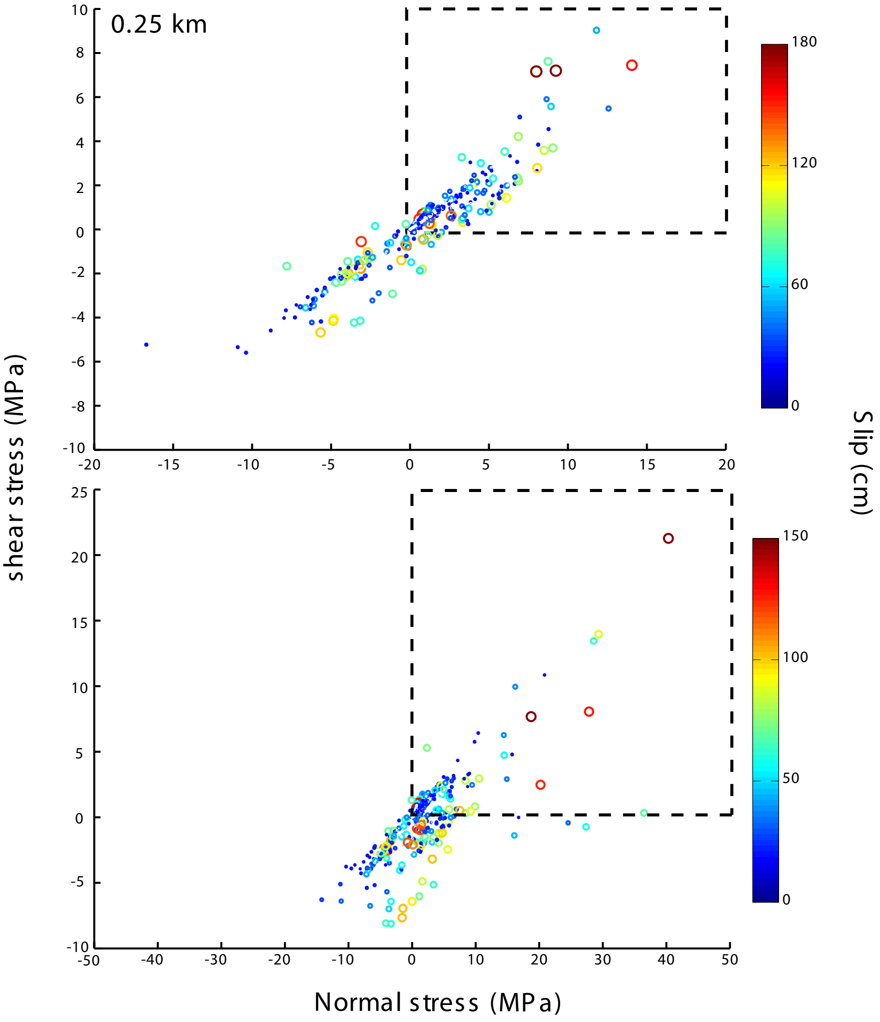

Figure 4.14: Correlation between stress change and fault slip for the June 2006 - June 2009 at 0.25 (*top*) and 0.75 km (*bottom*) depth. The size and colour of the circles represent the amount of slip while the boxed region highlights the area where ΔCFS is always greater than 0.

Dyke number	% of faults slipping with $\Delta CFS \geq$0.01 MPa at 0.25 km		
	Slip >0 m	Slip >0.1 m	Slip >0.2 m
1	88	78	73
2	59	36	35
3	92	100	100
4	93	84	95
5	62	100	100
6	61	46	25
7	98	100	100
8	74	100	100
9	70	55	25
10	70	26	24
11	64	25	22
12	61	0	0

Table 4.3: Percentage of slipping fault patches with ΔCFS of more than 0.01 MPa at 0.25 km depth

Dyke number	% of faults slipping with $\Delta CFS \geq$0.01 MPa at 0.75 km		
	Slip >0 m	Slip >0.1 m	Slip >0.2 m
1	81	74	19
2	55	25	0
3	89	100	100
4	89	84	39
5	65	100	100
6	63	52	54
7	79	78	27
8	80	100	0
9	71	45	0
10	75	23	7
11	72	32	18
12	67	0	0

Table 4.4: Percentage of slipping fault patches with ΔCFS of more than 0.01 MPa at 0.75 km depth

reduces the average to ∼50% and for the previous three intrusions to ∼43%. Interestingly the area surrounding the source region, inferred to be in the centre of the segment at between 8-10 km, is always in an area of unclamping which would enable magma to accumulate before it is intruded into adjacent regions of unclamping.

The stress changes presented in this Chapter are based on the opening distributions calculated by inverting InSAR data and as such are effected by the smoothing parameter discussed in Chapter 3, chosen to be 400 in most cases for this study. To assess the affect of the smoothing on the final solution I recalculate the opening distributions for the intrusions in June, July and September 2006 with smoothing factors of 100 and 1000. Although the smoothing parameter affects the magnitude of the opening along the dyke it has very little affect on the location of the intrusion and therefore similar amounts of opening are observed in unclamped sections. For the case where the smoothing factor is reduced the percentage of opening in unclamped sections of the rift become 86 and 88% for the July

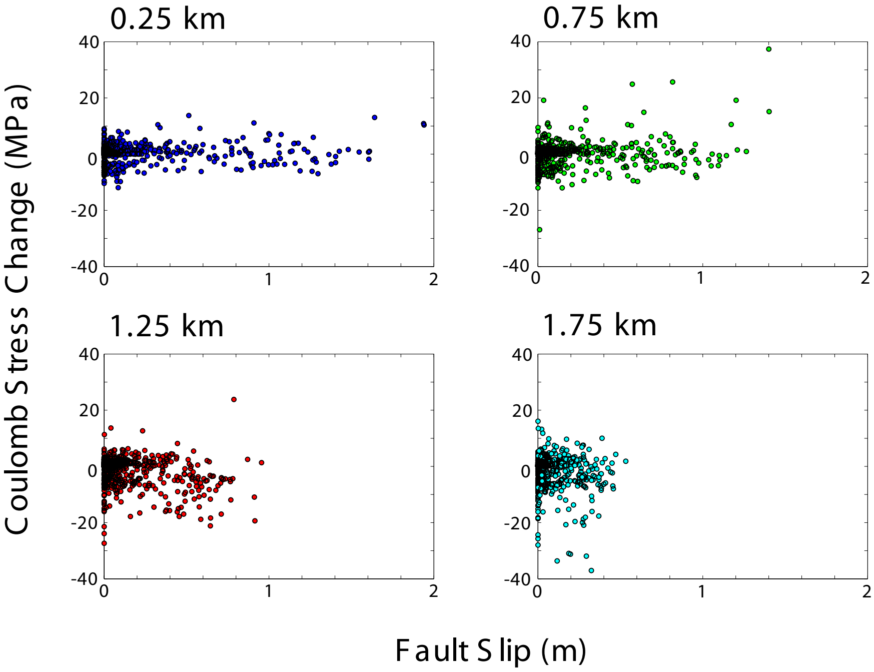

Figure 4.15: Fault slip plotted against Coulomb stress change at 0.25, 0.75, 1.25 and 1.75 km depth. *Top left* 0.25 km, *top right* 0.75 km, *bottom left* 1.25 km, *bottom right* 1.75 km.

and September intrusions respectively. Similarly, when the smoothing factor is increased the amount of opening in unclamped sections changes to 90 and 94%, similar to the values shown in Table 4.1.

There are a number of other factors which may influence the location of new magmatism which I do not consider in these simple models. I have not considered the stress change caused by the magma source beneath the centre of the segment which inflated between January and April 2006. However, the stress change induced by the inflating source is negligible compared with that caused by any of the new dykes. Also, I do not consider any relaxation of stresses after any of the dyke intrusions. However, Nooner et al. (2009) have shown that 95% of the relaxation signal observed is related to the September 2005 dyke intrusion rather than the recent dyke intrusions suggesting that this will have minimal affect on the stress change result. Alternatively, it could be argued that it is merely coincidence that the intrusions are located next to each other. However, if this were the case, that dykes intrude where dykes have happened before, it would be likely that all of the intrusions would stay confined to the Ado'Ale complex and preferentially reintrude earlier intrusions. This has been observed in Tertiary dykes in Iceland (Gudmundsson, 1983, 1984a) and from ophiolites (e.g. Kidd & Cann, 1974) where dykes are found to intrude

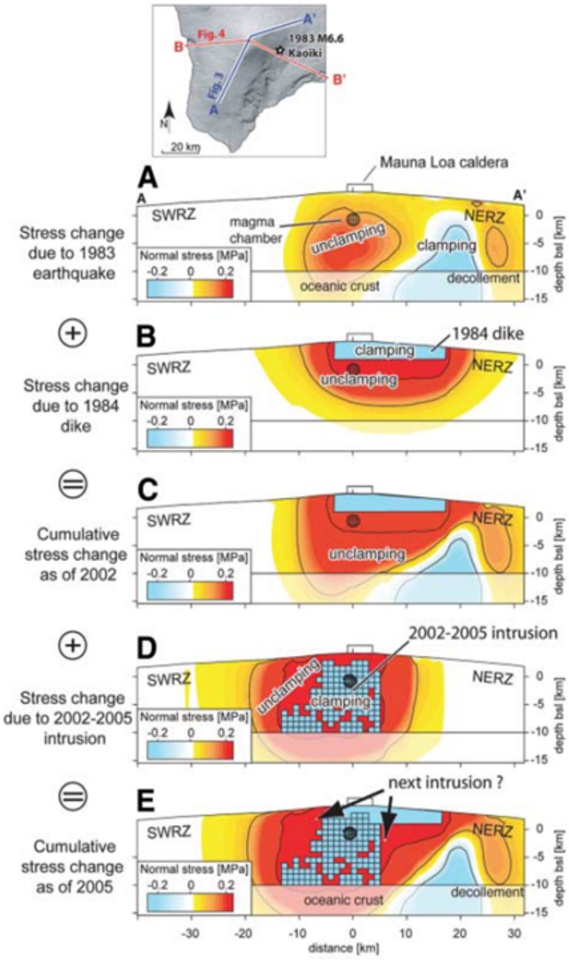

Figure 4.16: Changes in normal stress along Mauna Loa's rift zone due to (A) the 1983 M6.6 Kaoiki earthquake, (B) the dike associated with the 1984 eruption, and (D) the 2002 to 2005 rift intrusion. (C and E) The sum of the stress changes from (A) and (B) and (A), (B), and (D), respectively. The colour scale is saturated at ±0.2 MPa. Solid lines denote ±0.1 and ±1 MPa contours. The stress change is resolved in the direction normal to the overall strike of the SWRZ and NERZ along AA' after Amelung et al. (2007).

through the middle of earlier dykes. Early studies of dyke intrusions suggest that dyke intrusions occur when the magma pressure becomes greater than the stress perpendicular to the dyke plus the tensile strength of the host rock. As such, it has been postulated that the intrusion will then propagate along the pathway which requires least work. If earlier intrusions are present then this pathway becomes the centre of the previous dyke which will be be weaker than the surrounding material (Gudmundsson, 1984b).

Despite these simplifications, this result suggests that magma emplaced during the ongoing Dabbahu rifting episode is focused into regions of unclamping induced by previous dyking. This result indicates that the stress change, induced by a new dyke, is a controlling factor on the location of future events and should therefore be incorporated into routine volcanic

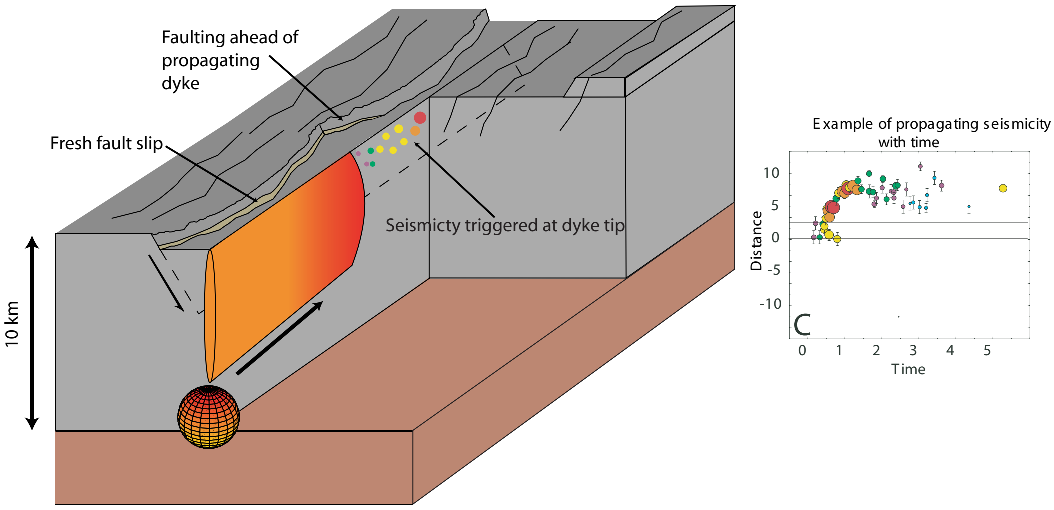

Figure 4.17: Schematic showing the effect of a propagating dyke on subsurface faults. The graph shows an example of how the earthquakes migrate as the tip of the dyke propagates in time.

hazard monitoring.

4.3.2 Influence of stress transfer on faulting in Afar

The results of the stress change calculations suggest that the majority of faulting associated with the 2006-2009 dyke sequences was limited to the upper 0.75-1 km of the crust, for intrusions emplaced near the surface, and to at least 2 km for the dyking events in September 2006, January 2007 and April 2008 which were emplaced at deeper levels. Field observations of faulting following some of the dyke intrusion show that many of the faults along the rift segment slipped at the surface in keeping with these results. Furthermore, seismicity from the June and July 2006 intrusions were spatially correlated to the deforming zone observed by InSAR (Keir et al., 2009) indicating that faults in the region above the dykes did fail. However, depth estimates for some of the more recent intrusions, which were unknown for the earlier events due to poor data coverage, show seismicity extending down to ~9 km well beyond the region where these models predict failure. The stress models presented here are all derived from the inversion of InSAR data which contain the deformation over a 35-day period. Although the models explain the observed deformation, they represent the dyke opening, and fault slip, after the dyke has been emplaced; the seismicity, on the other hand, is thought to represent the tip of the dyke as it propagates through the crust (Fig. 4.17). Although the stress models do not correlate with the modelled slip they do predict that failure will occur on faults located at the tips of the dyke suggesting that, for a propagating dyke, faulting will occur ahead of the intrusion as suggested by seismicity. Furthermore, faulting associated with the September 2005 intrusion extended some 30 km at either end of the dyke and has been attributed to the Coulomb stress change induced by the intrusion (Ayele et al., 2009) as supported by these models. Therefore, the models presented here suggest that fault slip observed around the Dabbahu segment occurred during dyke propagation and that any fault slip after dyke emplacement is confined to the upper 0.75-1 km.

The fault geometry used in this study will also effect the results of the stress change calculation. Although the geometry is representative of the general fault trend along the rift segment it is simplified and does not contain the detailed fault patterns observed in the field. Acquisition of LiDAR over the rift segment, however, will allow for the formation of a detailed fault map that, in conjunction with these models, could be used to examine the location of fault slip after a dyke has been intruded and determine which areas of the rift segment have been brought closer to failure.

Chapter 5

Observations and models of Post-rifting deformation in Afar

Increased displacement rates have been observed following many large earthquakes and magmatic events. Although an order of magnitude smaller than the displacements associated with the main event, the post-seismic or post-rifting deformation may continue for years to tens of years after the initial earthquake or dyke intrusion. In the case of post-rifting deformation, a number of mechanisms have been suggested to explain the deformation, thought to be caused by the transient response of the lithosphere after a sudden stress has been applied, including viscous relaxation (Foulger et al., 1992), continued magmatic injection at depth (de Zeeuw-van Dalfsen et al., 2004) and viscoelastic relaxation (Hofton & Foulger, 1996a,b).

In this Chapter I investigate some of the mechanisms used to explain post-rifting deformation and use InSAR time series, discussed in Chapter 2, to analyse and model the deformation following the September 2005 rifting event in Afar.

5.1 Mechanisms of Post-rifting deformation

5.1.1 Viscous relaxation models

Many of the early models of post-rifting relaxation were based on the observed deformation field following the 1975-84 Krafla rifting episode in North Iceland. Using GPS measured between 1987 and 1990 Foulger et al. (1992) proposed a simple two layer model consisting of an elastic lid overlying a Newtonian viscous layer. The deformation source is modelled as an infinitely long, vertical dyke with only non-zero displacement lying in the x-direction.

Assuming plane strain conditions in the elastic layer, a force balance between the traction on the base of the elastic layer with the elastic forces within the plate yield

$$\frac{\eta}{b}\frac{\partial u}{\partial t} = h\frac{\partial \sigma_{xx}}{\partial x} \tag{5.1}$$

where η and b are the viscosity and thickness of the viscous layer, h is the thickness of the elastic lid and σ_{xx} is the normal stress within that layer. Setting the elastic modulus, M, equal to $\frac{4\mu(\lambda+\mu)}{(\lambda+2\mu)}$, where λ and μ are the lam$\acute{e}$ moduli, and relating the stress to the strain such that

$$\sigma_{xx} = M\frac{\partial u}{\partial x}, \tag{5.2}$$

allows Equation 5.1 to be re-written in the form of the diffusion equation

$$\frac{\partial u}{\partial t} = k\frac{\partial^2 u}{\partial x^2} \tag{5.3}$$

where k $=\frac{Mhb}{\eta}$. The horizontal displacement field for a dyke with a half-width of U_0, intruded at $t = 0$, is then given by

$$u(x,t) = U_0 erfc\frac{x}{2\sqrt{\kappa T}}. \tag{5.4}$$

With knowledge of the elastic moduli, M, and the thicknesses of both the elastic and viscous layers the viscosity of the underlying layer can be determined. Although this simple viscous model is able to predict a similar displacement field to that observed after the Krafla rifting episode the boundary conditions and initial displacement are not a very realistic representation of the Earth's rheology.

5.1.2 Viscoelastic models

Lithospheric deformation associated with many near instantaneous geophysical phenomenon, such as earthquakes and magmatic intrusions, can be described by elastic theory. However, on longer timescales the lithosphere often exhibits some viscous characteristics as the imposed stresses are relaxed (e.g. glacial rebound). A number of different models have been suggested for describing viscoelasticty from non-linear power-law rheologies to more simple linear rheologies. The simplest of these is a Maxwell rheology, named after the Scottish physicist James Clerk Maxwell, which can be described in terms of a spring connected to a dashpot in series (Fig. 5.1).

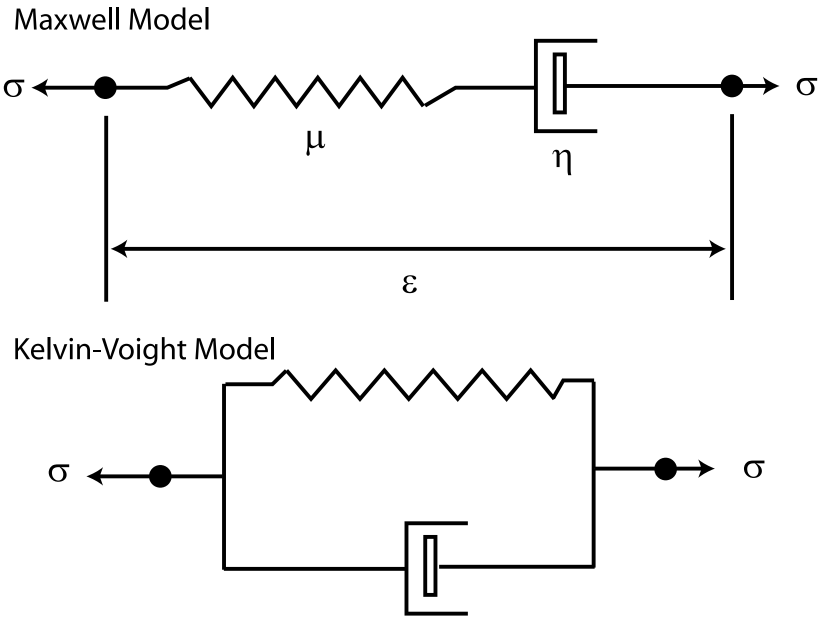

Figure 5.1: Schematic diagrams showing the model configuration for Maxwell and Voight viscoelastic models described in text.

Considering Figure 5.1 the stresses in the spring and dashpot are $\sigma = \mu\epsilon_s$ and $\sigma = \eta\dot{\epsilon}_d$, respectively, where ϵ_s is the strain in the spring, μ is the shear modulus, η is the viscosity and $\dot{\epsilon}_d$ is the strain rate in the dashpot. In the case of the Maxwell model, the total strain is then

$$\epsilon = \epsilon_s + \epsilon_d \tag{5.5}$$

and the strain rate

$$\dot{\epsilon} = \frac{\sigma}{\eta} + \frac{\dot{\sigma}}{\mu}. \tag{5.6}$$

If a sudden strain is applied to a Maxwell rheology at $t = 0$, and remains constant through time (i.e. $\dot{\epsilon} = 0$), then integrating Equation 5.6 with respect to time gives

$$\sigma = \sigma_0 e^{-\frac{\mu}{\eta}t}. \tag{5.7}$$

Equation 5.7 shows that for a Maxwell rheology the stress decays exponentially with a characteristic time constant, $\tau = \frac{\eta}{\mu}$, also known as the Maxwell relaxation time.

By rearranging the configuration of the spring and dashpot in the Maxwell model a number of other linear viscoelastic models can be formed. Commonly used models include the Kelvin (Voight) and standard linear solid models. In the case of the Kelvin-Voight model the spring and dashpot are placed in parallel (Fig. 5.1). Unlike Maxwell viscoelasticity, this model exhibits decelerating creep after a strain has been applied. This is because the spring can only extend as quickly as the dashpot. In the case where an external tensile stress has been removed a Kelvin type material will undergo compressive creep whereby the spring attempts to return to its original length causing the dashpot to retract to its original position (Haddon, 1995).

A number of studies have utilised linear rheologies and in particular Maxwell rheologies to explain the relaxation of stresses (e.g. Hofton & Foulger, 1996a,b; Nooner et al., 2009; Pedersen et al., 2009). However, analytic studies at pressures and temperatures equivalent to those in the upper mantle have suggested that rocks will deform by dislocation creep and, unlike the linear Maxwell model, require a power-law rheology of the form

$$\dot{\epsilon} = A\sigma^{n}e^{(-\frac{Q}{RT})} \tag{5.8}$$

where $\dot{\epsilon}$ is the strain rate, σ is the stress, n is the power-law exponent, A is a pre-exponential factor, and Q, R and T are the activation energy, universal gas constant and temperature. A non-linear rheology of this kind has been used to describe the post-seismic deformation observed following the Denali earthquake, Alaska (Freed et al., 2006) which they could not explain using a linear rheology.

5.2 Recent models of post-rifting relaxation in Afar

Following the September 2005 dyking event a network of continuous and campaign GPS were installed around the Dabbahu rift segment (Fig. 5.2, 5.3). Using 19 continuous and 30 campaign GPS stations Nooner et al. (2009) produced a GPS time series over the period 2005-2009 (Fig. 5.2). With the exception of sites situated on the two northern volcanoes, Dabbahu and Gabho, displacements at all continuous sites show a combination of steady motion and discrete offsets, resulting from the sequence of intrusions described in Chapter 3. Displacements recorded at all sites, with the exception of the aforementioned sites, are linear with time between dykes allowing the velocity to be computed at each site

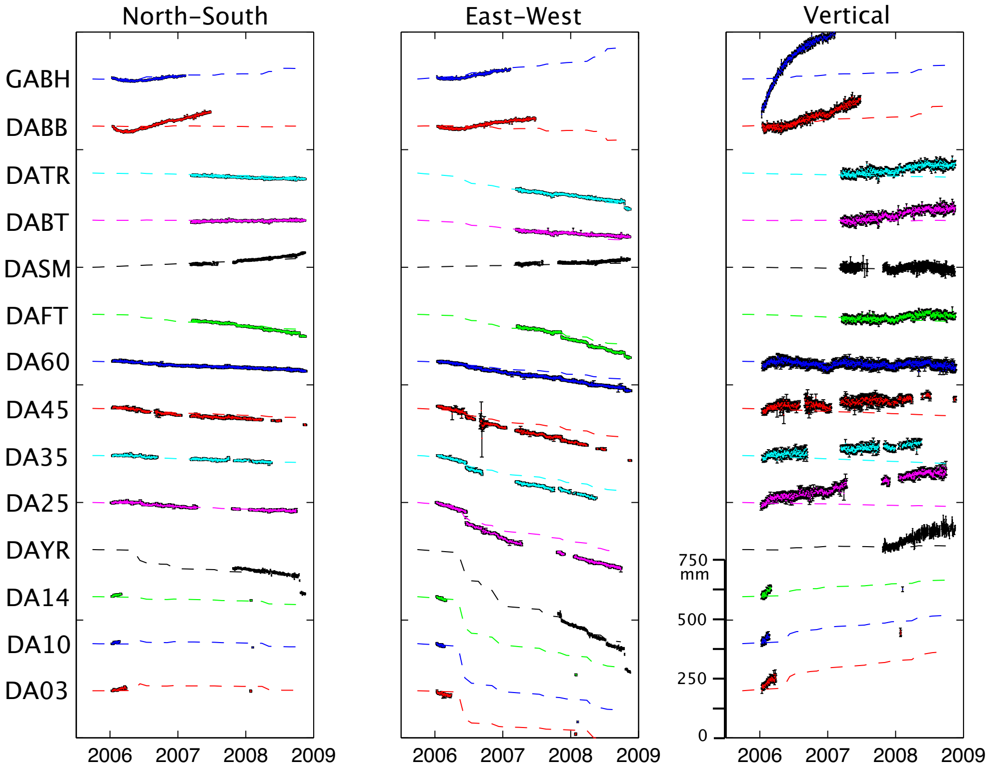

Figure 5.2: Position time series at continuous GPS sites. Site names are listed on the left side of the figure. Y-axis scale is indicated within each panel and is different for each of the north, east, and up components. Dashed lines show the displacements calculated using a viscoelastic relaxation model, after Nooner et al. (2009)

(Fig. 5.3). Velocities in the near field were 3 times faster than the secular Arabia-Nubia divergence rate over this period, similar to the velocities observed following the Krafla rifting episode (Foulger et al., 1992).

To model the deformation Nooner et al. (2009) use a 2-layer elastic-viscoelastic model. Due to the linearity of the velocity field a Maxwell rheology was used to represent the upper mantle which sits beneath an elastic crustal lid. The model was driven by the viscoelastic relaxation of the September 2005 dyke, 9 subsequent smaller intrusions and the Arabia-Nubia secular plate motions. The best-fitting model resulted in a 13.2 km elastic crust with a mantle viscosity of 5.2×10^{18}Pas, in keeping with other studies in Iceland (Foulger et al., 1992; Hofton & Foulger, 1996a,b) and Asal (Cattin et al., 2005a).

Although the model produces a reasonable fit to the horizontal velocities there is a significant misfit between the modelled and observed vertical velocity field (E. Calais, Perrs Comm 2009, Fig. 5.4). The use of GPS provides invaluable information on the temporal evolution of the velocity field. However, the sparsity of GPS sites make it difficult to

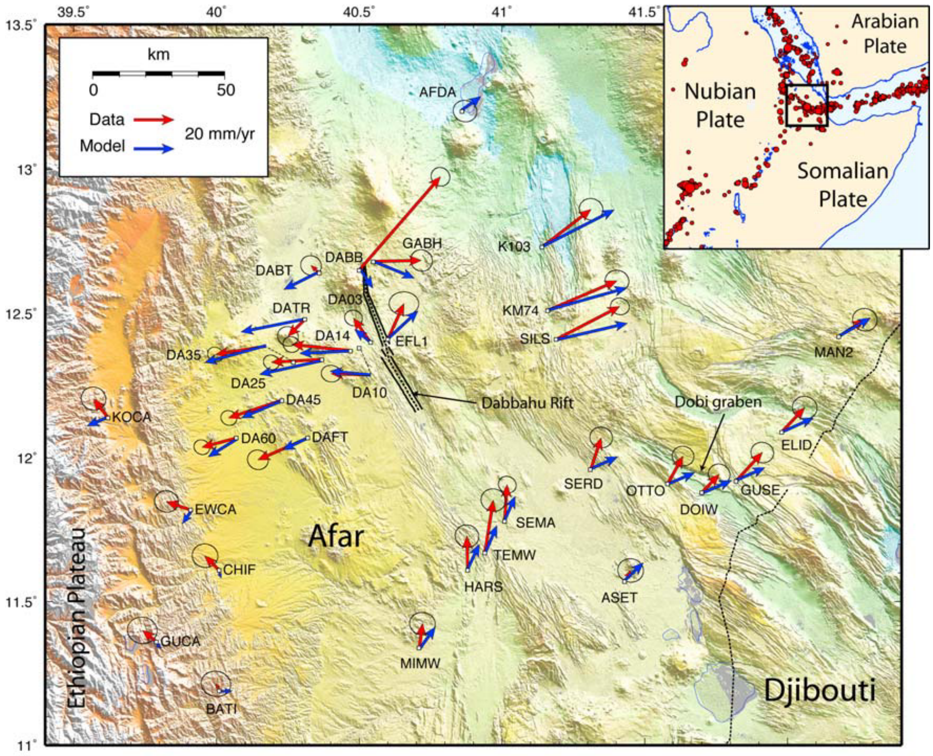

Figure 5.3: Relief map of northern Afar and study area with GPS and model results. Main figure shows the surface trace of the dike intrusions along the Dabbahu magmatic segment (black dashed line (Hamling et al., 2009; Wright et al., 2006)), along with GPS (red) velocities corrected for discrete dike offsets and best viscoelastic model velocities (blue). GPS velocities are shown with respect to the Nubian plate as defined by Stamps et al. [2008] Error ellipses associated with the GPS measurements are 95% confidence. Inset shows the location of the study area within northeastern Africa, with 1973 to present seismicity (red circles) from the NEIC database, after Nooner et al. (2009)

distinguish between post-rifting relaxation signals and the movement of magma through the Dabbahu segment. In the next section I use InSAR time series to increase the spatial resolution, unachievable with GPS alone, and provide additional constraints on the vertical deformation field.

5.3 InSAR analysis of Post-rifting deformation in Afar

Following the September 2005 rifting event regular ASAR images were acquired over the Afar region. I use three different tracks, one ascending and two descending, which cover the Dabbahu rift segment to compute a displacement time series using the algorithm described in Chapter 2. A total of 92 interferograms across all three tracks (Figs. 5.5, 5.12) were used in the analysis. Before computing the time series, all of the interferograms have

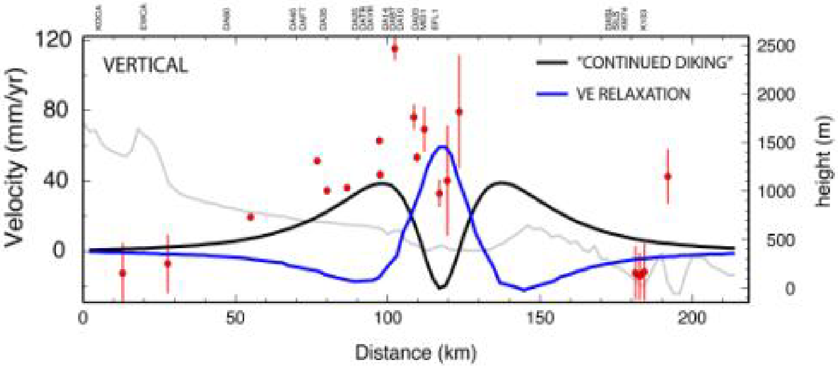

Figure 5.4: Vertical GPS displacements around the Dabbahu rift segment. Red dots are the GPS displacements projected onto a line passing through the centre of the rift segment. Blue and black lines show the predicted displacements by the continued dyking and viscoelastic relaxation models proposed by Nooner et al. (2009)

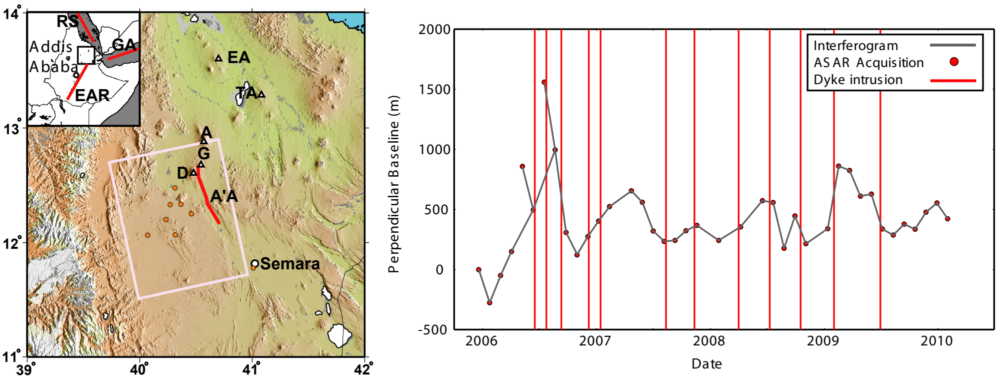

Figure 5.5: Baseline-time plot for ascending track 300. Grey solid lines represent interferograms formed for this study, red circles represent the ASAR acquisition date and the red lines represent each of the dyke intrusions

been resampled to give 360 m pixels to reduce the number of data points for the inversion.

5.3.1 Ascending track 300

The first acquisition on track 300 taken after the September 2005 dyke intrusion was on 19th December 2005. Additional images were, in general, taken every 35 days giving a total of 36 interferograms from 37 epochs between December 2005 and February 2010 (Figs. 5.5).

Using the interferograms in Figure 5.5, I solve for the best fitting displacement rate, at each time step, and for each pixel.

$$\frac{2\pi}{\lambda}\mathbf{T}\mathbf{r}_{los} = \mathbf{p} \tag{5.9}$$

where $\mathbf{p}$ is a vector containing the phase value for each interferogram at each coherent pixel, λ is the wavelength in mm and $\mathbf{T}$ is a matrix containing the time-spans for each of the interferograms. The inversion is weighted using a VCM, described in Chapter 2, accounting for atmospheric noise in each interferogram and the correlation between them. To test the effect of the smoothing on the final time series, I solve for the displacement rate with and without smoothing (Chapter 2). A comparison between the two solutions is shown in Figure 5.6. The major difference between the two solutions, not including the removal of small scale fluctuations, is that the smoothing assumes steady state deformation in time. For many geophysical applications this method is advantageous as it minimises the effects of noise in the data. However, in this study, where there has been a significant number of additional events causing discrete offsets in time, the assumption of steady state deformation breaks down such that any offset caused by a dyke intrusion will be smoothed between the epochs on either side of the intrusion event. To overcome this problem the inversion can be performed with the smoothing factor equal to zero when using the either the Laplacian smoothing or SVD methods. All of the displacement rates described in the rest of this chapter have been calculated using the SVD method due to better stability while solving without smoothing.

Comparison with GPS displacements

To validate the results from the InSAR time series analysis I compare the displacements from InSAR data with those derived from GPS. For each of the GPS stations shown in Figure 5.3 I convert the displacements into the satellites line-of-site and extract the displacement from the InSAR time series at pixels co-located with each of the GPS stations.

In general the displacements calculated by InSAR are in good agreement with the GPS (Fig. 5.7 and 5.8) and, with the exception of pixels on the two northern volcanoes (Fig. 5.8), show a linear displacement rate with time consistent with the GPS. For GPS sites DA25, DA45, DAFT and DAYR the rms misfit between the InSAR and GPS is 29, 24, 20 and 33 mm respectively. The misfits at other stations, where InSAR and GPS cover the same period, are given in Table 5.1. Some differences between the InSAR and GPS will arise due to the difference in the reference frame. All of the GPS displacements are

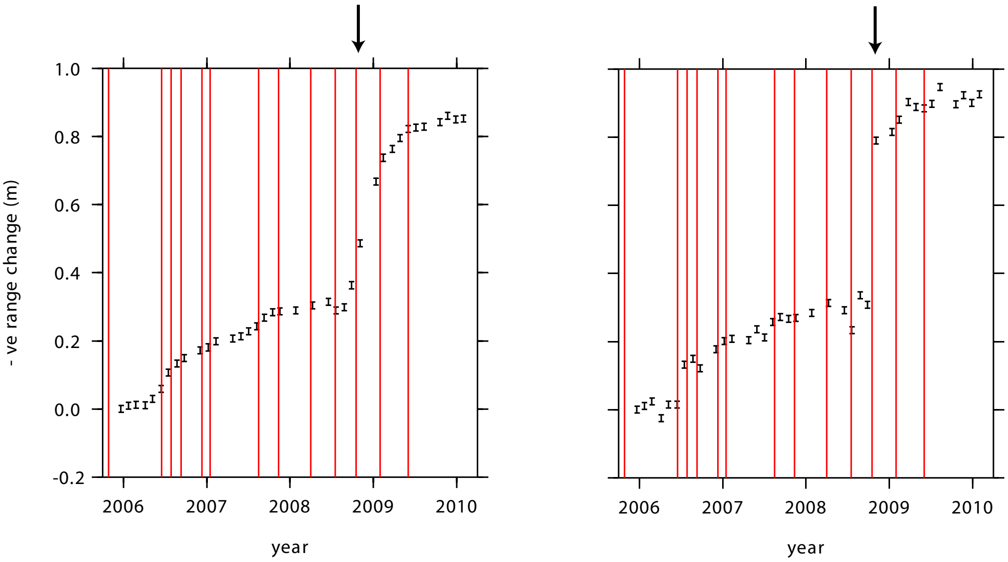

Figure 5.6: Comparison between InSAR time series with and without smoothing. InSAR displacement time series estimated at GPS site DA03 with smoothing on track 300 (*left*) and without smoothing (*right*). Red lines indicate a dyking event and the black arrow highlights the October 2008 intrusion where a large offset is observed when there is no smoothing.

calculated with respect to stable Nubia. The InSAR displacements on the other hand are relative to a reference pixel within the interferometric scene. A number of GPS sites have large data gaps, due to malfunctioning equipment or vandalism, preventing a continuous record since September 2005. Although the temporal resolution of the InSAR is limited by the frequency of acquisitions, it is able to provide a long term record of deformation from 2005 to present with relatively few gaps. This additional information allows gaps in the GPS time series to be filled to produce a continuous time series from 2005 to 2010. This is particularly useful for stations close to the rift axis, for example DA03 in Figure 5.7 which was vandalised soon after its installation, where there would be very little information to constrain the deformation in the near-field without InSAR.

Station Name	DA25	DA45	DAFT	DAYR	DA35	DA60	DABT	DATR
Misfit (mm)	29	24	20	33	8	17	17	30

Table 5.1: RMS misfits between InSAR and GPS for track 300

Estimating displacement rate from InSAR

Using the displacements calculated from the InSAR time series analysis I solve for the best fitting displacement rate, for each pixel, using a least squares matrix inversion. A

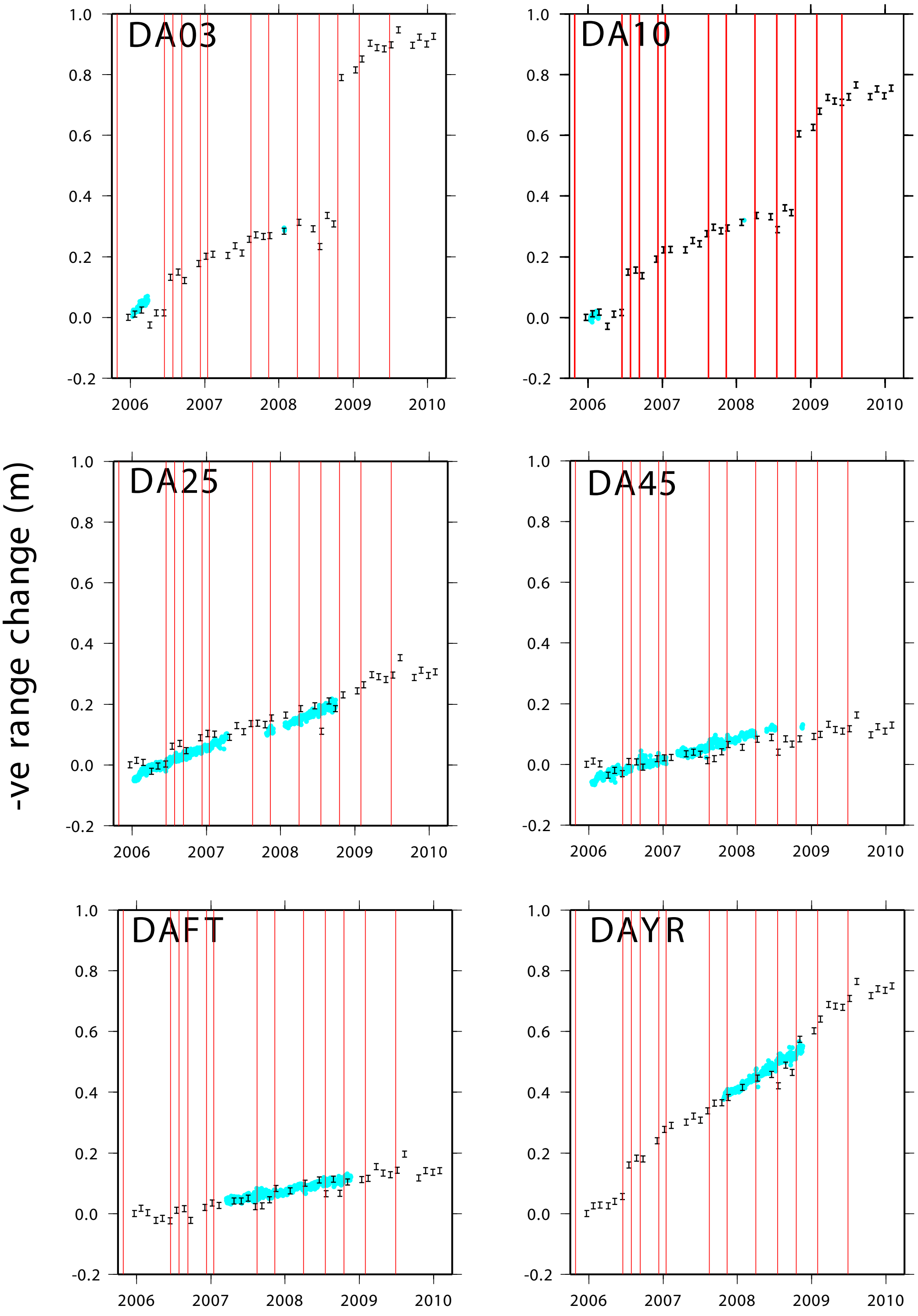

Figure 5.7: Comparison between displacement time series observed by InSAR and GPS at sites DA03, DA10, DA25, DA45, DAFT and DAYR. Blue dots show the GPS displacement projected into the satellites line of site, red lines show indicate dyking events and the black bars show the time series calculated by InSAR.

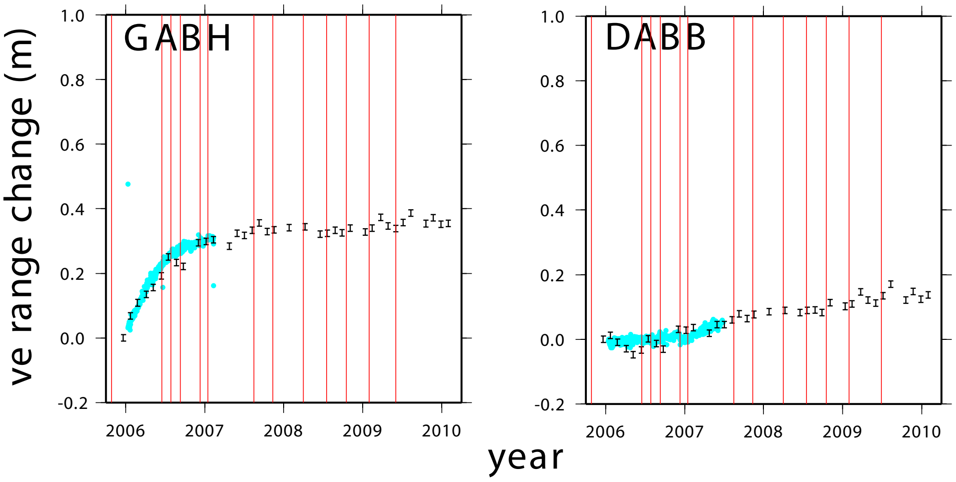

Figure 5.8: Comparison between displacement time series observed by InSAR and GPS at sites situated on the Dabbahu and Gabho volcanoes. Blue dots show the GPS displacement projected into the satellites line of site, red lines show indicate dyking events and the black bars show the time series calculated by InSAR.

number of factors must be taken into account when forming the design matrix, **A**, for the inversion. Results from both InSAR and GPS suggest that two different displacement rates for the periods before and after the June 2006 dyke intrusion. Furthermore, over the observation period an additional 12 dyke intrusions have been recorded introducing static offsets in the displacement time series. Therefore, the displacement at time t is given by

$$\begin{cases} u_t = u_{off} + r_1(t - t_0) + d_1 + ...d_n & t \leq t_{m_1} \\ u_t = u_{off} + r_1(t - t_0) + r_2(t - t_{r_1}) + d_1 + ...d_n & t > t_{m_1} \end{cases} \tag{5.10}$$

where u_t is the displacement at time t, u_{off} is an unknown offset at the beginning of the time series, r_1 is the displacement rate before June 2006, t_0 is the date of the 1st acquisition, d_n is an offset to account for each of the n dyke intrusions, r_2 is the displacement rate after the June 2006 intrusion, and t_{r_1} is the reference time of the 1st acquisition after the rate change. Writing in matrix form gives:

$$\begin{pmatrix} 1 & 0 & 0 & 0 & 0 & \cdots & 0 \\ 1 & t_1 - t_0 & 0 & 0 & 0 & \cdots & 0 \\ 1 & t_2 - t_0 & 0 & 0 & 0 & \cdots & 0 \\ 1 & t_3 - t_0 & 0 & 0 & 0 & \cdots & 0 \\ 1 & t_4 - t_0 & 0 & 0 & 0 & \cdots & 0 \\ 1 & t_5 - t_0 & 0 & 0 & 0 & \cdots & 0 \\ \vdots & \vdots & \vdots & \vdots & \vdots & \vdots & \\ 1 & 0 & 0 & 1 & 0 & \cdots & 0 \\ \vdots & \vdots & \vdots & \vdots & \vdots & \vdots & \\ 1 & 0 & t_n - t_{r_1} & 1 & 1 & 1 & 1 \end{pmatrix} \begin{pmatrix} u_{off} \\ m_1 \\ m_2 \\ d_1 \\ d_2 \\ \vdots \\ d_n \end{pmatrix} = \begin{pmatrix} 0 \\ \phi_1 \\ \phi_2 \\ \phi_3 \\ \phi_4 \\ \phi_5 \\ \vdots \\ \phi_{tr1} \\ \vdots \\ \phi_{t_n} \end{pmatrix} \tag{5.11}$$

where the second and third columns are times relating to the different displacement rate periods. The rows in the remaining columns are set as either 1 or 0 depending on whether there has been a dyke intrusion before the epoch. As a simple example consider the situation where five radar images have been acquired at times t_0, t_1, t_2, t_3 and t_4, after t_2 a dyke is intruded and subsequently the displacement rate changes. The corresponding matrix equation is then

$$\begin{pmatrix} 1 & 0 & 0 & 0 \\ 1 & t_1 - t_0 & 0 & 0 \\ 1 & 0 & t_2 - t_0 & 1 \\ 1 & 0 & t_3 - t_2 & 1 \\ 1 & 0 & t_4 - t_2 & 1 \end{pmatrix} \begin{pmatrix} u_{off} \\ m_1 \\ m_2 \\ d_1 \end{pmatrix} = \begin{pmatrix} \phi_1 \\ \phi_2 \\ \phi_3 \\ \phi_4 \end{pmatrix}. \tag{5.12}$$

The inversion is weighted using a variance-covariance matrix, Σ_r, such that equation 5.11 becomes

$$\mathbf{A}^T \Sigma^{-1} \mathbf{A} x = \mathbf{A}^T \Sigma^{-1} \mathbf{b}. \tag{5.13}$$

The results of the inversion are plotted in Figures 5.9. The spatial pattern of deformation is similar in both periods with peak displacements occurring in the centre and to the southeast of the rift segment (Figs. 5.9). In addition, during the pre-June 2006 period rapid inflation was observed at Gabho at a rate of ~40 cm/yr in the satellite's line-of-site. Pixels located close to Ado'Ale (SADA in Figure 5.9), where both uplift and westward motion is observed, show displacement rates of ~45 cm/yr while to the southeast a broad (~30 km) zone was subsiding at a rate of ~25 cm/yr. Far-field velocities at pixels colocated with GPS stations DA25, DAFT and DA60 all show movement away from the satellite during the first period which is most pronounced at DA60. Interestingly GPS, at the beginning of 2006 sites located to the north of SADA (DA03, DA10, DA14, etc) show a strong northward component to their motion before gradually becoming more east-west before the intrusion of the June 2006 dyke (Fig. 5.11). The formal errors for the ratemap are 9.9 mm/yr and 9.8 mm/yr for the first and second periods respectively with errors of ~8 mm for each of the steps associated with the dyke intrusions. The loss of coherence, especially in the vicinity and to the west of the rift axis, is a result of the June 2006 dyke intrusion. To improve the coherence, at least during the pre-June period, I split the data into two parts, pre- and post June 2006, greatly increasing the number of coherent pixels in the first period (Fig. 5.10).

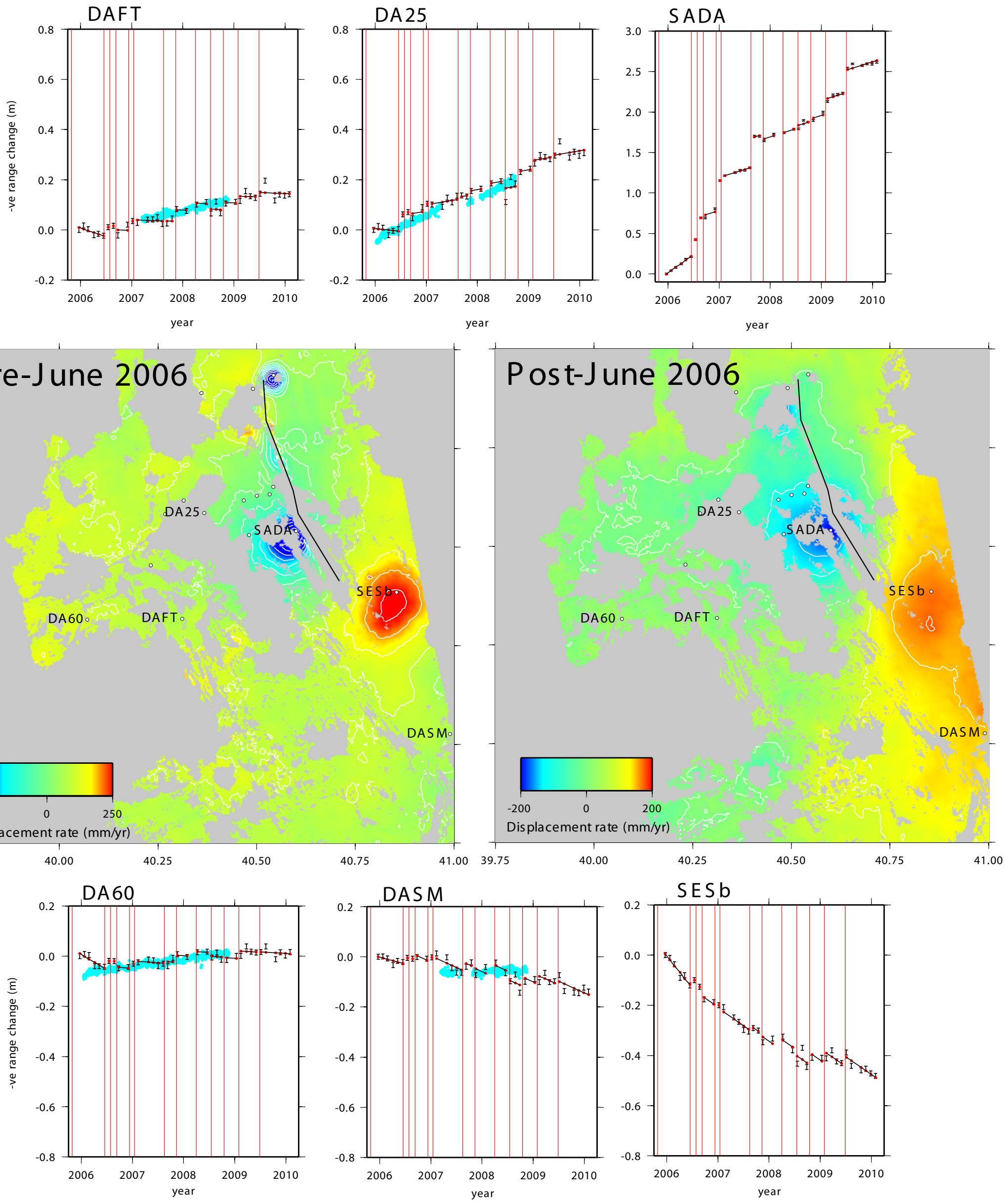

Figure 5.9: Displacement rates calculated using InSAR data from track 300 for the pre and post-June 2006 periods. Main figures show the displacement rates for all coherent pixels between December 2005 and May 2006 (*left*) and between June 2006 and February 2010 (*right*), blue colours indicate motion toward the satellite. White circles show the location of GPS sites around the rift segment. Time series for sites DA60, DAFT, DA25, SADA, SESb and DASM are plotted around the main figure. Blue dots show the displacements calculated by GPS, red lines indicate dyking events, black bars are the displacements estimated from InSAR and red dots and black lines are the predicted displacements from the inversion described above.

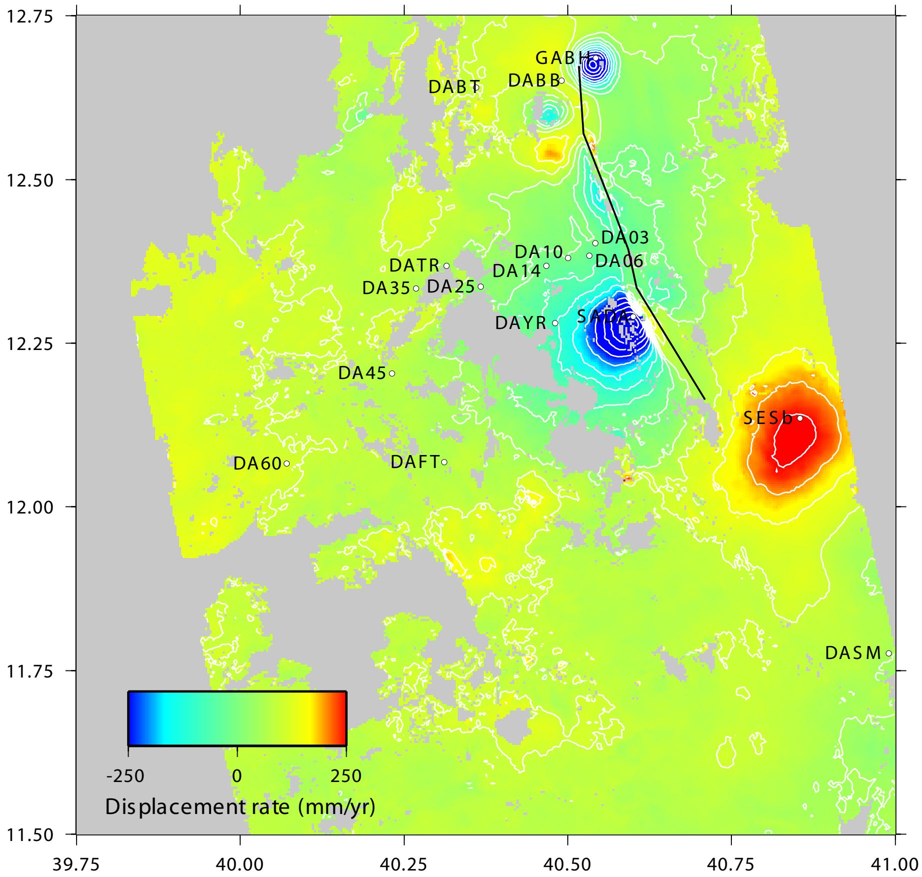

Figure 5.10: Displacement rate calculated using InSAR data from track 300 for only the pre-June 2006 period. Main figure shows the displacement rate for all coherent pixels between December 2005 and June 2006, blue colours indicate motion toward the satellite. White circles show the location of GPS sites around the rift segment.

After the June 2006 dyke intrusion peak displacements in the near field slow to ∼20 cm/yr (e.g. SADA, Fig. 5.9), similarly the rate of subsidence in the southeast also decreases to ∼14 cm/yr. Conversely, pixels away from the rift axis show an increased displacement rate, consistent with GPS observations, at rates of between ∼3.5 and 1.4 cm/yr at points located 25 (DA25) and 35 km (DA45) away from the September 2005 dyke plane. In addition, there are a number of discrete offsets caused by each of the new dyke intrusions. Although most significant in the near-field, where offsets of ∼25 cm are observed, there is still a noticeable offset at distances of ∼60 km (DA60, Fig. 5.9).

Unfortunately, due to the 1-D nature of InSAR measurements it is not possible to distinguish between horizontal and vertical deformations using a single interferometric track. The addition of GPS, which records the three dimensional displacement field, provides a method to isolate the horizontal and vertical displacements. However, this method is

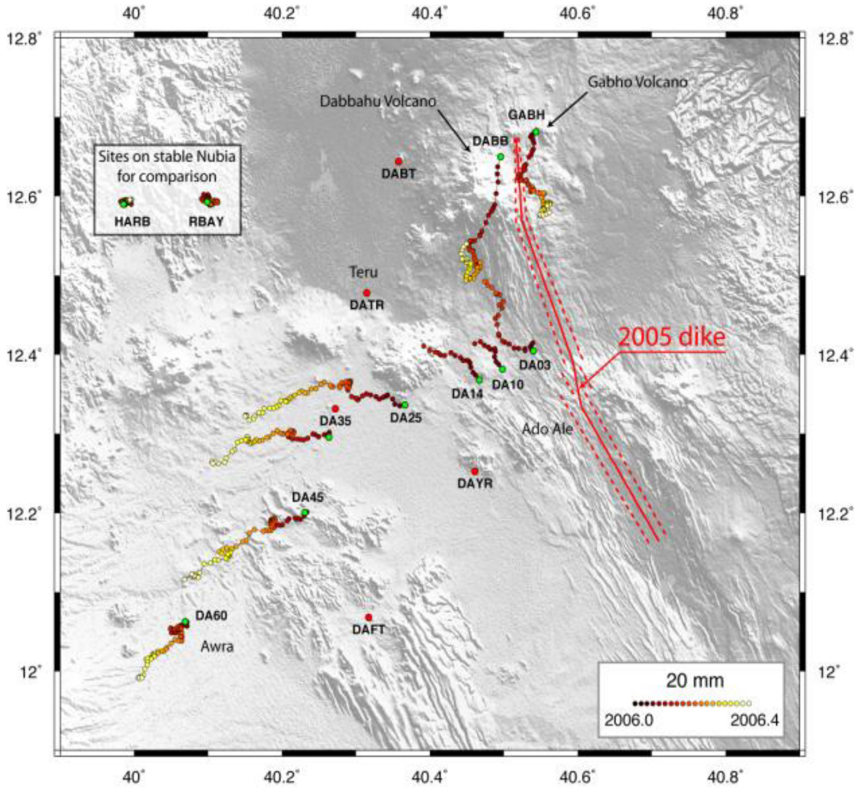

Figure 5.11: GPS site displacements between January and May 2006.

limited by the number of GPS points co-located with coherent pixels in the InSAR data. An alternative method to differentiate between the horizontal and vertical deformations is to use both ascending and descending radar images.

5.3.2 Descending tracks 49 and 464

Two descending datasets have been acquired over the Dabbahu segment, since September 2005, on tracks 49 and 464 (Fig. 5.12). The first acquisitions after the dyking event were on 2 December 2005 and 12 March 2006 respectively.

Using the same method described above I solve for the best fitting displacement rate at each pixel using a SVD inversion scheme. As before I solve for two displacement rates, corresponding to the pre and post June 2006 periods, and static offsets caused by new dyking. The results of the inversion are shown in Figures 5.13 and 5.14, as with the ascending track the displacement time series calculated using InSAR is consistent with GPS for both descending tracks (Table 5.2). Unfortunately, coherence is lost on track 49 due to a large temporal baseline between May 2006 and May 2007 and thus prevents a comparison with a large number of GPS sites located to the west of the rift axis. For

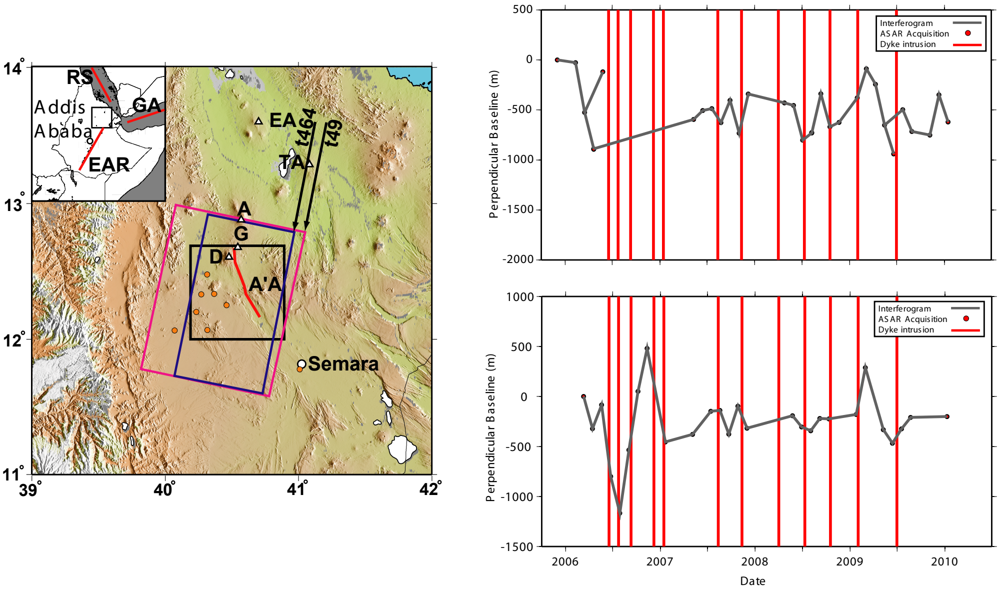

Figure 5.12: Baseline-time plot for descending tracks 49 and 464. Grey solid lines represent interferograms formed for this study, red circles represent the ASAR acquisition date and the red lines represent each of the dyke intrusions

coherent pixels, similar displacement rates are observed with peak rates occurring close to the rift axis near the Ado'Ale volcanic complex, on track 49 the subsiding region to the southeast of the rift segment (Fig. 5.14) shows a similar displacement rate to that observed in the ascending data set. Formal errors for the displacement rates are 33.1 and 12.2 mm/yr on track 464 and 9.9 and 13 mm/yr on track 49 respectively. The large error in the displacement rate for the pre-June period on track 464 is a result of there being only three images acquired during this time.

Station Name	DA25	DA45	DAFT	DAYR	DA35	DABT	DATR
Track 464 Misfit (mm)	19	15	14	10	22	13	14
Track 049 Misfit (mm)	28	15	20	36	21	24	25

Table 5.2: RMS misfits between InSAR and GPS for track 300

5.3.3 Separating horizontal and vertical deformations

By combining both ascending and descending SAR data it is possible, with certain assumptions, to retrieve the horizontal and vertical components of the displacement field by solving the following equation

$$\begin{pmatrix} los_{xd} & los_{yd} & los_{zd} \\ los_{xa} & los_{ya} & los_{za} \end{pmatrix} \begin{pmatrix} u_x \\ u_y \\ u_z \end{pmatrix} = \begin{pmatrix} r_d \\ r_a \end{pmatrix} \tag{5.14}$$

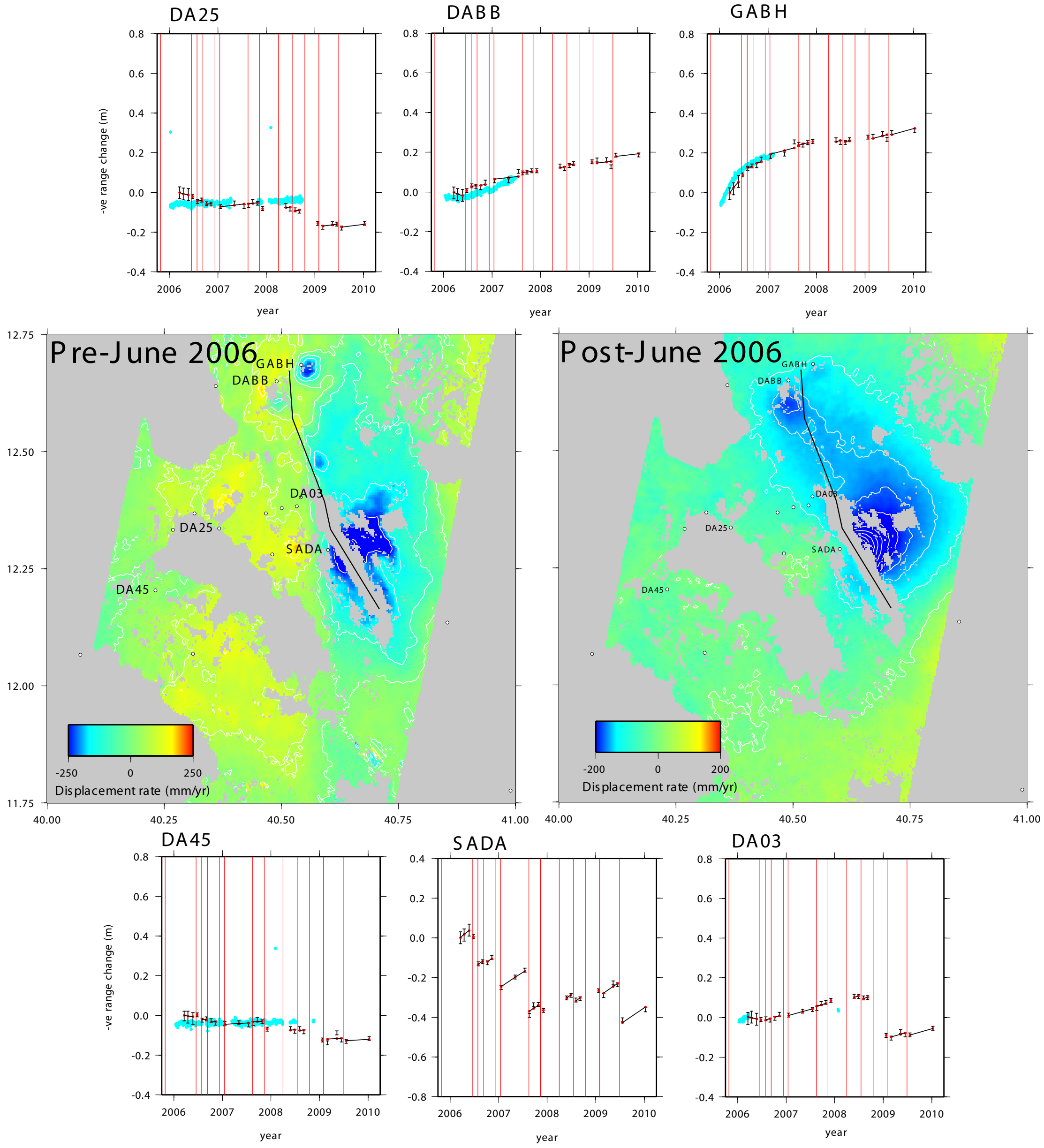

Figure 5.13: Displacement rates calculated using InSAR data from track 464 for the pre and post-June 2006 period. Main figures show the displacement rates for all coherent pixels between December 2005 and May 2006 (*left*) and June 2006 and February 2010 (*right*), blue colours indicate motion toward the satellite. White circles show the location of GPS sites around the rift segment. Time series for sites DA45, DA25, DABB, GABH, DA03 and SADA are plotted around the main figure. Blue dots show the displacements calculated by GPS, red lines indicate dyking events, black bars are the displacements estimated from InSAR and red dots and black lines are the predicted displacements from the inversion described above.

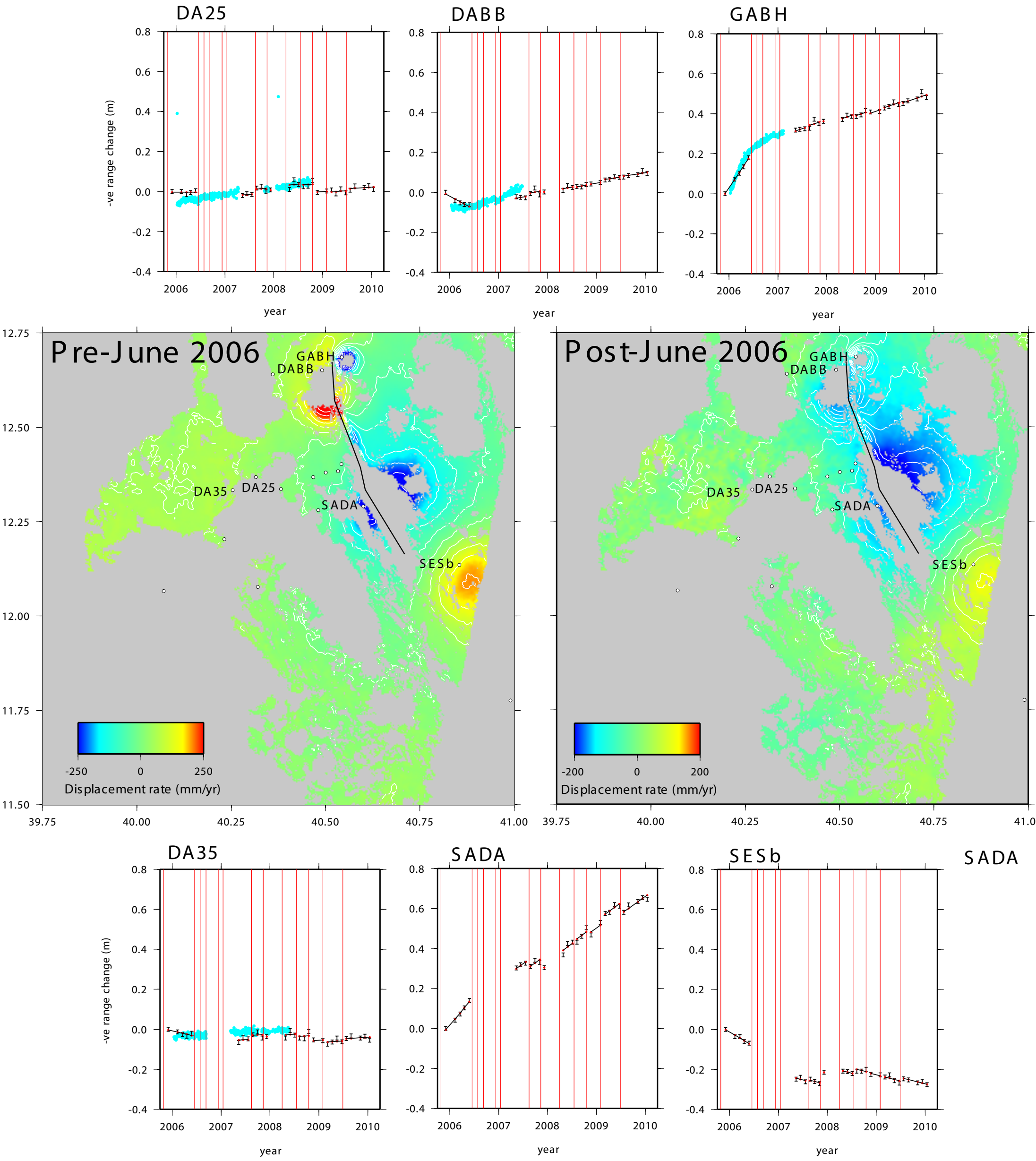

Figure 5.14: Displacement rates calculated using InSAR data from track 49 for the pre and post-June 2006 periods. Main figures show the displacement rates for all coherent pixels between December 2005 and May 2006 (*left*) and June 2006 and February 2010 (*right*), blue colours indicate motion toward the satellite. White circles show the location of GPS sites around the rift segment. Time series for sites DA45, DA25, DABB, GABH, SADA and SESb are plotted around the main figure. Blue dots show the displacements calculated by GPS, red lines indicate dyking events, black bars are the displacements estimated from InSAR and red dots and black lines are the predicted displacements from the inversion described above.

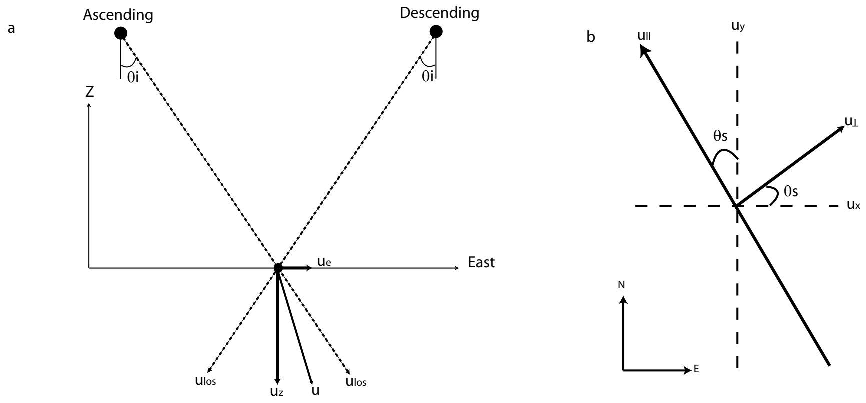

Figure 5.15: Geometry for separating the horizontal and vertical components of the displacement field. *a*: Geometry for the case where there is no northward component to the displacement. *b* Geometry for the Afar case where deformation is assumed to be only vertical and rift perpendicular.

where los_x, los_y and los_z are the three components of the satellites looking vector for the ascending ($_a$) and descending ($_d$) passes, u_x, u_y and u_z are the three components of the surface displacement and r is the range change measured by the satellite. However, because there are three unknowns and only two equations I need additional assumptions. Assuming that the viewing geometry for both the ascending and descending passes has no northward component (Fig. 5.15a) then this equation can be reduced by setting $u_y = 0$ as shown by Wright et al. (2004d) for the Nenana earthquake. Alternatively, around the Dabbahu segment, where the majority of deformation is perpendicular to the rift and vertical, Equation 5.14 can be modified to retrieve the vertical, u_z, and rift perpendicular, $u_{r\perp}$ displacements by assuming that $u_y = los_{ya} \tan\theta_s u_x$ where θ_s is the angle between the rift segment and north ($\sim 25°$). For the geometry in Figure 5.15b the range change for the ascending and descending interferograms is then

$$r_a = los_{xa}u_x + los_{ya}\tan\theta_s u_x + los_{za}u_z \tag{5.15}$$

and

$$r_d = los_{xd}u_x + los_{yd}\tan\theta_s u_x + los_{zd}u_z, \tag{5.16}$$

Therefore, the rift perpendicular and vertical displacements can be retrieved by solving the following equation using a least squares inversion which is weighted using a variance-covariance matrix based on the errors for the individual displacement rates on the ascending and descending data sets.

$$\begin{pmatrix} \cos\theta_s(los_{xd} + \tan\theta_s los_{yd}) + los_{zd} \\ \cos\theta_s(los_{xa} + \tan\theta_s los_{ya}) + los_{za} \end{pmatrix} \begin{pmatrix} u_{r\perp} \\ u_z \end{pmatrix} = \begin{pmatrix} r_d \\ r_a \end{pmatrix} \tag{5.17}$$

In order to retrieve the horizontal and vertical components of the deformation pixels in both ascending and descending data sets must be coherent. Therefore, to maximise the number of coherent pixels I perform the inversion using tracks 300 and 464. Because the first acquisition, after the September 2005 dyke intrusion, on track 464 is 4 months after the acquisition on track 300 I use only data acquired after the June 2006 dyke. The results of the inversion are plotted in Figure 5.16. The calculated displacements represent the total rift perpendicular and vertical displacements, assuming the linear rates calculated earlier for this period with all of the dyking events removed, between June 2006 and January 2010 referenced to a pixel located at 40.15E, 12.58N in the southwest of the scene.

The deformation is concentrated around the rift segment with the largest displacements occurring in the vicinity of Ado'Ale. Rift perpendicular displacements range from $\sim$0.45 m $\pm$0.064 west of the rift axis to $\sim$0.6 m $\pm$0.064 in the east with peak displacements occurring $\sim$20 km from the rift axis (Fig. 5.16). Horizontal displacements north of Ado'Ale are generally smaller with $\sim$10-20 cm of displacement. Displacements across profile A-A', in Figure 5.16, show eastward motion on the western flank of the rift segment. In the vertical, uplift is observed along most of the rift segment over a broad $\sim$50 km zone. Peak displacements of $\sim$0.75 m $\pm$0.032 are observed around Ado'Ale and, to the southeast of the segment, approximately 0.5 m of subsidence is observed (Fig. 5.16). However, due to the viewing geometry of the descending track this mostly falls outside of the scene. At the north of the segment $\sim$6 cm of uplift is observed at Gabho volcano with a further $\sim$40 cm at Dabbahu. The rift axis, to the north of Ado'Ale, where opening of the September 2005 dyke was largest also uplifts during this period by $\sim$15-20 cm.

A comparison between the rift perpendicular and vertical displacements calculated by InSAR and GPS is shown in Figure 5.17. GPS sites close to the rift segment have been omitted from the comparison as the measurement error was >1000 mm. For the rift perpendicular displacements, a good agreement is found between InSAR and GPS with a correlation coefficient of 0.8. The fit to the vertical displacements, however, shows a number of differences. In general, the difference between the InSAR and the GPS is $\sim$20-30 mm/yr with the GPS consistently showing a higher rate than the InSAR. The difference between the two measurements may be down to a number of factors. The InSAR displacements are relative to a pixel to the southwest of the rift segment whilst the GPS is referenced to stable Nubia. Also, when calculating the rift perpendicular

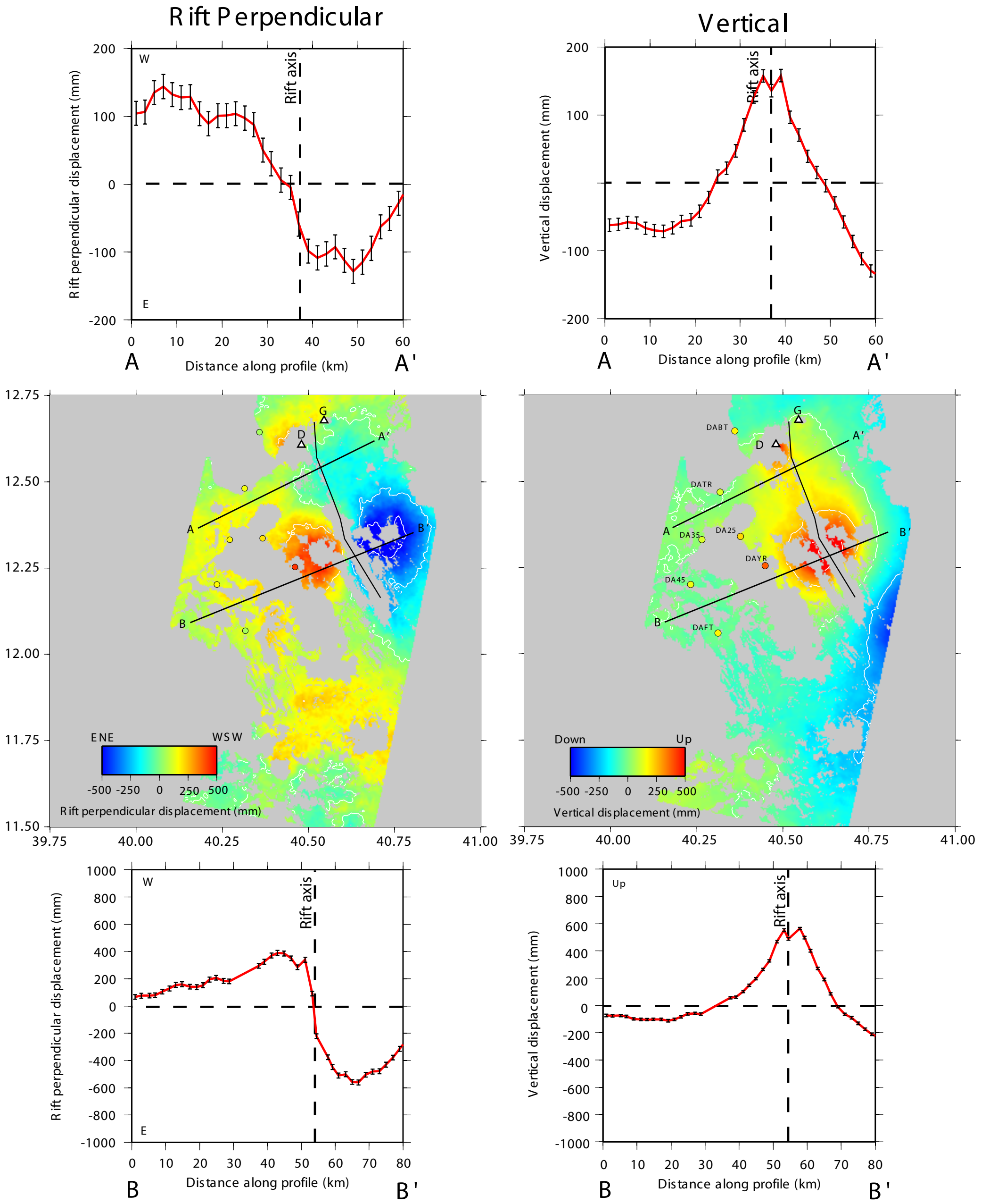

Figure 5.16: Rift perpendicular and vertical displacements between June 2006 and January 2010. White triangles represent Dabbahu (D) and Gabho (G) volcanoes, white circles show the location of GPS sites around the rift segment. *Top* and *bottom*: Displacement profiles along A-A' and B-B'

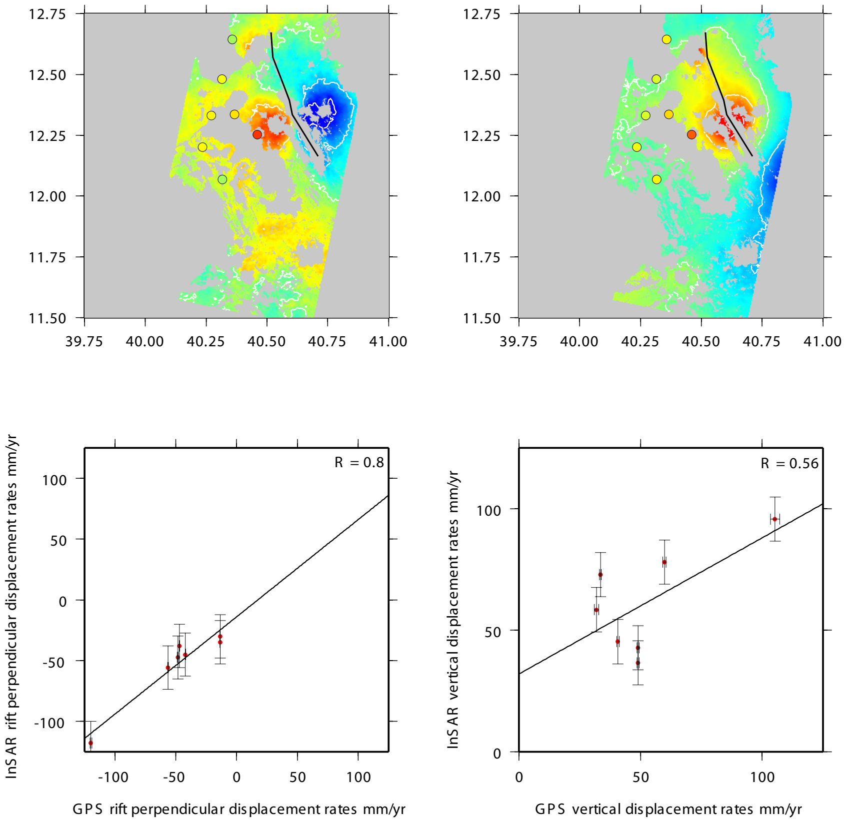

Figure 5.17: Comparison between rift perpendicular and vertical displacements calculated using InSAR and GPS. *Top left*: Rift perpendicular displacements calculated using InSAR with GPS site displacements projected onto map. *Top right*: Vertical displacements calculated using InSAR with GPS site displacements projected onto map. *Bottom left*: Correlation between the rift perpendicular displacements calculated by InSAR and GPS with error bars. *Bottom right*: Correlation between the vertical displacements calculated by InSAR and GPS with error bars.

and vertical displacements some of the rift parallel component is mapped into the vertical displacements. In order to adjust the InSAR displacements, such that they are in the Nubia reference frame, I invert for a best fitting plane and offset for both the rift perpendicular and vertical displacement fields. As a result, the fit to the rift perpendicular is improved with all of the colcated GPS displacements falling within the error bounds of the InSAR (±9 mm). However, despite the reference frame shift there is little improvement to the fit between the InSAR and GPS vertical displacement rates.

5.4 Modelling of Post-rifting deformation in Afar

As discussed in Section 5.2, the GPS and InSAR results following the September 2005 rifting event are, at least in these early stages of the post-rifting cycle, linear in time enabling the use of a Maxwell rheology to model the post-rifting deformation. I use a two-layered, semi-analytic, elastic-viscoelastic model developed by Yukitoshi Fukuhata. Based on the solutions given by Fukahata & Matsu'ura (2005, 2006) and Hashima et al. (2008) the code computes the viscoelastic deformation resulting from a finite rectangular dislocation. Each layer is assumed to be isotropic, homogeneous and either elastic or viscoelastic with the viscoelastic rheology being Maxwell in shear and elastic in bulk. The stress, σ, in the elastic layers is then

$$\sigma_{ij} = \lambda_l \epsilon_{kk} \delta_{ij} + 2\mu_l \epsilon_{ij} \tag{5.18}$$

and for viscoelastic layers

$$\dot{\sigma}_{ij} + \frac{\mu_l}{\eta_l}\left(\sigma_{ij} - \frac{1}{3}\sigma_{kk}\delta_{ij}\right) = \lambda_l \dot{\epsilon}_{kk}\delta_{ij} + 2\mu_l \dot{\epsilon}_{ij}, \tag{5.19}$$

where σ_{ij} and ϵ_{ij} are the stress and strain tensors, respectively, λ_l and μ_l are Lamés constants in the lth layer and η_l is the viscosity in the lth layer. To solve the viscoelastic problem the Laplace transform of Equation of 5.19 is taken giving

$$\tilde{\sigma}_{ij} = \hat{\lambda}_l(s)\tilde{\epsilon}_{kk}\delta_{ij} + 2\hat{\mu}_l(s)\tilde{\epsilon}_{ij} \tag{5.20}$$

where

$$\hat{\lambda}_l(s) = \frac{\lambda_l \tau_l s + K_l}{\tau_l s + 1}, \hat{\mu}_l(s) = \frac{\tau_l s \mu_l}{\tau_l s + 1} \tag{5.21}$$

and

$$\tau_l = \frac{\eta_l}{\mu_l} \tag{5.22}$$

K_l is the bulk modulus in the lth layer and s is the Laplace transform variable. Applying the correspondence principle of linear viscoelasticity (e.g. Lee, 1955; Morland & Lee, 1960), which states that under the same boundary conditions and in the same geometry the solution of a linear viscoelastic problem is analogous to that of an elastic body, the viscoelastic solution is directly obtained from the elastic solution. Direct comparison between Equations 5.18 and 5.20 shows that the Laplace transform of Equation 5.19 is formally identical to equation 5.18. Replacing the source time function with its Laplace transform, the elastic constants with the s-dependent moduli (Equation 5.21) and performing an inverse Laplace transform on the s-dependent solution then yields the viscoelastic solution

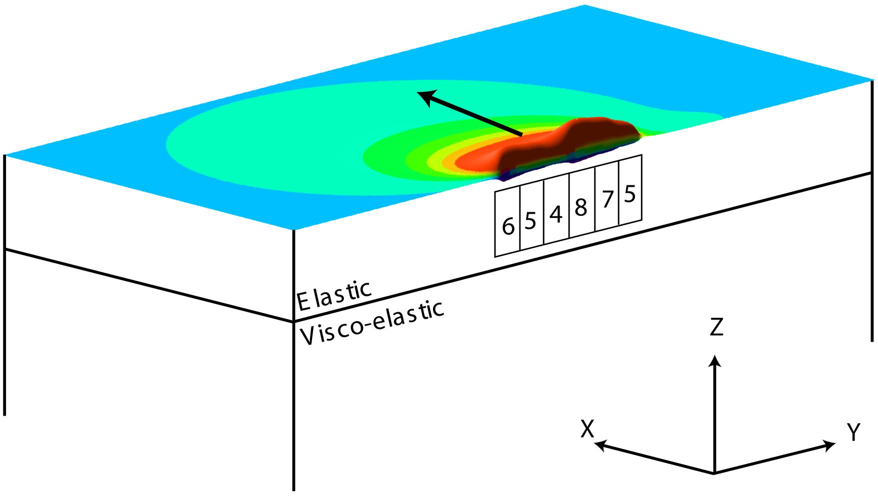

Figure 5.18: Viscoelastic model setup. Rectangular patches represent dyke opening in the X direction by the amount indicated at the centre of each patch.

(Fukahata & Matsu'ura, 2006).

5.4.1 Model setup

The source model is composed of six 10 km segments extending from 1-9 km depth to represent the opening distribution from the September 2005 dyke (Fig. 5.18). For all of the model calculations I use elastic parameters based on seismic data (Makris & Ginzburg, 1987) (Table 5.3) for both the elastic and viscoelastic layers.

Layer	V_p (m/s)	V_s (m/s)	Density (kg/m^3)
1	5.35	2.95	2600
2	7.1	3.7	3000

Table 5.3: Elastic properties used in the viscoelastic model

Using the parameters shown in Table 5.3 and the opening distribution shown in Figure 5.18 I generate a set of forward models with different elastic lid thicknesses (10-20 km) and viscosities (10^{17} - 10^{19} Pas) and compare the results with the InSAR observations by calculating the root mean square error.

$$D_{rms} = \sqrt{\frac{1}{N}\sum(d_{obs} - d_{mod})^2} \tag{5.23}$$

where d_{obs} and d_{mod} are the observations and model predictions respectively and N is the number of data points. Due to limitations in the code it was not possible to simulate the desired opening distribution in a single model run. However, due to the linear relationship between opening and surface displacement I was able to assemble the opening distribution by stitching a series of smaller dykes, with 1 m of opening, together and multiply each to give the distribution in Figure 5.18. For example, summing the surface displacements of two 10 km long dykes is equivalent to the surface displacement resulting from a 20 km-long dyke with the same opening.

Figures 5.19 and 5.20 show the observed rift perpendicular and vertical displacements for a range of lid thicknesses and viscosities of 10^{18} and $10^{18.5}$ Pas.

From Figures 5.19-5.20 the effect of the lid thickness and viscosity can be assessed. Changing the thickness of the elastic lid affects the rift perpendicular and vertical displacements in different ways. Displacements perpendicular to the rift decrease as the lid is thickened from 10 to 20 km (Fig. 5.19) whilst the vertical displacement increases with lid thickness (Fig. 5.19). For the example shown in Figure 5.19, the rift perpendicular component of the deformation is best approximated with a lid thickness of 17-20 km. Displacement profiles taken through the northern section of the rift and through the Ado'Ale region, however, show a significant difference in magnitude and wavelength along the rift's length. Along profile A, in Figure 5.19, the magnitude and wavelength of the deformation are best approximated with an elastic lid of 18 km, if a thinner elastic lid is used then the model over estimates the magnitude. Conversely, the displacements along profile B require a model with a thin lid to fit the observed magnitude but there is a significant misfit between the wavelengths of the deformation. Unlike the rift perpendicular displacements, which required a thick lid, the vertical deformation along profile A is best modelled with a lid thickness of 13 km. However, as with the rift perpendicular component, the model is unable to fit the vertical displacements along profile B. Increasing the lid thickness produces a better fit along this section of the rift segment but causes a significant misfit elsewhere.

Increasing the viscosity of the viscoelastic half-space from 10^{18} to $10^{18.5}$ Pas reduces the magnitude of the displacements for both the rift perpendicular and vertical components (Fig. 5.20). In this case displacement along profile B are significantly underestimated regardless of the lid thickness. Unlike the examples in Figure 5.19, using a viscosity of $10^{18.5}$ Pas to fit the rift perpendicular displacements requires a thin (12-13 km) lid while the the vertical is best approximated with a 16-17 km thick lid.

In order to determine the best fitting model the rms for each model is plotted in Figure

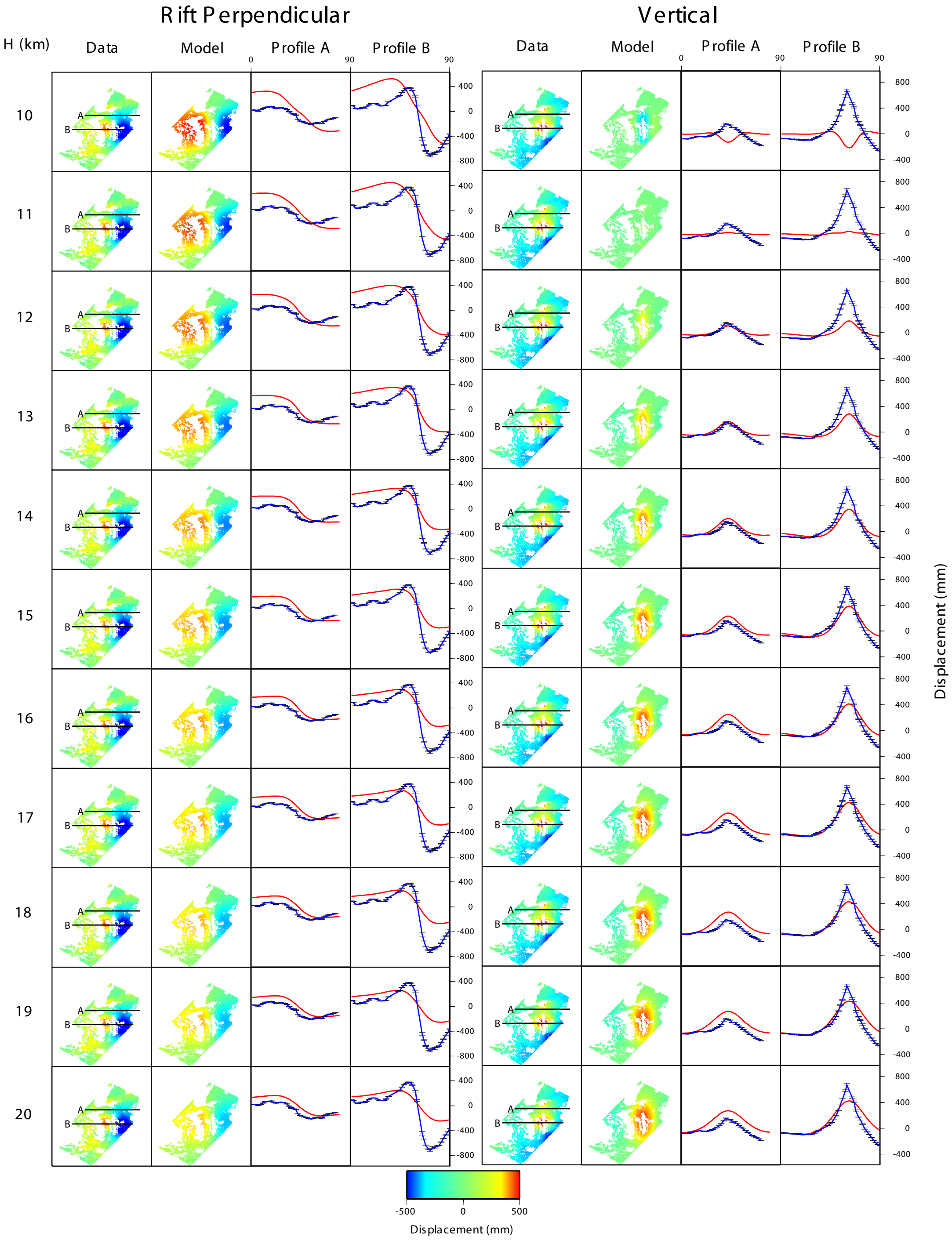

Figure 5.19: Rift perpendicular and vertical displacements for a set of forward models with varying elastic lid thicknesses and a viscosity of 10^{18} Pas. Left hand panels show the observed and modelled displacements with two profiles (*A-A'* and *B-B'*) shown in the right hand panels

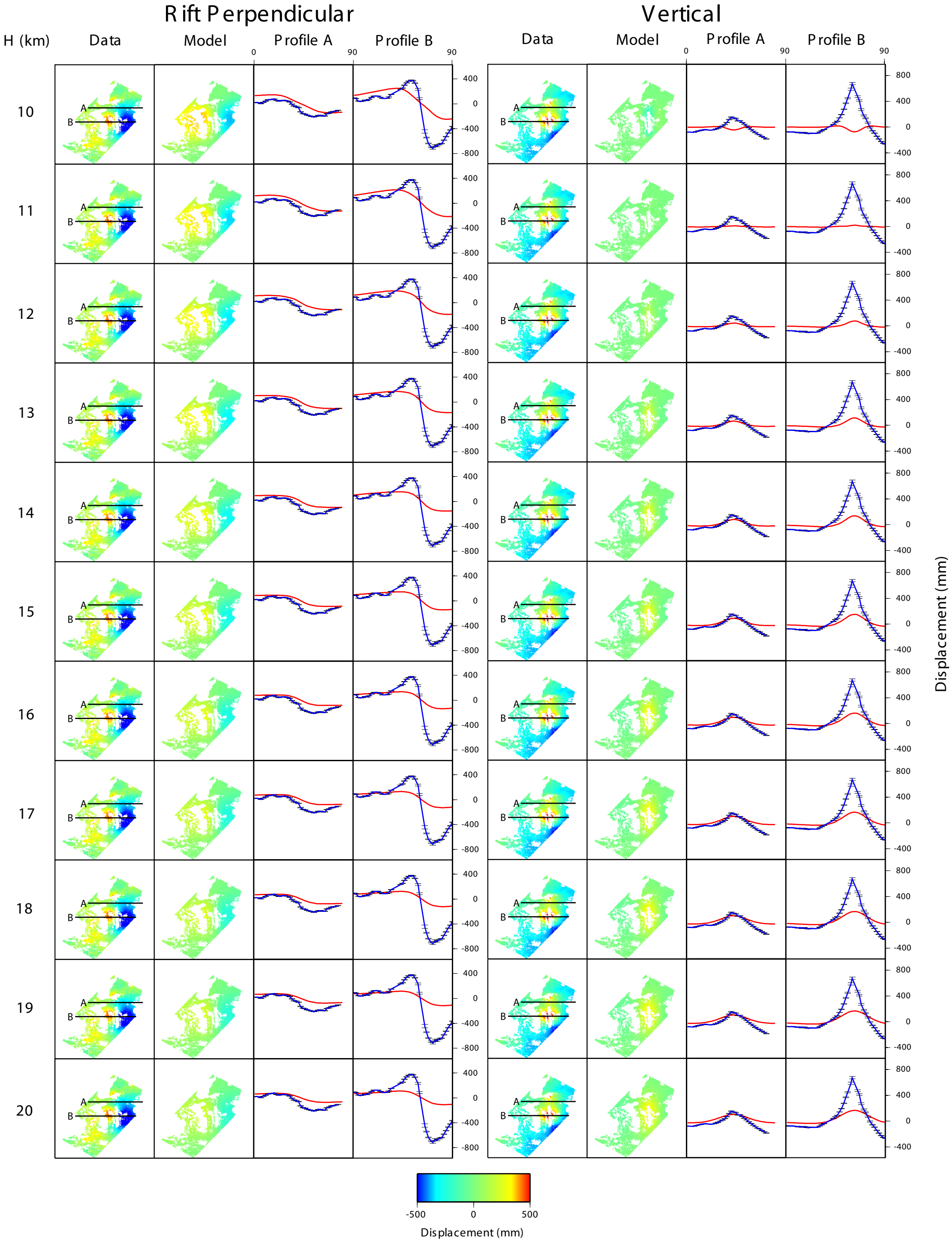

Figure 5.20: Rift perpendicular and vertical displacements for a set of forward models with varying elastic lid thicknesses and a viscosity of $10^{18.5}$ Pas. Left hand panels show the observed and modelled displacements with two profiles (*A-A'* and *B-B'*) shown in the right hand panels

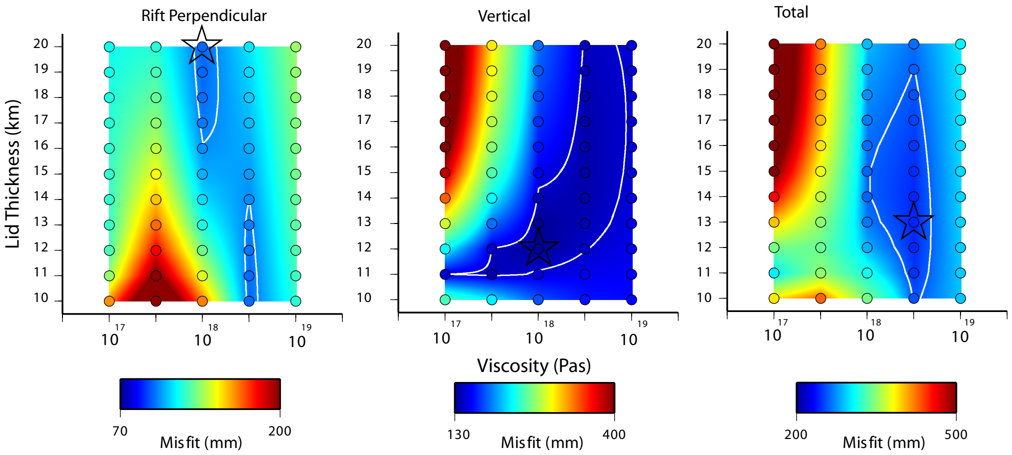

Figure 5.21: rms misfit for a range of viscoelastic forward models with varying viscosities and elastic lid thicknesses. *Left*: Misfit between modelled and observed rift perpendicular displacements. *Centre*: Misfit between modelled and observed vertical displacements. *Right*: Misfit between modelled and observed total displacement. In each case the star shows the location of the best fitting model, the white line marks the region of acceptable models based on the minimum misfit plus 5%

5.21. In the case of the rift perpendicular displacements there is a strong tradeoff between lid thickness and viscosity. An equally good fit is achieved with either a thick lid (19-20 km) and a lower viscosity (10^{18} Pas) or a thin lid (11-12 km) with a higher viscosity of $10^{18.5}$ Pas. For the vertical displacements, however, the best fitting model is obtained with a thin elastic lid and a low viscosity between 10^{17} and 10^{18} Pas.

Unfortunately the best fitting models for the rift perpendicular and vertical displacements do not agree. Therefore, to find the best fitting model I re-calculate the misfit to the total displacement by summing the misfits for the rift perpendicular and vertical displacements (Fig. 5.21). Combining the rift perpendicular and vertical displacements results in a best fitting model with a lid thickness of 13 km and a viscosity of $10^{18.5}$ Pas giving an rms misfit to the rift perpendicular, vertical and total displacements of ~98, ~130 and ~234 mm respectively (Fig. 5.22). However, it should be noted that similar misfits are found with a range of lid thicknesses from 10-19 km and with viscosities of 10^{18} - $10^{18.5}$ Pas.

It is evident from the residual plots shown in Figure 5.22 that there are a number of deforming areas around the rift segment which cannot be explained by this simple viscoelastic model. Rift perpendicular displacements are, in general, underestimated by the model and do not show the asymmetry observed about the rifts axis. Similarly, vertical displacements are underestimated and have large residuals (~500 mm) around the Ado'Ale volcanic complex. Furthermore, the region of subsidence to the southeast of the rift segment is not predicted by the model. To investigate this further I have taken a series of

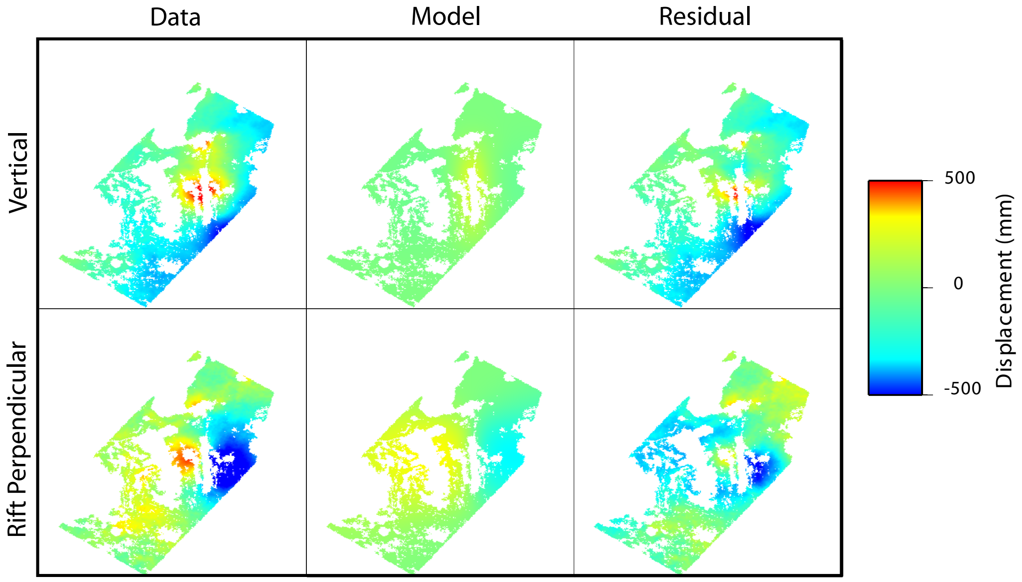

Figure 5.22: Best fitting viscoelastic model consisting of a 13 km thick elastic lid overlying a viscoelastic half-space with a viscosity of $10^{18.5}$. *Left*: Observed rift perpendicular and vertical displacements. *Centre*: Modelled rift perpendicular and vertical displacements. *Right*: Residual rift perpendicular and vertical displacements.

profiles through both the modelled and observed displacements (Fig. 5.23). In general, the modelled rift perpendicular displacements along profiles which cross the northern section of the rift segment (*A-A'* and *B-B'*) are in good agreement with the data. However, the vertical displacements are underestimated by the model along the same profiles. Across the centre of the segment (*C-C'*) there is a significant misfit between the modelled and observed displacements for both the rift perpendicular and vertical components. Unlike the observed displacement field, which shows deformation concentrated around Ado'Ale and to the southeast of the segment, the model predicts a much more uniform displacement field. This is most evident in profiles *C-C'*-*F-F'* where large differences are observed between the model and data.

5.5 Discussion

In this Chapter I have used InSAR time series to calculate the displacement rate around the Dabbahu rift segment and used a simple two-layered viscoelastic model to estimate the thickness of the elastic crust and viscosity of the underlying mantle. Using interferograms on both ascending and descending passes has enabled me to separate the rift perpendicular and vertical components of the deformation which have been used to compare with displacements predicted by the model.

The pattern of deformation around the Dabbahu segment since June 2006 shows a number of features which cannot be explained by the viscoelastic model described above. Although the model is able to predict the displacement around the northern section of the rift segment it is unable to reproduce the large displacements which have been observed around Ado'Ale. This is highlighted in profiles *C-C'* and *E-E'* which run perpendicular and parallel to the strike of the rift axis respectively (Fig. 5.23). In profile *C-C'* the model displacement is symmetric about the rift axis and predicts peak displacements of ∼200 mm and ∼150 mm for the rift perpendicular and vertical components (Table 5.4). The observed deformation, however, shows strong asymmetry across the rift axis and has peak displacements of ∼400 mm and ∼800 mm for the same two components. Similarly, modelled displacements along profile *E-E'* show a broad long wavelength signal while the observed deformation is ∼3 times larger and has a short wavelength peak displacement centred around Ado'Ale.

Profile	A-A'	B-B'	C-C'	D-D'	E-E'	G-G'
Rift perpendicular (mm)	53	62	351	212	110	171
Vertical (mm)	112	148	314	168	158	272

Table 5.4: RMS misfits between observed and modelled displacements

Despite the poor fit to the data the model provides some useful insights into the post-rifting processes which are ongoing around the Dabbahu segment. The large amounts of vertical deformation around Ado'Ale and the fact that the same area has been the origin of the sequence of dyke intrusions since June 2006 strongly suggests that much of this deformation is the result of magma accumulation rather than viscoelastic relaxation. Similarly the region to the southeast of the segment which began to subside following the 2005 rifting event cannot be explained by relaxation processes and must be the result of magma flowing at depth, most likely towards the Dabbahu segment. The fact that there is good agreement with the modelled displacements in the north of the segment, in an area which has been unaffected by new dyking, suggest that some relaxation processes may be occurring but are largely masked by large magnitude magmatic processes in the near-field. The best-fitting model presented here suggests a 13 km thick elastic crust overlying a mantle with a viscosity of $10^{18.5}$ Pas, similar to the result of Nooner et al. (2009) and to that reported in Iceland (Foulger et al., 1992; Hofton & Foulger, 1996a,b) and Asal (Cattin et al., 2005a).

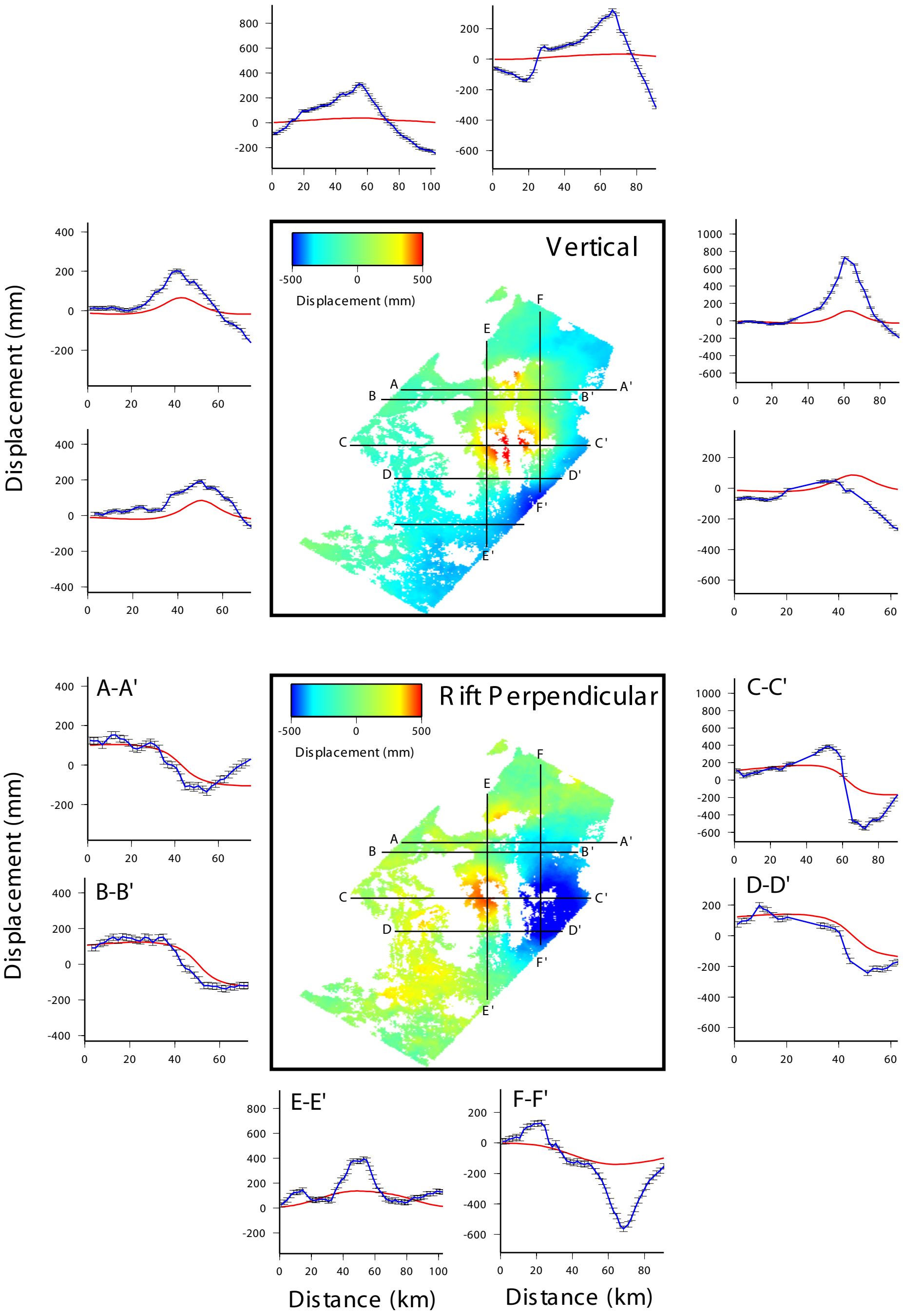

Figure 5.23: Rift perpendicular and vertical displacement profiles taken through the data and best fit model. Profile lines are shown in the middle panels, red lines indicate the modelled displacements and blue lines are the data for the corresponding profile.

Chapter 6

Discussion and Conclusions

This thesis documents the deformation associated with an ongoing rifting episode in Afar, Ethiopia. Using InSAR and GPS data I have modelled a sequence of twelve dyke intrusions emplaced between June 2006 and July 2009 (Chapter 3). Using elastic dislocation models I have determined the amount of dyke opening and estimated the volume of material intruded during each discrete event. Using these models I have presented a unique study linking the location of magmatic intrusions with dyke-induced stress changes and have shown a link between Coulomb stress change and dyke induced seismicity (Chapter 4). Finally, I have constructed an InSAR timeseries to calculate displacement rates around the rift segment and used viscoelastic relaxation models to compare with InSAR observations.

6.1 The Dabbahu Rifting episode, 2005 - ???

The September 2005 dyke intrusion, which ruptured the remote Dabbahu rift segment in Northern Ethiopia, marked the beginning of an ongoing rifting episode. Using Satellite Radar interferometry Wright et al. (2006) suggested a 60-km-long dyke intrusion with a maximum opening of 8 m and intruded volume of 2-2.5 km^3 (Grandin et al., 2009; Wright et al., 2006). Subsidence at Dabbahu and Gabho volcanoes suggested that the intrusion was fed from the north of the segment and propagated south, however, re-analysis of seismicity associated with the intrusions by Ayele et al. (2009) has shown three distinct feeding zones. Seismicity began beneath Dabbahu and Gabho before jumping to the Ado'Ale complex from which the dyke propagated both north and south.

Since September 2005 a sequence of twelve dyke intrusions have been observed in the vicinity and to the south of Ado'Ale. The sequence began in June 2006 with a 10-km-long, ~2 m wide intrusion originating from Ado'Ale before propagating to the north (Hamling et al., 2009; Keir et al., 2009). A further 4 dykes were emplaced between July 2006 and January 2007 intruding between ~0.05 and 0.1 km of material. In August 2007 a dyke intrusion ruptured the surface to the south of Ado'Ale causing a <0.004 km^3 fissural flow. The rifting episode continued in November 2007 with a large intrusion emplaced at the southern end of the segment, in 2008 there were three intrusions and in 2009 an additional two dykes were emplaced. Although the volume of each intrusion was an order of magnitude smaller than the initial September 2005 dyke, where ~2-2.5 km^3 of magma was intruded (Grandin et al., 2009; Wright et al., 2006), the sequence of intrusions has resulted in an additional ~1 km^3 of material being emplaced along the segment (Fig. 6.1). The time between intrusions has not been constant during the rifting episode. Between June 2006 and January 2007 magma was being intruded at a rate of ~0.4 km^3/yr after which there was a ~7 month period with no intrusions. When dyking resumed in August 2007 this rate dropped to ~0.3 km^3/yr. Assuming that all of the separation across the Dabbahu segment is accommodated by magma injection, the spreading rate is ~ 16 mm/yr and the crustal thickness is ~16 km then this would result in an emplacement rate of 0.015 km^3/yr. This suggests that magma must have been stored in the crust over the last few hundred years. There has now been a ~9 month period with no dyke intrusions. In order to sustain the current emplacement rate, assuming that a dyke is emplaced over the next few months, will require an intrusion with a volume of 0.25 km^3 some 33% larger than the October 2008 dyke.

To test whether there is any time dependence on the volume of the dyke intrusions I have plotted the time between intrusions against volume (Fig. 6.1). Interestingly, there seems to be very little correlation between the length of time between intrusions and their volume. For example, the dyking events in November 2007 and October 2008 were intruded ~3 months after the previous event and yet have two of the largest volumes while the intrusion in August 2007 occurred ~7 months after the previous intrusion and had a volume of ~0.05 km^3.

Seismicity data covering the first three intrusions suggested a source around Ado'Ale, however, there was no geodetic evidence of a deflating magma chamber such as that observed in Iceland and at Kilauea during dyke intrusions (Björnsson et al., 1977, 1979; Cervelli et al., 2002; Tryggvason, 1980, 1984, 1994). A large deflation signal, accompanying the intrusion in November 2007 provided the first clear evidence of a shallow (<10 km)

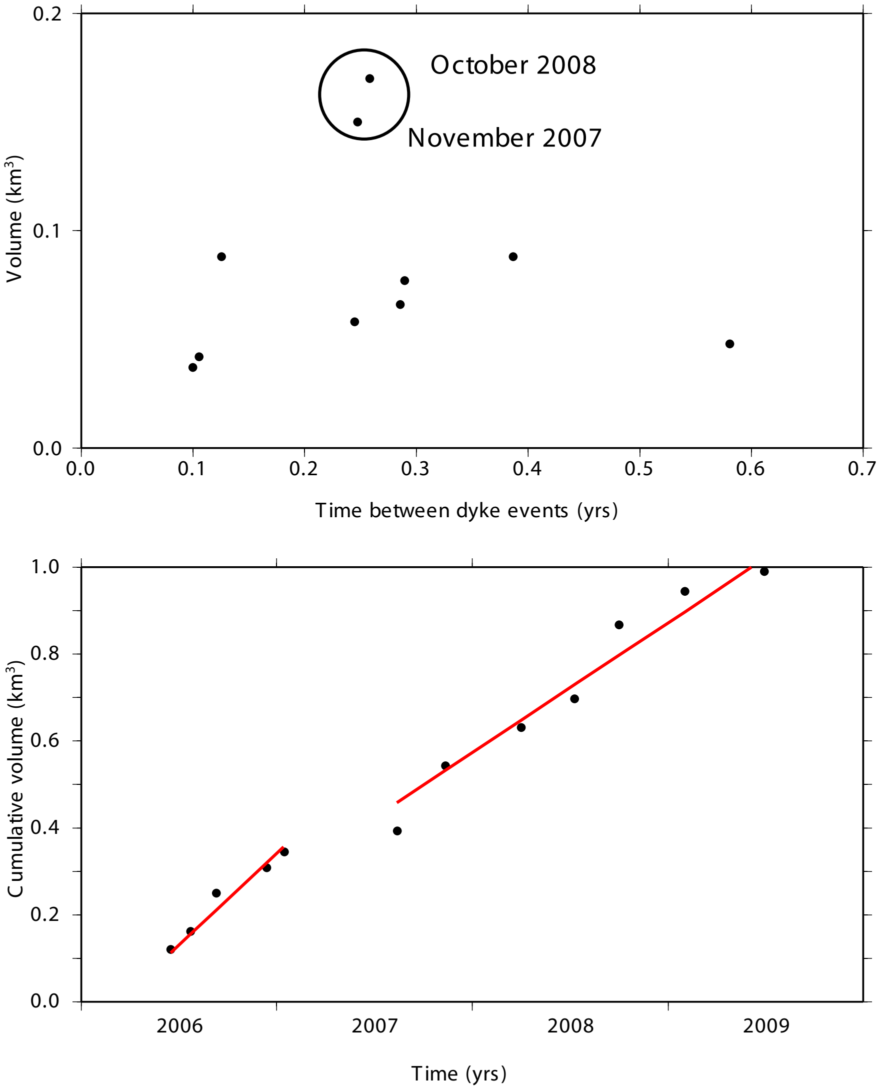

Figure 6.1: *Top*: Relationship between volume and time between intrusions. Black circle highlghts the large November 2007 and October 2008 intrusions. *Bottom*: Graph showing the change in volume with time during the 2006 - 2009 period. Red line shows the best fitting linear rates

deflating magma chamber in the centre of the rift segment. Interestingly, of the twelve dykes intruded between 2006 and 2009 only the two largest intrusions in November 2007 and October 2008 showed evidence of this deflating source. Assuming a Mogi type source, the amount of modelled deflation only accounts for a fraction (∼15%) of the estimated dyke volume. Explanations for this discrepancy, given in Chapter 3, include magma compressibility (Delaney & McTigue, 1994), incorrect Poisson's ratio (Johnson et al., 2000), or the difference in compliance between the magma chamber and the dyke (Rivalta & Segall, 2008).

During the Krafla rifting episode, rapid deflation of the caldera was observed coinciding with the injection of a new dyke. In Afar, only the two largest intrusions (0.15 and 0.17 km^3) have shown a deformation signal consistent with a deflating source. A possible explanation for this may be that, during the smaller intrusions, the magma supply rate was equal to the drainage rate, therefore causing no deflation of the source (Mériaux & Jaupart, 1995). For the larger intrusions, however, the supply rate to the shallow chamber may not have been enough to sustain the intrusion without some loss of volume causing the source to deflate.

Comparing the opening distributions of the September 2005 dyke intrusion with those of the subsequent events showed that new dyking events were largely emplaced into sections of the rift segment where opening of the main intrusion were lowest. Numerical simulations of the Krafla rifting event suggest that dyke propagation is largely controlled by differences in magma pressure and tectonic stress (e.g. Buck et al., 2006). As such, the tectonic stress in the southern section of the segment would have a higher tectonic stress than in the north and may therefore explain the distribution of magmatism since 2005. Figure 6.2 shows the distribution of opening along the rift segment from September 2005-June 2009. Assuming that the tectonic stress along the segment was spatially smooth prior to the onset of rifting and that the spreading rate has been relatively constant over the past 400-500 years then there are still large parts of the segment where the stresses have not been fully relieved. Observations of the Krafla rifting episode showed a significant increase in the number of eruptions toward the end of the rifting episode as the tectonic stress was relieved (Björnsson et al., 1979; Buck et al., 2006; Tryggvason, 1984). To date, only two fissural eruptions have been observed in Afar suggesting that, should a magma source remain, dyking will continue to occur until all of the stress has been relieved and that toward the end of the episode there will be an increase in the number of eruptive events (Ferguson et al., 2010).

6.2 The role of Stress during rifting events

Although the role of stress transfer on the location of earthquakes is well known (Harris & Simpson, 1996; King et al., 1994; Reasenberg & Simpson, 1992) its effect on the distribution of magmatic activity has previously been unclear and has only been amenable to testing for a few isolated cases (Amelung et al., 2007; Calais et al., 2008; Walter & Amelung, 2006). In Chapter 4, using elastic dislocation models, I was able to test the effects of stress transfer on a number of magmatic events.

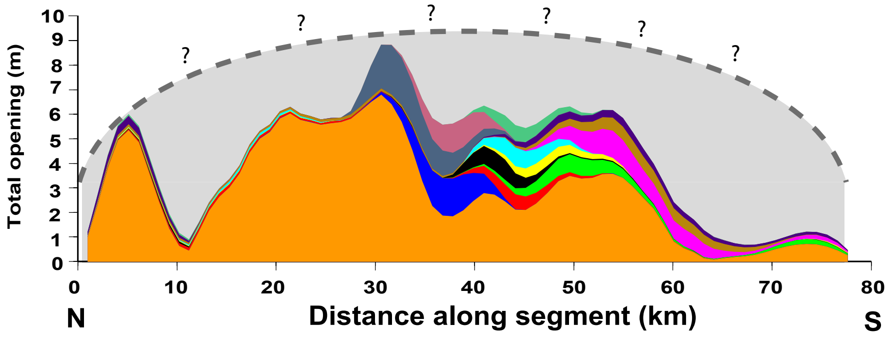

Figure 6.2: Depth averaged distribution of opening between September 2005 and June 2009. Coloured polygons represent the depth averaged opening for each of the dyke intrusions. Grey area shows the area where continued dyking may be expected.

The Dabbahu rifting episode is the first to be observed on land since the 1975-1984 Krafla events and is the first in the era of high-resolution satellite observations. Unlike studies of the Krafla episode, which were limited by the availability of high resolution data, this study has been able to reliably estimate the distribution of dyke opening enabling the calculation of the stress change induced by each intrusion.

As discussed in Section 6.1, all of the dykes emplaced since June 2006 have been intruded into sections of the rift segment where opening of the September 2005 dyke was lowest, leading to the conclusion that magma is preferentially intruded into regions of elevated tectonic stress. Analysis of the stress change induced by each individual event shows that, on average, 70% of dyke opening occurred in regions of increased tensile stress (unclamping) caused by the previous event. The likelihood of a random sequence of events to occur with the same percentage of opening is ~1 in 2 million suggesting that stress transfer is a controlling factor in the location of dyking along the rift segment.

The re-activation of faults during new dyking has been observed in the field (Fig. 6.3) and is predicted by the elastic dislocation models described in Chapter 3. To test the effect of the dyke intrusions on faults along the rift segment I calculated the change in Coulomb stress along modelled fault planes and compared the values with the amount of slip. The result of the stress change models suggests that much of the faulting along the Dabbahu segment, as modelled using InSAR data, must have occurred ahead of the dyke as it was propagating. This is supported by propagating seismicity which has been observed during the June and July 2006 dyke intrusions (Keir et al., 2009).

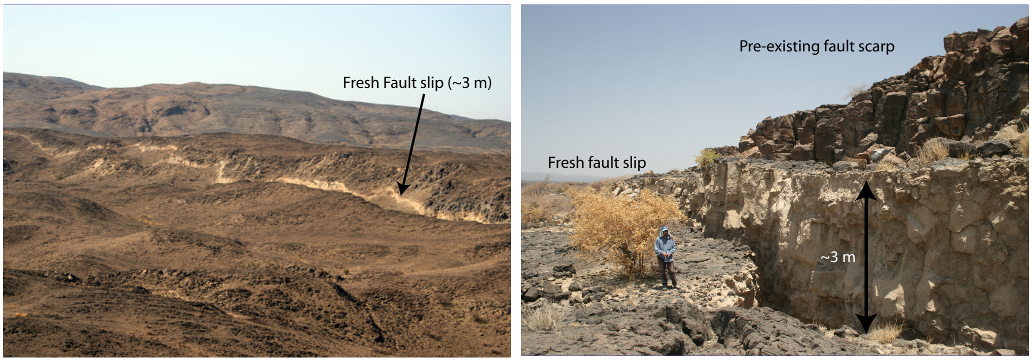

Figure 6.3: Field observations of fault slip along the Dabbahu rift segment, (photographs taken by Julie Rowland 2006)

6.3 Post-rifting deformation in Afar

Using 92 interferograms collected between September 2005 and February 2010 I calculated the background displacement rates resulting from the September 2005 dyke intrusion with the effects of new dyking removed. Two displacement rates are observed either side of the June 2006 dyke intrusion with an apparent decrease in the rate after the intrusion. By combining observations from ascending and descending tracks I was able to separate the line-of-site displacements into rift perpendicular and vertical components. Peak rift-perpendicular displacements of $\sim$0.8 m are observed over this period near the Ado'Ale volcanic complex decreasing to 0.1-0.2 m in the north. Uplift was concentrated in the centre of the segment where peak displacements reach 0.75 m, again, decreasing to $\sim$0.1 m in the northern section of the segment.

In Chapter 5 I use a two-layer viscoelastic model to fit InSAR observations of post-rifting deformation around the Dabbahu segment. These models are unable to produce a good fit to the observations. Significant misfits occur in the Ado'Ale region and to the southeast of the segment where the model underestimates the displacement. It is apparent from the residuals that the large amplitude displacements observed around Ado'Ale cannot be explained by viscoelastic relaxation. The large displacements near Ado'Ale coincides with the inferred source for all of the post-2005 intrusions and suggests that there has been significant accumulation of magma over this period. Deformation to the north of Ado'Ale, however, which has been largely unaffected by recent magmatic intrusions, can be approximated using a model with a crustal thickness of 12 km with a mantle viscosity of $10^{18.5}$ Pas. Interestingly, the best fitting models to the horizontal and vertical displacements do not agree with each other. Therefore, if only one of the deformation components is used the

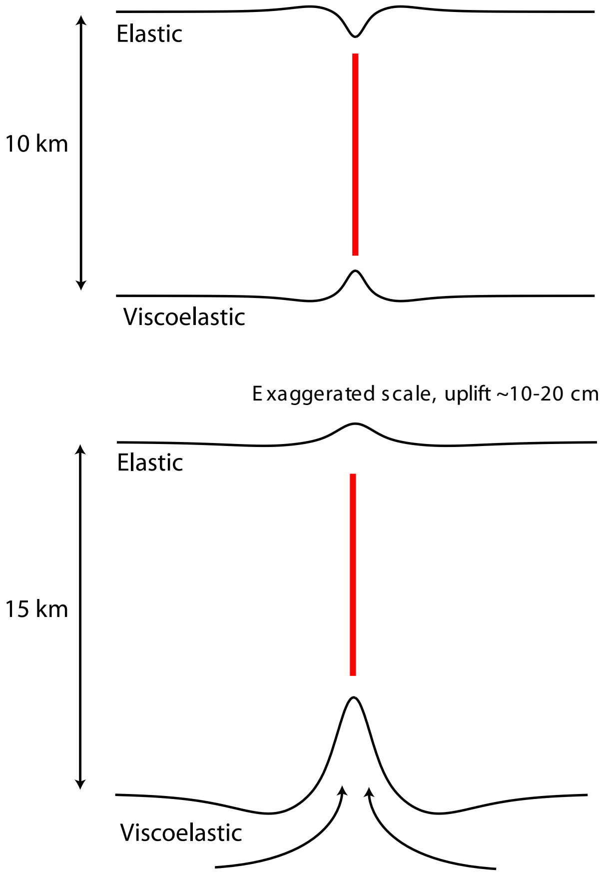

Figure 6.4: Schematic diagram illustrating the effect of the elastic lid thickness on vertical displacements.

result will be biased giving a different viscosity and lid thickness. Analysis of the vertical component of the deformation does give a lower limit on the thickness of the elastic lid as the magnitude of the uplift along the rift zone strongly depends on the thickness of the lid. In order to generate uplift along the rift axis the thickness of the elastic lid must be at least 12 km. If the elastic lid is thinner than this then subsidence will occur as the uplift caused by the flow of material in the viscoelastic layer is not enough to compensate the subsidence in the elastic layer (Fig. 6.4).

6.4 Repeat times of dyke intrusion

If all of the plate separation across plate boundaries is assumed to be accommodated by dyke intrusions then the average repeat time for an intrusion, of a given thickness, will be dependent on the spreading rate. Observations from ophiolites suggest that typical dyke intrusions are ∼1-1.5 m thick (Kidd & Cann, 1974), therefore, at fast spreading rates of 120 mm/yr a dyke would be intruded every 8 years and for a slow spreading rate of

20 mm/yr every ~50 years. However, studies of slow spreading ridges and of continental rifts show that a significant amount of extension may be accommodated by faulting rather than dyke injection meaning that a repeat time of 50 years may be an underestimate (Curewitz & Karson, 1998). During rifting episodes, however, the interval between dyke intrusions may be as little as ~3-4 months.

Rifting episodes along oceanic spreading centres, like those observed along the Juan de Fuca ridge (e.g. Dziak et al., 1995, 2007), typically involve the intrusion of a single dyke and frequently result in seafloor eruptions. Sub-aerial rifting episodes like those observed in Iceland and Afar, however, result in multiple intrusions emplaced over a short space of time with an individual repeat time of ~6 months (e.g. Einarsson & Brandsdóttir, 1980; Tryggvason, 1984). For a dyke intrusion to initiate the magma pressure must be greater than the horizontal compressive stress along the axis. For well developed oceanic systems, where magma is readily available and at high pressure, dyking will occur frequently once the magma pressure exceeds this stress which is continually reduced as the plates separate. In less developed magmatic systems, like those found in Afar and Iceland, however, where less magma is available for intrusion, the stresses are able to build up over much longer periods without dyke intrusion. The rifting episodes along the Krafla and Dabbahu segments resulted in multiple intrusions over a number of years. The fact that multiple dyking events were observed during both episodes suggests that there was sufficient magma pressure to overcome the horizontal compressive stress to initiate rifting but insufficient material to fully relieve the stresses built up by the long term plate separation. Models of dyke propagation by (Buck et al., 2006) suggest that after each dyking event the pressure of the magma in the chamber must increase in order to initiate the next dyking event (Fig. 6.5). Once the magma pressure has increased to to a level sufficient to breakout from the magma chamber the next event will be intruded in the direction of minimum compressive stress or areas of higher tectonic stress. This is supported by the observations in Afar where the inversion of geodetic data suggests that dykes intruded after the 2005 intrusion were emplaced in areas where the September 2005 dyke opening was smallest.

6.5 Comparison with Rifting in Krafla and Asal

Following the Krafla and Asal rifting episodes horizontal displacements were ~3 times larger than the time-averaged spreading rates between 1987-1990 at Krafla and between 1979-1985 at Asal (Cattin et al., 2005b; Hofton & Foulger, 1996b). Vertical displacements

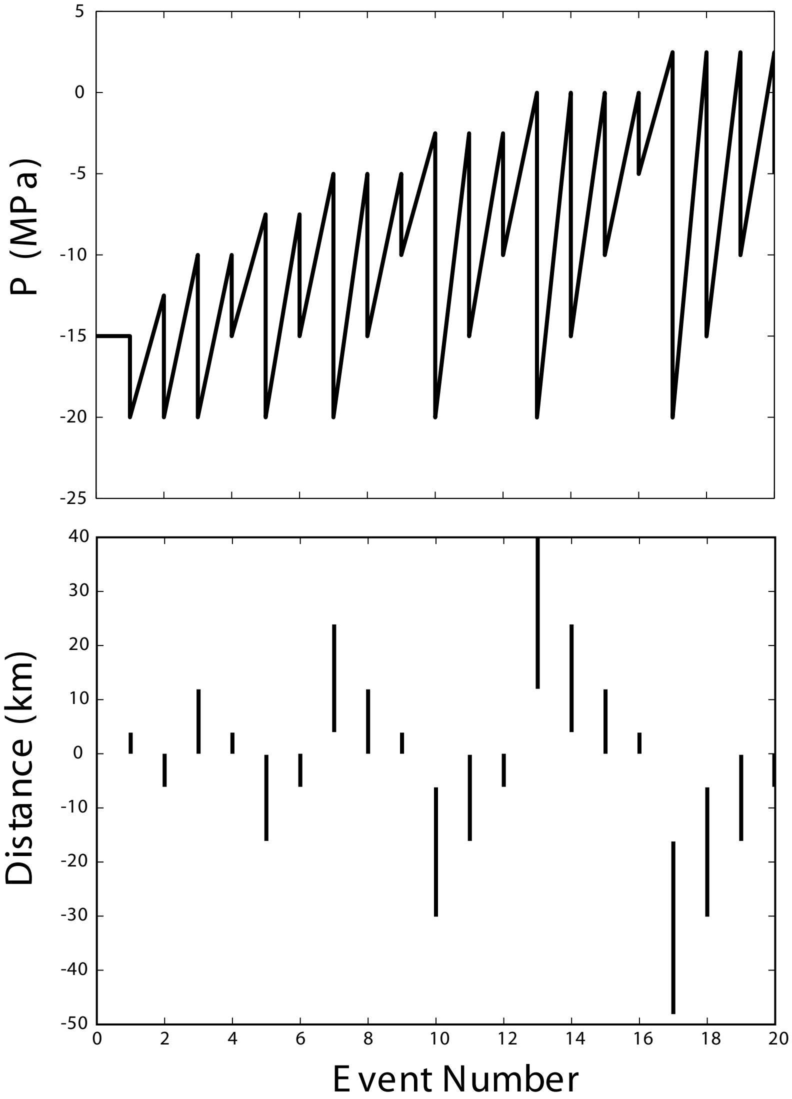

Figure 6.5: Numerical example of multiple dyking events with constant initial stress, after (Buck et al., 2006). *Top*: Change in pressure at the magma chamber after each of the 20 simulated events. *Bottom*: Horizontal range for dyke opening from the central magma chamber for each event

across the Krafla segment between 1987-1990 indicate uplift of ~5-10 cm (Heki et al., 1993; Pollitz & Sacks, 1996) while levelling data across the Asal rift revealed a wide zone of uplift, similar to that observed at Krafla, with a narrow region of subsidence observed at the rift axis (Cattin et al., 2005b). GPS and InSAR observations around the Dabbahu rift segment also show increased spreading rates and a broad zone of uplift following the onset of rifting in 2005. A number of different models have been used to describe the observed deformation following the Asal and Krafla rifting events. Models consisting of an elastic lid and viscoelastic half-space proposed by Hofton & Foulger (1996a,b) and Pollitz & Sacks (1996) were able to predict the post-rifting deformation around Krafla using GPS derived velocities after the rifting event had finished. A model of post-rifting deformation following the Asal rifting episode by Cattin et al. (2005b) incorporated the effect of regional stretching, viscous relaxation, magma intrusion and fault creep to describe rifting processes and concluded that post-rift dyke opening was responsible for most of the observed deformation.

Unlike post-rifting studies of Asal and Krafla, which have modelled deformation data with viscoelastic models to infer rheological parameters, the Dabbahu rifting episode is ongoing and, based on the Krafla rifting event, may continue over the next few years. Although there is evidence for post-rifting relaxation around the Dabbahu segment it is limited to the north of the segment away from Ado'Ale where large deformations are observed that cannot be explained by viscoelastic relaxation. Models of the Asal rifting event suggest that in the first years after the event deformation was primarily the result of dyke inflation, after which fault creep and regional stretching take over. It is apparent that much of the deformation around the Dabbahu segment is the result of magma accumulation around the Ado'Ale complex. Magma chambers beneath the long-lived Krafla (6-7 Myr (Sigmundsson, 2006)) and Asal systems are much shallower at between 2-4 km (Brandsdóttir et al., 1997; Van et al., 1981). Deflation events associated with dyke intrusion in November 2007 and October 2008 along the Dabbahu segment, however, suggest that a chamber may reside at ∼10 km depth (Ferguson et al., 2010; Hamling et al., 2009). There is no evidence of inflation beneath Ado'Ale prior to rifting in 2005, however, seismicity suggests that 4-5 days after activity began at the north of the segment the 2005 dyke propagated both north and south from Ado'Ale. This suggests that there was either a long lived chamber present before rifting or that the redistribution of stresses around the segment allowed material to flow into the segment. This idea is supported by the presence of a broad subsiding zone to the southeast of the segment that began subsiding immediately after the dyke intrusion in 2005 and has continued to subside while Ado'Ale has uplifted (Fig. 6.6).

The spatial and temporal evolution of rifting in Afar shows a number of similarities with the 1975-84 Krafla episode. Through the use of high resolution geodetic data sets, however, I have been able to explain the spatial distribution of magmatism during rifting and have shown that the distribution of stress along the segment is a controlling factor. Currently, deformation around the Dabbahu segment is dominated by migration and accumulation of magma. Studies from Krafla and Asal suggest that as the rifting event finishes viscoelastic relaxation will take over as the major deformation source and should allow a more complete picture of the rheology beneath Afar.

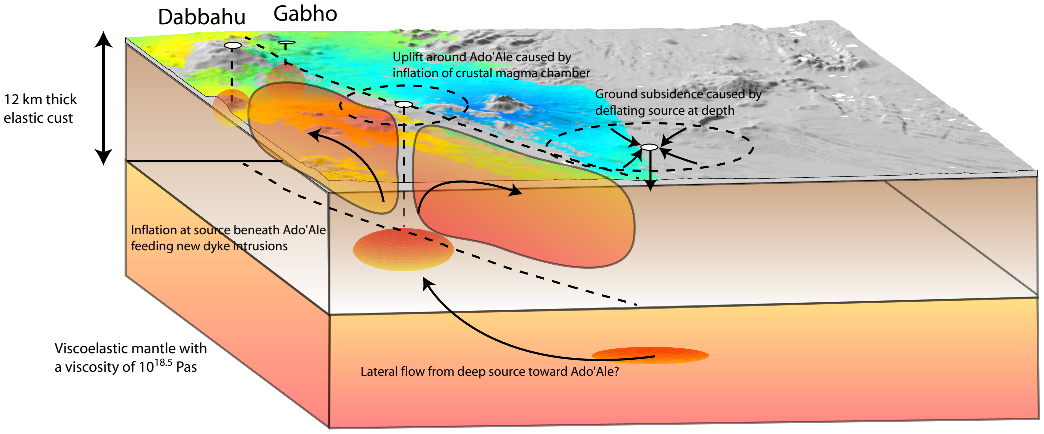

Figure 6.6: Schematic model for the distribution of deformation sources around the Dabbahu rift segment. Topography is overlain by the total deformation observed by InSAR between June 2006 and February 2010.

6.6 Future work

6.6.1 Continued monitoring

It is apparent from studies of the rifting cycle from Iceland that long-term monitoring of the Dabbahu segment is required to ensure that all co-rifting and post-rifting deformation is observed. Through the Afar Consortium, a range of geophysical data has been and will be collected up until 2012. However, if the rifting continues, as it did in Krafla, over the next 5 years then it is important that the area is monitored beyond this time. Furthermore, observation of the current rifting in Afar and from the Krafla episode suggest that processes relating to post-rifting deformation are difficult to identify while the system is still active. As such, it is imperative that geodetic data are collected after the episode has finished. In a remote area, such as Afar, InSAR plays a pivotal role in obtaining deformation data in a region where security can prevent field base measurements from being acquired. ENVISAT has been an invaluable asset for deformation studies across the globe since its launch in 2002 but is now approaching its end of life. A new satellite, *Sentinel-1* will be launched in 2012 and will provide worldwide coverage every 12 days, greatly increasing the volume of SAR data and, due its short repeat time, will reduce the errors in InSAR measurements. However, there is likely to be a window of at least one year where there will be no available C-band InSAR. In order to maintain regular acquisitions, other SAR platforms will need to be utilised to fill the gap. There are a number of options available including TerraSAR-X, ALOS and SAOCOM, which is due to launch in 2012. Both ALOS and SAOCOM operate in L-band with repeat times of 46 and 16 days respectively. Although L-band SAR has better coherence over vegetated surfaces, which is not a problem in Afar, the long repeat time of Alos may favour the use of TerraSAR-X with a shorter repeat time of 11 days.

6.6.2 Determination of the evolving stress field

There has been a large investment over the last decade into the affect of stress transfer on future earthquakes or volcanic events, most notably by the USGS. A number of studies have shown a link between increased stress on faults and the location of earthquakes. Studies of dyke intrusions along the Mauna Loa rift in Hawaii have also shown a link between the location of magma emplacement and increased tensile stress (Amelung et al., 2007). Similarly, in Chapter 4 I show that the location of dyke intrusions along the Dabbahu segment are controlled by the transfer of stress from the previous event. Continued monitoring of the Dabbahu segment will allow the calculation of stress change along the rift segment after each new event and provide a means to forecast the location of future activity. Although the impact on human life is relatively small in this remote part of Afar, the results of this thesis suggest that stress modelling should be routinely used as part of volcanic hazard monitoring. This will be further enhanced with the launch of new SAR sensors over the next few years where it will be possible to achieve almost real time monitoring of actively deforming areas at a variety of spatial resolutions.

6.6.3 Determining the rheology beneath Afar

As discussed earlier, the current phase of deformation around the Dabbahu segment is mostly related to magma movement through the volcanic system. Much of the modelling used to infer the viscosity structure beneath Iceland was conducted using geodetic data measured after the co-rifting episode had finished. Modelling of the post-rifting deformation presented in this thesis has shown that the deformation cannot be explained by viscoelastic processes alone. Although an estimate of lid thickness and viscosity could be made and is consistent with other studies (Nooner et al., 2009), observations of the post-rifting period should enable the development of more sophisticated viscoelastic models with varying rheoloies.

6.6.4 Amalgamating data sets

The large data sets collected through the Afar Consortium offer a unique opportunity to bring together multiple data sets to help form a better understanding of rifting processes. The combination of interferometric data and InSAR have already been used with some success to provide information on the temporal and spatial evolution of dyke intrusions along the Dabbahu segment. Work on creating a better velocity model for the Afar region is underway and will help to resolve the depth of earthquakes triggered by dyking. Furthermore, high resolution LiDAR data collected along the rift segment will allow InSAR data to be reprocessed at a much higher resolution where it will be possible to resolve slip on specific faults. Stress change calculations, discussed in Chapter 4, suggest that faulting is confined to the shallow crust and is likely to have occurred at the tip of the dyke as it propagates. The use of high resolution InSAR in conjunction with reliable depth estimates for earthquakes will allow the thourough testing of the interaction between dyke intrusion events and faulting. Currently, there are no reliable estimates for the location and depth of magmatic sources around the Dabbahu segment. Magnetotelluric data collected over the rift segment along with seismicity should provide better constraints on the distribution of melt along the segment providing invaluable information for magma modelling.

References

Abdallah, A., Courtillot, V., Kasser, M., Dain, A. Y. L., Lépine, J. C., Robineau, B., Ruegg, J. C., Tapponnier, P., & Tarantola, A., 1979. Relevance of Afar seismicity and volcanism to the mechanics of accreting plate boundaries, *Nature*, **282**.

Abebe, T., Manetti, P., Bonini, M., Corti, G., Innocenti, F., Mazzarini, F., & Pecksay, Z., 2005. Geological map (1:200000) of the Main Ethiopian rift and its implications for the volcano-tectonic evolution of the rift, *Geol. Soc. Amer. Chart and Map Series*, **MCH094**, 20pp.

Achauer, U., Maguire, P. K. H., Mechie, J., Green, W. V., & Working Group, T. K., 1992. Some remarks on the structure and geodynamics of the Kenya Rift, *Tectonophysics*, **213**, 257–268.

Acton, G. D. & Stein, S., 1991. Block rotation and continental extension in Afar: a comparison to oceanic microplate systems, *Tectonophysics*, **10**(3), 501–526.

Almond, D. C., 1986. Geological evolution of the Afro-Arabian dome, *Tectonophysics*, **331**, 302–333.

Amelung, F., Yun, S. H., Walter, T. R., Segall, P., & Kim, S. W., 2007. Stress Control of Deep Rift Intrusion at Mauna Loa Volcano, Hawaii, *Science*, **316**, 1026–1030.

Ayele, A., Jacques, E., Kassim, M., Kidane, T., Omar, A., Tait, S., Nercessian, A., de Chablier, J.-B., & King, G., 2007. The volcano-seismic crisis in Afar, Ethiopia, starting September 2005, *Earth Planet. Sci. Lett.*, **255**, 177–187.

Ayele, A., Keir, D., Ebinger, C., Wright, T. J., Stuart, G. W., Buck, W. R., Jacques, E., Ogubazghi, G., & Sholan, J., 2009. September 2005 mega-dike emplacement in the Manda-Harraro nascent oceanic rift (Afar depression), *Geophysics Research Letters*, **36**(L20306), doi:10.1029/2009GL039605.

Baer, G., Hamiel, Y., Shamir, G., & Nof, R., 2008. Evolution of a magma-driven earthquake swarm and triggering of the nearby Oldoinyo Lengai eruption, as resolved by InSAR, ground observations and elastic modeling, East African Rift, 2007, *Earth Planet. Sci. Lett.*, **272**, doi:10.1016/j.epsl.2008.04.052.

Bamler, R. & Hartl, P., 1998. Synthetic aperture radar interferometry, *Inverse Problems*, **14**.

Barberi, F. & Varet, J., 1970. The Erta ale volcanic range, *Bulletin Volcanologique*, **34**, 848–917.

Barberi, F. & Varet, J., 1975. Recent volcanic units of Afar and their structural significance, in *Afar Depression of Ethiopia: Proceedings of an International Symposium on the Afar Region and Related Rift Problems*, vol. 1, pp. 174–178, Schweizerbart, Stuttgart.

Barberi, F. & Varet, J., 1977. Volcanism of Afar: small-scale plate tectonics implication, *Geol. Soc. of Amer. Bull.*, **88**, 1251–1266.

Barberi, F., Tazieff, H., & Varet, J., 1972. Volcanism in the Afar depression: its tectonic and magmatic significance, *Tectonophysics*, **15**, 19–29.

Barberi, F., Chemine'e, H., & Varet, J., 1973. Long-lived lava lakes of the Erta ale volcano, *Revue de Géographie Physique et de Géologie Dynamique*, **15**, 347–352.

Barberi, F., Bonatti, E., Marinelli, G., & Varet, J., 1974. Transverse tectonics during the split of continent: Data from the Afar rift, *Tectonophysics*, **23**, 17–19.

Barisin, I., Leprince, S., Parsons, D., & Wright, T., 2009. Surface displacements in the September 2005 Afar rifting event from satellite image matching: Asymmetric uplift and faulting, *Geophysics Research Letters*, **36**(L07301), doi:10.1029/2008GL036431.

Barrat, J., Joran, J., Taylor, R., Fourcade, S., Nesbitt, R., & Jahn, B., 2003. Geochemistry of basalts from Manda Hararo, Ethiopia: LREE-depleted basalts in Central Afar, *Lithos*, **69**, 1 – 13.

Bastow, I., Stuart, G. W., Kendall, J. M., & Ebinger, C., 2005. Upper mantle seismic structure in a region of incipient continental breakup: northern Ethiopian rift, *Geophys. J. Int.*, **162**, 479 – 493.

Bastow, I., Nyblade, A. A., Stuart, G. W., Rooney, T. O., & Benoit, M. H., 2008. Upper mantle seismic structure beneath the Ethiopian hot spot: Rifting at the edge of the African low-velocity anomaly, *Geochem, Geophys, Geosyst*, **9**, Q12022.

Benoit, M. H., Nyblade, A. A., VanDecar, J. C., & Gurrola, H., 2003. Upper mantle P wave velocity structure and transition zone thickness beneath the Arabian Shield, *Geophysics Research Letters*, **30**.

Benoit, M. H., Nyblade, A. A., & VanDecar, J. C., 2006. Upper mantle P wave speed variations beneath Ethiopia and the origin of the Afar Hotspot, *Geology*, **34(5)**, 329–332.

Berardino, P., Fornaro, G., Lanari, R., & Sansosti, F., 2002. A new algorithm for surface deformation monitoring based on small baseline differential SAR Interferograms, *IEEE Trans. on Geoscience and Remote Sensing*, **40**, 2375–2383.

Berckhemer, H., Baier, B., Bartelson, H., Behle, A., Burkhardt, H., Gebrande, H., Makris, J., Menzel, H., Miller, H., & Vees, R., 1975. *Deep seismic soundings of the Afar region and on the highland of Ethiopia*, pp. 89 – 107, Schweizerbart, Stuttgart.

Berhe, S. M., Desta, B., Nicoletti, M., & Teferra, M., 1987. Geology, geochronology and geodynamic implications of Cenozoic magmatic province in W and SE Ethiopia, *Journal of the Geological Society, London*, **144**, 213–226.

Beyene, A. & Abdelsalam, M. G., 2005. Tectonics of the Afar Depression: A review and synthesis, *J. Aeronaut. Sci.*, **41**, 41–59.

Biggs, J., 2007. *InSAR Observations of the Earthquake Cycle on the Denali Fault, Alaska*, Ph.D. thesis, Department of Earth Sciences, University of Oxford.

Biggs, J., Wright, T., Lu, Z., & Parsons, B., 2007. Multi-interferogram method for measuring interseismic deformation: Denali Fault, Alaska, *Geophys. J. Int.*, **170**, 1165–1179.

Biggs, J., Amelung, F., Gourmelen, N., Dixon, T., & Kim, S. W., 2009. InSAR observations of 2007 Tanzania rifting episode reveal mixed fault and dyke extension in an immature continental rift, *Geophys. J. Int.*, **179**, 549–558.

Björnsson, A., Saemundsson, K., Einarsson, P., Tryggvason, E., & Gronvald, K., 1977. Current rifting episode in North Iceland, *Nature*, **266**, 318–323.

Björnsson, A., Johnsen, G., Sigurdsson, S., Thorbergsson, G., & Tryggvason, E., 1979. Rifting of a plate boundary in North Iceland 1975-1978, *J. Geophys. Res.*, **84**, 3029–3038.

Bosworth, W. & McClay, K., 2001. Structural and stratigraphic evolution of the Gulf of Suez Rift, Egypt: a synthesis, *Memoirs due Museum National dltistorire nationalle*, **186**, 567–606.

Brandsdóttir, B., Menke, W., Einarsson, P., White, R. S., & Staples, R. K., 1997. Faeroe-Iceland Ridge Experiment: 2. Crustal structure of the Krafla central volcano, *J. Geophys. Res.*, **102**, 7867–7886.

Bro, R. & Jong, S. D., 1997. A fast non-negativity-constrained least squares algorithm, *J. Chemometrics*, **11**, 392 – 401.

Buck, W. R., 2004. *Consequences of asthenospheric variability on continental rifting.*, pp. 1–30, Columbia University Press.

Buck, W. R., Martinez, F., Steckler, M. S., & Cochran, J. R., 1988. Thermal consequences of lithospheric extension: Pure and simple, *Tectonophysics*, **7**, 213–234.

Buck, W. R., Einarsson, P., & Brandsdóttir, B., 2006. Tectonic stress and magma chamber size as controls on dike propagation: Constrints from the 1975-1984 Krafla rifting episode, *J. Geophys. Res.*, **111**.

Buckley, S., 1998. *Slip along the Hayward fault, California estimated from space-based interferometry*, Ph.D. thesis, University of Texas, Austin, Texas.

Bürgmann, R., Rosen, P., & Fielding, E., 2000. Synthetic aperture radar interferometry to measure Earth's surface topography and it's deformation, *Annual Review of Earth and Planetary Sciences*, **28**, 169–209.

Burke, K., 1977. Aulacogens and continental breakup, *Annual Review of Earth and Planetary Sciences*, **5**, 371–396.

Calais, E., d'Oreye, N., Albaric, J., Deschamps, A., Delvaux, D., Déverchère, J., Ebinger, C., Ferdinand, R. W., Kervyn, F., Macheyeki, A., Oyen, A., Perrot, J., Saria, E., Smets, B., Stamps, D. S., & Wauthier, C., 2008. Strain accommadation by slow slip and dyking in a youthful continental rift, East Africa, *Nature*, **456**, 783–787.

Canales, J. P., Detrick, R. S., Carbotte, S. M., Kent, G. M., Diebold, J. B., Harding, A., Babcock, J., Nedimovic, M. R., & Ark, E. V., 2005. Upper crustal structure and axial topography at intermediate spreading ridges: seismic constraints from the southern Juan de Fuce Ridge, *J. Geophys. Res.*, **110**(B12104), doi:10.1029/2005/JB003630.

Cann, J. R., 1970. New Model for the Structure of the Ocean Crust, *Nature*, **226**(5249), 928–930.

Cann, J. R., 1974. A Model for Oceanic Crystal Structure Developed, *Geophys. J. R. Astr. Soc.*, **39**(1), 169–187.

Cattin, R., Doubré, C., Chabalier, J. B.-., King, G., Vigny, C., Avouac, J. P.-., & Ruegg, J. C.-., 2005a. Numerical modelling of quaternary deformation and post-seismic displacement in the Asal-Ghoubbet rift (Djibouti), (Africa), *Earth Planet. Sci. Lett.*, **239**, 352–367.

Cattin, R., Doubre, C., de Chabalier, J.-. B., King, G., Vigny, C., Avouac, J.-. P., & Ruegg, J.-. C., 2005b. Numerical modelling of quaternary deformation and post-rifting displacement in the Asal-Ghoubbet rift (Djibouti, Africa), *Earth Planet. Sci. Lett.*, **239**, 352–367.

Cauchy, A. L., 1823. Recherches sur l'Équilibre et le Mouvement Intérieur des Corps Solides ou Fluides, Élastiques ou non Élastiques, *Bull. Soc. Philomath*, **2**, 300–304.

Cavalié, O., Doin, M. P., Lasserre, C., & Broile, P., 2007. Ground motion in the Lake Mead area, Nevada, by differential synthetic aperture radar interferometry time series analysis: Probing the lithosphere rheological structure, *J. Geophys. Res.*, **112**(B03403), doi:10.1029/2006JB004344.

Cavalié, O., Lasserre, C., Doin, M. P., Peltzer, G., Sun, J., Xu, X., & Shen, Z. K., 2008. Measurement of interseismic strain across the Haiyuan fault (Gansu, China), *Earth Planet. Sci. Lett.*, **275**, 246–257.

Cayol, V., Dieterich, J. H., Okamura, A. T., & Miklius, A., 2000. High Magma Storage Rates Before the 1983 Eruption of Kilauea, Hawaii, *Science*, **288**, 2243–2346.

Cervelli, P., Segall, P., Amelung, F., Garbeil, H., Meertens, C., Owen, S., Miklius, A., & Lisowski, M., 2002. The 12 September 1999 Upper East Rift Zone dike intrusion at Kilauea Volcano, Hawaii, *J. Geophys. Res.*, **107**(B7).

Chery, J., Lucazeau, F., Daignieres, M., & Vilotte, J. P., 1992. Large uplift of the rift flanks; a genetic link with lithospheric rigidity?, *Earth Planet. Sci. Lett.*, **112**(1-4), 195–211.

Chorowitz, J., 2005. The East African rift system, *Journal of African Earth Sciences*, **43**, 379–410.

Chu, D. & Gordon, R. G., 1998. Current plate motions across the Red Sea, *Geophys. J. Int.*, **135**(2), 313–328(16).

Chu, D. & Gordon, R. G., 1999. Evidence for motion between Nubia and Somalia along the Southwest Indian Ridge, *Nature*, **398**, 64–67.

Cochran, J. R., 1983. Model for development of the Red Sea, *Am. Assoc. Pet. Geol. Bull*, **67**, 41–69.

Cochran, J. R., Martinez, F., Steckler, M. A., & Hobart, M. A., 1986. Conrad Deep, a new northern Red Sea Deep, origin and implications for continental rifting, *Earth Planet. Sci. Lett.*, **78**, 18–32.

Collier, J. S. & Sinha, M. C., 1990. Seismic images of the magma chamber beneath the Lau Basin back-arc spreading centre, *Nature*, **346**, 646–648.

Crane, K. & Bonatti, E., 1987. The role of fracture zones during early Red Sea rifting. Structural analysis using space shuttle radar and Landsat imagery, *Journal of the Geological Society, London*, **144**, 407–420.

Crisp, J. A., 1984. Rates of magma emplacement and volcanic output, *J. Volcanol. Geotherm. Res.*, **20**(3-4), 177–211.

Curewitz, D. & Karson, J. A., 1998. *Geological Consequences of Dike Intrusions at Mid-Ocean Ridge Spreading Centres*, pp. 117–136, American Geophysical Union.

Curlander, J. C. & McDonough, R. N., 1991. *Synthetic aperture radar - Systems and signal processing*, New York: John Wiley & sons, Inc.

de Zeeuw-van Dalfsen, E., Pedersen, R., Sigmundsson, F., & Pagli, C., 2004. Satellite radar interferometry 1993-1999 suggests deep accumulation of magma near the crust-mantle boundary at the Krafla volcanic system, Iceland, *Geophysics Research Letters*, **31**, 13611.

Delaney, J. R., Kelley, D. S., Lilley, M. D., Butterfield, D. A., Baross, J. A., Wilcock, W. S. D., Embley, R. W., & Summit, M., 1998. The Quantum Event of Oceanic Crustal Accretion: Impacts of Diking at Mid-Ocean Ridges, *Science*, **281**.

Delaney, P. & McTigue, D., 1994. Volume of magma accumulation or withdrawal estimated from surface uplift or subsidence, with application to the 1960 collapse of Kilauea Volcano, *Bull. Volcanol*, **56**, 417 – 424.

Desissa, M., Whaler, K., Houtot, S., Dawes, G., Fisseha, S., & Johnson, N., 2009. A magnetotelluric study of continental lithosphere in the final stages of break-up: Afar, Ethiopia, in *IAGA Assembly, Hungary*, no. 106-TUE-O1345-1158 in I06.

Detrick, R. S., Mutter, J. C., Buhl, P., & Kim, I. I., 1987. Multi-channel seismic imaging of a crustal magma chamber along the East Pacific Rise, *Nature*, **326**, 35–41.

Dugda, M., Nyblade, A., Julia, J., Langston, C., Ammon, C. A., & Simiyu, S., 2005. Crustal structure in Ethiopia and Kenya from reciever function analysis: Implications for rift development in eastern Africa, *J. Geophys. Res.*, **110**(B01303), doi:10.1029/2004JB003065.

Dziak, R. P., Fox, C. G., & Schreiner, A. E., 1995. The June-July 1993 seismo-acoustic event at CoAxial segment, Juan de Fuca Ridge: Evidence for a lateral dike injection, *Geophysics Research Letters*, **22**(2), 135–138.

Dziak, R. P., Bohnenstiehl, D. R., Fox, C. G., amd H. Matsumoto, D. D., Tolstoy, M., & Fornari, D. J., 2004. Evidence of a recent dike intrusion at the slow spreading Lucky Strike segment, Mid-Atlantic Ridge, *J. Geophys. Res.*, **109**(B12102), doi:10.1029/2004JB003141.

Dziak, R. P., Bohnenstiehl, D. R., Cowen, J. P., Baker, E. T., Rubin, K. H., Haxel, J. H., & Fowler, M. J., 2007. Rapid dike emplacement leads to eruptions and hydrothermal plume release during sea-floor spreading events, *Geology*, **35**, doi:10.1130/G23476A.1.

Dziak, R. P., Bohnenstiehl, D. R., Matsumoto, H., Fowler, M. J., Haxel, J. H., Tolstoy, M., & Waldhauser, F., 2009. January 2006 seafloor-spreading event at 9°50'N, East Pacific Rise: Ridge dike intrusion and transform fault interactions from regional hydroacoustic data, *Geochemistry Geophysics, Geosystems*, **10:Q06T06**, doi:10.1029/2009GC002388.

Eagles, G., Gloaguen, R., & Ebinger, C., 2002. Kinematics of the Danakil Microplate, *Earth Planet. Sci. Lett.*, **203**, 607–620.

Ebinger, C., Keir, D., Ayele, A., Calais, E., Wright, T. J., Belachew, M., Hammond, J. O. S., , Campbell, E., & Buck, R., 2008. Capturing magma intrusion and faulting processes during continental rupture: Seismicity of the Dabbahu (Afar) rift, *Geophys. J. Int.*, **174**, doi: 10.1111/j.1365–246X.2008.03877.x.

Ebinger, C. J., 2005. Continental break-up: the East African perspective, *Astronomy and Geopysics*, **46**, 16–21.

Ebinger, C. J. & Sleep, N. H., 1998. Cenozoic magmatism throughout east Africa resulting from impact of a single plume, *Nature*, **395**.

Ebinger, C. J., Yemane, T., WoldeGabriel, G., Aronson, J. L., & Walter, R. C., 1993. Late Eocene-recent volcanism and faulting in the southern Main Ethiopian Rift, *Journal of the Geological Society, London*, **150**, 99–108.

Einarsson, P., 1978. S-wave shadows in the Krafla caldera in NE-Iceland, evidence for a magma chamber in the crust, *Bull. Volcanol*, **41**, 1–9.

Einarsson, P., 1991. The Krafla rifting episode 1975 - 1989, in *Náttúra Mývatns (The Nature of Lake Mývatn)*, pp. 97 – 139, Icelandic Nature Sci. Soc., Reykjavík.

Einarsson, P. & Brandsdóttir, 1980. Seismological evidence for lateral magma intrusion during the 1978 deflation of the Krafla volcano in NE-Iceland, *J. Geophys. Res.*, **47**, 160– 165.

Elachi, C., 1987. *Introduction to the Physics and Techniques of Remote Sensing*, New York: John Wiley & sons, Inc.

Farr, T. & Kobrick, M., 2000. Shuttle Radar Topography Mission produces a wealth of data, *EOS Trans. AGU*, **81**, 583,585.

Ferguson, D. J., Barnie, T. D., Pyle, D. M., Oppenheimer, C., Yirgu, G., Lewi, E., Kidane, T., Carn, S., & Hamling, I., 2010. Recent rift related volcanism in Afar, Ethiopia, *Earth Planet. Sci. Lett.*, p. in revision.

Fialko, Y., 2006. Interseismic strain accumulation and the earthquake potential on the Southern San Andreas fault system, *Nature*, **441**, 968–971.

Ford, J. P., Blom, R. G., Crisp, J. A., Elachi, C., Farr, T. G., Saunders, R. S., Theilig, E. E., Wall, S. D., & Yewell, S. B., 1989. *Spaceborne radar observations: a guide for Magellen radar-image analysis.*, California Institute of Technology: Jet Propulsion Laboratory.

Forsyth, D. W. & Uyeda, S., 1975. On the relative importance of the driving forces of plate motion., *Geophys. J. R. Astr. Soc.*, **43**, 163–200.

Foulger, G. R., Kahn, C. H., Seeber, G., Einarsson, P., Julian, B. R., & Heki, K., 1992. Post-rifting stress relaxation at the divergent plate boundary in Northeast Iceland, *Nature*, **358**, 488–490.

Freed, A., Burgmann, R., Calais, E., & Freymueller, J., 2006. Stress-dependent power-law flow in the upper mantle following the 2002 Denali, earthquake, *Earth Planet. Sci. Lett.*, **252**, doi:10.1016/j.epsl.2006.10.011.

Fukahata, Y. & Matsu'ura, M., 2005. General expressions for internal deformation fields dua to a dislocation source in a multilayered elastic half-space, *Geophys. J. Int.*, **161**, 507–521.

Fukahata, Y. & Matsu'ura, M., 2006. Quasi-static internal deformation due to a dislocation source in a multilayered elastic/viscoelastic half-space and an equivalence theorem, *Geophys. J. Int.*, **166**, 418–434.

Gashawbeza, E. M., Klemperer, S. L., Nyblade, A. A., Walker, K. T., & Keranen, K. M., 2004. Shear-wave splitting in Ethiopia: Precambrian mantle anisotropy locally modified by Neogene rifting, *Geophysics Research Letters*, **31**, doi:10.1029/2004GL020471.

Ghebread, W., 1998. Tectonics of the Red Sea region reassessed, *Earth-Science Reviews*, **45**, 1–44.

Girdler, R. W. & Southren, T. C., 1987. Structure and evolution of the northern Red Sea, *Nature*, **330**, 716–721.

Girdler, R. W. & Styles, P., 1974. Two-stage sea-floor spreading, *Nature*, **247**, 7–11.

Goldstein, R. M. & Werner, C. L., 1998. Radar interferogram filtering for geophysical applications, *Geophysics Research Letters*, **25(21)**, 4,035–4,038.

Goldstein, R. M., Zebker, H. A., & Werner, C. L., 1988. Satellite radar interferometry: two-dimensional phase unwrapping, *Radio Science*, **23**(4), 713–720.

Grandin, R., Socquet, A., Binet, R., Klinger, Y., Jacques, E., Chabalier, J. B., King, G. C. P., Lasserre, C., Tait, S., Tapponnier, P., Deloeme, A., & Pinzuti, P., 2009. September 2005 Manda Hararo-Dabbahu rifting event, Afar (Ethiopia): Constraints provided by geodetic data, *Geophysics Research Letters*, **114**, doi:10.1029/2008JB005843.

Gudmundsson, A., 1983. Form and Dimensions of Dykes in Eastern Iceland, *Tectonophysics*, **95**, 295–307.

Gudmundsson, A., 1984a. Tectonic Aspects of Dykes in Northwestern Iceland, *Jökull*, **34**, 81–96.

Gudmundsson, A., 1984b. Formation of Dykes, Feeder-dykes, and the Intrusion of Dykes from Magma Chambers, *Bull. Volcanol*, **47**(3), 537–550.

Gudmundsson, A., Friese, N., Galindo, I., & Philipp, S. L., 2008. Dyke-induced reverse faulting in a graben, *Geology*, **36**, 123–126.

Haddon, Y. M., 1995. *Viscoelasticity of Engineering Materials*, Chapman and Hall, London, 1st edn.

Hálfdánarson, G., 1984. Mannfall í kjölfar Skaftárelda (Loss of human lives following the Laki eruption), in *Skaftárelda 1783-84: Ritgerdir og Heimildir*, pp. 139–162, Mál of Menning, Reykjavíc.

Hamling, I. J., Ayele, A., Bennati, L., Calais, E., Ebinger, C., Keir, D., Lewi, E., Wright, T. J., & Yirgu, G., 2009. Geodetic observations of the ongoing Dabbahu rifting episode: new dyke intrusions in 2006 and 2007, *Geophys. J. Int.*, **doi:10.1111/j.1365-246X.2009.04163.x**, 989–1003.

Hanssen, R. F., 2001. *Radar Interferometry: Data Interpretation and Analysis*, Kluwer Acad,. Norwell, MA, USA.

Harris, R. A., 1998. Introduction to special section: Stress triggers, stress shadows, and implications for seismic hazard, *J. Geophys. Res.*, **103**(B10), 24,347–24,358.

Harris, R. A. & Simpson, R. W., 1996. In the shadow of 1857 - the effect of the Great Ft. Tejon Earthquake on subsequent earthquakes in southern California, *Geophysics Research Letters*, **23**(3), 229–232.

Hart, W. K., WoldeGabriel, G., Walter, R. C., & Mertzman, S. A., 1989. Basaltic Volcanism in Ethiopia: Constraints on Continental Rifting and Mantle Interactions, *J. Geophys. Res.*, **94**(B6), 7731–7748.

Hashima, A., Takada, Y., Fukahata, Y., & Matsu'ura, M., 2008. General expressions for internal deformation due to a moment tensor in an elastic/viscoelastic multilayered half-space, *Geophys. J. Int.*, **175**, 992–1012.

Hayward, N. J. & Ebinger, C. J., 1996. Variations in the along-axis segmentation of the Afar Rift System, *Tectonics*, **15**, 244–257.

Heki, K., Foulger, G. R., Julian, B. R., & Jahn, C. H., 1993. Plate Dynamics Near Divergent Boundaries: Geophysical Implications of Postrifting Crustal Deformation in NE Iceland, *J. Geophys. Res.*, **98**(B8), 14,279–14297.

Hofmann, C., Courtillot, V., Feraud, G., Rochette, P., Yirgu, G., Ketefo, E., & Pik, R., 1997. Timing of the Ethiopian flood basalt event and implications for plume birth and global change, *Nature*, **389(6653)**, 838–841.

Hofton, M. A. & Foulger, G. R., 1996a. Postrifting anelastic deformation around the spreading plate boundary, north Iceland. 1. Modeling of the 1987-1992 deformation field using a viscoelastic Earth structure, *J. Geophys. Res.*, **101**(B11), 25403–25421.

Hofton, M. A. & Foulger, G. R., 1996b. Postrifting anelastic deformation around the spreading plate boundary, north Iceland. 2. Implications of the model derived from the 1987-1992 deformation field, *J. Geophys. Res.*, **101**(B11), 25423–25436.

Holbrook, W. S. & Kelemen, P. B., 1993. Large igneious province on the US Atlantic margin and implications for magmatism during continental breakup, *Nature*, **364**, 433–436.

Hooper, J. & Buck, W. R., 1993. The initiation of rifting at constant tectonic force: The role of diffusion creep, *J. Geophys. Res.*, **98**, 16213–16221.

Hreinsdóttir, S., Einarsson, P., & Sigmundsson, F., 2001. Crustal deformation at the oblique spreading Reykjanes Peninsula, SW-Iceland: GPS measurements from 1993-1998, *J. Geophys. Res.*, **106**, 13803–13816.

Hughes, G. W., Varol, O., & Beydoun, Z. R., 1991. Evidence for Middle Oligocene rifting of the Gulf of Aden and for Late Oligocene rifting of the southern Red Sea, *Marine and Petroleum Geology*, **8**, 354–358.

Jacques, E., King, G. C. P., Tapponier, P., Ruegg, J. C., & Manighetti, I., 1996. Seismic activity triggered by stress changes after the 1978 events in the Asal Rift, Djibouti, *Geophysics Research Letters*, **23**(18), 2481–2484.

Jestin, F., Huchon, P., & Gaulier, J. M., 1994. The Somalia plate and the East African Rift System: present-day kinematics, *Geophys. J. Int.*, **116**, 637–654.

Johnson, D., Sigmundsson, F., & Delaney, P., 2000. Comment on "Volume of magma accumulation or withdrawal estimated from surface uplift or subsidence, with the application to the 1960 collapse of Kilauea Volcano" by P.T. Delaney and D.F. McTigue, *Bull. Volcanol*, **61**, 491–493.

Jónsson, S., 2008. Stress interaction between magma accumulation and trapdoor faulting on Sierra Negra volcano, *Tectonophysics*, **doi:10.1016/j.tecto.2008.08.005**.

Jónsson, S., Zebker, H., Segall, P., & Amelung, F., 2002. Fault Slip Distribution of the 1999 M_w 7.1 Hector Mine, California, Earthquake, Estimated from Satellite Radar and GPS Measurements, *Bull., Seis. Soc. Am.*, **92**, 1377–1389.

Kazmin, V., Shifferaw, A., & Balcha, T., 1978. The Ethiopian basement: stratigraphy and possible manner of evolution, *International Journal of Earth Sciences (Geologische Runschau)*, **67**, 531–546.

Kazmin, V. G. & Byakov, A. F., 2000. Magmatism and crustal accretion in continental rifts, *J. Aeronaut. Sci.*, **30**, 555–568.

Keir, D., Hamling, I. J., Ayele, A., Calais, E., Ebinger, C. J., Wright, T. J., Jacques, E., Mohamed, K., Hammond, J. O. S., Belachew, M., Baker, E., Rowland, J., Lewi, E., & Bennati, L., 2009. Evidence for focused magmatic accretion at segment centers from lateral dike injections captured beneath the Red Sea rift in Afar, *Geology*, **37**(1), 59 – 62.

Keller, G. R., Prodehl, C., Mechie, J., Fuchs, K., Khan, M. A., Maguire, P. K. H., Mooney, W. D., Achauer, U., Davies, P. M., Meyer, R. P., Braile, L. W., Nyambok, I. O., & Thompson, G. A., 1994. The East African rift system in the light of KRISP90, *Tectonophysics*, **236**, 465–483.

Kendall, J. M., Stuart, G., Ebinger, C., Bastow, I., & Keir, D., 2005. Magma assisted rifting in Ethiopia, *Nature*, **433**, 614–618.

Kent, G. M., Singh, S. C., Harding, A. J., Sinha, M. C., Orcutt, J. A., Barton, P. J., White, R. S., Bazin, S., Hobbs, R. W., Tong, C. H., & Pyle, J. W., 2000. Evidence from three-dimensional seismic reflectivity images for enhanced melt supply beneath mid-ocean -ridge discontinuities, *Nature*, **406**, 614–618.

Keranen, K., Klemperer, S. L., Gloaguen, R., & working group, E., 2004. Three-demiensional seismic imaging of a protoridge axis in the Main Ethiopian rift, *Geology*, **32**, 949–952.

Kidd, R. G. W. & Cann, J. R., 1974. Chilling statistics indicate an ocean-floor spreading origin for the Troodos complex, Cyprus, *Earth Planet. Sci. Lett.*, **24**(1), 151–155.

King, G. C. P., Stein, R. S., & Lin, J., 1994. Static Stress Changes and the Triggering of Earthquakes, *Bull., Seis. Soc. Am.*, **84**, 935–953.

King, R. W. & Bock, Y., 2005. *Documentation for the GAMIT GPS processing software Release 10.2*, Massachusetts Institute of Technology, Cambridge,USA.

Kruskal, J. B., 1956. On the Shortest Spanning Subtree of a Graph and the Travelling Salesman Problem, *Proc. Am. Math. Soc.*, **7**(1), 48–50.

Kusznir, N. J. & Park, R. G., 1987. *The extensional strength of the continental lithosphere: Its dependence on geothermal gradient, and crustal composition and thickness*, pp. 32–52, Geological Society Special Publication 28; London.

Kusznir, N. J. & Ziegler, P. A., 1992. The mechanics of continental extension and sedimentary basin formation: A simple-shear / pure-shear flexural cantilever model, *Tectonophysics*, **215**, 117–131.

LaBreque, J. L. & Zitellini, N., 1985. Continuous sea-floor spreading in Red Sea, an alternative interpretation of magnetic anomaly pattern, *Am. Assoc. Pet. Geol. Bull*, **69**, 513–524.

LaFemina, P. C., Dixon, T. H., Malservisi, R., Árnadóttir, T., Stirkell, E., Sigmundsson, F., & Einarsson, P., 2005. Geodetic GPS measurements in south Iceland: Strain accumulation and partitioning, *J. Geophys. Res.*, **110**, doi:10.1029/2005JB003675.

Lahitte, P., Gillot, P.-Y., & Courtillot, V., 2003. Silicic central volcanoes as precursors to rift propagation: the Afar case, *Earth Planet. Sci. Lett.*, **207**, 103–116.

Lee, E. H., 1955. Stress analysis in visco-elastic bodies, *Q. Appl. Math.*, **13**, 183–190.

Li, Z., Muller, J. P., & Fielding, E., 2005. Interferometric synthetic aperture radar (InSAR) atmospheric correction: GPS, Moderate Resolution Imaging Spectroradiometer (MODIS), and InSAR integration, *J. Geophys. Res.*, **110**(B03410), doi:10.1029/2004JB003446.

Li, Z., Muller, J. P., Cross, P., Albert, P., Fischer, J., & Bennartz, R., 2006. Assessment of the potential of MERIS near-infrared water vapour products to correct ASAR interferometric measurements, *Int. J. Rem. Sens*, **27**, 349–365.

Macdonald, K. C., 1982. MID-OCEAN RIDGES: Fine Scale Tectonic, Volcanic and Hydrothermal Processes Within the Plate Boundary Zone, *AREP*, **10**, 155–190.

MacKenzie, G. H., Thybo, G. H., & Maguire, P., 2005. Crustal velocity structure across the Main Ethiopian Rift: results from 2-dimensional wide-angle seismic modelling, *Geophys. J. Int.*, **162**, 996–1006.

Maguire, P. K. H., Swain, C. J., Masotti, R., & Khan, M. A., 1994. A crustal and upper-most mantle cross-sectional model of the Kenya rift derived from seismic and gravity-data, *Tectonophysics*, **236**(1-4), 217–249.

Maguire, P. K. H., Keller, G. R., Klemperer, S. L., Mackenzie, G. D., Keranen, K., Harder, S., O'Reilly, B., Thybo, H., Asfaw, L., Khan, M. A., & Amha, M., 2006. Crustal structure of the northern Main Ethiopian Rift from the EAGLE controlled-source survey; a snapshot of incipient lithospheric break-up, in *The Afar Volcanic Province within the East African Rift System. Geological Society, London, Special Publications*, The Geological Society of London.

Mahatsente, R., Jenztsch, G., & Jahr, T., 1999. Crustal structure of the Main Ethiopian Rift from Gravity data: 3-dimensional modelling, *Tectonophysics*, **313**, 363–382.

Makris, J., 1975. *Afar and Iceland - a geophysical comparison*, pp. 379 – 390, Schweizerbart, Stuttgart.

Makris, J. & Ginzburg, A., 1987. The Afar Depression: transition between continental rifting and sea-floor spreading, *Tectonophysics*, **141**, 199–214.

Makris, M. J. & Rhim, R., 1991. Shear-controlled evolution of the Red Sea: pull-apart model, *Tectonophysics*, **198**, 441–466.

Manighetti, I., Tapponnier, P., Gillot, P. Y., Jacques, E., Courtillot, V., Armijo, R., Ruegg, J. C., & King, G., 1998. Propagation of rifting along the Arabia-Somalia plate boundary: Into Afar, *J. Geophys. Res.*, **103**(B3), 4947 – 4974.

Massonnet, D. & Feigl, K. L., 1998. Radar Interferometry and its application to changes in the Earth's surface, *Rev. Geophys.*, **36**, 441–500.

Massonnet, D., Rossi, M., Carmona, C., Adragna, F., Peltzer, G., Feigl, K., & Rabaute, T., 1993. The displacement field of the Landers earthquake mapped by radar interferometry, *Nature*, **364**.

McClusky, S., Reilinger, R., Ogubazghi, G., Amleson, A., Healeb, B., Vernant, P., Sholan, J., Fisseha, S., Asfaw, L., Bendick, R., & Kogan, L., 2010. Kinematics of the southern Red Sea-Afar Triple Junction and implications for plate dynamics, *Geophysics Research Letters*, **37**(L05301), doi:10.1029/2009GL041127.

McKenzie, D., 1978. Some remarks on the development of sedimentary basins, *Earth Planet. Sci. Lett.*, **40**, 25–32.

McKenzie, D. P., Davies, D., & Molnar, P., 1970. Plate Tectonics of the Red Sea and East Africa, *Nature*, **226**, 243–248.

McTigue, D. F., 1987. Elastic Stress and Deformation Near a Finite Spherical Magma Body: Resolution of the Point Source Paradox, *J. Geophys. Res.*, **92**(B12), 12,931 – 12,940.

Mechie, J., Keller, G. R., Prodehl, C., Gaciri, S., Braile, L. W., Mooney, W. D., Gajewski, D., & Sandmeier, K. J., 1994a. Crustal structure beneath the Kenya Rift from axial profile data, *Tectonophysics*, **236**, 179–200.

Mechie, J., Keller, G. R., Prodehl, C., Khan, M. A., & Gaciri, S. J., 1997. A model for the structure, composition and evolution of the Kenya rift, *Tectonophysics*, **278**, 95–119.

Menzies, M. A., Baker, J., Bosence, D., Dart, C., Davidson, I., Hurford, A., Al'Kadasi, M., McClay, K., Al'Kadasi, A., & Yelland, A., 1992. *The timing of magmatism, uplift and crustal extension: Preliminary observations from Yemen*, pp. 293–304, Geological Society Special Publication 68; London.

Mériaux, C. & Jaupart, C., 1995. Simple fluid dynamic models of volcanic rift zones, *Earth Planet. Sci. Lett.*, **136**, 223–240.

Mogi, K., 1958. Relations between the Eruptions of Various Volcanoes and the Deformations of the Ground Surfaces around them, *Bull., Earthq. Res. Inst.*, **239**, 352–367.

Montenat, C., d'Estevou, P. O., & Purser, B. H., 1998. *The Suez Rift and the northwestern Red Sea Neogene sedimentation and tectonic evolution*, pp. 173–199, Oxford and IBH Publishing Company, New Dehli, Iindia.

Morland, L. W. & Lee, E. H., 1960. Stress analysis for linear viscoelastic materials with temperature variation, *Trans. Soc. Rheol*, **4**, 233–263.

Muller, R. D., Sdrolias, M., Gaina, C., & Roest, W. R., 2008. Age, spreading rates and spreading symmetry of the world's ocean crust, *Geochemistry Geophysics, Geosystems*, **9**, doi:10.1029/2007GC001743.

Nooner, S. L. & Chadwick, W. W., 2010. Volcanic inflation measured in the caldera of Axial Seamount: Implications fro magma supply and future eruptions, *Geochemistry Geophysics, Geosystems*, **10**(2), doi:10.1029/2008GC002315.

Nooner, S. L., Bennati, L., Calais, E., Hamling, I. J., Wright, T. J., Buck, W. R., & Lewi, E., 2009. Post-rifting relaxation in the Afar region, Ethiopia, *Geophysics Research Letters*, **36**(L21308), doi:10.1029/2009GL040502.

Nyblade, A. A. & Pollack, H. N., 1992. A gravity model for the lithosphere in western Kenya and northeastern Tanzania, *Tectonophysics*, **212**(3-4), 257–267.

Okada, Y., 1985. Surface Deformation due to Shear and Tensile Faults in a Half-space, *Bull., Seis. Soc. Am.*, **75**, 1135–1154.

Okada, Y., 1992. Internal Deformation due to Shear and Tensile Faults in a Half-space, *Bull., Seis. Soc. Am.*, **82**(2), 1018–1040.

Okada, Y. & Kasahara, K., 1990. Earthquake of 1987, off Chiba, central Japan and possible triggering of the eastern Tokyo earthquake of 1988, *Tectonophysics*, **172**, 351–364.

Olsen, K. H. & Morgan, P., 1995. *Progress in understanding continental rifts*, Elsevier - Amsterdam.

Oppenheimer, C. & Francis, P., 1998. Implications of longeval lava lakes for geomorphilogical and plutonic processes at Erta 'ale volcano, north Afar, *J. Volcanol. Geotherm. Res.*, **80**, 101–111.

Pagli, C., Sigmundsson, F., Árnadóttir, T., Einarsson, P., & Sturkell, E., 2006. Deflation of the Askja volcanic system: Constraints on the deformation source from combined inversion of satellite radar interferograms and GPS measurements, *J. Volcanol. Geotherm. Res.*, **152**, 97–108.

Pagli, C., Wright, T. J., Ebinger, C. J., Barnie, T. D., & Ayele, A., 2009. Inflate, Pause, Erupt, Recharge: the 1008 Alu eruption in the Erta'Ale volcanic system (Ethiopia), *EOS Trans. AGU*, **90**(54), Fall meet. Suppl, T31B–1813.

Pallister, J. S., 1987. Magmatic history of Red Sea rifting: Perspective from the central Saudi Arabia coastal plain, *Geol. Soc. Am. Bull*, **98**, 400–417.

Parsons, B., Wright, T., Rowe, P., Andrews, J., Jackson, J., Walker, R., Khatib, M., Talebian, M., Bergman, E., & Engdahl, E. R., 2006. The 1994 Sefidabeh (eastern Iran) earthquakes revisited: new evidence from satellite radar interferometry and carbonate dating about the growth of an active fold above a blind thrust fault, *Geophys. J. Int.*, **164**, 202 – 217.

Pedersen, R. & Sigmundsson, F., 2004. Insar based sill model links spatialy offset areas of deformation and seismicity for the 1994 unrest episode at Eyjafjallajokull volcano, Iceland, *Geophysics Research Letters*, **31**(14), L14610.

Pedersen, R., Jónsson, S., Árnadóttir, T., Sigmundsson, F., & Feigl, K. L., 2003. Fault slip distribution of two June $M_W6.5$ earthquakes in South Iceland estimated from joint inversion of InSAR and GPS measurements, *Earth Planet. Sci. Lett.*, **213**, 487–502.

Pedersen, R., Sigmundsson, F., & Masterlark, T., 2009. Rheologic controls on inter-rifting deformation of the Northern Volcanic Zone, Iceland, *Earth Planet. Sci. Lett.*, **281**, 14–26.

Peltzer, G., Crampe, F., Hensley, S., & Rosen, P., 2001. Transient strain accumulation and fault interaction in the Eastern Californian shear zone, *Geology*, **21**, 975–978.

Pollitz, F. F. & Sacks, I. S., 1995. Consequences of stress changes following the 1891 Nobi earthquake, Japan, *Bull., Seis. Soc. Am.*, **85**, 796–807.

Pollitz, F. F. & Sacks, I. S., 1996. Viscosity structure beneath northeast Iceland, *J. Geophys. Res.*, **101**(B8), 17771–17793.

Pollitz, F. F. & Sacks, I. S., 1997. The 1995 Kobe, Japan, earthquake: A long-delayed aftershock of the offshore 1944 Tonankai and 1946 Nankaido earthquakes, *Bull., Seis. Soc. Am.*, **87**, 1–10.

Press, W. H., Flannery, B. P., Teukolsky, S. A., & Vetterling, W. T., 1986. *Numerical Recipes*, Cambridge University Press.

Reasenberg, P. A. & Simpson, R. W., 1992. Response to regional seismicity to the static stress change produced by the loma prieta earthquake, *Science*, **255**, 1687–1690.

Rivalta, E. & Segall, P., 2008. Magma compressibility and the missing source for some dyke intrusions, *Geophysics Research Letters*, **35**, doi:10.1029/2007GL032521.

Rosen, P. A., Hensley, S., Joughin, I. R., Li, F. K., Madsen, S. N., Rodriguez, E., & Goldstein, R. M., 2000. Synthetic aperture radar interferometry, *Proceedings of the IEEE*, **88(3)**, 333–382.

Rosen, P. A., Hensley, S., Peltzer, G., & Simons, M., 2004. Updated Repeat Orbit Interferometry Package Released, *EOS Trans. AGU*, **85(5)**, 35.

Rosendahl, B. R., Kilembe, E., & Kaczmarick, K., 1992. Comparison of the Tanganyika, Malawi, Rukwa and Turkana rift zones from analyses of seismic reflection data, *Tectonophysics*, **213**, 235–256.

Rowland, J. V., Baker, E., Ebinger, C. J., Keir, D., Kidane, T., Biggs, J., Hayward, N., & Wright, T. J., 2007. Fault growth at a nascent slow-spreading ridge: 2005 Dabbahu rifting episode, Afar, *Geophys. J. Int.*, **171**, 1226–1246.

Rubin, A. & Pollard, D., 1988. Dyke-induced faulting in rift zones in Iceland and Afar, *Geology*, **16**, 413–417.

Ruegg, J. C., 1975. *Main results about the crustal and upper mantle structure of the Djibouti region TFAI*, pp. 89 – 107, Schweizerbart, Stuttgart.

Scharoo, R. & Visser, P., 1998. Precise orbit determinatino and gravity field improvement for the ERS satellites, *J. Geophys. Res.*, **103**, 8113–8127.

Schilling, J. G., Kingsley, R., Hanan, B., & McCully, B., 1992. Nd-Sr-Os isotropic variations along the Gulf of Aden: evidence for mantle-plume lithosphere interaction, *J. Geophys. Res.*, **97**, 10,927 – 10,966.

Schmidt, D. A. & Burgmann, R., 2003. Time-dependent land uplift and subsidence in the Santa Clara valley, California, from a large interferometric, synthetic aperture radar dataset, *J. Geophys. Res.*, **108**, 8534–8543.

Schouten, H., Klitgord, K. D., & Whitehead, J. A., 1985. Segmentation of mid-ocean ridges, *Nature*, **317**(19), 225–229.

Segnör, A. M. & Burke, K., 1978. Relative timing of rifting and volcanism on earth and its tectonic implications, *Geophysics Research Letters*, **5**, 419–421.

Sigmundsson, F., 2006. *Iceland Geodynamics: Crustal Deformation and Divergent Plate Tectonics*, Springer-Praxis, Chichester.

Singh, S. C., Crawford, W. C., Carton, H., Seher, T., Combier, V., Cannat, M., Canales, J. P., Düsünür, D., Escartin, J., & Mirander, J. M., 2006. Discovery of a magma chamber and faults beneath a Mid-Atlantic Ridge hydrothermal field, *Nature*, **442**(7106), 1029–1032.

Solomon, S. C., Richardson, R. M., & Bergman, E. A., 1980. Tectonic stresses: Models and magnitudes, *J. Geophys. Res.*, **85**, 6086–6092.

Souriot, T. & Brun, J. P., 1992. Faulting and block rotation in the Afar triangle, East Africa; the Danakil "crank arm" model, *Geology*, **20**, 911–914.

Specht, T. D. & Rosendahl, B. R., 1989. Architecture of the Lake Malawi Rift, East Africa, *J. Aeronaut. Sci.*, **8**(2-4), 355–382.

Stamps, D. S., Calais, E., Saria, E., Hartnady, C., Nocquet, J. M., Ebinger, C. J., & Fernandes, R. M., 2008. A kinematic model for the East African Rift, *Geophysics Research Letters*, **35**(L05304), doi:10.1029/2007GL032781.

Steckler, M. S., 1985. Uplift and extension in the Gulf of Suez, indications of induced mantle convection, *Nature*, **317**, 135–139.

Stein, R. S., 1999. The role of stress transfer in earthquake occurrence, *Nature*, **402**, 605–609.

Steketee, J. A., 1958. On volterra's dislocation in a semi-infinite elastic medium, *Can. J. Phys.*, **36**, 192–205.

Stern, R. J., 1985. Arc assembly and continental collision in the Neoproterozoic East African Orogen—implication for the consolidation of Gondwanaland, *Annual Review of Earth and Planetary Sciences*, **22**, 319–351.

Stuart, G., Bastow, I., & Ebinger, C., 2006. Crustal structure of the northern Main Ethiopian Rift from receiver function studies, in *The Afar Volcanic Province within the East African Rift System. Geological Society, London, Special Publications*, The Geological Society of London.

Sturkell, E., Einarsson, P., Sigmundsson, F., Geirsson, H., Ólafsson, H., Pedersen, R., de Zeeuw-van Dalfsen, E., Linde, A. T., Sacks, S. I., & Stefánsson, R., 2006. Volcano geodesy and magma dynamics in Iceland, *J. Volcanol. Geotherm. Res.*, **150**, 14–34.

Sultan, M., Becker, R., Arvidson, R. E., Shore, P., Stern, R. J., Alfy, Z. E., & Guinness, E. A., 1992. Nature of the Red Sea crust: a controversy revisited, *Geology*, **20**, 593–596.

Swain, C. J., Khan, M. A., Wilton, T. J., Maguire, P. K. H., & Griffiths, D. H., 1981. Seismic and gravity surveys in the Lake Baringo-Tugen Hills area, Kenya-rift-valley, *Journal of the Geological Society*, **138(JAN)**, 93–101.

Tefera, M., Chernet, T., & Haro, W., 1996. Explanation of the Geological Map of Ethiopia, *Ethiopian Institute of Geological Surveys, Addis Ababa*, **3**, 79.

Thordarson, T. & Self, S., 2003. Atmospheric and environmental effects of the 1783-1784 Laki eruption: A review and reassessment, *J. Geophys. Res.*, **108**(D1), doi:10.1029/2001JD002042.

Tiberi, C., Ebinger, C., Ballu, V., Stuart, G., & Oluma, B., 2005. Inverse models of gravity data from the Red Sea - Aden -East African Rift triple junction zone, *Geophys. J. Int.*, **163**, 775 – 787.

Toda, S., Stein, R. S., & Sagiya, T., 2002. Evidence from the 2000 Izu Islands swarm that seismicity is governed by stressing rate, *Nature*, **419**, 58–61.

Toda, S., Stein, R., Lin, J., & Sevilgen, V., 2008. Coulomb 3.1.09: Greaphic-rich deformation and stress change software for earthquake, tectonic and volcano research and teaching, `http://quake.usgs.gov/research/deformation/modeling/coulomb/newfeatures.html`.

Tolstoy, M., Bohnenstiehl, D. R., & Edwards, M. H., 2001. Seismic character of volcanic activity at the ultraslow-spreading Gakkel Ridge, *Geology*, **29**, 1139–1142.

Tolstoy, M., Cowen, J. P., Blake, E. T., Fornari, D. J., Rubin, K. H., Shank, T. M., Waldhauser, F., Bohnenstiehl, D. R., Forsythe, D. W., Holmes, R. C., Love, B., Perfit, M. R., Weekly, R. T., Soule, S. A., & Glazer, B., 2006. A sea-floor spreading event captured by seismometers, *Science*, **314**, 1920–1922.

Tryggvason, E., 1980. Subsidence events in the Krafla area, North Iceland, *J. Geophys.*, **47**, 141–153.

Tryggvason, E., 1984. Widening of the Krafla fissure swarm during the 1975-1981 Volcano-tectonic episode, *Bull. Volcanol*, **47(1)**, 47–69.

Tryggvason, E., 1994. Surface deformation at the Krafla volcano, North Iceland, 1982-1992, *Bull. Volcanol*, **56**, 98–107.

Turcotte, D. L. & Schubert, G., 2002. *Geodynamics*, Cambridge University Press, 2nd edn.

Utstins, I. A., Renne, P. R., Wolfenden, E., Baker, J., & amd M. Menzies, D. A., 2002. Matching conjugate rifted margins: $\hat{4}0$Ar/$\hat{3}9$Ar chronostratigraphy of pre- and syn-rift bimodal flood volcanism in Ethiopia and Yemen, *Earth Planet. Sci. Lett.*, **198**, 289–306.

Vadon, H. & Sigmundsson, F., 1997. Crustal deformation from 1992-1995 at the Mid-Atlantic Ridge, SW Iceland, mapped by satellite radar interferometry, *Science*, **275**, 193–197.

Vail, J. R., 1985. Pan-African (late Precambrian) tectonic terranes and reconstruction of the Arabia-Nubian Shield, *Geology*, **13**, 839–842.

Van, N. P., Boyer, D., Mouël, J. L. L., & Coutillot, V., 1981. Identification of a magma chamber in the Ghoubbet-Asal rift (Djibouti) from a magnetotelluric experiment, *Earth Planet. Sci. Lett.*, **208**, 372–380.

Varet, J., 1978. Geology of Central and Southern Afar (Ethiopia and Djibouti Republic), *Centre Natl. de la Rec. Sci., Paris*, p. map and 124 pp.

Vellutini, P., 1990. The Manda-Inakir Rift, Republic of Djibouti: a comparison with the Asal Rift and its geodynamic interpretation, *Tectonophysics*, **172**, 141–153.

Vigny, C., Huchon, P., Khanbari, J. C., & Asfaw, L. M., 2006. Confirmation of Arabia plate slow motion by new GPS data in Yemen, *J. Geophys. Res.*, **111**(B02402).

Vigny, C., de Chablieer, J.-B., Ruegg, J.-C., P. Huchon, K. L. F., Cattin, R., Asfaw, L., & Kanbari, K., 2007. Twenty-five years of geodetic measurements along the Tadjoura-Asal rift system, Djibouti, East Africa, *J. Geophys. Res.*, **112**(B06410).

Walter, R. & Amelung, F., 2006. Volcano-earthquake interaction at Mauna Loa volcano, Hawaii, *J. Geophys. Res.*, **111**, B05204.

Wegener, A., 1929. *The Origin of the Continents and Oceans*, London, UK: Methuen.

Wernicke, B., 1985. Uniform-sense normal simple shear of the continental lithosphere, *Can. J. Earth Sci.*, **22**, 108–125.

Wiley, C. A., 1965. Pulsed doppler radar methods and apparatus, *United States Patent No*, **3,196,436**.

WoldeGabriel, G., Aronson, J., & Walter, R., 1990. Geology, geochronology, and rift basin development in the central sector of the Main Ethiopian Rift, *Geol. Soc. Am. Bull*, **102**, 183–197.

Wolfenden, E., Ebinger, C., Yirgu, G., Deino, A., & Ayalew, D., 2004. Evolution of the northern Main Ethiopian rift: birth of a triple junction, *Earth Planet. Sci. Lett.*, **224**, 213–228.

Wright, R., Flynn, L. P., Garbeil, H., Harris, A. J. L., & Pilger, E., 2004a. MODVOLC: near-real-time thermal monitoring og global volcanism, *J. Volcanol. Geotherm. Res.*, **135**, 29–49.

Wright, T., Parsons, B., & Fielding, E., 2001. Measurements of interseismic strain accumulation across the North Anatolian Fault by satellite radar interferometry, *Geophysics Research Letters*, **28**(6), 2117–2120.

Wright, T., Parsons, B., England, P., & Fielding, E., 2004b. InSAR observations of low slip rates on the major faults of western Tibet, *Science*, **305**, 236–239.

Wright, T. J., 2000. *Crustal Deformation in Turkey form Synthetic Aperture Radar Interferometry*, Ph.D. thesis, Faculty of Physical Sciences, University of Oxford.

Wright, T. J., Parsons, B. E., Jackson, J. A., Haynes, M., Fielding, E. J., & England, P. C., 1999. Source Parameters of the 1 October 1995 Dinar (Turkey) earthquake from SAR interferometry and seismic bodywave modelling, *Earth Planet. Sci. Lett.*, **172**, 23–37.

Wright, T. J., Lu, Z., & Wicks, C., 2003. Source model for the M_w 6.7, 23 October 2002, Nenana Mountain Earthquake (Alaska) from InSAR, *J. Geophys. Res.*, **30**(18).

Wright, T. J., Lu, Z., & Wicks, C., 2004c. Constraining the Slip Distribution and Fault Geometry of the M_W 7.9, 3 November 2002, Denali Fault Earthquake with Interferometric Synthetic Aperture Radar and Global Positioning System Data, *Bull., Seis. Soc. Am.*, **94**(6B), 175–189.

Wright, T. J., Parsons, B. E., & Lu, Z., 2004d. Towards mapping surface deformation in three dimensions using InSAR, *Geophysics Research Letters*, **31**(LO1607), doi:10.1029/2003GL018827.

Wright, T. J., Ebinger, C., Biggs, J., Ayele, A., Yirgu, G., Keir, D., & Stork, A., 2006. Magma-maintained rift segmentation at continental rupture in the 2005 Afar dyking episode, *Nature*, **442**, 291–294.

Yirgu, G., Ayele, A., & Ayalew, D., 2006. Recent seismovolcanic crisis in northern Afar, Ethiopia, *EOS Trans. AGU*, **87(33)**, 325 – 336.

Yirgu, G., Ayele, A., Fisseha, S., Chernet, T., & Damtev, A. K., 2007. Afar field trip preliminary report, `http://www.see.leeds.ac.uk/afar/afar_text/preliminary_report.pdf`.

Zebker, H., Rosen, P., & Goldstein, R. M., 1994. On the derivation of coseismic displacement fields using differential radar interferometry: The Landers earthquake, *J. Geophys. Res.*, **99**, 19,617–19,634.